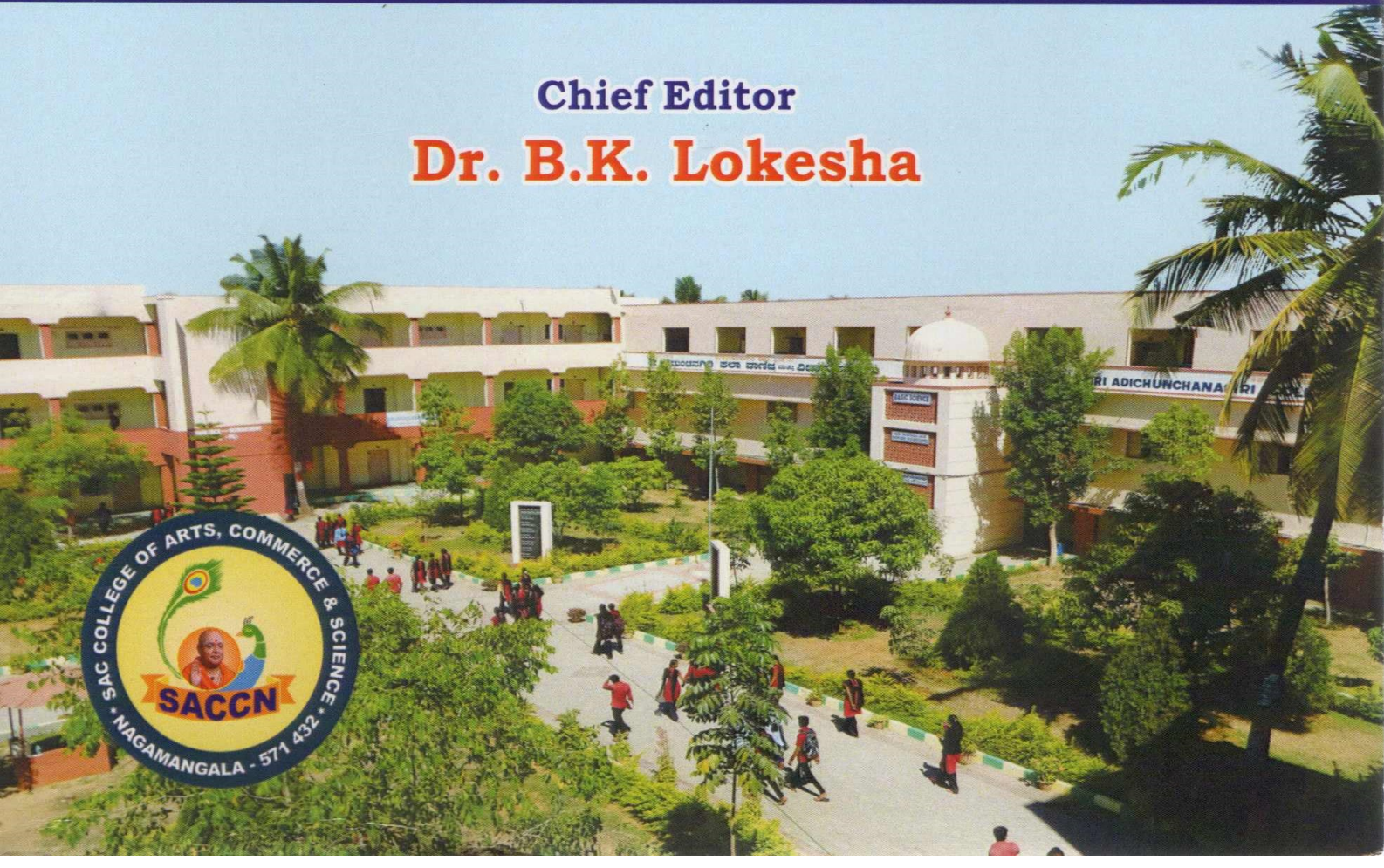


RECENT TRENDS IN PHYSICS WITH EMPHASIS ON DISCOVERY OF GOD PARTICLE

Chief Editor

Dr. B.K. Lokesh



RECENT TRENDS IN PHYSICS WITH EMPHASIS ON DISCOVERY OF GOD PARTICLE

The volume of the scholarly papers presented on 02nd February 2021 on
International Level Seminar held at BGS Auditorium, SAC College, Nagamangala

Chief Editor
Dr. B. K. Loksha

Editorial Board
Dr. T. Shivalingaswamy
Prof. S. Boregowda
Dr. M.K.Manjunath
Prof. M.P. Sunilkumar



**Sri Adichunchanagiri College of
Arts, Commerce and Science**

Nagamangala, Mandya Dist, Karnataka State, India-571432

“Recent Trends in Physics with Emphasis on Discovery of God Particle”

(The volume of the scholarly papers presented on 02nd February 2021 on International Level Seminar held at BGS Auditorium, SAC College, Nagamangala)

Website : www.sacngm.org

Blog : www.saccngm.blogspot.in

E-mail : saccngm@gmail.com

Edited by :

Dr. B.K. Loksha, Principal, SAC College, Nagamangala

Dr. T. Shivalingaswamy, HoD of Physics, Govt. College (Autonomous), Mandya

Prof. S. Boregowda, HoD of Physics, SAC College, Nagamangala

Dr. M.K. Manjunath, HoD of Kannada, SAC College, Nagamangala

Prof. M.P. Sunilkumar, HoD of English, SAC College, Nagamangala

Published by : **Niveditha Prakashana**
#3437, 1st Floor, 4th Main Road,
9th Cross, Shastrinagar, BSK 2nd Stage
Bengaluru- 560028, Mob: 9448733323

ISBN No. : **978-93-88956-41-3**

Pages : xvi+276=292

Year of Publication : 2021

Edition : First

Paper Used : 70 Gsm Maplitho

@ Copyright : Individual Authors

Type Setting : Dr. M.K. Manjunath

Cover Page : Sahanagraphics, Bangalore, M : 9342196255

Printed : Om Sri Priters, Bengaluru

The Management

The establishment of Sri Adichunchanagiri College of Arts, Commerce & Science in the lovely and serene atmosphere of Sri Adichunchanagiri Kshetra in 1975 was a discovery of an oasis in a desert for the students in and around Nagamangala Taluk. The college is an example of Gurukula system even in the modern times. The college was established under the auspice of Sri Adichunchanagiri Sikshana Trust, a reputed religious, social and cultural institution in Karnataka State, India. The then President of the trust his Holiness Jagadguru Padmabhushana Sri Sri Sri Dr. Balagangadharanatha Mahaswamiji started the college with the Prime intention of providing higher education to the rural students who were deprived of the same for want of accessibility.

The present 72nd pontiff of Sri Adichunchanagiri Mutt and the president of Sri Adichunchanagiri Sikshana Trust (R.), His Holiness Jagadguru Sri Sri Sri Dr. Nirmalanandanatha Mahaswamiji, a great visionary and an ocean of knowledge, is giving a new dimension to the institution with a cultural-spiritual touch and a scientific outlook.

Today, higher education is no longer a luxury but a necessity. Our Swamiji has made higher education not only accessible but also affordable to the rural students. Majority of the students at Kshethra are boarders of the mutt.

The Place

To comply with the policy of having a First Grade College in every Taluk Headquarters the college was shifted to Nagamangala town in 1988.

Majority of the students are commuting every day from various corners of Nagamangala Taluk and even from the adjacent taluks like Mandya, K.R.Pet (Mandya Dist), Turuvekere & Kunigal (Tumkur Dist), C.R. Patna (Hassan Dist) etc., Thanks to the Govt. of Karnataka for providing concessional bus-pass to the students.

The College

In 1975, B.A degree course had HEP, HES & HEG combinations. B.Com degree was also introduced in the same year. Presently, there are HEP, HES, HEG & HEE combinations. B.Sc., Degree was introduced from the academic year 2006-07 with Physics, Maths, Computer Science and Chemistry as electives.

Post-graduation course in Commerce (M.Com) was started from the academic year 2014-15. The college is permanently affiliated to the prestigious University of Mysore.

The Seminar

Theoretical and Particle Physics is a branch of Physics that uses and extends fundamental theories of physics to understand the basic structure of the universe. A grasp of this subject demands a thorough knowledge of physical process, theories, mathematical and numerical methods. Anchored in basic truth and natural sciences, it has applications across various domains of science and in practical devices.

This seminar intends to be among the best academic efforts of the institution to bring together the global participants to share their ideas on the recent developments and prevailing trends in the fundamental aspects related to Theoretical and Particle Physics. It is a platform for fostering communication among Researchers, Teachers as well as the scholars zealous of bettering their understanding of the subject and the techniques involved therein. The chief purpose of the seminar is to acquaint the participants with the current research trends on the topic addressed and to throw considerable light on the subject 'God Particle'.

Topics for the Technical Sessions

1. Physics of Organic Light Emitting Diodes (OLEDs) - (Session – 1)
2. Discovery of God Particle (Higg's Boson) - (Session - 2)

Sub-Themes and Areas of Discussion

1. Quantum Computation and Information.
2. Quantum Cryptography.
3. Quantum Teleportation.
4. Theoretical and Experimental aspects of Nano science and Nano Technology.
5. Mechanics of Microelectronic Mechanical System (MEMS)
6. Paradoxes in Relativity (Special and General).
7. Quantum Mechanics of Superconductor.
8. Cryogenics Theory.
9. Quantum Statistics.
10. Nuclear and Particle Physics.

Chief Patron

His Holiness Jagadguru

Sri Sri Sri Dr. Nirmalanandanatha Mahaswamiji

President, SAC Mutt & SAC Shikshana Trust (R.)

Patrons

Sri Sri Purushothamanandanatha Swamiji

General Secretary, SAC Shikshana Trust (R.)

Sri SriPrasannanatha Swamiji

General Secretary, SAC Mutt.

Seminar Director

Dr. B.K. Lokesh, Principal

Seminar Co-ordinator

Sri S. Boregowda, H.O.D. of Physics

Members of Advisory Committee

Dr. N.S. Ramegowda, CEO, SAC Shikshana Trust(R.)

Dr. T. Shivalingaswamy, Asst. Professor & HOD of Physics,
Govt. College (Autonomous), Mandya

Dr. N.G. Prakash, Special Officer CMJ..CP Grams.. &
E-Janaspandana, DCE, Bengaluru

Organizing Secretaries

Prof. B.S. Ramakrishnegowda, IQAC Coordinator

Smt. M. Gunavathi, H.O.D of Computer Science

Sri C.T. Chandrashekar, Asst. Professor, Dept. of Physics

Sri A.J. Sharathbabu, Asst. Professor, Dept. of Mathematics

Kum. B.J. Deepa, Asst. Professor, Dept. of Mathematics

Technical Co-ordinator

Dr. M.K. Manjunath

Asst. Professor, Dept. of Kannada

|| JAI SRI GURUDEV ||



Yugayogi Paramapoojya Jagadguru Padmabhushana
Sri Sri Sri Dr. Balagangadharanatha Mahaswamiji
Founder President, Sri Adichunchanagiri Shikshana Trust (R.)

|| JAI SRI GURUDEV ||



Paramapoojya Jagadguru
Sri Sri Sri Dr. Nirmalanandanatha Mahaswamiji
President, Sri Adichunchanagiri Shikshana Trust (R.)

Divine Message

|| Jai Sri Gurudev ||

Physics is one of the most vital scientific disciplines, and its fundamental goal is to comprehend how the universe behaves. Physics is also one of the ancient academic disciplines. Over much of the past two millennia, physics, chemistry, biology and certain branches of mathematics were part of natural philosophy, but during the Scientific Revolution in the 17th Century these natural sciences emerged as unique research endeavours in their own way. Understanding the recent developments in every field will result in the holistic development.

Isaac Newton's laws of motion and universal gravitation were major milestones in classical physics. The discovery of new laws in thermodynamics, chemistry and electromagnetics are the results of greater research efforts during the Industrial Revolution.

Albert Einstein, the renowned physicist and one among the two pillars of modern physics worked on the photoelectric effect and the theory of relativity led to a revolution in 20th century physics. Modern physics began in the early 20th century with the work of Max Planck in quantum theory and Albert Einstein's theory of relativity. $E = Mc^2$ is Albert Einstein's theory of special relativity that expresses the fact that mass and energy are the same physical entity and can be changed into each other. In the equation, the increased relativistic mass (M) of a body times the speed of light squared (c^2) is equal to the kinetic energy (E) of that body. Both these theories came about due to inaccuracies in classical mechanics in certain situations.

The process of 'unifying' forces continues even today and electromagnetism and the weak nuclear force are now considered to be two aspects of the electroweak interaction. Physics hopes to find an ultimate

reason as to why nature is as it is. The Higgs boson is a particle in the Standard Model of physics. In the 1960s Peter Higgs was the first person to suggest that this particle might exist. The Higgs particle is a boson. Bosons are thought to be particles which are responsible for all physical forces. The Higgs boson is an elementary particle in the Standard Model of particle physics produced by the quantum excitation of the Higgs field, one of the fields in particle physics theory. It is named after physicist Peter Higgs who in 1964 along with five other scientists proposed the Higgs mechanism to explain why some particles have mass. This mechanism required that spinless particle known as a boson should exist with properties as described by the Higgs Mechanism theory. This particle is called the Higgs boson. The Higgs boson has often called the God Particle.

International Seminars on “Recent Trends in Physics with Emphasis on Discovery of God Particles” is a way of creating the awareness among various researchers and in turn make them contribute more to the field of physics. We wish all the very best for the team and congratulate the principal and staff members for their continuous efforts in the research field. We wish all the best in all the future endeavours of everyone.

We beseech the Divine blessings of Lord Kalabyraveswara and Poojya Sri Guruji. May God bless you all...

Ever Yours in the Service of the Lord,



(Sri Nirmalanandanatha Swamiji)

Message

The pioneering attempt of Sri Adichunchanagiri College of Arts, Commerce and Science Nagamangala, in organising an International Seminar on **“Recent trends in Physics with emphasis on the discovery of God Particle”**, is not only appreciable in motivating the faculty members but also in dreaming about participating in such ventures by the students for every such pioneering attempts, which would cultivate leadership skills among them and marks a difference in the present context. I congratulate the principal Dr. B.K. Lokesh and his research mentality faculty team for organising this International level seminar.

It is pleasure to know that the organising team is successful in getting as many as 31 research articles, of which five from abroad, 4 from different States other than Karnataka and the remaining from the state of Karnataka. Sri Adichunchanagiri College of Arts, Commerce and Science, Nagamangala, is being the first higher education institution started by our Sri Adichunchanagiri Shikshana Trust(R.) management in 1975 under the benevolent leadership, guidance and support of our most reverend Jagadguru Byravaikya Padmabhushana Sri Sri Sri Dr. Balagangadharanatha Mahaswamiji and now being guided, encouraged and supported by our great mentor and spiritual leader, the president of our SAST, his Holiness Jagadguru Sri Sri Sri Dr. Nirmalanandanatha Mahaswamiji and proficiently assisted by Poojya Sri Sri Purushothamanandanatha Swamiji.

Our country is now on the threshold of 21st Century and now being guided by National Education Policy 2020, which is providing both great opportunities and equally big challenges in the era of Accreditations (NAAC, NBA), ranking of similar higher education institutions (NIRF) and global ranking institutions (THE).

The role and importance of Physics in this context is well projected by our Paramapoojya Sri Sri Sri Dr. Nirmalanandanatha Mahaswamiji in his

message, which is worth to be noted by all the participating research scholars, faculty members and students.

Sri Adichunchanagiri College of Arts, Commerce and Science Nagamangala, has already obtained B++ grade under NAAC accreditation and is making strenuous effort to get 'A' grade in the upcoming NAAC accreditation, and such a kind of International level seminars will become a feather in its cap besides getting other honours. The door is still more open for our college to register for National ranking of Institutions (NIRF) and looking for becoming an Autonomous college being the first Higher Education Institutions of our SAST.

I sincerely wish a great success in this International level seminar and my advice to faculty and students to take best advantage of these ventures. My good wishes and continued support to all our SAST Institutions with special attention to Sri Adichunchanagiri College of Arts, Commerce and Science Nagamangala will always be there. Finally, I wish for hurdle less conduct of this event.

Dr. N.S. Ramegowda
CEO, SAST (R.)
Former Vice-Chancellor, KSOU, Mysuru

From the Chief Editor's Desk.....

The present era is age of remarkable surge in Innovations and discoveries. Every stream of knowledge is advancing at an unprecedented pace. Covid – 19 pandemic that severely interrupted economic and social activities across the globe, proved incapable of extinguishing the zeal for research. Research activities in the domain of Physical Sciences too continued unabated, unravelling the mysteries of the physical world and boosting the quality of day to day life. Commensurate to this creative imagination of the Avant grade researchers is the responsive imagination and avidity of the physics Academia across the world to learn these novel ideas.

‘Current trends in Physics’ is a mirror to the contemporary research work carried out across the globe and hopes to kindle interest among the students, researchers, teachers and aficionados of physics to acquaint themselves with the knowledge added.

The fact that this book is the outcome of the labour of love of several Physics enthusiasts is incontestable. However, it was conceptualised by none other than His Holiness Sri Sri Sri Dr. Nirmalanandanatha Mahaswamiji, the 72nd pontiff Sri Adichunchanagiri Mutt, President of Adichunchanagiri Shikshna Trust(R), a vast repository of knowledge – both oriental and occidental, and a great visionary. It was his ‘Let there be light all around’ spirit that inspired us to present this book to the Academic world.

My sincere gratitude to Poojya Sri Sri Purushothamanandaswamiji, General Secretary, Adichunchanagiri Shikshna Trust(R), Poojya Sri Sri Prasannanathaswamiji, General Secretary, Sri Adichunchanagiri Mutt for their blessings and inspiration at various stages of this International Level Seminar. I express my

deepest gratitude to Dr. NS. Ramegowda, CEO, Sri Adichunchanagiri Shikshana Trust.

The hard work, spirit of service and enthusiasm of the Department of Physics and the Internal Assurance cell (IQAC) of our college, the organising committee, Advisory Committee and the Technical Committee towards strategizing and conducting this international Seminar on “Recent Trends in Physics with Emphasis on the Discovery of God Particle” is absolutely worthy of commendation. The support lent by the teaching and nonteaching staff of our college in holding this event is admirably acknowledged. The research contributions of the participants from the substance of this book and their efforts both at research and documentation are deeply appreciated. The editorial committee toiled unceasingly to publish this volume and richly deserve our praise.

A final word – If this volume instills a spirit of enquiry and a habit of deep thinking among readers, our efforts at bringing out this volume will have found fruition. It is this that we seek.

Dr. B.K. Loksha
Principal

From the desk of Editors....

My sincere pranamas to His Holiness Jagadguru Sri Sri Sri Dr. Nirmalanandanatha Mahaswamiji, the President of the Adichunchanagiri Shikshana Trust(R), His Holiness Sri Sri Sri Purushothamanandanatha swamiji, the general secretary of SAC Shikshana Trust(R) and His Holiness Sri Sri Sri Prasannanatha swamiji, the general secretary of SAC Mutt, for their blessings in bringing out this book.

“I would like to tell the young men and women before me not to lose hope and courage. Success can only come to you by courageous devotion to the task lying in front of you”.

--- Dr. A.P.J. Abdul Kalam

My sincere thanks to Sri S. Boregowda-seminar coordinator, Dr. B.K. Lokesha-seminar director, Smt. M. Gunavathi-organising secretary and Dr. M.K Manjunath for giving me this task of editing the research articles and bringing this proceedings book.

In this hard time of Covid-19 pandemic, it was a challenging task to organise an international conference in a rural college. I appreciate the courage shown by the organising committee and the support extended by the management.

Teaching and research are two sides of the same coin which helps in improving higher education and creating a better society around us. However, in the present scenario, our education system is challenged by heterogeneous conditions such as infrastructural, social and regional issues. The quality of research has always been overlooked in our country due to such issues. Many countries around the world are trying to reinforce the quality of research along with higher education, India

too has come up with the National Education Policy (NEP) 2020 to revamp the whole education system. At this apt time, Sri Adichunchanagiri college of Arts, Commerce and Science, Nagamangala, has come forward to organise a one day international conference to encourage research culture in educational institutions on par with the global standards.

We received a good response to our invitation. It was a challenging task to select the research articles for publication. Based on the themes, the proceeding book covers research articles on various theoretical principles of physics such as variational method, WKB method, quantum cryptography etc. Several research articles focussing on synthesis, characterisation of various nanostructures for potential applications are included. There are also articles on new generation micro-electro mechanical systems.

I hearty thank Internal Quality Assurance Cell, Organising committee, Advisory committee, Technical committee of one day international level seminar on “Recent trends in Physics with emphasis on the discovery of God Particle”, for their support.

I greatly appreciate the efforts of other members of editorial committee for their contribution in bringing out this book.

Best Regards

Dr. T. Shivalingaswamy
On behalf of the editorial team

Index

| Sl. No. | Name of the Paper | Name of the Authors | Page No |
|---------|--|---|-----------|
| 01. | Ground State Energy of Relativistic Quantum Harmonic Oscillator using Variational Principle | Felan Amal Akhil E. J Aiswarya Vijayan Adithya Prabhakaran V | 01 |
| 02. | Eigenenergies of a Relativistic Particle in an Infinite Range Linear Potential Using WKB Method for Different Boundaries | Anjana Simon Athira K Shashank Rao Felan Amal | 06 |
| 03. | Additional Variation Parameter to Gaussian Function and its Effect on Ground State Energy | Akhil E .J Adithya Prabhakaran V Aiswarya Vijayan Felan Amal | 13 |
| 04. | Evolution of Lorentzian Light Wave Packet | Rashmi P.E Dr. B. A Kagali Dr. T. Shivalingaswamy | 19 |
| 05. | A comparative study of hydrogen bond interactions and intermolecular close contacts in 2, 3, 4, 6, 7, 8 substituted quinoline derivatives | Dr. M. Prabhuswamy | 22 |
| 06. | Printing of Organic Light Emitting Devices for large area applications | Dr. Wim Deferme | 32 |
| 07. | Intellectual and Cultural Impact of Relativity | S. Boregowda C. T. Chandrashekhara M. Gunavathi | 51 |
| 08. | Mondriaan paintings by large area organic light emitting diodes | Maikel Kellens Musa Aydogan Bram Claessen Jerey Gorissen Inge Verboven Rachith S. N Dr. Ir. Wim Deferme | 65 |
| 09. | Quantum Cryptography | Shobha .M | 77 |
| 10. | Design and Simulation of Photoacoustic setup for Formaldehyde Gas Sensing | Rachith S.N Veda S.N | 84 |
| 11. | Synthesis and Characterisation of Sodium Oxide Nanoparticles | Dr. Mallikarjuna I. Triveni M.K. | 94 |

| | | | |
|-----|---|--|------------|
| | | Dr. Shivalingaswamy T. | |
| 12. | Microwave Oven Aided Synthesis of Potassium Oxide Nanoparticles | Eliezer Vishwas S.N.Namitha Dr. T. Shivalingaswamy | 105 |
| 13. | Hierarchical CeO₂:Sm³⁺ architectures synthesized via solution Combustion route for microwave and electronic device applications | M. V. Hemantha Reddy T. Sreenivasulu Reddy Dr. K. M. Girish | 116 |
| 14. | Zinc oxide nanoparticles; Green synthesis using Moringa oleifera leaves, characterization and study on its Anticorrosive property | K. C. Suresh Dr. G. N. Venkatareddy Dr. A. Balamurugan | 124 |
| 15. | Synthesis and characterization of TiO₂ and TiO₂ doped PVA films | Dr. M. Vishwas | 132 |
| 16. | Hydrothermal Synthesis of Single Phase Monoclinic ZrO₂ Nano Crystals: Structural and Optical Studies | Dr. M. Rajendra Prasad Anthony Seleen | 137 |
| 17. | Nanomanufacturing and Industrial Application of Nanotechnologies | Bakula Keerthi Chandra | 143 |
| 18. | A study of Nano structures-CQDs | Dr. Rohini V.S Nandini Y.V Nayana J. Rachana J. Rajanish T.N | 152 |
| 19. | A Review on Synthesis of Carbon Nanotubes and Its Applications | M. Thavarani N. Abinaya | 158 |
| 20. | High Energy Electron Beam Irradiation Effects on Ultra High Molecular Weight Polyethylene (UHMWPE) | Dr. Ashok G. V Dr. Shiva Prasad N. G Dr. Niranjana Prabhu.T Dr. Harish .V | 166 |
| 21. | Photon attenuation studies on human teeth and its substitutes | Dr. Harish .V Dr. Shiva Prasad N. G Narasimhamurthy K. N Shashikumar T. S Navitha .G Dr. Ashok G. V | 176 |
| 22. | Measurement of indoor radon, thoron and their progeny concentration and Estimation of annual inhalation dose rates in Chikmagalur city, Karnataka, India | Dr. Srinivasa .E Guruswamy .K Soundar .R Suresh .S Dr. Rangaswamy D. R | 188 |

| | | | |
|-----|--|--|------------|
| | | Dr. Sannappa .J | |
| 23. | Concentration of radon in drinking water samples around Nuggihalli-Holenarsipur schist belts, Karnataka State, India | Dr. R. S. Niranjana Dr. C. Ningappa V. Nandakumar C. N. Harshavardhana | 197 |
| 24. | Intermolecular Interactions Studies in Binary Mixtures of Curcumin Particles with Primary Alcohols | Dr. Manjunatha .M. S Dr. Sannappa .J | 208 |
| 25. | Comparative Study of the Elemental Concentration in Soil Sample of Open Site and Solid Waste Sites of Bengaluru Region of Karnataka, India | Dr. Sudarshan .M Sathya Narayana .P Gowtham .S Shilpa .D Jagadeesha B. G | 213 |
| 26. | Application and Development of MEMS Technology in Industry | Raghavendra J L | 224 |
| 27. | MEMS Sensor Technologies for Humanist Applications in Safety and Environmental Sensing | C. T. Chandrashekhara S. Boregowda M. Gunavathi | 232 |
| 28. | Normal Co-Ordinate Analysis of High Temperature Superconductor $\text{PrH}_{0.1-x}\text{Ba}_2\text{Cu}_3\text{O}_7$. | Dr. K. Sonamuthu | 241 |
| 29. | Study of Phase transition of mixture of Smectic and Cholesteric Liquid Crystal with temperature | Dr. P. Srinivas M. Sushma Dr. J. Mahadeva | 254 |
| 30. | Thermo-Optical Studies on Reentrant Smectic Phase of Liquid Crystalline Materials | Dr. T.N. Govindaiah | 259 |
| 31. | Estimation of Inhalation and Ingestion dose from Radon concentration in drinking water from Yallapur and Sirsi Taluks of Uttara Kannada district, Karnataka, India. | Suresh .S Srinivasa .E Sandeep Dongre Sannappa .J | 266 |

Ground State Energy of Relativistic Quantum Harmonic Oscillator using Variational Principle



- Felan Amal
- Akhil E. J
- Aiswarya Vijayan
- Adithya Prabhakaran V

Abstract

In this paper we have extended the variational method to relativistic quantum harmonic oscillator and obtain its ground state energy. The effect of additional variational parameters is studied and the obtained results are compared with those available in literature.

Keywords : Variational method, relativistic system, harmonic oscillator.

Introduction

Quantum mechanics has been a successful theory to solve only very few problems in a mathematically rigorous sense. To understand experimental observations and to describe them realistically the theoretician needs an as wide as possible repertoire of approximation methods. Hence, one is obliged to replace not achievable exact solutions by well-founded approximations, which do not adulterate the essential physical aspects.

Although a few approximations like perturbation theory, variational method, WKB approximations etc. are available in non-relativistic quantum mechanics, the number of approximations techniques in relativistic quantum mechanics are limited.

In this paper we extend the variational method to obtain the upper bound to energy of relativistic quantum harmonic oscillator. The operator method is used to

estimate the ground state energy and effect of adding constants or a polynomial in the wave function on energy.

Variational principle applied to relativistic quantum harmonic oscillator

We choose the trial wave function to be,

$$\Psi(x) = Ae^{-\alpha x^2} \quad (1)$$

a Gaussian, where α is a variational parameter and A is the normalization constant with value

$$A = \left(\frac{2\alpha}{\pi}\right)^{\frac{1}{4}}$$

Consider the relativistic energy expression,

$$W^2 = p_x^2 c^2 + m^2 c^4$$

Following the instruction of B.Mirza et.al, we couple the momentum with an interaction as follows:

$$p_x \rightarrow p_x - im\omega x$$

$$p_x^\dagger \rightarrow p_x + im\omega x$$

Under such coupling we have

$$p_x^2 = \frac{1}{2} [p_x p_x^\dagger + p_x^\dagger p_x]$$

With the above transformations energy expression becomes,

$$W = \sqrt{p_x^2 c^2 + m^2 \omega^2 x^2 c^2 + m^2 c^4}$$

Following the variational method we evaluate the expectation value of W

$$\langle W^2 \rangle = \langle p_x^2 c^2 + m^2 \omega^2 x^2 c^2 + m^2 c^4 \rangle \quad (2)$$

$$\langle W^2 \rangle = \left\langle -\hbar^2 c^2 \frac{d^2}{dx^2} + m^2 x^2 \omega^2 c^2 + m^2 c^4 \right\rangle$$

on solving we get

$$\langle W^2 \rangle = \hbar^2 c^2 |A|^2 \sqrt{\frac{\pi\alpha}{2}} + |A|^2 \frac{m^2 \omega^2 c^2}{2} \frac{\sqrt{\pi}}{(2\alpha)^{\frac{3}{2}}} + m^2 c^4 \quad (3)$$

We have from quantum mechanics

$$\Delta W = \sqrt{\langle W^2 \rangle - \langle W \rangle^2}$$

If W is sharp, then $\Delta W=0$,

$$\langle W^2 \rangle = \langle W \rangle^2 \text{ or } \langle W \rangle = \sqrt{\langle W^2 \rangle} \quad (4)$$

Therefore,

$$\langle W \rangle = \sqrt{\hbar^2 c^2 |A|^2 \sqrt{\frac{\pi\alpha}{2}} + |A|^2 \frac{m^2 \omega^2 c^2}{2} \frac{\sqrt{\pi}}{(2\alpha)^{\frac{3}{2}}} + m^2 c^4}$$

On substitution of A we get

$$\langle W \rangle = \sqrt{\hbar^2 c^2 \alpha + \frac{m^2 \omega^2 c^2}{4\alpha} + m^2 c^4} \quad (5)$$

Minimising $\langle w \rangle$ with respect to α , we have

$$\frac{d}{d\alpha} \langle W \rangle = \frac{1}{2} \left(\hbar^2 c^2 \alpha + \frac{m^2 \omega^2 c^2}{4\alpha} + m^2 c^4 \right)^{-\frac{1}{2}} \cdot \left(\hbar^2 c^2 - \frac{m^2 \omega^2 c^2}{4\alpha^2} \right) = 0$$

$$\left(\hbar^2 c^2 - \frac{m^2 \omega^2 c^2}{4\alpha^2} \right) = 0$$

$$\alpha = \frac{m\omega}{2\hbar} \quad (6)$$

Substituting (6) in (5) we get

$$\langle W \rangle_{min} = \left(\frac{\hbar c^2 m\omega}{2} + \frac{\hbar m\omega c^2}{2} + m^2 c^4 \right)^{\frac{1}{2}}$$

$$\langle W \rangle_{min} = \sqrt{\hbar m\omega c^2 + m^2 c^4}$$

In the next case we introduce another variational parameter b as follows,

$$\Psi(x) = A e^{-ax^2 + bx} \quad (7)$$

With this choice the normalization constant is

$$|A|^2 = \sqrt{\frac{2a}{\pi}} e^{-b^2/2a} \quad (8)$$

Evaluating $\langle W \rangle$:

Solving for (2) With the wave function given by (7) we have

$$\langle W^2 \rangle = \left\langle -\hbar^2 c^2 \frac{d^2}{dx^2} + m^2 \omega^2 x^2 c^2 + m^2 c^4 \right\rangle$$

or

$$\langle W^2 \rangle = a \hbar^2 c^2 + \frac{m^2 \omega^2 c^2}{4a^2} (a + b^2) + m^2 c^4 \quad (9)$$

Again assuming W to be sharp we have

$$\langle W \rangle = \sqrt{a \hbar^2 c^2 + \frac{m^2 \omega^2 c^2}{4a} + \frac{m^2 \omega^2 c^2 b^2}{4a^2} + m^2 c^4} \quad (10)$$

Minimizing with respect to a and b,

$$\frac{d}{db} \langle W \rangle = \frac{1}{2} \left(a \hbar^2 c^2 + \frac{m^2 \omega^2 c^2}{4a} + \frac{m^2 \omega^2 c^2 b^2}{4a^2} + m^2 c^4 \right)^{-1/2} \frac{m^2 \omega^2 c^2 b}{2a^2} = 0$$

This yields $b = 0$.

$$\text{Then, } \frac{d}{da} \langle W \rangle = \frac{1}{2} \left(a \hbar^2 c^2 + \frac{m^2 \omega^2 c^2}{4a} + \frac{m^2 \omega^2 c^2 b^2}{4a^2} + m^2 c^4 \right)^{-1/2} \left(\hbar^2 c^2 - \frac{m^2 \omega^2 c^2}{4a^2} \right) = 0$$

or

$$a = \frac{m\omega}{2\hbar} \quad (11)$$

substituting back to equation (10) we get

$$\langle W \rangle_{min} = \sqrt{\frac{1}{2} m \omega \hbar c^2 + \frac{1}{2} m \omega c^2 \hbar + m^2 c^4} = \sqrt{m \omega \hbar c^2 + m^2 c^4} \quad (12)$$

on expanding (12) binomially we get

$$W = mc^2 + \frac{1}{2} \omega \hbar + \frac{1}{8} \frac{\omega^2 \hbar^2}{mc^2} + \dots \quad (13)$$

Clearly the total relativistic energy is decomposed into the rest energy, non-relativistic energy and relativistic corrections. This result is in good agreement with that obtained by Nagalakshmi Rao *et. al.*

Conclusion

Here we have extended the variational method to relativistic quantum harmonic oscillator where we have chosen two different trial wave functions. It was found that the ground state energy is same for both wave functions and the obtained results are exactly matching with the solutions available in literature. The effect of additional variational parameters doesn't alter the energy value. This method may be used to estimate ground state energy of similar relativistic quantum systems.

Acknowledgement

We thank Dr. T Shivalingaswamy for his valuable suggestions and fruitful discussions.

References

1. Strange P, Relativistic Quantum Mechanics, Cambridge: Cambridge University Press, 1998
2. J J Sakurai, Modern Quantum Mechanics, Addison-Welsey, 1995
3. Nagalakshmi Rao and B. Kagali. On the energy spectrum of the one-dimensional Klein Gordon oscillator, 05, 2007.
4. T. Shivalingaswamy and B. Kagali, Rayleigh-Ritz variational method for spin-less relativistic particles, Int. Journal of Science and Research, Vol. 3 Issue 8, August 2014.

* * * * *

❖ **Felan Amal, Akhil E J, Aiswarya Vijayan, Adithya Prabhakaran V**,
Department of Physics, St. Philomena's College (Autonomous), Mysore -
570015, Karnataka, India, **Ph:** 9632878721, **E-mail:**
felanamal@stphilos.ac.in

Eigenenergies of a Relativistic Particle in an Infinite Range Linear Potential Using WKB Method for Different Boundaries

❖ **Anjana Simon**
❖ **Athira K**
❖ **Shashank Rao**
❖ **Felan Amal**

Abstract

In this paper we study the eigenenergies of a relativistic particle in an infinite range linear potential using WKB method with one and two rigid boundaries. The obtained results are compared with the standard results available in literature.

Keywords : WKB Method, Relativistic Particle.

Introduction

One of the most prominent feature of universe is motion . Mechanics, the branch of science, was developed to describe the motion and different forces in nature. The Newtonian mechanics deals with motion of ordinary particle moving with ordinary speed. Relativistic mechanics deals with motion of particles with high speed, nearly speed of light. But it is found that they are inadequate to explain the behaviour of particles in the microscopic fields.

Quantum mechanics was developed to overcome these inadequacies. In quantum mechanics, a state of a particle is represented by a wave function, which contains all the information regarding the particle. Wave function of a particle is obtained by solving Schrödinger equation. But it is not always easy to get the exact solution of Schrödinger equation. So in last century a number of approximation methods have been developed to obtain information about the system which can't solve by Schrödinger equation. Some of the important approximation methods are Perturbation theory, Variational principle, WKB approximation.

In this study we are using WKB approximation. The aim of our discussion is to understand the work done by T. Shivalingaswamy and B.A Kagali on 'Eigenenergies of a relativistic Particle in an Infinite Range linear potential using WKB method' and extend that to one rigid wall and two rigid wall boundaries.

WKB Approximation

The Wentzel Kramer Brillouin method is useful for the approximate treatment of systems with slowly varying potentials, that is the potential which are almost constant over a region in the order of de Broglie wave length. WKB method is a semi-classical approximation. Here in this method we are using the power series expansion of wave function in terms of reduced Planck's constant . We will consider the points where kinetic energy equal to potential energy, and find a matching wave function. This leads to quantization condition, from which approximate values of energies determined for ground states and excited states. The extension of this approximation to relativistic case is possible if relativistic equation is reduced to Schrodinger equation form. Here in this study we discuss the same by considering a spin-less particle in an infinite range linear potential

Choose a simple well shaped effective potential with two classical turning points x_1 and x_2 as shown in figure 1

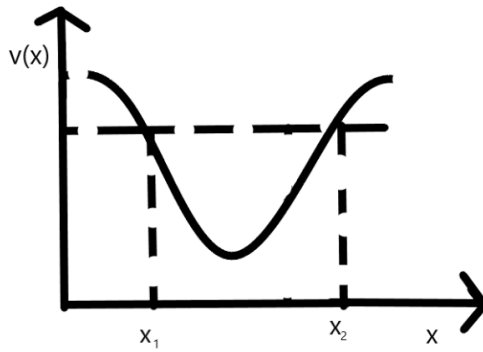


Figure 1: Well shaped potential with two classical turning points.

In Relativistic Quantum theory, the one dimensional relativistic equation can be transformed into Schrödinger form as:

$$\frac{d^2\psi}{dx^2} + \frac{2M}{\hbar^2} [E_{eff} - v_{eff}] \psi = 0 \quad (1)$$

$$\text{Effective energy } E_{eff} = \frac{E^2 - M^2 c^4}{2Mc^2}$$

$$\text{Effective potential } v_{eff} = \frac{2EV(x) - V^2(x)}{2Mc^2}$$

Second term in equation(1) become

$$\left[\frac{2M}{\hbar^2} E_{eff} - V_{eff} \right] = \frac{P_R^2}{\hbar^2} \quad (2)$$

where $P_R = \sqrt{\frac{(E - v(x))^2 - M^2 c^4}{c^2}}$, momentum of relativistic particle

$$\frac{d^2 \Psi}{dx^2} + \frac{P_R^2}{\hbar^2} \Psi = 0 \quad (3)$$

When potential varies smoothly, the wave function become

$$\Psi(x) = \phi(x) \exp \pm \frac{i}{\hbar} \int P_R(x) dx$$

The WKB Approximation fails near the turning points so we need the exact solution of Schrödinger equation near x_1, x_2 . Let us now look for the exact solution of Schrödinger equation near x_2

If $|x - x_2|$ is small, within the region $|x - x_2|$ we can represent a potential by straight line whose slope equal to the potential at turning points

Then we get $V(x) = E + (x - x_2)F_0$

$$\frac{d^2 \psi}{dx^2} - \frac{2nF_0}{\hbar^2} (x - x_2) \psi(x) = 0$$

By applying change of variable, we can write the above equation as

$$\frac{d^2 \psi(y)}{dy^2} - y \psi(y) = 0 \quad (4)$$

Solution of above equation can be written in the form of Airy functions.

Near classical turning points, momentum of the particle is

$$P^2(x) = -(2m\hbar F_0)^{2/3} y$$

Using this momentum we solve WKB equation and insert solution on Airy function to get wave function at $x = x_2$ as

$$\psi_2(x) = \frac{C_2}{\sqrt{P(x)}} \sin \frac{i}{\hbar} \int P(x') dx' + \frac{\pi}{4} \quad (4)$$

Similarly at $x = x_1$

$$\Psi_{1(x)} = \frac{D}{\sqrt{P(x)}} \sin \frac{i}{\hbar} \int p(x') dx' + \frac{\pi}{4} \quad (5)$$

Since (3) and(4) represents the same wave function in the same region both equations are equal .Then the equation become $D \sin \theta_1 = C_2 \sin \theta_2$.This satisfy the following relation $\theta_1 + \theta_2 = (n + 1)\pi$ and $D = (-1)^n C_2$

Define quantization condition as

$$\int_{x_1}^{x_2} P_R(x) dx = \left(n + \frac{1}{2}\right) \pi \hbar \quad (6)$$

Here choose potential $V(x) = k|x|$

Define condition at turning points and take $x = \frac{\epsilon}{k} y$,get limits as

$x_{1,2} = \pm \left[1 - \frac{mc^2}{E}\right]$ then quantization rule become

$$\frac{2\epsilon}{kc} \int_0^{\frac{1-mc^2}{E}} [E^2(1-y)^2 - m^2c^4]^{\frac{1}{2}} dy = \left(n + \frac{1}{2}\right) \pi \hbar \quad (7)$$

On solving the above equation,

$$E\sqrt{E^2 - m^2c^4} - \left(n + \frac{1}{2}\right) \pi \hbar kc = m^2c^4 [\log(E + \sqrt{E^2 - m^2c^4}) - \log(mc^2)] \quad (8)$$

It is a transcendental equation and can be solve using octave.

We now extend this method to single rigid wall and two rigid wall boundary conditions.

For Single rigid wall, the quantization is given by,

$$\int_{x_1}^{x_2} P(x) dx = \left(n + \frac{3}{4}\right) \pi \hbar \quad (9)$$

Using this condition transcendental equation becomes

$$E\sqrt{E^2 - m^2c^4} - \left(n + \frac{3}{4}\right) \pi \hbar kc = m^2c^4 [\log(E + \sqrt{E^2 - m^2c^4}) - \log(mc^2)] \quad (10)$$

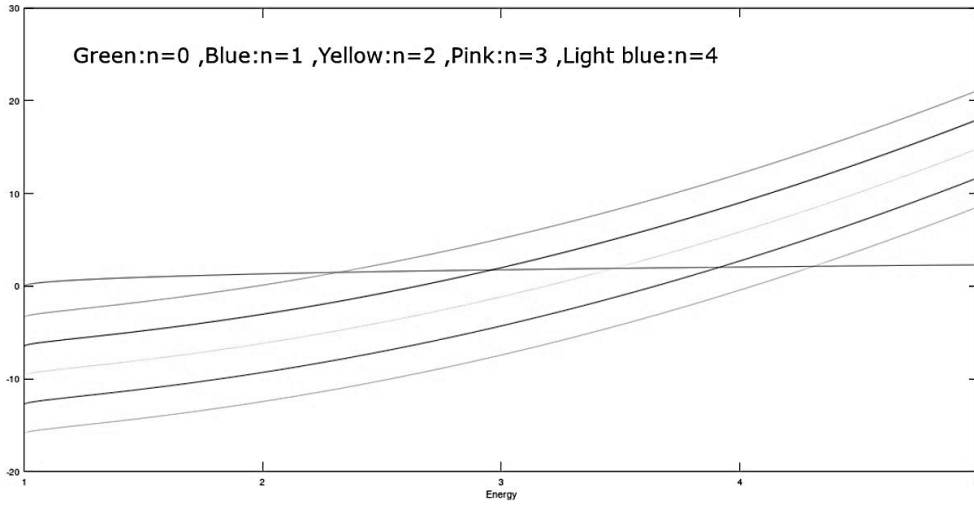


Figure 2: A plot of LHS Vs RHS of equation (10) for different values of n.

For two rigid wall, quantization rule takes the form

$$\int_{x_1}^{x_2} P(x) dx = n\pi\hbar \quad (11)$$

Using this condition transcendental equation

$$E\sqrt{E^2 - m^2c^4} - n\pi\hbar = m^2c^4[\log(E + \sqrt{E^2 - m^2c^4}) - \log(mc^2)] \quad (12)$$

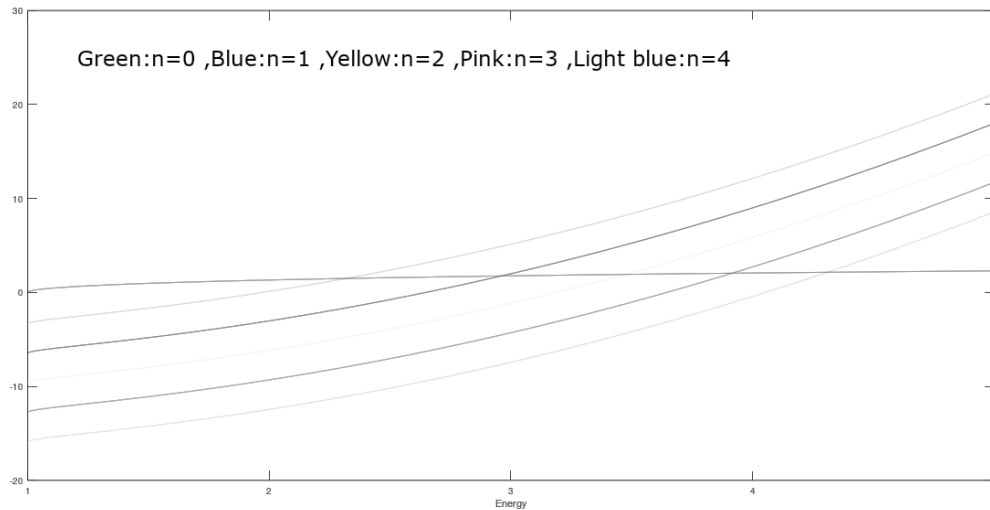


Figure 3: A plot of LHS Vs RHS of equation (12) for different values of n.

The transcendental equations (10) and (12) are plotted using octave as shown in figure 2 and figure 3.

| n | E_{WKB} nonrelativistic | E_{WKB} relativistic | E_{WKB} Single rigid wall | E_{WKB} Two rigid wall | E_{exact} |
|----------|---|--|---|--|-------------------------------|
| 1 | 1.842 | 1.807 | 1.9664 | 1.5016 | 1.855 |
| 3 | 3.240 | 2.801 | 2.9034 | 2.6049 | 3.244 |

The above table, the eigenenergies of non-relativistic, relativistic particle with no boundaries, single and two rigid wall is evaluated by WKB method and is compared with the exact value (Casaubon, 2007) for $n=1$ and 3

Conclusion:

Here we have studied the work on 'Eigenenergies of a Relativistic Particle in an Infinite Range Linear Potential using WKB methods' by Prof. T Shivalingaswamy and Prof. B. A Kagali and extended that to single rigid wall and two rigid wall cases. We found that eigenenergies obtained are matching with the exact energies especially for lower values of n as in case of open boundary. This appears to correspond to single rigid wall condition, thus this method surely an important technique to obtain eigenenergies of particle with specific potential for which solutions are not available in the relativistic regime with different boundaries.

Acknowledgement

We thank Dr. T Shivalingaswamy for his valuable suggestions and fruitful discussions.

Reference :

1. T. Shivalingaswamy and B. A Kagali, Eigenenergies of a Relativistic particle in an Infinite Range Linear Potential Using WKB method, European Journal of Physics Education, vol 2 No2.

2. R Shankar (2010), Principles of Quantum mechanics, 2nd edition, Springer, Third Indian reprint.
3. Nouredine Zettili, Quantum mechanics -concepts and applications, Wiley, 2018.
4. Casaubon, R. (2007). Variation Principle for a Linear Potential. Turk. J. Phy.31, 117-121.

* * * * *

❖ **Anjana Simon, Athira K, Shashank Rao, Felan Amal**, P.G. Department of Physics, St. Philomena's College (Autonomous), Mysore-570015, Karnataka, India, **Ph:** 9632878721, **E-mail:** felanamal@stphilos.ac.in

Additional Variation Parameter to Gaussian Function and its Effect on Ground State Energy



- Akhil E .J
- Adithya Prabhakaran V
- Aiswarya Vijayan
- Felan Amal

Abstract

In this paper we obtain the ground state energy of quantum harmonic oscillator using the Rayleigh-Ritz variational method. The effect of additional variational parameters are studied.

Keywords: Variational Method, Harmonic Oscillator.

Introduction

Classical mechanics is a precise and powerful theory that explains the motion of the macroscopic bodies. However, as we move to microscopic domain, the classical description fails to explain the dynamics of physical systems. Finding solutions to such microscopic physical systems led to the development of quantum mechanics, which was successful in manifesting the discreteness of nature, even though the concepts conflicted with the notions derived from observations of the everyday world. Using de Broglie hypothesis Erwin Schrödinger developed an equation which was the primary key which unlocked the secrets of microscopic world.

In quantum mechanics a moving particle is represented by the normalized wave function ψ which contains all the information regarding the dynamics of the particle. Solving Schrödinger's equation gives the possible eigenstates and eigenvalues for a given potential. This equation can be exactly solved for a limited number of systems. But for most of the cases Schrödinger's equation can't be solved

exactly to find the eigenfunctions of the Hamiltonian, where we must rely on the approximate methods. A few popular approximation methods that are used to study such systems include time independent and dependent Schrödinger perturbation theory, the variational method and the WKB method.

In our present work we explore the utility of variational principle to obtain an upper bound for ground state energy for quantum harmonic oscillator using trial wave functions with two variational parameters.

Energy of Quantum Harmonic Oscillator

Variational theorem states that the energy of any trial wave function E is always an upper bound to the exact ground state energy. The basic idea of the variational method is to guess a trial wave function for the problem, which consists of some adjustable parameters called variational parameters. These parameters are adjusted until the energy of the trial wave function is minimized. The resulting trial wave function and its corresponding energy are variational method approximations to the exact wave function and energy.

$$E_{gs} \leq \langle \psi | H | \psi \rangle \equiv \langle H \rangle$$

Suppose if we want to find the ground state energy for the one- dimensional harmonic oscillator

$$H = -\frac{\hbar^2}{2m} \frac{d^2}{dx^2} + \frac{1}{2} m \omega^2 x^2 \quad (1)$$

Of course, we already know the exact answer, in this case, $E_g = \frac{1}{2} \hbar \omega$.

We will add a constant to the exponential of the trial wave function and check and study its effects on the ground state energy.

Let the trial wave function be

$$\Psi(x) = A e^{-bx^2+c} \quad (2)$$

Where A is the normalization constant having the value

$$A = \left(\frac{2b}{\pi}\right)^{\frac{1}{4}} e^{-c}$$

Now, we evaluate the expectation value of the Hamiltonian using the relation $\langle H \rangle = \langle T \rangle + \langle V \rangle$. where T and V are the kinetic and potential energy operators of the harmonic oscillator.

Consider

$$\begin{aligned} \langle T \rangle &= \frac{-\hbar^2}{2m} |A|^2 e^{2c} \int_{-\infty}^{+\infty} e^{-bx^2} \frac{d^2}{dx^2} (e^{-bx^2}) dx = \\ &= \frac{-\hbar^2}{2m} |A|^2 e^{2c} \int_{-\infty}^{+\infty} e^{-bx^2} \frac{d}{dx} (-2xb e^{-bx^2}) dx \end{aligned}$$

or

$$\langle T \rangle = \frac{-\hbar^2}{2m} |A|^2 e^{2c} \int_{-\infty}^{+\infty} e^{-bx^2} (4b^2 x^2 e^{-bx^2} - 2b e^{-bx^2}) dx \quad (3)$$

solving the integral gives

$$\langle T \rangle = \frac{\hbar^2}{2m} |A|^2 b \sqrt{\frac{\pi}{2b}} e^{2c}$$

Substituting the value of $|A|^2$ we get

$$\langle T \rangle = \frac{\hbar^2}{2m} b \quad (4)$$

Again,

$$\langle V \rangle = \frac{1}{2} m\omega^2 |A|^2 e^{2c} \int_{-\infty}^{+\infty} e^{-2bx^2} (x^2) dx = \frac{1}{2} m\omega^2 |A|^2 e^{2c} \frac{1}{2} \frac{\sqrt{\pi}}{(2b)^{\frac{3}{2}}}$$

Substituting the values of $|A|^2$, we get

$$\langle V \rangle = \frac{m\omega^2}{8b}$$

Therefore,

$$\langle H \rangle = \langle T \rangle + \langle V \rangle = \frac{\hbar^2 b}{2m} + \frac{m\omega^2}{8b} \quad (5)$$

Minimizing with respect to b;

$$\frac{d}{db} \langle H \rangle = \frac{\hbar^2}{2m} - \frac{m\omega^2}{8b^2} = 0 \quad \rightarrow \quad b = \frac{m\omega}{2\hbar}$$

Therefore, we have,

$$\langle H \rangle_{\min} = \frac{1}{2} \hbar \omega$$

Now let's choose an additional linear term in the exponential of the wave function in the form

$$\Psi(x) = Ae^{-ax^2+bx} \quad (6)$$

$$\text{Where } |A|^2 = \sqrt{\frac{2a}{\pi}} e^{-b^2/2a}$$

Evaluating $\langle T \rangle$:

$$\langle T \rangle = \frac{-\hbar^2}{2m} |A|^2 \int_{-\infty}^{+\infty} e^{-ax^2+bx} \frac{d^2}{dx^2} [e^{-ax^2+bx}] dx \quad (7)$$

or

$$\langle T \rangle = \frac{-\hbar^2}{2m} |A|^2 \int_{-\infty}^{+\infty} e^{-2ax^2+bx} [4a^2x^2 - 4abx - 2a + b^2] dx \quad (8)$$

Evaluating the integral,

$$4a^2 \int_{-\infty}^{+\infty} x^2 e^{-2ax^2+bx} dx = (a + b^2) \sqrt{\frac{\pi}{2a}} e^{b^2/2a} \quad (9)$$

$$-4ab \int_{-\infty}^{+\infty} x e^{-2ax^2+2bx} dx = -2b^2 \sqrt{\frac{\pi}{2a}} e^{b^2/2a} \quad (10)$$

$$-2a \int_{-\infty}^{+\infty} e^{-2ax^2+2bx} dx = -2a \sqrt{\frac{\pi}{2a}} e^{b^2/2a} \quad (11)$$

$$b^2 \int_{-\infty}^{+\infty} e^{-2ax^2+2bx} dx = b^2 \sqrt{\frac{\pi}{2a}} e^{b^2/2a} \quad (12)$$

Substituting equation (9),(10),(11) and (12) in equation (8), we get

$$\langle T \rangle = \frac{a\hbar^2}{2m} |A|^2 \sqrt{\frac{\pi}{2a}} e^{b^2/2a}$$

Substituting the value of $|A|^2$

$$\langle T \rangle = \frac{a\hbar^2}{2m}$$

Similarly,

$$\langle V \rangle = \frac{1}{2} m\omega^2 |A|^2 \int_{-\infty}^{+\infty} x^2 e^{-2ax^2+bx} dx$$

$$\langle V \rangle = \frac{m\omega^2}{8a} + \frac{m\omega^2 b^2}{8a^2} \quad \text{----- (13)}$$

Therefore,

$$\langle H \rangle = \frac{a\hbar^2}{2m} + \frac{m\omega^2}{8a} + \frac{m\omega^2 b^2}{8a^2}$$

According to variational principle, this exceeds E_g for any 'a' and 'b' to get the tightest bound. Let's minimize $\langle H \rangle$ with respect to a and b

$$\frac{d}{db} \langle H \rangle = \frac{2m\omega^2 b}{8a^2} = 0$$

Which implies $b = 0$.

Again,

$$\frac{d}{da} \langle H \rangle = \frac{\hbar^2}{2m} - \frac{m\omega^2}{8a^2} = 0$$

or

$$a = \frac{m\omega}{2\hbar}$$

Therefore finally we get

$$\langle H_{\min} \rangle = \frac{m\omega}{2\hbar} \frac{\hbar^2}{2m} + \frac{m\omega^2}{8} \frac{2\hbar}{m\omega}$$

$$= \frac{1}{2} \hbar\omega$$

Conclusion

In the present method we have chosen different trial wave functions for the harmonic oscillator problem and verified that addition of constants to the exponential of the trial wave functions doesn't induce any change in the ground

state energy of the system. Further, this method with two variational parameters can be used to obtain precise values of any quantum system.

Acknowledgement

We thank Dr. T Shivalingaswamy for his valuable suggestions and fruitful discussions.

References

1. David J Griffiths, Introduction to Quantum Mechanics, Pearson, 2016.
2. J J Sakurai, Modern Quantum Mechanics, Addison-Wesley, 1995.
3. Ryzhik and Gradshteyn, Table of integrals, Series, and Products, Elsevier Academic Press, 2007.

* * * * *

- **Akhil E J, Adithya Prabhakaran V, Aiswarya Vijayan, Felan Amal,** Department of Physics, St. Philomena's College (Autonomous), Mysore - 570015, Karnataka, India, **Ph:** 9632878721, **E-mail:** felanamal@stphilos.ac.in

Evolution of Lorentzian Light Wave Packet



- **Rashmi P.E**
- **Dr. B. A Kagali**
- **Dr. T. Shivalingaswamy**

Abstract

The time evolution of a wave packet is an important and interesting concept in quantum mechanics. In this short article the evolution of an electromagnetic wave packet that has a Lorentzian shape is deduced and interesting results are inferred.

1. Lorentzian light wave packet.

Let us consider the evolution of electromagnetic wave packet that has Lorentzian shape. Hence the initial wave packet may be taken as

$$\psi(x, 0) = \frac{A}{x^2 + a^2} \quad (1)$$

A simple schematic of this wave packet [1] is as shown in figure 1.

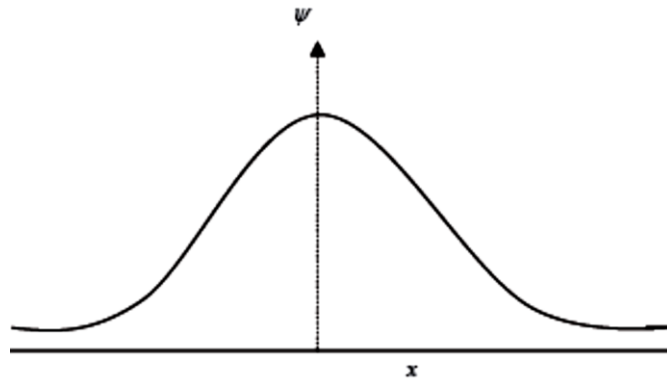


Figure 1: Schematic of Lorentzian light wave packet

The wave packet is located at the origin to begin with. The wave number decomposition of the packet will be given by

$$\tilde{\psi}(K) = \frac{1}{\sqrt{2\pi}} \int e^{iKx} \psi(x,0) dx \quad (2)$$

Thus, we get

$$\tilde{\psi}(K) = \frac{1}{\sqrt{2\pi}} \int_{-\infty}^{+\infty} \frac{(\cos Kx + i \sin Kx) A}{x^2 + a^2} dx \quad (3)$$

Now using the result [2], [3]

$$\int_0^{\infty} \frac{\cos ax}{x^2 + b^2} dx = \frac{\pi}{2b} e^{-ab} \quad (4)$$

We can obtain

$$\tilde{\psi}(K) = \frac{1}{\sqrt{2\pi}} \frac{A\pi}{a} e^{-Ka} \quad (5)$$

2. The evolution of Lorentzian light wave packet

Thus, the wave packet at a later time t can be obtained from

$$\psi(x,t) = \frac{1}{\sqrt{2\pi}} \int \tilde{\psi}(K) e^{-iKx-i\omega t} dK \quad (6)$$

Where $\omega = Kc$ for an electromagnetic wave [4]. Substituting the above expression for $\tilde{\psi}(K)$, we get

$$\psi(x,t) = \frac{1}{\sqrt{2\pi}} \left[\int_{-\infty}^0 \frac{1}{\sqrt{2\pi}} \frac{A\pi}{a} e^{+Ka} e^{-iKx-i\omega t} dK + \int_0^{\infty} \frac{1}{\sqrt{2\pi}} \frac{A\pi}{a} e^{-Ka} e^{-iKx-i\omega t} dK \right] \quad (7)$$

On simplification we get

$$\psi(x,t) = \frac{A}{2a} \left[\int_{-\infty}^0 e^{K(a-ix-ict)} dK + \int_0^{\infty} e^{-K(a+ix+ict)} dK \right] \quad (8)$$

On performing the integration, we get,

$$\psi(x,t) = \frac{A}{2a} \left[\frac{1}{(a-ix-ict)} + \frac{1}{(a+ix+ict)} \right] \quad (9)$$

Therefore

$$\psi(x,t) = \left[\frac{A}{a^2 + (x+ct)^2} \right] \quad (10)$$

3. Results and Discussion

We have obtained the time evolution of Lorentzian light wave packet from which, we notice an interesting result that the wave packet remains Lorentzian. It simply moves like a particle with velocity c . There is no change in its width. It would be interesting to note the same for wave packets of other different shapes.

References

1. B.H Bransden and C.J Joachain, *Quantum mechanics*, (Pearson Education India, 2004).
2. I.S Gradshteyn and I.M Ryzhik, *Table of Integrals, Series and Products*, (New York Academic Press, 1965).
3. S. Wolfram, *The Mathematica book*, (Cambridge University Press, 1996).
4. Bhang Singh Guru et.al., *Electromagnetic Field Theory Fundamentals*, (Cambridge University Press, 2004).

* * * * *

- ❖ **Rashmi P.E**, Asst. Professor, Department of Physics, Government College for Women, Mandya-571401, Karnataka, India, **Ph:** 9844126321, **E-mail:** rashmi.pe@gmail.com
- ❖ **Dr. B. A Kagali**, Former Professor, Department of Physics, Bangalore University, Bangalore-560056, Karnataka, India
- ❖ **Dr. T. Shivalingaswamy**, Asst. Professor, HOD of Physics, Government College (Autonomous), Mandya-571401, Karnataka, India, **E-mail:** tssphy@gmail.com

A comparative study of hydrogen bond interactions and intermolecular close contacts in 2, 3, 4, 6, 7, 8 substituted quinoline derivatives

○ Dr. M. Prabhuswamy

Abstract

The quinoline ring being substituted by the functional groups such as methyl, methoxy, hydroxyl, bromine, nitrogen dioxide, and chlorophenyl at different positions exhibit planar conformation in quinoline derivatives, 8-Methoxy-2-methylquinoline-4-ol (**1**), 3-Bromo-8-nitroquinoline (**2**), 2-(4-Chlorophenyl)methyl-4-(3-methylphenyl)quinoline (**3**) and 6,7-Dimethoxy-2,4-diphenylquinoline (**4**). The hydrogen bond interactions and inter molecular close contacts involved in the stabilization of crystal and molecular structure structures of **1**, **2**, **3** and **4** were compared *via* Hirshfeld surface analysis.

Keywords: Quinoline; Molecular structure; Hydrogen bond interactions; Hirshfeld surface.

1. Introduction

Quinoline derivatives play central role in the process of discovery of drugs because of their wide range of chemical reactivity and manifold biological activities. Different substituted quinolines were shown to be antibacterial [1], anti-inflammatory [2], antitubercular [3], antimalarial [4], anticancer [5], antibiotic [6], antihypertensive [7], tyrokinase platelet derived growth factor-receptor tyrosine kinase inhibitor [8], antihuman immunodeficiency virus [9], antimicrobial [10], antiviral [11], antitumor [12], immunomodulatory [13] antileishmanial [14] and antifungal [15]. They were found to be biological synthons and at present they are attracting much attention in the development of new drugs [16-18]. 2-Methyl quinoline was used as an antimalarial drug and to prepare various newer antimalarial drugs. A comparison of antibacterial and antifungal activity of some novel quinoline

clubbed compounds with standard drugs show that the presence of methoxy and halogen groups in the phenyl ring increases the antimicrobial activity [19]. Quinoline derivatives are ideally suited for further modifications to obtain more efficacious antibacterial and antituberculosis agents. Modifications in the main structural fragment of quinoline based drugs might bring improvement in their pharmacological properties in terms of strength and direction of interaction [20]. The compound 2-Methyl-4-phenyl-3-acetoxyquinoline was able to show antioxidant properties and was found to be efficacy against free radicals due to the presence of different substituents [21] and might be useful in preventing free radical induced disorders like cardiovascular disease, diabetes, cancer *etc.* [22]. Derivatives of 6-Methoxy-2-methylquinolin-4-yl exhibited a very good antibacterial, antifungal and antitubercular activities [23].

2. Materials and methods

The synthesis, crystal and molecular structure parameters of quinoline derivatives; 8-Methoxy-2-methylquinoline-4-ol (**1**) [24], 3-Bromo-8-nitroquinoline (**2**) [25], 2-(4-Chlorophenyl)-6-methyl-4-(3-methylphenyl)quinoline (**3**) [26] and 6,7-Dimethoxy-2,4-diphenylquinoline (**4**) [27] were reported earlier. A schematic representation of the structure of quinoline is shown in Fig. 1.

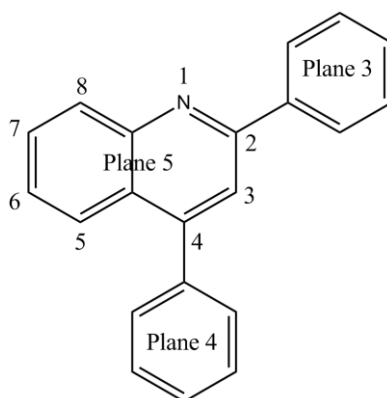


Figure 1: A schematic representation of the structure of substituted quinoline.

The hydrogen bond interactions and inter molecular close contacts involved in the stabilization of crystal and molecular structures of **1**, **2**, **3** and **4** were compared *via* Hirshfeld surface analysis.

3. Results and Discussion

3.1 Comparison of crystal and molecular structure parameters

Quinoline derivatives **1** and **3** crystallize in the monoclinic crystal systems with space group $P2_1/c$ whereas **2** and **4** crystallizes in the orthorhombic and triclinic crystal systems with space groups $Pbca$ and $P-1$ respectively.

Table 1: Comparison of crystal and molecular structure parameters.

| Compound | Quinoline derivatives | | | |
|---------------------------|-------------------------------|------------------|-------------------|--------------------|
| | 1 | 2 | 3 | 4 |
| CCDC Number | 793924 | 1000711 | 059099 | 981089 |
| Empirical formula | $C_{11}H_{11}NO_2 \cdot H_2O$ | $C_9H_5BrN_2O_2$ | $C_{23}H_{18}ClN$ | $C_{23}H_{19}NO_2$ |
| Crystal system | Monoclinic | Orthorhombic | Monoclinic | Triclinic |
| Space group | $P2_1/c$ | $Pbca$ | $P2_1/c$ | $P-1$ |
| Conformation of quinoline | Planar | Planar | Planar | Planar |
| Hydrogen bond interaction | O—H...O C—H...O | C—H...O | C—H...Cl | C—H...N C—H...O |

A comparison of the crystal and molecular structure parameters of compounds **1**, **2**, **3** and **4** are depicted in Table 1. Compounds **1**, **2** and **4** have exhibited C—H...O type of hydrogen bond interactions which were absent in compound **3**. Further it is analyzed that compound **1** has showed O—H...O hydrogen bond interactions which was absent in **2**, **3** and **4**. The compound **4** also exhibited C—H...N type of hydrogen bond interactions which was absent in **1**, **2**, and **3**. The unit cell of compound **4** consists of two asymmetric units (A and B) and the comparison of dihedral angles between the planes of various substituents of the quinoline with respect to its plane is given in Table 2.

| Compounds → Dihedral angle (°) ↓ | Quinoline derivatives | | | | |
|-------------------------------------|-----------------------|---|----------|----------|----------|
| | 1 | 2 | 3 | 4 | |
| | | | | A | B |
| Between plane 3 and 5 | - | - | 2.5 (1) | 30.3 (7) | 24.1 (7) |
| Between plane 4 and 5 | - | - | 55.4 (9) | 61.0 (6) | 56.6 (6) |

The dihedral angle values between plane 3 and 5, and plane 4 and 5 for A and B of **4** were in close agreement, showing that the molecular structure of the asymmetric units A and B were almost similar to each other. It was seen that the dihedral angle values between plane 4 and 5 in **3** and **4** were also in close agreement with one other. A significant difference of 27.8° (with respect to A) and 21.6° (with respect to B) in the dihedral angle between plane 3 and 5 of **3** and **4** were also observed.

3.2 A comparison of Hirshfeld surface analysis

The Hirshfeld surface analysis [28–30] of **1**, **2**, **3** and **4** were carried out to visualize the intermolecular interactions, responsible for the stabilization and formation of 3D supra molecular frame work in the crystal lattices. The hydrogen bond interactions were visualized through the dark red spots obtained on the Hirshfeld surfaces, as a result of hydrogen bond acceptors of types O14—H14...O15, O15—H15B...O14, O15—H15A...O11 and C13—H13C...O15 in **1** (Fig. 2); C2—H2...O13 and C9—H9...O12 in **2** (Fig. 3); and C18—H18...Cl12 in **3** (Fig. 4) and C21—H21A...O12B in **4** (Fig. 5).

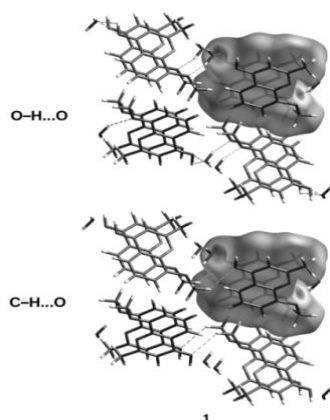


Figure 2: The visualization of $O-H\cdots O$ and $C-H\cdots O$ hydrogen bond interactions in **1**.

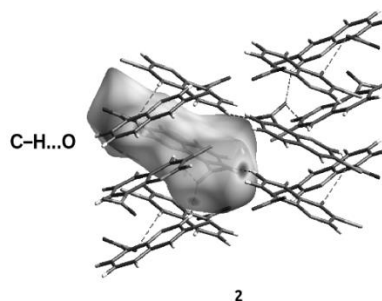


Figure 3: The visualization of $C-H\cdots O$ hydrogen bond interactions in **2**.

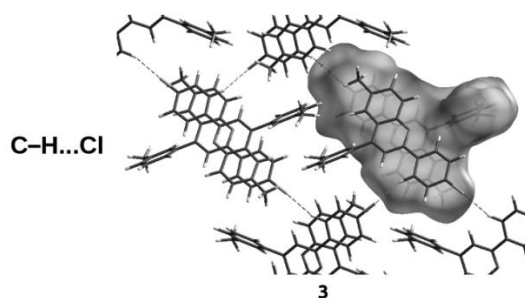


Figure 4: The visualization of $C-H\cdots Cl$ hydrogen bond interactions in **3**.

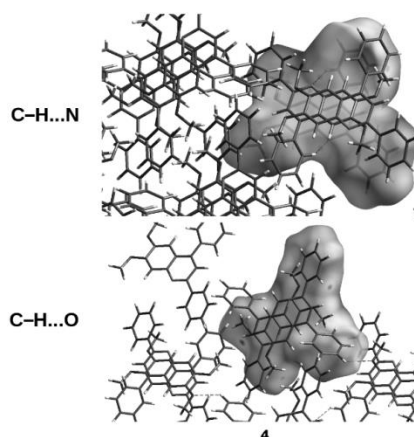


Figure 5: The visualization of $C-H\cdots N$ and $C-H\cdots O$ hydrogen bond interactions in **4**.

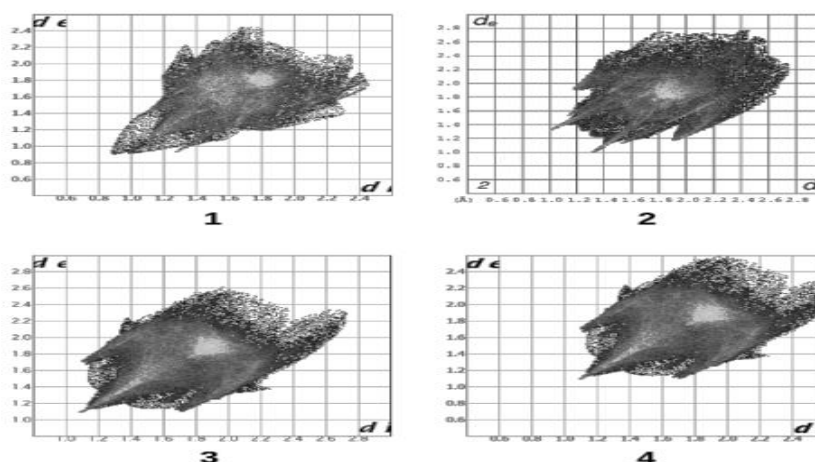


Figure 6: Fingerprint plots for molecules of compounds **1**, **2**, **3** and **4**.

The combination of d_e and d_i in the form of 2D fingerprint plot [31] gives the summary of intermolecular contacts in the crystal lattice. Fingerprint plots for the molecules of compounds **1**, **2**, **3** and **4** are shown in **Fig. 6**. The H \cdots H short contacts appear almost as a single blunt spike of sky blue colour, in the region $0.86 \text{ \AA} < (d_e + d_i) < 0.90 \text{ \AA}$ in **1**, where as they appear as two closely lying blunt spikes in the region $1.21 \text{ \AA} < (d_e + d_i) < 1.30 \text{ \AA}$ in **2**, as a single sharp spike of sky blue colour in the region $1.08 \text{ \AA} < (d_e + d_i) < 1.12 \text{ \AA}$ in **3** and as almost merged blunt spike in the region $0.97 < (d_e + d_i) < 1.16 \text{ \AA}$ in **4**. The C \cdots H close contacts were seen as a two very wide and blunt spikes in the region $1.05 \text{ \AA} < (d_e + d_i) < 1.32 \text{ \AA}$ in **1**, but as a two wide and blunt spikes in the region $1.50 \text{ \AA} < (d_e + d_i) < 1.86 \text{ \AA}$ in **2**, as a two wide and quite sharp spikes in the region $1.12 \text{ \AA} < (d_e + d_i) < 1.67 \text{ \AA}$ in **3** and as a two wide and sharp beak like spikes in the region $1.10 \text{ \AA} < (d_e + d_i) < 1.65 \text{ \AA}$ in **4**. The N \cdots H inter molecular contacts become noticeable as a two broad spikes in the region $1.24 \text{ \AA} < (d_e + d_i) < 1.66 \text{ \AA}$ in **1**, as a two highly sharp elongated spikes in the region $1.11 \text{ \AA} < (d_e + d_i) < 1.52 \text{ \AA}$ in **2**, as a two broad spikes in the region $1.20 \text{ \AA} < (d_e + d_i) < 1.60 \text{ \AA}$ in **3** and as a two wide and curved spikes in the region $1.10 \text{ \AA} < (d_e + d_i) < 1.58 \text{ \AA}$ in **4**. The O \cdots H inter molecular contacts become noticeable as a two highly sharp elongated spikes in the region $1.20 \text{ \AA} < (d_e + d_i) < 1.75 \text{ \AA}$ in **1**, as a two highly sharp elongated spikes in the region $0.98 \text{ \AA} < (d_e + d_i) < 1.31 \text{ \AA}$ in **2** and as a two wide and sharp spikes in the region $1.05 \text{ \AA} < (d_e + d_i) < 1.45 \text{ \AA}$ in **4**.

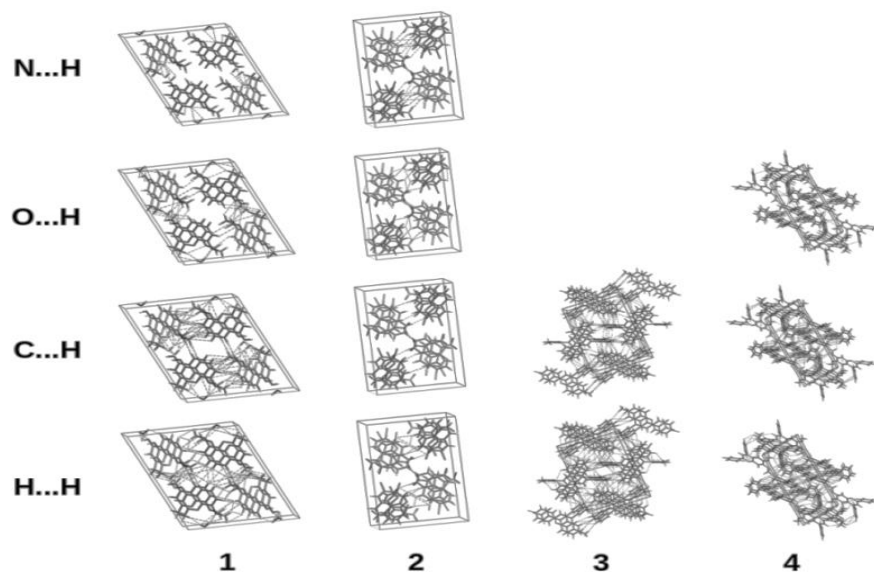


Figure 7: Inter molecular close contacts in molecules of compounds **1**, **2**, **3** and **4**.

The intermolecular close contacts in molecules of compounds **1**, **2**, **3** and **4** are shown in Fig. 7. And their contributions are given in Table 3.

Table 3: Inter molecular close contacts (%) for Hirshfeld surfaces of **1**, **2**, **3** and **4**.

| Compound | H...H | C...H | N...H | O...H | |
|----------|----------|-------|-------|-------|---|
| 1 | 52 | 16 | 4 | 17 | |
| 2 | 12 | 7 | 6 | 30 | |
| 3 | 54 | 18 | 2 | - | |
| 4 | A | 53 | 26 | 4 | 9 |
| | B | 53 | 30 | 4 | 8 |

Conclusion

The quinoline ring adopts planar conformation in all the four compounds **1**, **2**, **3** and **4** and, the crystal and molecular structures of these compounds were compared and analysed. The structures of **1**, **2**, **3** and **4** were stabilized by O—H...O, C—H...O, and C—H...Cl interactions which lead to the formation of supramolecular frame work in the crystal lattices. The major contributions for the Hirshfeld surfaces were H...H in compounds **1**, **3** and **4**, and O...H in compound **2**.

Acknowledgements

The author, M. Prabhuswamy is grateful to the Department of Studies in Physics, University of Mysore, Karnataka, India, for providing the National single crystal X-ray diffractometer facility.

References

1. Chen Y. L., Fang K. C., Sheu J. Y., Hsu S. L., Tzeng C.C. Synthesis and antibacterial evaluation of certain quinoline derivatives. *J. Med. Chem.*, 44(14) (2001) 2374–2377.
2. Roma G., Braccio M. D., Grossi G., Mattioli F., Ghia M. 1, 8-Naphthyridines IV. 9-Substituted N, N- dialkyl-5-(alkylamino or cycloalkylamino) [1,2,4] triazolo[4,3-a] [1,8]naphthyridine-6-carboxamides, new compounds with anti-aggressive and potent anti-inflammatory activities. *Eur. J. Med. Chem.*, 35(11) (2000) 1021–1035.
3. Lilienkamp A., Mao J., Wan B., Wang Y., Franzblui S. G., Kozikowski A. P. Structure activity relationships for a series of quinoline based compounds active against replicating and nonreplicating Mycobacterium tuberculosis. *J. Med. Chem.*, 52(7) (2009) 2109–2118.
4. Nasveld P., Kitchener S. Treatment of acute vivax malaria with tafenoquine. *Trans. R.Soc. Trop. Med. Hyg.*, 99(1) (2005) 2–5.
5. Denny W. A., Wilson W. R., Ware D.C., Atwell g. J., Milbank J. B., Stevenson R. J. Anti-cancer 2,3- Dihydro-1H-pyrrolo[3,2-f]quinoline complexes of cobalt and chromium. *U. S. Patent.*, (2006) 7064117.
6. Mahamoud A., Chevalier J., Davin-Regli A., Barbe J., Pages J. M. Quinoline derivatives as promising inhibitors of antibiotic efflux pump in multidrug resistant Enterobacter aerogenes isolates. *Curr. Drg. Targ.*, 7(7) (2006) 843–847.
7. Muruganatham N., Sivakumar R., Anbalagan N., Gunasekaran V., Leonard J. T. Synthesis, anticonvulsant and antihypertensive activities of 8-substituted quinoline derivatives. *Biol. Pharm. Bull.*, 27(10) (2004) 1683–1687.
8. Maguire M. P., Sheets K. R., McVety K., Spada A. P., Zilberstein A. A new series of PDGF receptor tyrosine kinase inhibitors: 3-substituted quinoline derivatives. *J. Med. Chem.*, 37(14) (1994) 2129–2137.
9. Strekowski L., Mokrosz J. L., Honkan V. A., Czarny A., Cegla M. T., Wydra R. L., Patterson S. E., Schinazi R. F. Synthesis and qualitative structure-activity relationship analysis of 2-(Aryl or heteroaryl)quinoline-4-amines, a new class of anti-HIV-1 agents. *J. Med. Chem.*, 34(5) (1991) 1739–1746.
10. Abdel-Moty S. G., Abdel-Rahman M. H., Elsherief H. A., Kafafy A. H. N.

- Synthesis of some quinoline thiosemicarbazone derivatives of potential antimicrobial activity. *Bull. Pharm. Sci.*, 28(1) (2005) 79–93.
11. Normand-Bayle M., Bénard C., Zouhiri F., Mouscadet J. F., Leh H., Thomas C. M., Mbemba G., Desmaële D., d'Angelo J. New HIV-1 replication inhibitors of the styrylquinoline class bearing aryl/acyl groups at the C-7 position: Synthesis and biological activity. *Bioorg. Med. Chem. Lett.*, 15(18) (2005) 4019–4022.
 12. Hazeldine S. T., Polin L., Kushner J., White K., Corbett T. H., Biehl J., Horwitz J. P. Part 3: synthesis and biological evaluation of some analogs of the antitumor agents, 2-4-[(7-Bromo-2-quinolinyl)oxy]phenoxypropionic acid. *Bioorg. Med. Chem.*, 13(4) (2005) 1069–1081.
 13. He J. F., Yun L. H., Yang R. F., Xiao z. Y., Cheng J.P., Zhou W. X., Zhang Y. X. Design, synthesis and biological evaluation of novel 4-Hydro-quinoline-3-carboxamide derivatives as an immunomodulator. *Bioorg. Med. Chem. Lett.*, 15(12) (2005) 2980–2985.
 14. Dardari Z., Lemrani M., Bahloul A., Sebban a., Hassar M., Kitane S., Berrada M., Boudouma M. Antileishmanial activity of a new 8-hydroxyquinoline: preliminary study. *Farm.*, 59(3) (2004) 195–199.
 15. Vargas M. L.Y., Castelli M. V., Kouznetsov V.V., Urbina G. J. M., Lopez S. N., Sortino M., Enriz R. D., Ribas J. C., Zacchino S. In vitro antifungal activity of new series of homoallylamines and related compounds with inhibitory properties of the synthesis of fungal cell wall polymers. *Bioorg. Med. Chem.*, 11(7) (2003) 1531–1550.
 16. Simeon M., John N., Georgia L., Eleni K., Vasilike G., Dimitrios T., Pavlos N. Penetration of linezolid into sternal bone of patients undergoing cardiopulmonary bypass surgery. *Int. J. Antimicrob. Agen.*, (Letters to the Editor), 29(6) 742–744.
 17. Kaila N., Janz K., DeBernardo S., Bedard P. W., Camphausen r. T., Tam S., Tsao D. H., Keith J. C. Jr., Nickerson-Nutter C., Shilling A., Young-Sciame r., Wang Q. Synthesis and biological evaluation of quinoline salicylic acids as P-selectin antagonists. *J. Med. Chem.*, 50(1) (2007) 21–39.
 18. Andersen K. E., Lundt B. F., Jørgensen A. S., Braestrup C. Oxadiazoles as bioisosteric transformations of carboxylic functionalities II. *Eur. J. Med. Chem.*, 31(5) (1996) 417–425.
 19. Avnish A. P., Arvind G. Synthesis of novel heterocyclic compounds and their biological evaluation. *Der. Pharm. Chem.* 2(1) (2010) 215–223.
 20. Zieba A., Wojtyczka R. D., Kepa M., Idzik d. Azinyl sulphides –CXVIII. Antimicrobial activity of novel 1-methyl-3-thio-4-aminoquinolinium salts. *Fol. Microb.*, 55(1) (2010) 3–9.
 21. Brahmayya M., Venkateswara rao B., Viplvapasrad U., Basaveswara Rao M. V., Raghu Babu K., Kishore babu B., Rajkumar K., Praveen Ch., Giribabu N., Vijaya M., Padmarao Ch V., Srinivasa Rao N. Synthesis of quinolines and their *invitro*

- antioxidant activities under solvent free conditions by using the SiO₂-Zn-MgO as a novel and reusable catalyst. *J. App. Pharm. Sci.*, 2(10) (2012) 41–44.
22. Ghinet A., Farce A., Oudir S., Pommery J., Vamecq J., Henichart J. P., Rigo B., Gautret P. Antioxidant activity of new benzo[de]quinolines and lactams: 2D-quantitative structure-activity relationships. *Med. Chem.*, 8(5) (2012) 942–946.
 23. Vora P. J., Mehta A. G. Synthesis, characterization and antimicrobial efficacy of quinoline based compounds. *IOSR. J. App. Chem.*, 1(4) (2012) 34–39.
 24. Prabhuswamy Mallappa, Sandeep Sadanand Laxmeshwar, Madan Kumar Shankar, Manjula Mallappa, Ranganathan Sathish Kumar, Gundibasappa K Nagaraja, Neratur K Lokanath. Synthesis, characterization and crystal structure of 8-Methoxy-2-methylquinoline-4-ol: a window into the world of quinoline modifications. *Struct. Chem. Commun.*, 2(3) (2011) 114–117.
 25. Kuninobu Y., Nishi M., Kanai M. 5-Position-selective C-H trifluoromethylation of 8-aminoquinoline derivatives. *Org. Biomol. Chem.*, 14(34) (2016) 8032–8100.
 26. Prabhuswamy M., Swaroop T. R., Madan Kumar S., Rangappa S., Lokanath N. K. 2-(4-Chlorophenyl)-6-methyl-4-(3-methylphenyl)quinoline. *Acta Cryst.*, E68 (2012) o3250– o3250.
 27. Prabhuswamy M., Madan Kumar S., Swaroop T. R., Rangappa S., Lokanath N. K. 6, 7-Dimethoxy-2, 4-diphenylquinoline. *Acta Cryst.*, E70 (2014) o165– o165.
 28. Spackman M.A., Byrom P.G. A novel definition of a molecule in a crystal, *Chem. Phys. Lett.*, 267 (1997) 215–220.
 29. Spackman M. A., Jayatilaka D. Hirshfeld surface analysis, *CrystEngComm*. 11 (2009) 19–32.
 30. Wolff S. K., Grimwood D. J., McKinnon J. J., Turner M. J., Jayatilaka D., Spackman M. A. *CrystalExplorer* (Version 3.1), (2012).
 31. Spackman M. A., McKinnon J. J. Finger printing intermolecular interactions in molecular crystals. *CrystEngComm*, 4 (2002) 378–392.

* * * * *

- ❖ **Dr. M. Prabhuswamy**, Asst. Professor, Department of Science Education (Physics), JSS Institute of Education, Sakaleshpur-573134, Karnataka, India, **Ph:** 9741516970 **E-mail:** prabhumallappa@gmail.com

Printing of Organic Light Emitting Devices for large area applications



❖ Dr. Wim Deferme

Abstract

The primary purposes of lighting remain visibility and safety, but our quality of life can be improved by creating a complete visual environment that includes needs like health and communication. Therefore, it is indispensable to go passed rigid, planar lighting towards flexible lighting. This also implies the use of inexpensive application techniques suitable for continuous manufacturing like printing techniques. Suited to fulfil these lighting needs are the organic light emitting diode (OLED) thanks to the thin flexible and printable layers. However, when working towards the printing and coating of Organic Light Emitting Diodes, adaptations in materials and formulations, optimized layer formation and inventive stack build-ups are needed. In this work, we describe the transition towards the ultrasonic spray coating and inkjet printing of OLEDs focusing on the printing and coating technology and the layer formation. Ultrasonic spray coating will be applied for ultrathin coatings and inkjet printing will be applied for narrow linewidth structures for transparent and conductive electrodes.

Keywords — OLEDs, printing, large area deposition, flexible substrates

I. INTRODUCTION

Organic electroluminescence was introduced by Bernanose et al. in 1953 by exciting organic films at a very high AC voltage of 500 V – 2000 V [1]. In 1963 Pope et al. however demonstrated electroluminescence from a single crystal anthracene by

applying a DC voltage [2]. The publication of Tang and Van Slyke introduced the first small molecules OLED (SM-OLED) in 1987 [3]. In its most basic form, an organic light emitting diode is constructed out of an emissive layer (EML) sandwiched between two electrodes. Small molecules were the first building blocks of the EML and could only be applied using expensive and non roll-to-roll compatible vacuum deposition techniques, but nowadays they are also applicable using wet chemical deposition techniques [4]. Their material properties are however relatively easy adaptable. In 1990 a group at the University of Cambridge replaced the small molecules with a conjugated polymer polyparaphenylenevinylene (PPV) and therefore developed the first polymer OLED (P-OLED) [5]. Contrary to small molecules, polymers have a good chemical stability and can be deposited using low-cost solution processing techniques [6].

In 1992 Gustafsson et al. fabricated the first flexible OLED on polyethylene terephthalate (PET) using poly[2-methoxy-5-(2'-ethylhexyloxy)-1,4-phenylenevinylene] (MEH-PPV) as an active emissive layer [7]. Five years later Gu et al. demonstrated a SM-OLED on a thin plastic substrate precoated with indium tin oxide (ITO) [8]. During the following decades these first publications gave rise to a worldwide research resulting in highly flexible and efficient OLEDs fabricated with innovative materials mostly on plastic-like materials and metal foils applied by a variety of both vacuum deposition and solution processing techniques. Today, the OLED technology is challenging well-established mainstream display technologies and emerges in the lighting industry. White OLEDs (WOLEDs) are intensively studied for applications in displays and lighting. Displays based on WOLED pixels and OLED displays, based on red, green and blue emitters, are already available in end-user products such as smart-phones and televisions. The viability of all emerging lighting and display technologies is assessed by their luminous power efficiency and this parameter is notwithstanding of prime importance for the end-user applications. The luminous power efficacy is the ratio of the integral light emitted by the light source per electrical input power. The power of the light emitted by a light source, its luminous flux, is measured in lumen and corrected for the photometric response of the human eye [9]. Figure 1 shows the improvements of WOLEDs over the past 20 years as compared to the luminous power efficacy of the conventional white-light sources.

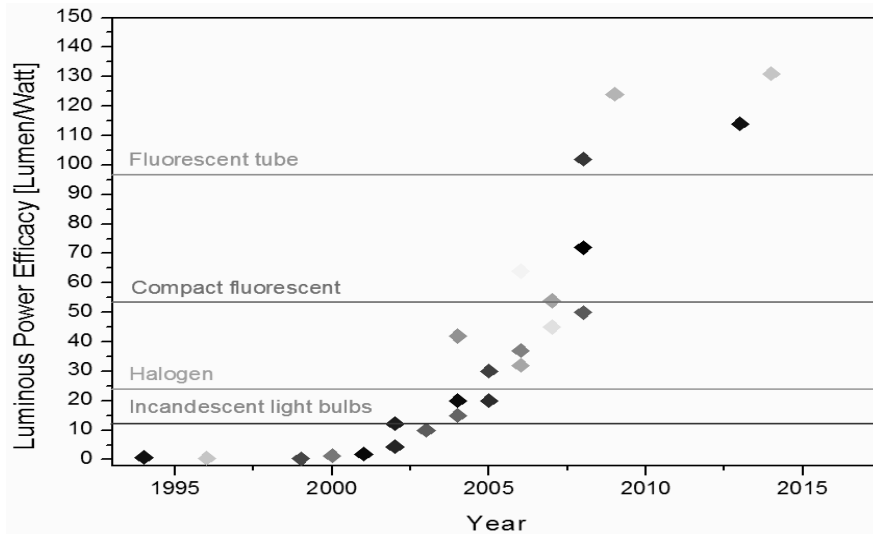


Figure 1: The luminous power efficacy, expressed in lumen per Watt, improvement of WOLEDs over the past 20 years (adapted from [10]).

An important milestone in the luminous power efficacy timeline is 2003. Here WOLEDs reached, under laboratory conditions, an efficacy of 15 lm/W surpassing the incandescent light bulb for the first time. However, currently, it's not yet clear if these values can be reached in mass production processes for commercial applications [10]. OLEDs are often referred to as the future in solid state lighting due to their light weight and thin layers, flexibility, high efficiencies and non-expensive and environment friendly fabrication techniques. In addition they just require an applied direct current (DC) voltage of around 3-5 V to ensure light emission, which makes them eligible for many applications like wearables amongst others. Although a lot of progress has been made, there are some remaining challenges to be dealt with, for example their limited lifetime and fast degradation under ambient conditions [11]. In this work, we describe the step from vacuum deposition and small scale spin coating to large area deposition of OLEDs via, for example, ultrasonic spray coating and other printing technologies.

II. MATERIALS AND METHODS

OLED build-up

The most basic structure of an OLED is illustrated in figure 2(a), a single layer of conjugated polymer is sandwiched between two electrodes. The first

electrode, the anode, on top of the transparent substrate is a transparent conductor to facilitate light extraction from the device. Since the first reported OLED, indium tin oxide (ITO) is the most commonly used transparent anode [12]. The solution processable polymer layer, also known as the emissive layer, determines the electroluminescent spectrum of the device. The top electrode, the cathode, is a metal deposited by thermal evaporation. When discussing devices, it is convenient to make use of the band diagram structure of the OLED, in forward bias as shown in figure 2(b). The indicated HOMO and LUMO level reflect the average energy levels of the entire film. The workfunction of the anode and cathode are denoted respectively χ_a and χ_c . The difference in workfunction between the anode and cathode give rise to a so called “built-in potential” (V_{bi}) [13], which must be overcome in order for current to flow and for the OLED to be in the forward bias regime ($V_{bias} > V_{bi}$). The forward bias regime is achieved by applying a positive direct current (DC) voltage, e.g.: 3V-10V from the anode to the cathode.

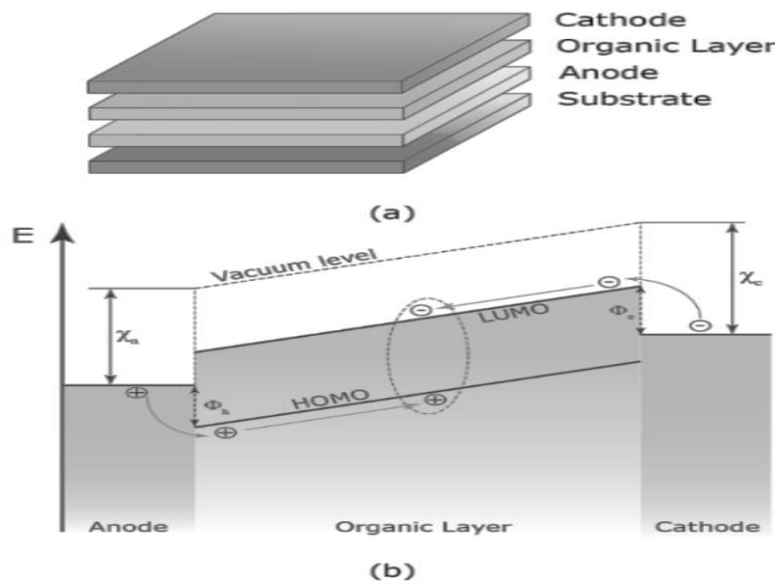


Figure 2: Structure (a) and band diagram (b) of prototypical OLED. (a) The OLED consists out of a single organic layer sandwiched between an anode and a cathode on top of a substrate. (b) The band diagram of the OLED under forward bias, adapted from [33].

Under forward bias, the electrodes facilitate charge injection, holes from the anode and electrons from the cathode. Under the local electric field, typically in

order of 10^6 V/m, the charge carriers are transported through the polymer layer. Inside the organic layer the holes and electrons recombine to form excitons. These excitons can then decay radiative or non-radiative. Thus there are three fundamental processes underpinning the OLED device operation: charge injection, charge transport and recombination [14].

For both holes and electrons the charge injection process is dominated by a charge injection barrier, the transparent anode – organic layer interface barrier (Φ_h) and the organic layer – metal interface barrier (Φ_e), respectively. The vacuum level is defined as the minimum energy needed to remove an electron from a solid. The energy difference between the LUMO and vacuum level is the electron affinity (A_e). The energy separation between the HOMO and vacuum level is the ionization energy (I_E). According to the Mott-Schottky rule of molecular orbital interfaces, the interface barriers can be expressed as follows [15]:

$$\Phi_e = \chi_c - A_e - \Delta \quad (1.1)$$

$$\Phi_h = I_E - \chi_a + \Delta \quad (1.2)$$

However at the electrode/organic interface vacuum level alignment is not achieved due to the formation of an interface dipole [16]. This interface dipole induces an abrupt change (Δ) that can be as high as 1 eV in the vacuum level at the interface. There are several possible theories on its origin and at the present there is no final confirmed theory [17].

Over the past decades classical models like Fowler-Nordheim tunnelling and Thermionic emission have been applied to describe the injection of charge carriers into disordered organic-semiconductors [15]. However these models are not adequate as they describe delocalized charge carrier injection into solids, an overview can be found in [18]. Currently more advanced models are under investigation to describe the injection of electrical current into organic semiconductors like the Hopping injection: Arkhipov model and Emtage/O'Dwyer model [19].

The charge transport mechanism in disordered organic-semiconductors is currently not well understood [16]. The constituent molecules of the disordered organic solid are kept mainly together by weak van der Waal's interaction. This implies that adding, removing or moving a charge carrier (hole or electron) on a molecule will lead to a significant distortion of the molecule's geometry i.e.:

changes in bond length of neighbouring bonds which in turn changes the energetic state. Upon acquiring a charge, the molecule tends to lower its total energy by reorganizing its internal structure. This energy is referred to as the reorganization energy (λ) [20]. The particular combination of a charge with its induced distortion is called a polaron. When an electron is added an electron-polaron is formed, removing an electron will create a hole-polaron. The mobility (μ) of these organic semiconducting materials is low ($\mu \approx 10^{-6} \text{ cm}^2/\text{Vs}$) compared to inorganic semiconductors like crystalline silicon ($\mu \approx 10^3 \text{ cm}^2/\text{Vs}$). The charge carrier transport is viewed as a hopping transport where the electrons hop from one molecule to the next, in contrast to inorganic semiconductors where the transport is considered as ballistic. This hopping charge transport formalism is currently extensively studied e.g.: polaron hopping, hopping in a disordered density of state, variable range hopping and a more macroscopic approach the drift-diffusion framework, a detailed overview can be found [21].

As both charge carries, under influence of an externally applied electric field, are injected and transported in opposite directions through the organic semiconductor, electron-hole pairs, excitons, are formed. Recently it was shown that Langevin-type and Shockley-Read-Hall (SRH) recombination processes both occur in OLEDs [22]. The SRH recombination process assumes that free holes can only recombine with trapped electrons and vice versa. The charge carriers get trapped in film defects and impurities. The trap level is situated inside the energy gap, between the HOMO and LUMO energy levels. This trap-mediated recombination process is often non-radiative or weak radiative and predominant at low bias voltages [23]. In contrast to the SRH recombination process, the Langevin model describes the recombination of electrons and holes that are both free [13]. In essence the recombination of electrons and holes will occur when they are within each other's Coulomb attraction radius. More precisely when the associated Coulomb potential is equal or larger than the thermal energy kT . The radiative process in OLEDs is dominated by Langevin type recombination and is therefore essential to the improvement of these devices [22], [23].

It is evident that a single-layer OLED, anode/polymer/cathode, is not the most efficient design, as shown in Figure 2. As electrons and holes are injected and transported through the device it is essential that they form excitons and recombine radiative. However it is also possible that the electrons reach the anode and the holes reach the cathode without forming excitons, recombining and generating light.

Furthermore, formed excitons near the cathode can also be quenched, the energy of the formed exciton is transferred to the metal non-radiative [22]. To ensure a respectable electroluminescent (EL) yield, multilayer device architectures are employed. This was already the case with Tang's first OLED, which was a two-layer OLED architecture consisting of a diamine layer and an Alq₃ layer [12]. In this device the diamine layer acts as a hole transporting layer (HTL) and the Alq₃ layer acts as the emissive layer (EML). Due to the different HOMO and LUMO levels of both materials, the electrons are blocked at the interface increasing the probability of exciton formation.

To achieve high efficient OLEDs, multilayer architectures are used [10], aside from the emissive layer, a multitude of interlayers are employed. Each interlayer is specifically tailored for its function within the OLED. Such an OLED could encompass to following interlayers: a hole injection layer (HIL); a hole transport layer (HTL); an electron blocking layer; an electron injection layer (EIL); an electron transport layer (ETL) and a hole blocking layer (HBL), as shown in figure 3. The purpose of these interlayers is to facilitate the injection and transport of both charge carriers towards the EML and confine the created excitons. The injection interlayers HIL and EIL reduce the injection barriers for the injection of holes and electrons (respectively). The blocking layers HBL and EBL lower the leakage current, electrons and holes that reach the opposite electrode and confine the generated excitons in the emissive layer.

Towards obtaining a predefined emission spectrum from the OLED, the emissive layer can be modified or comprise out of a stack of emissive layers [10]. A single layer can be blend with lumiphores or an emissive layer stack can be used with several emitting layers on top of each other. Other techniques to obtain the desired emission spectrum encompass the use of multiple monochrome OLED stacks connected by charge generation layers or spatially multiplexing monochromic OLEDs [10]. These methods are commonly employed for the purpose of generating white light, to obtain so called WOLEDs.

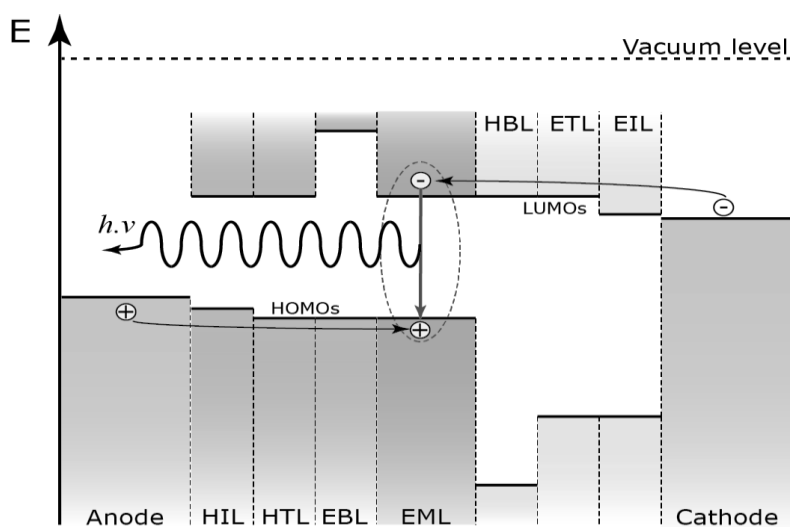


Figure 3: Energy Level diagram of a high efficient OLED stack. (HIL: hole injection layer; HTL: hole transport layer; EBL: electron blocking layer; EIL: electron injection layer; ETL: electron transport layer; HBL: hole blocking layer)

OLED Fabrication

Solution processing of organic optoelectronics holds the promise of cost efficient, high throughput production of large area devices. In contrast to vacuum deposition, solution processing techniques are more conveniently upscalable and more advanced printing techniques allow thin film patterning during the deposition. However, if large-scale solution processing proves to be problematic or impossible, the concept of organic optoelectronic devices would become a scientific curiosity with little consequence to mankind [24]. At the present time, all the layers of a typical OLED device can be deposited via a solution processing thin film deposition technique [25]. The transparent electrode, typically ITO, has been spin-cast from a monodisperse ITO nanocrystal solution [26] and spin-coated from solution prepared by means of sol-gel chemistry [27]. The polymer interlayers and active materials have been deposited by a multitude of coating and printing techniques [28] but also recently small-molecule based thin films have been deposited from solution whereas previously this was done via thermal evaporation [29]. Metallic electrodes have been fabricated via the deposition of a nano-particle solution [30].

We are, however, not quite there yet as a large research effort is needed before these proof-of-concept laboratory solution processing techniques can be transferred to industrial scale. Replacement of physical vapour deposition (PVD) processes of thin-film electrodes, e.g.: thermal evaporation, sputtering, by solution deposition processes has commenced. However, their optoelectronic properties are still not as good as their PVD processed counterparts, e.g.: ITO [26]. Furthermore, the most widely used solution deposition technique for all organic layers in the OLED device is spin coating because of its excellent thin film forming property with a wide variety of solution and substrate properties. With more roll-to-roll compatible, scalable coating and printing techniques the substrate surface properties and ink formulations are, however, highly critical [24].

Ultrasonic spray coating is a large-surface high-throughput technique used in a variety of sectors, e.g.: medical, automotive, electronics, food processing. The deposition of thin polymer films has been demonstrated by a commercially available hand held airbrush [31]. Although, the use of airbrushes is a cost-effective, high-throughput method, ultrasonic spray nozzles offer more precise control of the spray deposition [32]. It is a contactless deposition technique capable of creating sub-millimetre patterns and of coating non-conformal 3D substrates.

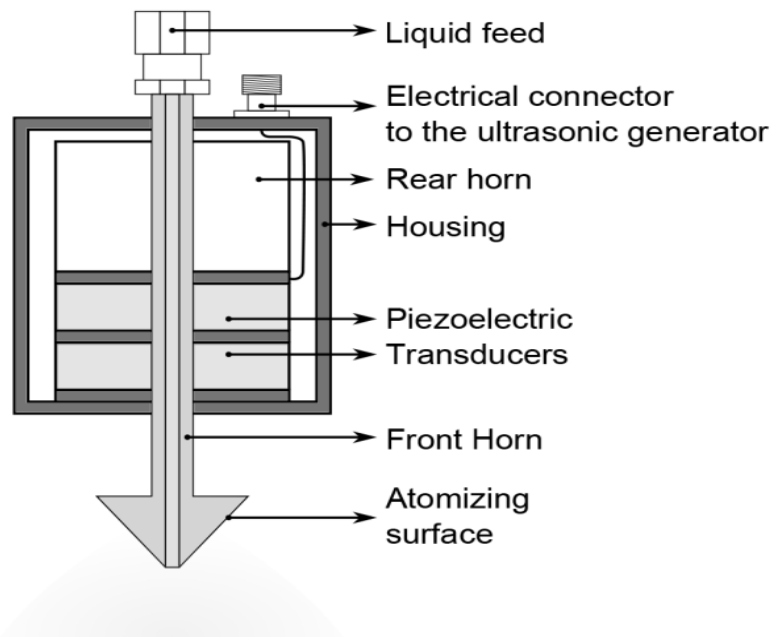


Figure 4. Illustration of an ultrasonic nozzle.

An ultrasonic nozzle, as depicted in figure 4, employs standing waves to atomize the solution. Ultrasonic nozzles employ standing waves to atomize the liquid. These standing waves are a result of the mechanical vibrations produced by the (ceramic) piezoelectric transducers inside the ultrasonic nozzle. The ultrasonic generator which is connected to the ultrasonic nozzle supplies an electrical signal, with amplitude A_e and frequency f_e , to the transducers. This results in a mechanical vibration with an amplitude $A_m \propto A_e$ and a frequency $f_m = f_e$. The frequencies typically used for ultrasonic nozzle are situated in the Low Frequency band (LF) and range from 20kHz up to 150 kHz. The produced standing waves along the length of the nozzle form an anti-node at the atomizing surface, here the amplitude is maximum. Nozzle dimensions are governed by the operating frequency (i.e.: resonance frequency), in multiples of $1/2$ the wavelength. In general higher frequency nozzles produce smaller droplets. Through the length of the nozzle runs the liquid feed orifice. As the liquid emerges onto the atomizing surface, the kinetic energy is dissipated causing atomization of the liquid. The atomization process relies on liquid being introduced onto the atomizing surface and the correct vibrational amplitude of the atomizing surface. When the vibrational amplitude is below the critical amplitude the liquid will not have sufficient energy to atomize. If the vibrational amplitude is too high the liquid is literally ripped apart, and large “chunks” of fluid are ejected. The rate of atomization only relies on the rate at which the liquid is delivered. The formed low velocity spray is hereafter directed toward the substrate by a nitrogen carrier gas (nitrogen shroud). The micrometre droplet size is governed by the vibrational frequency and solution properties e.g.: surface tension and density. Hereby a high uniform droplet size spray is obtained. In recent years, organic solar cells (OSCs) were successfully (ultrasonically) spray coated [33]. Furthermore, transparent electrode materials with high conductive PEDOT:PSS [34], zinc oxide (ZnO) [35] and nanoparticle-based silver top contacts [36] were ultrasonically spray coated to produce efficient OSCs.

In the next section of this paper we will focus on ultrasonic spray coating as the technique for large area deposition of thin films. Also inkjet printing for the top electrode is investigated and discussed.

III. RESULTS

Influence of ultrasonic vibrations:

Ultrasonic mechanic vibrations applied to the polymer-solvent mixtures has been known to potentially cause polymer backbone scission (cleavage), reducing the average polymer chain length [37]. Scission of the conjugated polymer backbone can cause an increase in the ionization potential of the polymer and increase the HOMO-LUMO energy gap, directly affecting the photoluminescence efficacy and emission spectrum of the OLED [38].

To allow proper comparison of the ultrasonic spray coating technique and the spin coating technique, the effect of ultrasonic atomization in ambient conditions were analysed first. The pristine polymer solution, stored in an inert atmosphere glove box, was ultrasonically atomized at the nozzle of the spray coater system in ambient conditions, collected and brought back into the inert atmosphere glove box system ('labelled ultrasonically atomized solution').

To explore the effects of ultrasonication of the Super Yellow polymer in solution, GPC was performed to determine the (average) molar mass distribution for a pristine and an ultrasonically atomized solution. No evidence of polymer scission of the conjugated backbone was however found. Extensive cleavage of the conjugated polymer backbone would also become apparent in the absorption spectrum. A significant reduction in the length of the Super Yellow polymer chains would cause a blue shift in the thin film absorption spectrum [38]. However, there is no evidence of such a shift after ultrasonic atomization of the Super Yellow solution as can be found in the paper of Gilissen et al [39].

The side-chain integrity of the ultrasonically atomized Super Yellow polymer was further investigated by FTIR and ^1H NMR spectroscopy. Comparison of the FTIR spectra obtained from the ultrasonically atomized and pristine Super Yellow polymer shows near-identical vibrational bands (see figure 5), indicating that the chemical structure of the Super Yellow polymer after ultrasonic atomization remains unaffected (i.e. no new functional groups are created). Extensive side-chain cleavage would be visible by a decrease in the C-H stretching vibration intensity. The ^1H NMR spectra, recorded for the pristine and ultrasonically atomized solutions, confirm these results (see figure 5). The small spikes, observable in the ^1H NMR spectrum of the pristine solution (blue), can be attributed to remnants of solvents after drying the solution prior to the measurement. These solvent spikes are typically narrow, have a low intensity and can be found at their characteristic chemical shift value e.g.: 3.5 ppm corresponds to diethyl ether, 1.85 ppm corresponds to tetrahydrofuran and 1.5 ppm corresponds to water.

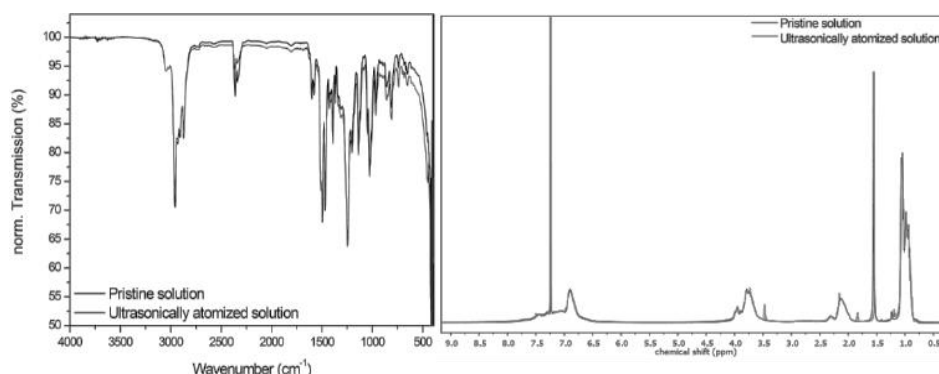


Figure 5. FTIR (left) and H-NMR (right) of the pristine and the ultrasonically atomized solution showing no influence of the ultrasonic vibrations on the polymer characteristics.

A series of Super Yellow OLEDs were prepared via spin coating using either the pristine solution or the ultrasonically atomized Super Yellow solution. The active layers of the devices prepared from both solutions were spin coated inside the glove box. **Error! Reference source not found.** shows the luminous power efficacies of both sets of devices as a function of the applied bias voltages. The overall low efficacies can be related to the active layer thickness (~ 25 nm), resulting from the low concentration used to prepare both solutions, 2.5 mg/mL, which was a precondition for a good ultrasonic atomization. Over the whole bias voltage range, both sets of devices showed comparable luminous power efficacies. These results suggest that ultrasonic atomization in ambient conditions has little (or no) influence on the device performance.

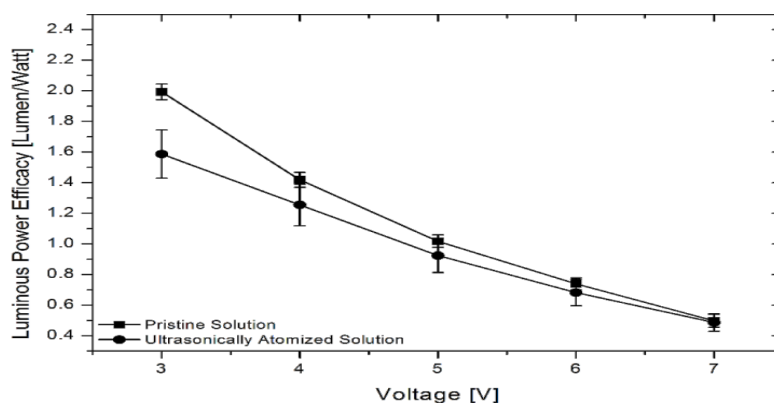


Figure 6. Experimental luminous power efficacies of the spin coated OLEDs from pristine and ultrasonically atomized Super Yellow solutions.

Layer optimization:

As shown in the previous section, the ultrasonic atomisation has no effect on the molecular structure of the dissolved conjugated polymers. This is the most crucial precondition of this deposition technique to be a viable alternative. In this section, the film forming properties of ultrasonic spray coating is treated.

The first step in the investigation of the film forming techniques is to select a solvent or multiple solvent mixture and polymer concentration, which allow good ultrasonic atomisation. Furthermore, the selected solvent(s) – polymer mixture should also be compatible with the substrate or the previously deposited layer. Beyond the film forming properties, the drying behaviour of the deposited films is also of key importance, as they require a post-deposition annealing step in an inert atmosphere. Therefore, solvent evaporation should be avoided during and after deposition.

After systematic variation of different Super Yellow solvent mixtures, it was observed that a Super Yellow solution in 1,2-dichlorobenzene with a concentration of 2.5 mg/mL yielded an excellent combination of both aerosol formation properties and spreading, wetting and drying behaviour of the mixture on the substrate. Uniform substrate coverage was obtained by tuning the ultrasonic spray coater parameters. The nano-scale morphology of spin coated and ultrasonically spray coated Super Yellow films, prepared from the same solution, were investigated by AFM as can be seen in **Error! Reference source not found. 7.**

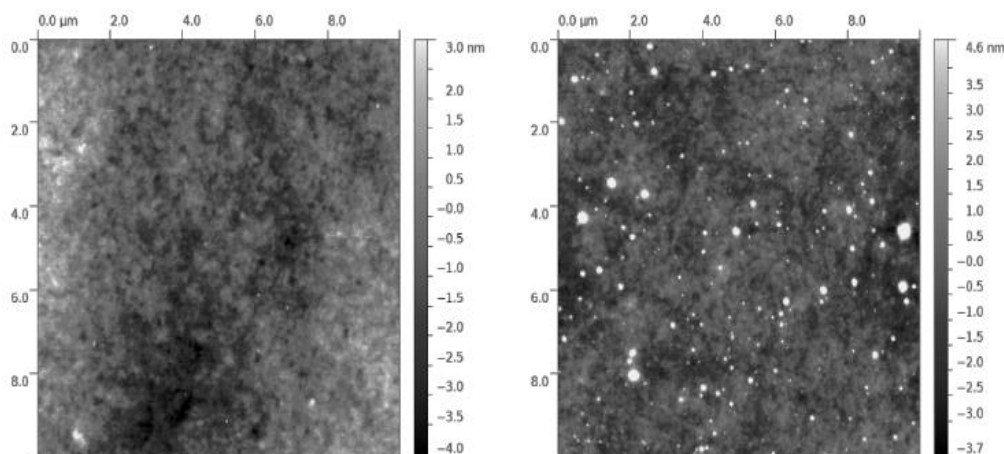


Figure 7. AFM topography image (10 μm by 10 μm) of (left) spin coated Super Yellow film (right) ultrasonically spray coated Super Yellow film.

The ultrasonically spray coated film has a similar topography and root mean square (rms) surface roughness as the spin coated film, 2.8 nm and 1.2 nm, respectively, determined by a scan length of 10 μm .

The overall film thickness can vary by the concentration of the solution, the solution flow rate and the nozzle speed. To achieve the optimal Super Yellow layer thickness of 80 nm and find a relation between the final film thickness and solution concentration, the concentration of the solution was varied from 1 mg/ml to 3 mg/ml with increments of 0.5 mg/ml. All the Super Yellow films were ultrasonically spray coated from their specific Super Yellow – oDCB concentration with their individual spray coating parameters, e.g.: flow rate, nozzle speed, to yield full substrate coverage and uniform low roughness films.

The solution concentration is not the most practical parameter to vary when optimizing the active layer thickness of an OLED. For each variation of the solution concentration a new solution batch has to be made using relative expensive conjugated polymers and organic solvents. However the ultrasonic spray deposition technique also allows deposition control by varying the solution flow rate and nozzle speed at constant solution concentration. By varying the solution flow rate, the amount of solution that emerges at the atomizing surface of the nozzle is changed per unit of time and thus the spray density is varied. The resulting Super Yellow film thickness as function of the flow rate at a constant nozzle speed of 15 mm/s, using a 2.5 mg/ml Super Yellow - oDCB solution was tested. At flow rates lower than 0.4 ml/min non-uniform and partially covered films were observed. At flow rates higher than 2.0 ml/min atomization at the ultrasonic nozzle was hindered.

By varying the nozzle speed at a constant flow rate the final film thickness can also be tuned. The solution, 2.5 mg/ml Super Yellow – oDCB, was supplied to the ultrasonic nozzle at a constant flow rate of 1.5 ml/min.

These results show that for a single solution concentration a wide range of film thicknesses can be deposited. The thickness of the emissive layer is of crucial importance for the charge transport in the OLED [40]. The ability of this deposition technique makes it an ideal candidate for solution processing of OLEDs on an industrial scale as well as on laboratory scale.

Printed top electrode:

The top electrode has to be transparent since the light has to pass through the top of the OLED. In recent years extensive research has been conducted on

innovative materials for transparent electrodes [41]. In this paper, two different approaches to acquire a transparent top cathode are followed, inkjet printed metal grids and thermally evaporated very thin metal layers as shown in figure 8 [42]. Ag grids with hexagonal and triangular structures with a thickness of 150-250 nm were inkjet printed on glass substrates and sintered at 200 °C. To obtain a very thin and transparent cathode, gold (Au) layers were thermally evaporated onto glass samples with a varying thickness of 1-15 nm.

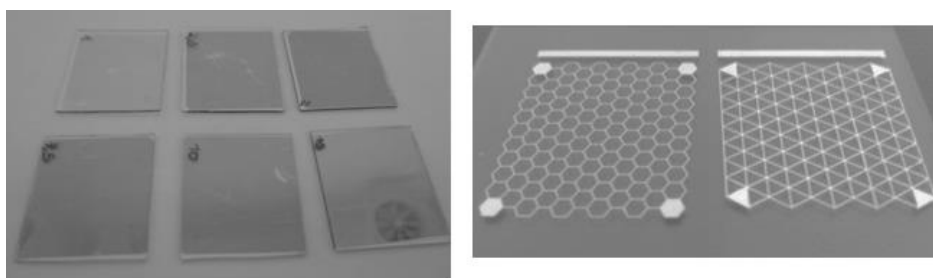


Figure 8. Thermally evaporated Au layers and inkjet printed structures on glass substrates

Both the grids and the thin layers were examined for their sheet resistance and their transparency. For the transparency, it is clearly shown that the Ag grids show a much higher transparency (70-90 %) than the Au layers (25-70 %). The hexagonal structured grids have the highest transparency. On the side of conductivity, the grids showed a lower sheet resistance of $0.82 - 2.7 \Omega/\square$ than the thin metal layers which obtained $3.2 - 123.7 \Omega/\square$.

If one only looks at these two characteristics the Ag grids are clearly pushed forward as the winner. There is however a deal breaker, the used commercially available ink has to be sintered at 200 °C, a temperature that will terminate the underlying layers. A solution for this could be the usage of new commercially available Ag inks, based on precursors instead of Ag nanoparticles, which can be sintered at a much lower temperature [34].

To obtain the necessary built-in potential between the two electrodes, a low work function material, Ca for example, has to be inserted before the cathode. To apply this layer, mostly vacuum deposition techniques are used. However, several attempts are there to replace this Ca by polymeric materials such that in the end, the full OLED can be solution processed using a combination of ultrasonic spray coating and inkjet printing.

IV. CONCLUSION

In this work, we successfully show the transition of production of OLEDs from vacuum deposition towards printing and coating technology. Ultrasonic Spray Coating is applied to deposit the active light emitting layer of the OLED. Firstly, the influence of the ultrasonic vibrations on the stability of the polymer is studied whereafter ink formulation and optimized spray parameters are studied for optimized ultrathin coatings. Finally, inkjet printing is applied to replace vacuum deposited top electrodes. Ag nanoparticle-based inks is applied to print narrow structures and patterns in the form of honeycombs to achieve both high conductive and transparent electrodes. This work shows that the combination of different printing techniques can result in the transition towards fully printed, large area Organic Light Emitting Devices.

V. REFERENCES

- [1] A. Bernanose, M. Compte, and P. Vouaux, "Sur un nouveau mode d'émission lumineuse chez certains composés organiques.pdf," *J. Chim. Phys.*, vol. 50, 1953.
- [2] M. Pope, H. P. Kallmann, and P. Magnante, "Electroluminescence in organic crystals [16]," *J. Chem. Phys.*, vol. 38, no. 8, pp. 2042–2043, 1963.
- [3] C. W. Tang and S. A. Vanslyke, "Organic electroluminescent diodes," *Appl. Phys. Lett.*, vol. 51, no. 12, pp. 913–915, 1987.
- [4] J. J. Shiang and A. R. Duggal, *Organic Electroluminescence*. 2007.
- [5] A. B. H. J.H. Burroughes, D.D.C. Bradley, A.R. Brown, R.N. Marks, K. Mackay, R.H. Friend, P.L. Burns, "Light-emitting diodes based on conjugated polymers," *Nature*, vol. 347, pp. 539–541, 1990.
- [6] S. Hameed and P. Predeep, "POLYMER LIGHT EMITTING DIODES - A REVIEW ON materials and techniques," vol. 26, pp. 30–42, 2010.
- [7] G. Gustafsson, Y. Cao, G. M. Treacy, F. Klavetter, N. Colaneri, and a J. Heeger, "Flexible Light-Emitting-Diodes Made from Soluble Conducting Polymers," *Nature*, vol. 357, no. 6378, pp. 477–479, 1992.
- [8] G. Gu, P. E. Burrows, S. Venkatesh, and S. R. Forrest, "Vacuum-deposited , nonpolymeric flexible organic light-emitting devices," *Opt. Lett.*, vol. 22, no. 3, pp. 172–174, 1997.
- [9] S. R. Forrest, D. D. C. Bradley, and M. E. Thompson, "Measuring the Efficiency of Organic Light-Emitting Devices**," *Adv. Mater.*, vol. 15, no. 13, pp. 1043–1048, Jul. 2003.

- [10] M. C. Gather, A. Köhnen, and K. Meerholz, "White organic light-emitting diodes," *Adv. Mater.*, vol. 23, no. 2, pp. 233–248, 2011.
- [11] J. Wang et al., "Key issues and recent progress of high efficient organic light-emitting diodes," *J. Photochem. Photobiol. C Photochem. Rev.*, vol. 17, pp. 69–104, Dec. 2013.
- [12] C. W. Tang and S. A. VanSlyke, "Organic electroluminescent diodes," *Appl. Phys. Lett.*, vol. 51, no. 12, pp. 913 – 915, 1987.
- [13] M. Kemerink, "Organic electronics lecture 5: Simple device models (lecture notes)." TU Eindhoven, 2012.
- [14] P. W. M. Blom and M. C. J. M. Vissenberg, "Charge transport in poly (p-phenylene vinylene) light-emitting diodes," *Mater. Sci. Eng.*, vol. 27, pp. 53–94, 2000.
- [15] M. Kemerink, "Organic electronics lecture 6: Contacts and injection (lecture notes)." TU Eindhoven, Eindhoven, 2012.
- [16] S. Braun, W. R. Salaneck, and M. Fahlman, "Energy-level alignment at organic/metal and organic/organic interfaces," *Adv. Mater.*, vol. 21, no. 14–15, pp. 1450–1472, 2009.
- [17] R. Coehoorn, "Organic Electronics lecture 8: Interfaces (lecture notes)." TU Eindhoven, 2012.
- [18] J. C. Scott, "Metal–organic interface and charge injection in organic electronic devices," *J. Vac. Sci. Technol. A Vacuum, Surfaces, Film.*, vol. 21, no. 3, p. 521, 2003.
- [19] T. Van Woudenberg, "Charge Injection Into Organic Semiconductors," 2005.
- [20] S. C. J. Meskers, "Organic electronics lecture 1a: pi-conjugated molecules (lecture notes)." TU Eindhoven, 2012.
- [21] S. D. Baranovskii, O. Rubel, F. Jansson, and R. Osterbacka, "Description of Charge Transport in Disordered Organic Materials," *Adv. Polym. Sci.*, vol. 223, no. June 2009, pp. 45–71, 2010.
- [22] M. Kuik, L. J. a. Koster, a. G. Dijkstra, G. a. H. Wetzelaer, and P. W. M. Blom, "Non-radiative recombination losses in polymer light-emitting diodes," *Org. Electron.*, vol. 13, no. 6, pp. 969–974, Jun. 2012.
- [23] G. A. H. Wetzelaer, M. Kuik, H. T. Nicolai, and P. W. M. Blom, "Trap-assisted and Langevin-type recombination in organic light-emitting diodes," *Phys. Rev. B*, vol. 83, no. 165204, pp. 1–5, 2011.

- [24] F. C. Krebs, "Fabrication and processing of polymer solar cells: A review of printing and coating techniques," *Sol. Energy Mater. Sol. Cells*, vol. 93, no. 4, pp. 394–412, Apr. 2009.
- [25] P. de Bruyn, D. J. D. Moet, and P. W. M. Blom, "All-solution processed polymer light-emitting diodes with air stable metal-oxide electrodes," *Org. Electron.*, vol. 13, no. 6, pp. 1023–1030, Jun. 2012.
- [26] J. Lee, S. Lee, G. Li, M. a. Petruska, D. C. Paine, and S. Sun, "A facile solution-phase approach to transparent and conducting ITO nanocrystal assemblies," *J. Am. Chem. Soc.*, vol. 134, no. 32, pp. 13410–13414, 2012.
- [27] Z. Chen, W. Li, R. Li, Y. Zhang, G. Xu, and H. Cheng, "Fabrication of highly transparent and conductive indium-tin oxide thin films with a high figure of merit via solution processing," *Langmuir*, vol. 29, no. 45, pp. 13836–42, 2013.
- [28] R. R. Søndergaard, M. Hösel, and F. C. Krebs, "Roll-to-Roll fabrication of large area functional organic materials," *J. Polym. Sci. Part B Polym. Phys.*, vol. 51, no. 1, pp. 16–34, Jan. 2013.
- [29] L. Hou, L. Duan, J. Qiao, D. Zhang, G. Dong, L. Wang, and Y. Qiu, "Efficient solution-processed small-molecule single emitting layer electrophosphorescent white light-emitting diodes," *Org. Electron.*, vol. 11, no. 8, pp. 1344–1350, Aug. 2010.
- [30] C. Girotto, B. P. Rand, S. Steudel, J. Genoe, and P. Heremans, "Nanoparticle-based, spray-coated silver top contacts for efficient polymer solar cells," *Org. Electron.*, vol. 10, no. 4, pp. 735–740, Jul. 2009.
- [31] F. C. Krebs, "Fabrication and processing of polymer solar cells: A review of printing and coating techniques," *Sol. Energy Mater. Sol. Cells*, vol. 93, no. 4, pp. 394–412, Apr. 2009.
- [32] L. Hou, L. Duan, J. Qiao, D. Zhang, G. Dong, L. Wang, and Y. Qiu, "Efficient solution-processed small-molecule single emitting layer electrophosphorescent white light-emitting diodes," *Org. Electron.*, vol. 11, no. 8, pp. 1344–1350, Aug. 2010.
- [33] C. Girotto, B. P. Rand, S. Steudel, J. Genoe, and P. Heremans, "Nanoparticle-based, spray-coated silver top contacts for efficient polymer solar cells," *Org. Electron.*, vol. 10, no. 4, pp. 735–740, Jul. 2009.
- [34] K. Norrman, a. Ghanbari-Siahkali, and N. B. Larsen, "6 Studies of spin-coated polymer films," *Annu. Reports Sect. "C" (Physical Chem.*, vol. 101, p. 174, 2005.

- [35] N. Sahu, B. Parija, and S. Panigrahi, “Fundamental understanding and modeling of spin coating process: A review,” *Indian J. Phys.*, vol. 83, no. 4, pp. 493–502, Aug. 2009.
- [36] P. Yimsiri and M. R. Mackley, “Spin and dip coating of light-emitting polymer solutions: Matching experiment with modelling,” *Chem. Eng. Sci.*, vol. 61, no. 11, pp. 3496–3505, Jun. 2006.
- [37] S.-R. Tseng, H.-F. Meng, K.-C. Lee, and S.-F. Horng, “Multilayer polymer light-emitting diodes by blade coating method,” *Appl. Phys. Lett.*, vol. 93, no. 15, p. 153308, 2008.
- [38] B. H. Spreitzer, H. Becker, E. Kluge, W. Kreuder, H. Schenk, and R. Demandt, “Soluble Phenyl-Substituted PPVs New Materials for Highly Efficient Polymer LEDs **,” *Adv. Mater.*, vol. 10, no. 16, pp. 1340–1343, 1998.
- [39] Gilissen. K et.al. , “Ultrasonic spray coating as deposition technique for the light-emitting layer in polymer LEDs”, *Organic Electronics*, 20 pp. 31-35, 2015.
- [40] Y. Shi, J. Liu, and Y. Yang, “Device performance and polymer morphology in polymer light emitting diodes: The control of thin film morphology and device quantum efficiency,” *J. Appl. Phys.*, vol. 87, no. 9, p. 4254, 2000.
- [41] Han, T.-H., Jeong, S.-H., Lee, Y., Seo, H.-K., Kwon, S.-J., Park, M.-H., & Lee, T.-W. (2015). Flexible transparent electrodes for organic light-emitting diodes. *Journal of Information Display*, 316(March 2015)
- [42] Vandevenne, G., Marchal, W., Verboven, I., Drijkoningen, J., ... (2016). A study on the thermal sintering process of silver nanoparticle inkjet inks to achieve smooth and highly conducting silver layers, *PSSA*, 213(6), 1403–1409

* * * * *

- ❖ **Dr. Wim Deferme**, Associate Professor, Hasselt University, Institute for Materials Research (IMO), Wetenschapspark 1, 3590 Diepenbeek, Belgium, (IMEC vzw, division IMOMEC, Wetenschapspark 1, 3590 Diepenbeek, Belgium) **E-mail:** wim.deferme@uhasselt.be

Intellectual and Cultural Impact of Relativity



- **S. Boregowda**
- **C. T. Chandrashekhara**
- **M. Gunavathi**

Abstract

This article would clarify how in the Philosophy of Physics, Beliefs and Morality of Science, the principle of relativity can be used, where the reason for relativity comes from, why no culture is better than another. It will become apparent that cultural relativity, in contrast with scientific. Finally, we will argue that relativity, when it is seen that there are moral truths and that its role is to determine the presence of moral truths, is refuted. The contrast between the philosophy of science, cultural and moral philosophy, and the movement to defend cultural relativity. The view of relativity that there are no moral realities, and thus no culture, is better than everything else. The aim of this paper is to defend the relativity theory of Einstein: consequences outside science? Physical theory and the morality of science. Perhaps the biggest lesson from Einstein and his relativity philosophies is that reality is not as it appears to be. A distortion, a cognitive fabrication and we interpret as genuine because of how our minds take over the world, around and inside us. Science extends our view of reality, showing what sometimes seem to be strange associations and possibilities that are unexpected. AS we continue our struggle to understand nature and its mysteries, it is good to remember the everlasting words of Einstein: "What I see in Nature is a magnificent structure that we can comprehend, only very imperfectly, and that must fill a thinking person with a feeling of humility."

Introduction

Relativity, a wider physical theory founded by Albert Einstein, a German-born physicist. Einstein overthrew several ideas underlying earlier physical theories with his theories of special relativity (1905) and general relativity (1915), redefining

the basic principles of space, time, matter, electricity, and gravity in the process. Relativity is, beside with minor system, fundamental to modern physics. Relativity provides the basis for the explanation of planetary phenomena and the universe's own geometry.

"Special relativity" is limited to objects that move with reference in inertial frames, i.e. in a state of uniform motion, with regard to each other. Beginning with the principle of special relativity, the action of light draws conclusions that are contradictory to daily practice, but thoroughly supported by experiments. Special relativity showed that the speed of light is a limit that any material object can touch, but not reach; it is the basis of science's most famous equation, $E = mc^2$; and it has led to other tantalizing findings, such as the "twin paradox."

'General relativity' is concerned with gravity in the universe, one of the basic powers. Gravity explains macroscopic behaviour, and hence general relativity, describes large-scale physical phenomena, such as: planetary dynamics, star formation and death, black holes, and the evolution of the universe. Physical science and human life have been significantly influenced by special and general relativity, most dramatically in nuclear energy and nuclear weapons applications. In addition, the fundamental categories of space and time, relativity and its rethinking, have provided a framework for certain philosophical, social, and artistic interpretations that have shaped human culture in various ways.

Reactions in general culture

The effect of relativity on science has not been limited. At the beginning of the 20th century, special relativity performed on the scene and general relativity became widely recognized after the First World War, when a new sense of "modernism" was established in art and literature. Einstein's 1921 Nobel Prize in Physics (awarded for his work on the photonic origin of light) and the widespread belief that relativity was so complex that few could comprehend it rapidly transformed Einstein and his theories into cultural icons.

Soon after their advent, the notions of relativity were commonly applied and misapplied. The idea was interpreted by some philosophers as simply implying that all things are relative, and they used this term in arenas far removed from physics. In *The Modern Theme*, for example, the Spanish humanist, philosopher, and essayist José Ortega y Gasset wrote in (1923). He said that the ground-breaking nature of

Einstein's thinking was also taken up by the American art critic Thomas Craven, who contrasted the split between classical and modern art in 1921, to the split between Newtonian and Einsteinian conceptions of space and time.

Some have seen particular relationships emerging from the notion of a four-dimensional continuum of space and time between relativity and art. In the 19th century, geometry advances led to widespread interest in a fourth spatial dimension, imagined as lying somewhere, with the ordinary measurements, length, width, and height, at right angles to all three.

The four-dimensional universe of Einstein, with three dimensions of space and one of time, is conceptually distinct from the four dimensions of space. But the two kinds of four-dimensional world, the new art of the 20th century, were conflated in perception. The art historian Paul LaPorte wrote that, "The new pictorial idiom created by Cubism, by applying the concept of the space-time variety to it, is most acceptably explained."

Typically, when relativity was first revealed, the public was shocked by its complexity, a justified reaction to the abstract mathematics of general relativity. But the theory's abstract, no visceral nature also caused reactions to its clear breach of common sense.

General culture has embraced the principles of relativity in contemporary use, the impossibility of faster-than-light flight, $E = mc^2$, time dilation and twin paradox, the expanding universe, and black holes and wormholes, to the point that they are automatically recognized for science fiction works in the media and provide plot devices. Beyond their purely scientific theories, some of these ideas have gained meaning; "black hole" can mean an unrecoverable financial drain in the business world, for instance.

Philosophical considerations

In 1925, the British philosopher Bertrand Russell proposed that Einstein's work would lead to fresh philosophical ideas. Indeed, relativity has had a great influence on philosophy, illuminating those questions that go back to the ancient Greeks. Aristotle recalls the theory of the ether, invoked in the late 19th century, to bring light waves. He divided the universe into earth, air, fire, and water, reflecting

the ether (ether) as the fifth element, the pure celestial sphere. The last vestiges of this theory were removed by the Michelson-Morley experiment and relativity.

Relativity, as developed in Euclid's Elements, also altered the definition of geometry (c. 300 BCE). The scheme of Euclid relied on the axiom, "a straight line is the shortest distance between two points," which seemed to be obviously valid, among others. In Euclid's Optics, straight lines also played a special function as paths, accompanied by light rays. It is now understood that space-time is curved, similar to stars; there are no straight lines and light follows curved geodesics. The geometry of Euclid, like Newton's law of gravity, correctly defines existence under certain conditions, but its axioms are not entirely essential and universal, since the universe often contains non-Euclidean geometries.

In vision of its theoretical scope, Einstein's relativity is among the most important and powerful of scientific theories, reorganizing the view of people's presence, its capacity to explain the entire universe, and its influence beyond science.

Philosophy of Physics

The philosophy of physics is less of an analytical discipline, but for more than 400 years theoretical physics and modern Western philosophy have been informing and upsetting one another than an intellectual frontier. Since the beginning of modern science, many of Western culture's deepest philosophical commitments have been vividly questioned with regard to the character of matter, the essence of space and time, the issue of determinism, the sense of probability and chance, the potential of understanding, and much more. A vibrant dialogue between physics and a distinctly modern Western philosophical tradition, Sir Isaac Newton (1642–1727), was well under way, an exchange that has flourished to the present day.

This paper explores the philosophical foundations, along with their metaphysical and epistemological motives and consequences, of the most general physical theories of modern science. For care, from a philosophical viewpoint, see science, theory, of the elements of scientific investigation.

The Philosophy of Space and Time

The Newtonian concept of the universe: The physical furniture of the universe, according to Newton, consists wholly of infinitesimal material points, generally referred to as particles. Extended objects, or objects that take up finite volumes of space, are treated as particle assemblies, and the behaviour of objects is defined, at least in theory, by the behaviour of the particles they are made up of. Particle characteristics include mass, electrical charge, and location.

The Newtonian idea is both systematic and deterministic. It is complete in the sense that, if it were possible to list what particles existed, what their masses, electric charges, and other intrinsic properties were, and what places they occupied, for each moment of the past time, The list would be absolutely everything that could be known about the universe's physical history; it would include all that existed and any event that happened.

The Newtonian conception is deterministic in the sense that, if it were possible to list the location and other intrinsic properties of each particle in the universe for a particular moment in time, as well as how the position of each particle shifts as time flows, the whole future history of the universe would be predictable with absolute certainty in every detail. This determinism, however, has been considered by many thinkers as incompatible with deep and significant ideas about what it is to be a human being or to lead a human life, ideas such as freedom and obligation, liberty, spontaneity, imagination, and the obvious "openness" of the future.

What is space?

Relations and absolutism

Newtonian mechanics, predicts the movements of particles, or how the locations of particles, in space change over time. But, the very likelihood that there is a theory that predicts how particle positions shift in space requires that, over time, there is a certain factual question about what position each particle occupies in space. In other words, such a theory requires that space itself be a thing that exists independently, the kind of thing that a particle might occupy, a certain part of, or the kind of thing relative to which a particle might move. However, there happens to be a long and distinguished metaphysical history of doubting that there might be such a thing.

The question is based on the fact that it is impossible even to consider how a calculation could be made of the absolute location in space, of any particle, or of any particle assembly. For example, what observation would decide if every single particle in the universe had suddenly shifted to a place precisely one million kilometres to the left of where it had been before? It is at least erroneous, and maybe even incoherent, to suppose, according to some theorists, that there are factual problems regarding the cosmos to which human beings cannot, in theory, have empirical access. A "fact" is necessarily something that, at least in theory, is verifiable by some kind of measurement. Therefore, just if it is relational, something may be a reality about space, about the distances between particles. Talking about evidence, about "absolute" positions, is all nonsense.

Relations, as this view of the existence of space is called, states that space is not a thing that exists separately, but merely a mathematical representation of the infinity of various spatial relationships that particles which have with each other. In the opposite view, known as absolutism, space is a thing that exists independently, and what facts about the universe, it does not actually coincide with what can be described by measurement in theory.

The Newtonian structure of the universe, on the face of it, is dedicated to an absolute idea of space. Newtonian mechanics maintains that particle locations, and not just their relative positions, shift over time, and argues that the rules regulate the movement of a particle entirely, alone in the universe. Relations, on the other hand, is committed to the proposition that even asking what these laws could be is nonsensical.

What is time?

It is clear that there are also consequences for the existence of time for the empirical considerations that have been brought to bear on concerns about the nature of space. First, remember that the location of one within "absolute time" is no more detectable than the place of one within absolute space. Therefore, from an objective point of view, there can be no question of reality as to what absolute time it is at present. In addition, Mach argued that there can be no clear observational access to the lengths of time intervals; the most important thing that can be decided is whether an occurrence happens before, after, or at the same time as another event.

In Newtonian mechanics, a "clock" (or a "good clock") with a certain form of dynamic structure is a physical device. Whether something is a clock (or a good

clock) has little to do with similarities between the clock face configurations from a relational perspective. In the configuration of the clock face and "how much time has passed" and "what time it is" or between adjustments, because, for a relationships, there are no details about what time it is, or how much time a certain phase takes. A good clock is simply a physical device, with parts associated with the physical properties in their locations, By way of a clear and strong rule of the rest of the universe. To the degree that time intervals are even understandable, they are not determined, but rather described, from this viewpoint, by changes in clock faces.

Relationist theory of space, more precisely to design a relationist theory of both space and time, can be extended to the above technique used for fashioning. In other words, one continues by systematically discarding the commitments of Newtonian mechanics with regard to absolute space and absolute time, which do not bear directly on interparticle distance sequences, while preserving only those which do.

Of instance, the final points in the preceding section also relate to the rationalist theory of space and time, to the empirical equivalence of the rationalist theory with Newtonian mechanics, to locality, and to the theory's applicability to isolated subsystems of the universe.

Quantum theory and the structure of space and time

Among quantum theory and the special theory of relativity, there are some fairly basic tensions. While they have been in plain view since the 1970s, until the turn of the 21st century, the determination to deal with them did not take hold directly.

Second, all iterations of quantum mechanics (all attempts to solve the problem of measurement) are dedicated to explaining, at least partly in terms of wave functions, the states of physical systems. The wave functions of systems composed of more than one particle However, in a much larger dimensional space, known as a configuration space, they are clearly not expressible as functions of space and time; they are invariably functions of time and place. And it appears that the fundamental relativistic requirement of Lorentz invariance) cannot even be described in a configuration space.

Furthermore, there is a very intimate relation between Lorentz invariance and locality, dating to the beginning of the special theory of relativity. While the relationship is now understood not to be a matter of logical implication, none of the

non-local Lorentz-invariant models of basic physical theories have the same kind of non-locality as quantum mechanics. In other words, all variants of quantum mechanics mean that the invariance of Lorentz is incorrect. Moreover, each of those proposals requires that there be an absolute, non-Lorentz-invariant simultaneity norm.

In Lorentz's long-neglected approach to physical phenomena, associated with the special theory of relativity, these tensions have created a wide and unparalleled revival of interest. There can be little doubt that these issues and their consequences for the much-discussed project, the reconciliation of quantum mechanics and the general theory of relativity, will be a primary concern for the near future of the philosophical foundations of physics.

Einstein's theory of relativity: implications beyond science?

In 1905, Albert Einstein published his special theory of relativity, and his general theory of relativity was made public in 1915. For these accomplishments, he is often heralded as the most influential thinker of the 20th century and possibly in modern history. His name is taught to elementary school children across the country as a potential role model, and his image is easily recognizable to the majority of our population. "Einstein" and "genius" have become virtually interchangeable in our society. Arguably, it is the superficial simplicity that causes many to accept $E = mc^2$ as Einstein's major contribution to science: five simple characters, simple algebra—how hard could it be? We need only look at the backs of cereal boxes, television commercials, and newspaper advertisements to see the famous equation used to signify education and knowledge. While the audience may not understand what these letters stand for, or the far-reaching implications of the theory of relativity, the equation itself has become a symbol. The use of the phrase signals the lay audience to regard what follows as intelligent, knowledgeable, and accurate. The meaning of this phrase to the scientific community is understandably much different. As a graduate student, much of my academic life while growing up has been geared towards science. One of the questions I remember asking is, "What does $E = mc^2$ mean?" When I was lucky, I received the answer, "energy equals mass times the speed of light squared" and for a while I was content with that literal response. Yet, while "energy equals mass times the speed of light squared" tells me what $E = mc^2$ stands for, it still does not tell me what it means. As I learn more, I realize that the applications of this deceptively simple equation are what give it meaning,

whether they are in the construction of the atomic bomb or the study of particle physics. But this mass-energy equivalence is only one aspect of relativity—and only special relativity at that—and yet it is the most commonly cited example of Einstein's work. However, the great majority influence Einstein is credited with is due to the implications of relativity as a concept beyond science. While Einstein's work did create new branches of study in physics and revolutionize astronomy, the impact on daily life, philosophy, and society are much more important. It is through the aftermath of his two theories on relativity that Einstein has truly risen to fame in a variety of audiences and for many reasons.

At first glance, it seems difficult to acknowledge practical, every day implications of Einstein's theories of relativity. We rarely find ourselves confronted with the dilemma of considering disparate inertial frames or extremely high velocities approaching the speed of light. However, the applications to nuclear energy production and synchronization of the global positioning system (GPS) satellites around the earth indicate an effect of relativity on our day-to-day activities. Nuclear energy has helped alleviate a portion of our reliance on non-renewable resources for our energy needs. And as those needs increase and our resources are depleted, we will be continually drawn towards the promises nuclear energy has already fulfilled for other parts of the world that have more readily accepted it as a major energy supplier. It is also difficult to imagine the military and combat today without conjuring images of nuclear warheads and nuclear-powered submarines. These technologies rely on relativity through GPS. However, GPS enables not only the Department of Defence, but also the commuter who has just taken a wrong turn and the couple searching for a restaurant. Another practical aspect of our lives that has been impacted by relativity is almost so basic that it often escapes conscience awareness. Einstein's postulates regarding relativity challenged much of the way traditional science had viewed certain physical aspects of the universe. Put simply, he stated that the laws of physics (and science) are the same for all observers, regardless of their speed, and that the speed of light was constant for all observers, regardless of their speed. For example, if a person traveling 60 miles per hour on a bus throws an object at 30 miles an hour, this object will appear to be moving at 90 miles per hour—both speeds combined—to a person standing still on the ground, but only 30 miles per hour to the person on the bus. However, if the person on the bus shoots a light beam, and a person standing still on the ground also sees it, the speed of the light will be the same for both people on the ground and people on the

bus—186,000 miles per second. The extra 60 miles per hour of velocity from the bus means nothing. Initial intuition tells us this does not make sense—speed is determined by distance over time. So, if the speed of light doesn't change, that means distance and time must change to always reach the correct number. Therefore, one of relativity's most extraordinary consequences is realized: time itself is relative! Things that we thought were fixed, constant, and known were not really any of those. Time (and length) were dependent on your viewpoint, and the circumstances (i.e. inertial reference frame) in which you viewed these "constants" affected the properties which you measured. Time is often agreed upon as the only constant thing in our universe.

Einstein dared to say that we must now re-interpret how we view the world around us. Such a radical concept turned science on its head, and it became widely acknowledged that this discovery had somehow affected the lives of everyone on the planet—rather, the lives of everyone had always been affected by properties that had only just been discovered and acknowledged. Einstein's theories of relativity have not only affected our daily lives in such basic ways as how we heat our homes, reach our destinations, and measure our days. His theories of relativity were used by philosophers, politicians, and activists to turn moral philosophy upside-down. Relativity fuelled postmodernism and philosophic relativism. Prior to relativity, philosophers such as Aristotle, Kant, and Mill argued that there was an absolute truth and an absolute way of approaching various aspects of life. For example, a businessman who comes across a child drowning in a pond is obligated to save the child's life. However, now armed with relativity, facts are no longer absolute, but instead dependent upon your viewpoint, your own "philosophical" inertial reference frame. Right and wrong now vary from person-to-person, an idea which was so readily accepted because that now meant that each one of our viewpoints could be considered valid, as there was no absolute truth to be had. Of course, it should be noted that this philosophical argument is not always accepted by the laws and social norms we produce. Another societal implication of Einstein's theories is due to his humble background. The child of immigrants, Jewish, and poor, Einstein was the quintessential American. He had earned his success and thus, we could too. Power and fame were not just for the rich and established. Education became the ticket to success for many less fortunate in the United States. He exemplified the importance of diversity and openness at a time when the world was not ready to see that which was different. Due to his fame and prominence after the

publication of his theories of relativity, Einstein became an everyday hero. Amazingly, he was able to use his influence to comment on social and national policies such as nuclear warfare, education, and human rights. Through all of these realms of influence, it becomes obvious that Einstein is not simply a brilliant physicist, but a man who changed his world in ways that he could not have even foreseen. It is for these reasons that he has often been called the most influential person of modern history, and that the greatest impact of his work on relativity was not on our science, but on our society.

Philosophical Interpretations Theory of Relativity

As stated before, preconditions and requirements for a good interpretation We did not only want to examine all the historical cases of successful or unsuccessful interpretations, but also to find out what could be learned from the errors made there-which of these errors could have been avoided and how? In this context, only those instances where anything went wrong and resulted in misinterpretations were important. The proliferation of contemporary interpretations between 1910 and ca. of Einstein's relativity theories 1930 helped me to formulate the following preconditions for sound interpretations that resist side-tracks, such as the concept or statement distortion at hand,

1. Interpreters should display humility and open-mindedness-it is they who are walking on international soil, so they must learn about the method, the principles of argumentation, and the scientific facts and laws to be obeyed. Though it sounds very trivial, in the case of Einstein's interpreters, this precondition was by no means fulfilled.
2. A detailed understanding of the scientific mathematical language in which the theory is formulated should be pursued by philosophical interpreters. Only then can they really grasp its structure; only then can they get a sense of the influence of intra theoretical derivations and of the harmony (or as scientists sometimes say: the beauty) of it. Otherwise, the inevitable outcome is a partial, scattered interpretation, in which certain axioms, theorems or statements are overemphasized while others are illegitimately overlooked. A strong indication of the non-observance of this precondition is the selectivity of most modern interpretations.
3. If there are contradictions between the interpretation structure and certain findings of the interpretation of scientific theory, there should be a

willingness to update these underlying philosophical assumptions, that is, to meet the current challenge to the conventional philosophical outlook. In the revision of conventional principles and assumptions, while philosophers seem to be very conservative.

4. In scientific debate, philosophical perspectives are not the best place for a criticism of the processes, aims, or findings of scientific theories, since only scientific standards determine on their adequacy. The consistency of theories does not require philosophers to judge. There is no need for philosophers to judge the correctness of hypotheses.
5. The crudest types of misinterpretation can be avoided when the previously described preconditions are met. But still, a wide range of contrasting interpretations of one and the same theory will exist. Any parameters for a comparison of these interpretations are useful to have, We suggested the following ones:

BREADTH: The total amount of scientific material incorporated into the interpretation. Compare the difference in quality between Reichenbach Philosophies der Raum-Zeit and Myerson/Metz's accounts of law of Relativity against the lean traces of relativity theory in the Writings of Natorp, Driesch, Brunschvicg and many others.

DEPTH: In their interpretations, only a few authors tried to include more nuanced themes, such as Reichenbach's discussion of the repetition of the Michelson-Morley experiments, Metz's explanation of the sense of relativistic length contractions, Eddington's idiosyncratic but at least stimulating treatment in his Space, Time, and Gravitation of the field equations of general relativity.

CORRECTNESS: Only a few interpreters really understood those fields that were still under debate among scientists of the time, for example, the issue of singularities in general relativity, the debates about different models of cosmology, and also Russell's vision of a coordinate-free form of general relativity. Historical context: E.g., Cassirer's well-founded claim that Einstein's relativity theory constitutes a further stage in the gradual substitution of material substances with mathematical forms, Meyerson's original, but debatable thesis of Hegelian traces in Einstein's Deduction Relativist.

Naturalness in interpreting:

In my view, these key conditions encourage one to approach conflicting interpretations of scientific theories in the same reasonable, logical manner in which science philosophers have sought to deal with competing scientific theories for many days. The general theory of relativity does not seem to have received an equally balanced consideration by contemporaries..

We realize that the above preconditions and parameters would be as divisive as the similar suggestions for the theoretical assessment criteria have been. But at least they could cause the start of a debate on comparative assessments of philosophical interpretations of scientific theories. This should be an important subject on the agenda of philosophers of science in the light of on-going debates on the philosophical understanding of quantum mechanics, quantum field theories, etc.

Conclusion

In an effort to describe the cultural disparity more systematically and comprehensively in the consistency of self-concept, this thesis introduced the theory of cognitive relativity by expanding the corresponding distinction between relativism and absolutism. The study established, in self-concept, the measure of cognitive relativity and who informed an analytic worldview in general. Higher cognitive relativity was demonstrated in all three attributes: self-concept, physical, psychological, and social. The social or relational attribute, in particular, yielded a striking difference, and the psychological attribute also revealed strong variations between the philosophy of physics, cultural and moral science. Before taking out the effects of covariates, person and interdependent self-construction, the physical attribute did not display as strong a difference, but the difference was still statistically important. The thesis was intended to investigate the possibility of extending this alternate viewpoint to the study of cultural differences. Thus, by no way are the results definitive. Cognitive relativity measurement scales need greater refinement to ensure higher reliability and validity. In addition, the measurement scales, universal analytical worldviews, need to be established through future research to specifically test the relationship between cognitive relativity and various kinds of worldviews.

References

1. Frederick E. Woodbridge Professor of Philosophy, Columbia University. Author of Quantum Mechanics and Experience and others.
2. *Oct 20, 2008* Einstein's theory of relativity: implications beyond science?
3. Charles Howard Candler Professor of Physics Emeritus, Emory University, Atlanta. Author of Empire of Light, Universal Foam
4. Hung, E. H.-C. 1997. The Nature of Science: Problems and Perspectives. California: Wadsworth Publishing Company
5. Pojman, L. 2008. "Who's to Judge what's Right or wrong?" in Taking Sides: Clashing Views on Moral Issues, ed. S. Stephen, 11th ed. McGraw-Hill/Dushkin
6. Markus, H. R., & Kitayama, S. (1998). The cultural psychology of personality. *Journal of Cross-cultural Psychology*, 29, 63–87.
7. Such, E. M. (2002). Culture, identity consistency, and subjective well-being. *Journal of Personality and Social Psychology*, 83, 1378–1391.
8. Kashima, Y., Kashima, E., Farsides, T., Kim, U., Struck, F., Werth, L., & Yuki, M. (2004). Culture and context-sensitive self: The amount and meaning of context-sensitivity of phenomenal self differ across cultures. *Self and Identity*, 3, 125–141.
9. Bertalanffy, L. (1969). *General systems theory: Foundations, development, applications*. New York: George Braziller, Inc.

* * * * *

- ❖ **S. Boregowda**, Asst. Professor & HOD of Physics, Sri Adichunchanagiri College of Arts, Commerce and Science, Nagamangala-571432, Karnataka, India, **Ph:** 9164061264, **E-mail:** sbygowda@gmail.com
- ❖ **C. T. Chandrashekhara**, Asst. Professor, Department of Physics, Sri Adichunchanagiri College of Arts, Commerce and Science, Nagamangala-571432, Karnataka, India.
- ❖ **M Gunavathi**, Asst. Professor, Department of Computer Science, Sri Adichunchanagiri College of Arts, Commerce and Science, Nagamangala-571432, Karnataka, India.

Mondriaan paintings by large area organic light emitting diodes



- Maikel Kellens, Musa Aydogan
- Bram Claessen, Jerey Gorissen
- Inge Verboven, Rachith S. N
- Dr. Ir. Wim Deferme

Abstract

Stability of the organic light emitting diodes (OLEDs) is a major concern, as the devices built-in a nitrogen environment in the glovebox will degrade exponentially if exposed to air. Glass in combination with UV curable epoxy provides an excellent encapsulation thereby allowing the OLEDs to be used outside the glovebox. However, an inkjet printed silver ink-based bus-bar is required to allow the uniform distribution of charges from the electrodes. This increases the fabrication time and cost. In this work, a conductive adhesive IQ-BOND 5611 from the company Roartis is used as a dual-purpose adhesive. Along with the encapsulation properties it also provides conductive pathways for the charge distribution thereby acting as a bus-bar. To demonstrate the effectiveness of the conductive adhesive, a Modriaan painting is designed, fabricated and tested. The results are compared with that of a standard UV curable epoxy. Obtained results show that the conductive adhesive exhibits a good conducting property and to tap in the encapsulation properties, the complete device should be covered with this adhesive which limits its application in encapsulation.

Keywords — OLEDs, encapsulation, epoxy, conductive adhesive, Mondriaan painting

I. INTRODUCTION

OLEDs differ from regular LEDs (Light Emitting Diode) because they do not use n and p-type semiconductors. OLEDs use organic molecules to produce electrons

and holes. Elementary, OLEDs are built up with six distinctive layers. This layer structure can be seen in Figure 1. The top and bottom layers are made of glass or plastic and are there to protect the structure. The bottom layer on which the stack is built is called the substrate. The top layer is called the seal. Just like the regular LEDs, OLEDs use negative (cathode) and positive (anode) terminals. Sandwiched between cathode and anode, the emissive and conductive layers are found. These layers are made from organic molecules. The emissive layer is where the light is produced and is located next to the cathode. Hence, the conductive layer is located next to the anode [1,2]. This sandwich of layers produces light when a potential difference is applied across the anode and cathode. Due to the flow of electricity, the cathode acts as an electron recipient, and the anode acts as an electron donor. This causes the emissive layer to become negatively charged, akin to the n-type layer in the standard LED. The conductive layer, on the other hand, is getting a positive charge, analogous to the p-type layer in the standard LED. In the process of recombination, an electron and a hole join in the emissive layer. This results in the release of energy in the form of a photon.

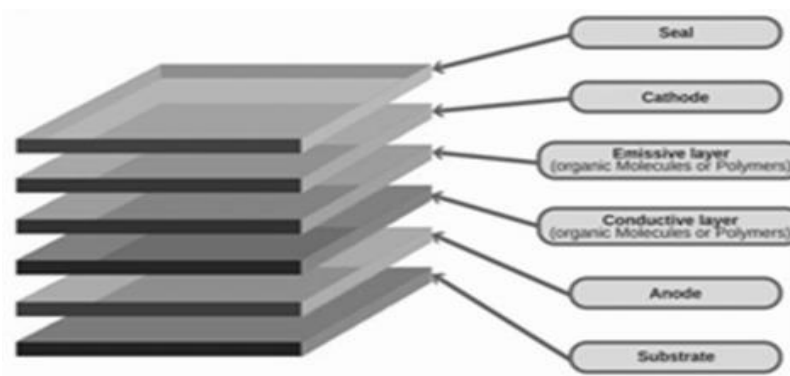


Figure 1: OLED structural layers [2]

Lab-scale OLEDs built inside a glovebox have exhibited superior performance for decades[2]. Stability of these devices was always an issue[3], however, if placed inside a glovebox, these OLEDs could last for two years without showing any sign of degradation. For external use, sophisticated encapsulation has been recommended by many [4-6] and has shown a significant improvement in the stability of the OLEDs used outside the glovebox. Most of these novel structures have in general glass substrates on top of the OLED architecture. These glass substrates are placed on top of the OLEDs by using epoxy, which when cured will not allow the permeability of the atmospheric air into OLEDs and these epoxy will

not react with the OLEDs, thereby not affecting the performance of the OLEDs adversely. However, for a large area OLEDs, the anode current from the ITO is not uniformly distributed, and OLEDs illuminate close to contact circuit, making the application of OLEDs for large area lighting very difficult. However, expensive thermal deposition of a bus-bar is an exciting alternative and renders a very good result. However, expensive vacuum deposition increases the cost of the OLEDs. Recently inkjet-printed silver inks were used as a bus-bar [7] and the obtained results are similar to that of vacuum deposited bus-bars. Recently there is a huge interest in electrically conductive adhesives for the application of encapsulation as it can serve the dual purpose of encapsulation and bus-bar conduction. Therefore, in this work, we have incorporated conductive adhesive IQ-BOND 5611 (Roartis) for the application of OLEDs encapsulation and bus-bar. To demonstrate the feasibility of these for the large area deposition, OLEDs with $5\text{cm} \times 5\text{cm}$ are fabricated. This demonstrator, in the form of a Mondriaan painting, displays the feasibility of large OLEDs panels in a modular design. Pieter Cornelis Mondriaan was a 20th-century Dutch painter whose abstract art compositions are the foundation of this demonstrator.

II. MATERIALS AND METHODS

Design

In the design process, the colours of the OLEDs had to be determined. Depending on the colour wishes, the production process differs. Different materials are needed to produce OLEDs with different colours. Furthermore, the OLEDs' size is defined by the size of the glass plates. The visual design was made with modularity and structure in mind. The OLEDs need to be replaceable. The glass sides of the OLEDs and the electronics should not be visible. Therefore, the black bars in the design are used to cover these aspects. This can be seen in Figure 2. The OLED colours are red, blue, and super yellow.

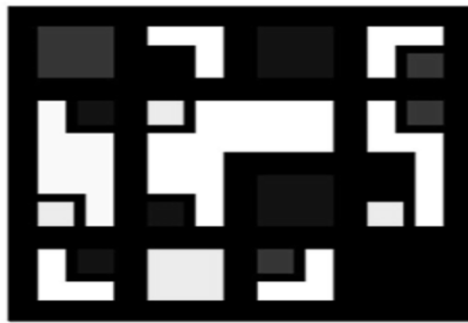


Figure 2: Visual design of the OLED art demonstrator

Structural design:

The structural design brings everything together. It holds the electronics and the OLEDs in place and ensures the function as a demonstrator. For this, several plexiglas plates were designed. To achieve the desired visual design, a base plate is needed to facilitate a fixed placement. Next, OLED holders are needed to house the OLED modules without damaging them, along with an alignment plate to align the modules into their exact place. Last, a top plate is required to finalize the design and to keep the modules from falling out. Please refer to Figure 3 for the structural design.

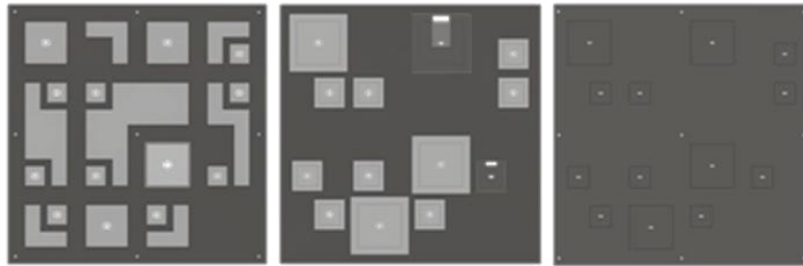


Figure 3: Structural design of the OLED art demonstrator. Right: OLED base plate. Middle: Baseplate + OLED holder + alignment plate. Left: OLED top plate on top of the alignment and base plate.

OLED Fabrication:

In this section, the fabrication process of the OLEDs is described[8,9]. The fabrication process consists of multiple steps that need to be completed adequately to produce working OLED panels.

Creating the pattern and Etching: 150nm of Indium Tin Oxide (ITO) on a glass substrate was used as an anode as the ITO was deposited uniformly over 5cm × 5cm Glass substrate. To avoid a short circuit between the top cathode and the ITO connected to the anode, some parts of the ITO had to be etched away. This was done by covering the ITO with plastic, except the 1cm by 0.5cm area that needs to be etched away. The exposed area is treated with HCL for 30 minutes[10,11]. At the end of the 30 minutes, the ITO is etched away uniformly. It is visible in Figure 4 (a) and (b).



Figure 4. (a) ITO patterning to etch ITO for the contact (b) ITO etching by HCl for 30 min

Cleaning ITO-samples: The next step is to clean the samples, and this is done so there is no dust left on the glass. This would cause malfunctioning OLEDs. The cleaning protocol for the ITO substrate is as follows: 30min ultrasonication in soap water, 20min ultrasonication in Mili Q water (De-Ionized water), 10 min ultrasonication in Acetone, 10 min ultrasonication in IPA. Remove the remainder of IPA by blowing nitrogen gas for 30 sec. To increase the surface energy and to remove the monolayer of organic impurities, the cleaned ITO substrates were exposed to UV-Ozone treatment for 30 min.

Spin coating: The PEDOT:PSS layer is used to improve the conductivity and hole injection. This layer is deposited by spin coating. Spin coating is a technique to deposit a thin layer. To coat the sample, it is spun at a rotational speed of 3000 for 40 sec and with an acceleration of 3000 while a few drops of PEDOT:PSS are dropped on the sample. The final layer of PEDOT:PSS is around 30nm[12,13]. This followed by placing the samples on a hot plate for annealing. Annealing is used to reduce the surface roughness, enhance the optical transmittance, decrease the hole barrier, and increase the surface energy and polarity. The annealing of the PEDOT:PSS is done in an inert atmosphere for 15 min at 130°C[8,9,12,13]. The next step is to transfer the samples into the glovebox, the O₂ and H₂O level is controlled here and is always below one ppm. In the glovebox, the active layers (Super Yellow, Super Blue, Super Red, and Super Green) are deposited at a rotational speed of 750 rpm for 60 sec with an acceleration of 750[14]. This followed by thermal evaporation of 30nm of Ca as an electron injection layer and 100nm of Al as Cathode, which can be seen in Figure 5.

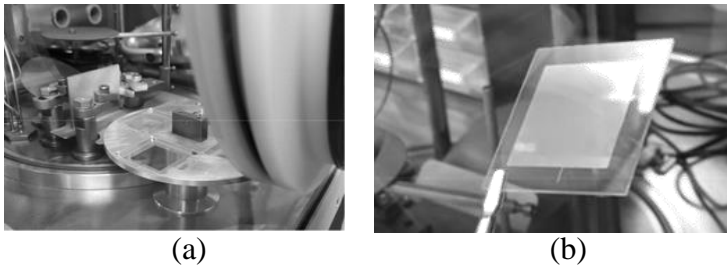


Figure 5(a). Samples after Super Yellow deposition, before samples after Al deposition

Encapsulation of OLEDs:

The encapsulation of OLEDs is a necessary step as it is vital to its longevity. Humidity and oxygen commonly found in the atmosphere damage the OLEDs. By encapsulating the OLEDs, it is possible to shield the structures from the outside atmosphere [15]. Because of the temperature-sensitive nature of OLEDs, high-heat curable encapsulation techniques were not an option. Initially, the OLEDs were encapsulated using epoxy resin after a busbar was applied around the active area using conductive inkjet printing. To simplify this process, an alternative was found as IQ-BOND 560x CE(-SMP), which is an electrically conductive adhesive. More specifically, a two-component, silver-filled adhesive. The idea was to use this conductive adhesive to construct a busbar but also to encapsulate the OLEDs without the use of some epoxy resin. This adhesive stands out because of its room temperature curability.

Electronics:

For the electronics side of the project, the components, schematics, and PCB are crucial to providing power to all of the OLED modules. As can be seen in Figure 6, every OLED has an own driver, and this driver exists out of a transistor and a resistor. The transistor is only used as a switch and does not need to switch high currents, high voltages, or on high frequencies. For that reason, a simple BC547 NPN-BJT was used. The resistor is used to drive the right current through the OLED. The voltage over the OLED is fixed because it is a diode. Therefore, if the voltage source is fixed, the voltage over the resistor is also fixed. As a result of this, the current through the resistor, and an extension through the OLED in series, depends on the value of the resistor.

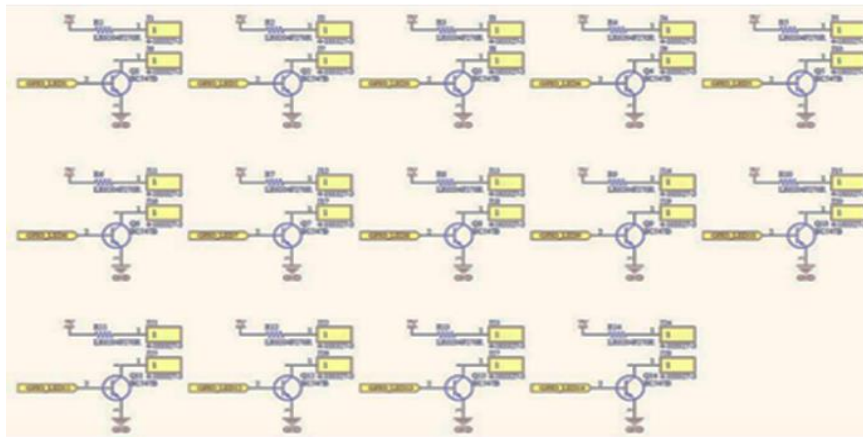


Figure 6: OLED drivers schematic

The voltage used to drive the OLEDs is 7V. This voltage was used, so it was easier to set the right current for the OLEDs. As mentioned before, the blue OLEDs can need a voltage up to 5V. If the voltage source of the driver was 5V, there would be no room for the resistor to set the current. The 7V for the driver is achieved by boosting the 5V from the power supply with a boost converter. The reason a 5V power supply was used, and not a 7V or 12V or something, is that 5V can be powered by USB. USB ports are everywhere and using a portable power bank is easy. Therefore, starting from a 5V input was the way to go.

To control the transistor in the driver, an ESP32 was used. This microcontroller has more than enough GPIO pins and can source enough current to drive the transistors. Between the ESP32 and the transistor is a resistor to set the maximum current. The GPIO pins do not control current, they only set a high or low voltage. This high voltage is 3.3V, and the low voltage is connected to the ground. The ESP32 can be powered with 5V so no other logic is needed here. The ESP32 can connect to a WI-FI network, so in the future, the software could be updated in such a way that the OLEDs can be controlled with any smart platform.

A PCB was made to have a flush connection between all components. The schematic of the PCB can be seen above. The design is not complicated but has a lot of tracks from all the GPIO pins to the transistors. The PCB is double-sided, this made the design easier and smaller. A picture of the finished PCB is shown in Figure 7.

Software:

The software is not essential for the project, all the OLEDs would light up if the transistors were all just pulled up. However, this would not fully show what is possible. Therefore, a little demo program was written with code to blink lights and turn them on and off in groups, etc.

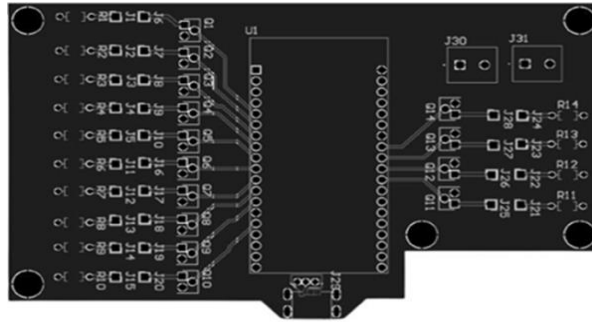


Figure 7. Double-sided PCB with space left open for boost converter

III. RESULTS

Preliminary test results:

The first few OLEDs showed some issues. Along with being run without a current limiter, which damages the samples rapidly, some additional issues can be pointed out. In Figure 8(a) a sample is shown, where only part of the actual OLED is working. A large amount of surface area is just not illuminated. It is thought that this is caused by a short between the active area and the bus-bar. When looking at Figure 8(b), the entire surface area is lit up. However, the illumination is not uniform, with the brightest part in the lower-left corner and the darkest part in the top right corner. The cause here lies with insufficient conductivity within the sample, as the bus-bar is not applied homogeneously, its resistance and thus also its conductivity is not homogeneous. Finally, in Figure 8(c) a near-perfect sample is seen.



Figure 8(a) Malfunctioning blue OLED sample (b) Unevenly lit red OLED sample and (c) Super yellow OLED sample with small inconsistencies

The samples that worked inside the glove-box did not work anymore once they were exposed to the conditions outside the glove-box. As can be seen from Figure 9, the OLEDs started to oxidize, which means that the encapsulation properties of the conductive adhesive were not enough. All samples after these preliminary ones were encapsulated with epoxy resin, and the conductive adhesive was only used for the busbar.

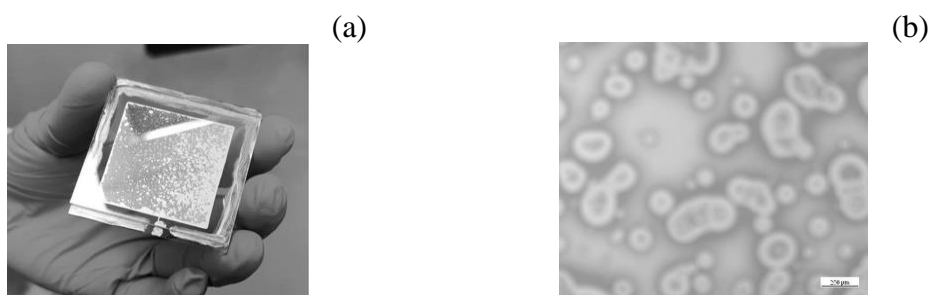


Figure 9(a) image of the encapsulated OLEDs with the oxidation of aluminium electrode **(b)**Microscopic image of the aluminium oxidation

Improved encapsulation with epoxy:

After the conclusion that the conductive adhesive was not sufficient on its own, for proper encapsulation, a UV curable epoxy resin was used to improve the encapsulation. Figure 10 (a) shows how an epoxy droplet is sandwiched in between the glass plates of the OLED. This droplet is spread out over the whole surface except the pads used to make external electrical connections. See Figure 10(b) for the UV curing lamp inside the glove-box during the curing session.

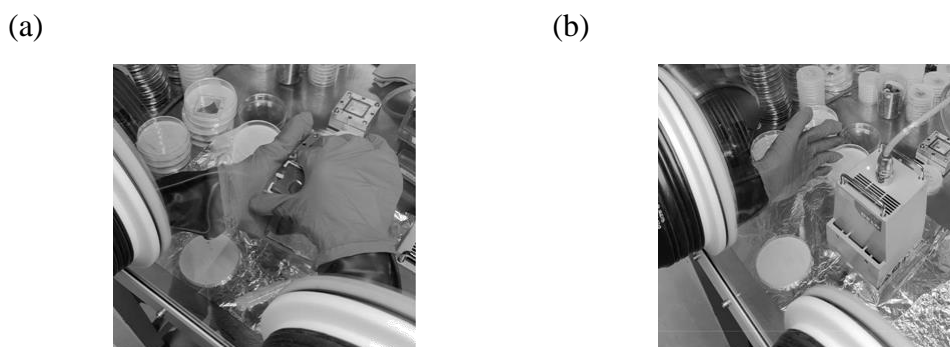


Figure 10 (a). Encapsulation with UV curable epoxy resin inside the glove-box **(b)** UV curing during encapsulation inside the glove-box

OLED yield:

As was explained in the preliminary test results, the encapsulation with conductive adhesive was not sufficient on its own, and an epoxy resin was used to provide the much necessary encapsulation to protect the OLED from oxidizing. So the conductive adhesive was only used for the busbar, but tests showed that it was not suited for this function either. During preliminary tests not so long after the encapsulation process, the OLEDs turned out to be working fine as can be seen in Figures 11(a) and (b). But after attachment of the cabling to the OLEDs a week after the preliminary tests, the majority of the samples did not work anymore. This suggests that the life-time of the conductive adhesive is not long enough to be used in this application.

(a)



(b)

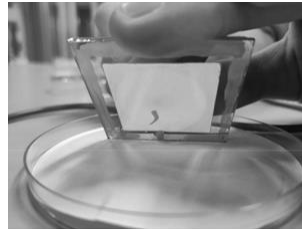


Figure 11 (a) Blue OLED working during preliminary tests **(b)** Yellow OLED working during preliminary tests

IV. CONCLUSION

In this work, we successfully display the possible usage of conductive adhesive in combination with epoxy for the bus-bar and encapsulation of an OLEDs application. To demonstrate the same, Mondriaan painting was designed and developed by large-area OLEDs. Encapsulated devices had limited lifetime, owing to the stability of the conductive adhesive itself. However, it opened a wide possibility of using conductive adhesive in conjunction with epoxy for a large area, flexible and stable OLEDs fabricated at low cost.

V. REFERENCES

- [1] T. Tsujimura, "OLED Display Fundamentals and Applications," 2nd ed. Hoboken: John Wiley & Sons Inc, 2017, pp 12-14.
- [2] Wang, H., Xie, L., Peng, Q., Meng, L., Wang, Y., Yi, Y., & Wang, P. (2014). Novel thermally activated delayed fluorescence materials-thioxanthone derivatives and their applications for highly efficient OLEDs. *Advanced Materials*, 26(30), 5198–5204.
- [3] Tsang, D. P. K., & Adachi, C. (2016). Operational stability enhancement in organic light-emitting diodes with ultrathin Liq interlayers. *Scientific Reports*, 6.
- [4] Wu, J., Fei, F., Wei, C., Chen, X., Nie, S., Zhang, D., ... Cui, Z. (2018). Efficient multi-barrier thin-film encapsulation of OLED using alternating Al₂O₃ and polymer layers. *RSC Advances*, 8(11), 5721–5727.
- [5] Eun Gyo Jeong, et al.(2020) A review of highly reliable flexible encapsulation technologies towards rollable and foldable OLEDs, *Journal of Information Display*, 21:1, 19-32
- [6] C.Y. Li, et all June 2008 *Proceedings - Electronic Components and Technology Conference*, IEEE Xplore.
- [7] Dongjo Kim, et all, Ink-Jet Printing of Silver Conductive Tracks on Flexible Substrates December 2006 *Molecular Crystals and Liquid Crystals* 459(1),
- [8] G.Wang, X. Tao, R. X.Wang, "Fabrication and characterization of OLEDs using PEDOT:PSS and MWCNT nanocomposites", *Composites Science and Technology*, vol. 68, ed. 14, pp 2837-2841, 2008
- [9] K. Gilissen, J. Stryckers, P. Verstappen, J. Drijkoningen, G.H.L. Heintges, L. Lutsen, J. Manca, W. Maes, W. Deferme, "Ultrasonic spray coating as deposition technique for the light-emitting layer in polymer LEDs," *Organic Electronics*, vol. 20, 2015, pp 31-35
- [10] Han, S. H., Rho, J., Lee, S., Kim, M., Kim, S. I., Park, S., ... Chung, T. D. (2020). In Situ Real-Time Monitoring of ITO Film under a Chemical Etching Process Using Fourier Transform Electrochemical Impedance Spectroscopy. *Analytical Chemistry*,
- [11] Oh, S., Jung, H., Kim, Y. H., Kim, M., Yoo, E., Choi, Y. J., ... Lee, H. H. (2013). Characterization of ITO etching by spontaneously evaporated fume of hydrogen chloride. *Microelectronic Engineering*, 103, 173–176.

- [12] Benor, A., Takizawa, S. ya, Pérez-Bolívar, C., & Anzenbacher, P. (2010). Efficiency improvement of fluorescent OLEDs by tuning the working function of PEDOT:PSS using UV-ozone exposure. *Organic Electronics*, 11(5), 938–945.
- [13] Wang, G. F., Tao, X. M., & Wang, R. X. (2008). Fabrication and characterization of OLEDs using PEDOT:PSS and MWCNT nanocomposites. *Composites Science and Technology*, 68(14), 2837–2841.
- [14] Burns, S., Macleod, J., Trang Do, T., Sonar, P., & Yambem, S. D. (2017). Effect of thermal annealing Super Yellow emissive layer on efficiency of OLEDs. *Scientific Reports*, 7.
- [15] T. Tsujimura, "OLED Display Fundamentals and Applications," 2nd ed. Hoboken: John Wiley & Sons Inc, 2017, pp 79-90.

* * * * *

- **Maikel Kellens, Musa Aydogan, Bram Claessen, Jerrey Gorissen**, Hasselt University, Institute for Materials Research (IMO), Wetenschapspark 1, 3590 Diepenbeek, Belgium.
- **Inge Verboven, Rachith S. N, Dr. Ir.Wim Deferme**, Hasselt University, Institute for Materials Research (IMO), Wetenschapspark 1, 3590 Diepenbeek, Belgium (IMEC vzw, division IMOMECE, Wetenschapspark 1, 3590 Diepenbeek, Belgium) *E-mail:* maikel.kellens@student.uhasselt.be, Rachith.shanivaranthe@uhasselt.be

Quantum Cryptography

○ Shobha .M

Abstract:

Quantum Cryptography is one of the emerging topics in the field of computer Industry. Quantum Cryptology is an approach to securing communications by applying the phenomena of quantum physics. Quantum Cryptography provides secure communication, whose security depends only on the validity of quantum theory. This article summarizes the current state of quantum cryptology. We describe results from an apparatus and protocol that is designed to implement the quantum key distribution by which two users who share no secret information (without having any private or public keys known before hand) initially exchange a random quantum ransmission consisting of very faint flashes of polarized light.

Keywords : Quantum Cryptography systems, Large Scale distributed computational systems, Cryptosystems, Quantum physics.

1. Introduction:

Quantum Cryptography is an Exciting new field which has the potential to enable highly secure digital communication using existing technology. Quantum Cryptography is an effort to allow two users of a common communication channel to create a body of shared and secret information. Quantum Cryptography is one of the few commercial applications of quantum physics at the single quantum level. The article presents the different between classical cryptographic techniques and quantum cryptology, and applications of each. In another section presents the Quantum key distribution and current progress in Quantum Cryptology.

2. Classical Cryptology:

Cryptography came in the fifth century BC and was invented by the Spartans of Greece. Cryptography is the study of mathematical techniques related to the aspects of information security, such as confidentially, data integrity and entity

authentication, digital signatures. Classical Cryptography is based on the mathematics and it relies on the computational difficulty of factorizing large number.

In the classical cryptography the original data i.e the plain text is transformed into encoded format i.e cipher text So that we can transmit this data through insecure communication channels. A data string which known as key is used to control the transformation of the data from plain text to chipper text. This arrangement helps to keep data safe as it required the key for extracting the original information from the cipher text. Without the key no one can read the data. In this technique it is assumed that the only authorized receiver has the key.

Classical Cryptography has two types of techniques:

➤ **Symmetric Cryptography:**

In the symmetric cryptography a single key is used for encrypting and decryption the data. This encryption key is private key. This is the limitation of this encryption technique that this private key must be distributed only among the authorized sender and receiver.

➤ **Asymmetric Cryptography:**

In the asymmetric cryptography a pair of key, i.e., public key and private key is used for encryption and decryption. A sender can use its public key to encrypt the data and on receiver end receiver can decrypt the data by using its private key. This technique overcomes the problem of key distribution.

Advantages of Classical Cryptography:

- While employing the one-time pad, it is unbreakable.
- It is easy to do manually, no computer required.
- It protects the plain text from casual snooping.

Disadvantages of Classical Cryptography:

- While employing the one-time pad, it is cumbersome and requires a personal meet up to exchange the pads. If not employing the OTP, anyone who is even remotely interested in knowing what you wrote and knows about cryptography will be able to break the encryption.

3. Quantum Cryptography:

The idea of Quantum Cryptology was first proposed in the 1970. Charles H. Bennet and Gilles Brassard developed the concept of Quantum Cryptography in 1984. One aspect of quantum cryptography is to create cryptographic protocols to protect quantum states that do have the property that they cannot be copied. Quantum Cryptography is based on physics and it relies on the laws of quantum mechanics. It is arising technology which emphasizes the phenomena of quantum physics in which two parties can have secure communication based on the invariabilities of the laws of the quantum mechanics. Quantum mechanics is the mathematical framework or set of rules for the construction of physical theories.

In fact, quantum cryptography rests on two pillars of 20th century quantum mechanics- the Heisenberg Uncertainty principle and the principle of photon polarization.

Heisenberg Uncertainty Principle:

This principle says that if you measure one thing, you cannot measure another thing accurately. For example, if you apply this principle to human, you could measure a person's height, but you can't measure his weight. The only odd thing about this principle is that it becomes true only for the instant at which you try to measure something. This principle is applied to the photons. Photons have wave like structure and are polarized or tilted in certain direction. While measuring photon polarization, all subsequent measurements are get affected by the choice of measures that we made for polarization. This principle plays the vital role to prevent the efforts of attacker in quantum cryptography.

Photon Polarization Principle:

This principle refers that, an eavesdropper cannot copy the unique quantum bits, i.e., unknown quantum state, due to the no-cloning principle. If an attempt is made for measuring any properties, it will disturb the other information.

➤ Advantages of Quantum Cryptography:

It establishes secure communication by providing security based on fundamental laws of physics instead of mathematical algorithms or computing technologies used today.

- It is virtually unhackable.
- It is simple to use.
- Less resource is needed in order to maintain it.
- It is used to detect eavesdropping in QKD (Quantum Key Distribution). This is due to the fact that it is not possible to copy the data encoded in quantum state.
- The performance of such cryptography systems is continuously improved.

➤ **Disadvantages of Quantum Cryptography:**

- The world wide implementation of this can take up lots of jobs and hence unemployment will increase.
- While traveling through the channel polarization of photon may change due to various causes.
- Quantum cryptography lacks many vital features such as digital signature, certified mail etc.
- The largest distance supported by QKD is about 250 KM at a speed of 16 bps through guided medium.

4. Quantum Key Distribution:

Quantum Key Distribution (QKD) is a relatively new cryptographic primitive for establishing a private encryption key between two parties. QKD is a means of distributing keys from one party to another, and detecting eavesdropping. It allows two parties to establish a common random secret key by taking advantage of the fact that quantum mechanics does not allow for distinguishing non-orthogonal states with certainty. Quantum Key Distribution (QKD) is based on the principles of quantum information-secure cryptographic keys that do not depend on these constraints, at least on a protocol level.

Quantum key distribution (QKD) is a secure communication method for exchanging encryption keys only known between shared parties. The communication method uses properties found in quantum physics to exchange cryptographic keys in such a way that is provable and guarantees security.

QKD enables two parties to produce and share a key that is then used to encrypt and decrypt messages. Specifically, QKD is the method of distributing the key -- not the key itself or the messages it can enable users to send.

Key distribution on a conventional scale relies on public key ciphers that use complicated mathematical calculations and, therefore, require a prohibitive amount of processing power to break. The viability of public key ciphers, however, faces several issues, such as the constant implementation of new strategies used to attack these systems, weak random number generators and general advances in computing power. In addition, quantum computing will make much of today's public key encryption strategies unsafe and out of date.

QKD works on a scale much different from conventional key distribution in that QKD uses a quantum system that relies on basic and fundamental laws of nature to protect the data, rather than relying on mathematics. As an example, the no-cloning theorem states that it is impossible to create identical copies of an unknown quantum state, which prevents attackers from simply copying the data in the same manner that they can copy network traffic today. Additionally, if an attacker disturbs or looks at the system, the system will change in such a way that the intended parties involved will know. This is a process that is not vulnerable to increased processing power.

How does QKD work?

QKD works by transmitting many light particles, or photons, over fiber optic cables between parties. Each photon has a random quantum state, and collectively, the photons sent make up a stream of ones and zeros. This stream of quantum states that make up ones and zeros are called *qubits* -- the equivalent of bits in a binary system. When a photon reaches its receiving end, it'll travel through a beam splitter, which forces the photon to randomly take one path or another into a photon collector. The receiver will then respond to the original sender with data regarding the sequence of the photons sent, and the sender will then compare that with the emitter, which would have sent each photon. Photons in the wrong beam collector are discarded, and what's left is a specific sequence of bits. This bit sequence can then be used as a key to encrypt data. Any errors and data leakage are removed during a phase of error correction and other post-processing steps. Delayed privacy

amplification is another post-processing step that removes any information an eavesdropper might have gained about the final secret key.

There are many different types of QKD, but two main categories are prepare-and-measure protocols and entanglement-based protocols. Prepare-and-measure protocols focus on measuring unknown quantum states. This type of protocol can be used to detect eavesdropping, as well as how much data was potentially intercepted. Entanglement-based protocols focus around quantum states in which two objects are linked together, forming a combined quantum state. The concept of entanglement means that measurement of one object thereby affects the other. In this method, if an eavesdropper accesses a previously trusted node and changes something, the other involved parties will know.

By implementing quantum entanglement or quantum superposition's, just the process of trying to observe the photons will change the system, making an intrusion detectable.

Other more specific types of QKD include discrete variable QKD (DV-QKD) and continuous variable QKD (CV-QKD). DV-QKD will encode quantum information in variables using a photon detector to measure quantum states. An example of a DV-QKD protocol is the BB84 protocol. CV-QKD encodes quantum information on the amplitude and phase quadrants of a laser, sending the light to a receiver. The Silberhorn protocol uses this method.

Some examples of QKD protocols are the following:

- BB84
- Silberhorn
- Decoy state

Satellite QKD:

The satellite carries out QKD operations with distinct ground stations to establish independent secret keys with each of them. The satellite holds all keys, while the stations only have access to their own keys. To enable any pair of stations—for example, station A and B—to share a common key, the satellite combines their respective keys K_A and K_B and broadcasts their bit-wise parity $K_A \oplus K_B$. Using this announcement, the stations can retrieve each other's keys because $K_A \oplus (K_A \oplus K_B) = K_B$ and $K_B \oplus (K_A \oplus K_B) = K_A$. Since the original

keys are independent secret strings, their bit-wise parity is just a uniformly random string, so the parity announcement does not reveal any useful information to potential eavesdroppers. However, since the satellite holds all keys, access to the data obtained by the satellite would give an adversary complete knowledge of the key. Therefore, in this setting, the satellite must be trusted.

Conclusion:

It is concluded that to transmit sensitive information between two or more points, some stronger technique is needed. It's sure that Quantum key distribution and other quantum encryption methods will allow us to secure sensitive information more effectively in the future. Quantum encryption is a powerful and positive step in the right direction, toward a future in which we can feel more secure about how and what we share. Thus, we can also expect a considerable feedback from QKD into basic physics, which leads to a new perspective on the foundations of quantum mechanics. The perspective can be more "practical" than "philosophical."

References

1. C. Bennett and G. Brassard, "Quantum Cryptography:Public Key Distribution and Coin Tossing," International Conference on Computers, Systems, and Signal Processing, Bangalore, India, 1984.
2. A. Ekert, "Quantum Cryptography Based on Bell's Theorem," Phys. Rev. Lett. 67, 661 (5 August 1991).
3. Ekert, Artur. "What is Quantum Cryptography?" Centre for Quantum Computation –Oxford University.Conger., S., and Loch, K.D. (eds.). Ethics and computer use. Commun. ACM 38, 12 (entire issue).
4. Johnson, R. Colin. "MagiQ employs quantum technology for secure encryption." EE Times. 6 Nov. 2002..
5. Mullins, Justin. "Quantum Cryptography's Reach Extended." IEEE Spectrum Online. 1 Aug. 2003.
6. Petschinka, Julia. "European Scientists against Eavesdropping and Espionage." 1 April 2004. 7. Salkever

* * * * *

❖ **Shobha M.**, BGS College of Education, B G Nagara, Nagamangala Taluk, Mandya District-571811, **Ph:** 9591699418, **E-mail:** shobha.m20@gmail.com

Design and Simulation of Photoacoustic setup for Formaldehyde Gas Sensing



- Rachith S.N
- Veda S.N

Abstract

A Helmholtz resonator based Photo Acoustic (PA) cell for Formaldehyde gas sensor has been designed and simulated. The sensor has the PA cell with mechanical chopper and a tuneable interband cascade laser (ICL) source operating at 3.5 μm . For a mixture of Formaldehyde gas with air, the resonant frequency of the PA cell was found to be 2880 Hz. Simulations of the PA cell was carried out using COMSOL Mutiphysic and the simulated resonant frequency was found to be 2850 Hz. The results show that with miniaturization of the PA cell, one can achieve the selectivity to detect the presence of the target gas using Photo Acoustics, as reported earlier in literature.

Keywords- Photacoustics, Opto-Mechanical Chopper, Formaldehyde, Acoustic Chamber.

INTRODUCTION

The necessity of gas sensor has increased dramatically over the past few years due to the extensive usage of dangerous chemicals in many common applications. Formaldehyde in specific, is a volatile organic compound, which is infamously known as the reason behind sick building syndrome [1,2,3]. Formaldehyde is emitted from paints, plywood etc.[4] which are used by common man. Inhalation of Formaldehyde leads to harmful diseases like cancer [5] and hence has to be avoided.

Many types of gas sensors like ultrasonic, infrared point, infrared imaging etc have evolved over the years. But the advantage of a Photo acoustic sensor is that it can be miniaturized and reused for any number of times.

In 1880 A. Graham Bell, had discovered the Photo Acoustic (PA) effect while working on a solid selenium cell [6]. Since human ears were the detectors, the experiments with PA were difficult to conduct and record. Even after the invention of carbon microphone during late 1800 by various independent researchers, Study on PAS didn't take a leap forward, until 1938, Viengerov [7] used PAS with infrared source as an excitation source for gas molecules and a microphone to analyze the presence of different gases. Since infrared has limited excitation capability, this was not used for trace gas detection. During 1960 a breakthrough in PA Gas detection was achieved by using laser light as an excitation source, and an extensive research in PA with laser light was conducted by Kreuzer [8,9]. Dewey et al. and Kamm independently worked on PA cell with resonance mode of operation by tuning the laser source for the resonance frequency of PA chamber[10,11]

During 1970s and 1980s CO and CO₂ lasers were extensively used for PAS due to the obvious advantages like high output power, tunability and could even detect gas in ppbV level. But due to size constraints of CO and CO₂ lasers, this PA setup could not be used for mobile applications.

Interband cascade laser (ICL) developed by Rui Q. Yang in 1994[12] has eliminated the size constraints and was successfully used in PA cell to detect trace gas.[13-16]

Excitation frequency was modulated by Pulsed laser source by F, Gao et.al [17] and successfully used in trace gas detection, but the price of pulsed laser was the constrain in making it less expensive. V. F. Duma et.al [18-21] had extensively worked on design of mechanical chopper and its application in optical spectroscopy with lease expensive setup.

The present work concentrates on the detection of formaldehyde gas with a resonant PA cell with an Opto mechanical chopper and a tunable ICL as an excitation source.

Section II deals with the modeling of sensor setup and the third section shows details of the simulation results which is followed by the conclusion.

MODELING OF SENSOR

The Photo acoustic effect is a process in which light is absorbed in a material and the molecules in the material expands and contracts by giving of soundwaves

with low frequency. The proposed sensor is designed to detect the low frequency and low amplitude signal emanating from the material.

The basic block diagram of a photoacoustic setup has three main parts; The laser source, an opto-mechanical chopper and a chamber with microphone for gas detection. The macro scale sensor setup is shown in figure 1.

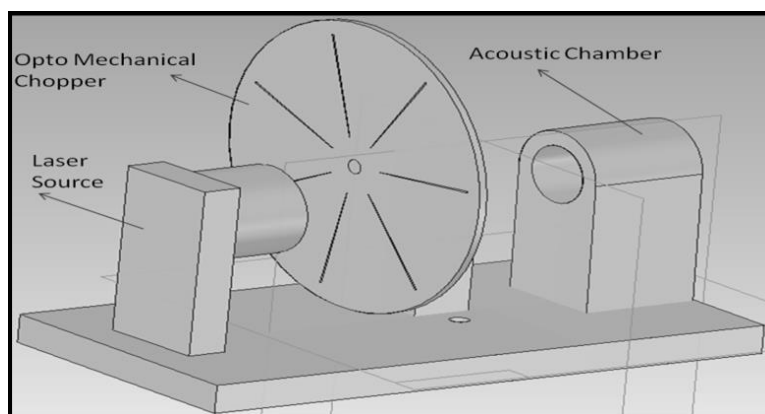


Fig 1. Block diagram of photo acoustic setup

Laser Source

Hitran spectrum has given two absorption signature of formaldehyde [23,24], namely 1771 cm^{-1} and 2832.5 cm^{-1} . Since the absorption spectrum of moisture is close to 1171 cm^{-1} , in the present work the wave number of 2832.5 cm^{-1} , so as to minimize the interference problem. At the wave number of 2832.5 cm^{-1} , the wavelength of light source which excites the target gas is around $3.5\mu\text{m}$. Accordingly a tunable interband cascade laser at $3.53\text{ }\mu\text{m}$ has been selected to excite our target molecule.

Opto- Mechanical Chopper

Once the laser source is decided the critical part of the setup is the mechanical chopper. A commercially available SR 540 chopper has an operating frequency range of 4 Hz to 4kHz with equal slit distance for both on and off region, but for the detection of formaldehyde gas one needs to have an on time and off time which must be custom designed.

The design consideration of an opto mechanical chopper is based on the

- a) Hitran absorption spectrum of formaldehyde gas with a wave number of 2832.5 cm^{-1}

- b) Modulating frequency of the laser in order to excite the target molecule which is around 2700Hz[25]

For the target gas, the total time period required for modulating the laser source is 42 n sec with a duty cycle of 1.4% that is it has an ON time of 0.0588 nsec and OFF time of 41.412 nsec. In this work an opto mechanical chopper is proposed instead of a pulsed laser[18-22] to achieve the modulation of the laser light source.

Many researchers have come up with different designs for different types of chopper wheels with linear edge window [9,10] and circular edge window[11,12] and the same is discussed by et.al in [8].

For the gas sensor application in the present work linear edged window is selected, with the wave pattern shown in figure 2.

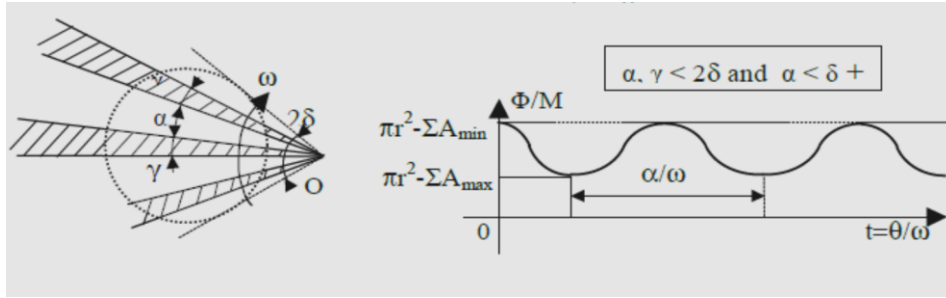


Fig 2. Wave pattern of linear edge window.[18-22]

Where,

R_1 and R_2 are respectively the minimum and maximum radius of the window.

α , angle of the window;

γ , angle of the wing (the opaque portion of the wheel) without its circular margins;

General relationship between them is

$$\alpha + \gamma = 2\pi/n$$

general configuration is $\alpha \neq \gamma$;

$2r$ = diameter of the light beam in the plane of the wheel;

2δ = angle of the section of the beam as seen from the pivot 'O' of the wheel;

ω = constant rotational speed

From the figure 2 it is seen that when the opto mechanical chopper slices the laser light, a linear wave having a wavelength equal to the ratio of angle of the window and the rotational speed of the chopper is achieved. This wave is linear in nature as can be seen in figure 2.

The geometrical specification of the chopper wheel is shown in Figure 3.

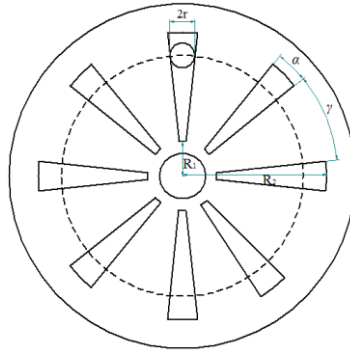


Fig3.Geometric characteristics of the chopper wheel [18-22]

For the absorption requirements of formaldehyde gas, it is found that for a mechanical disc of 5 cm radius, at a distance of 4 cm from the center of chopper wheel, the path length for the ON time is 0.5 mm and the path length for the OFF time is 35.21 mm. For this data it was found out that 7 slits in a mechanical chopper could be accommodated as shown in figure 4.

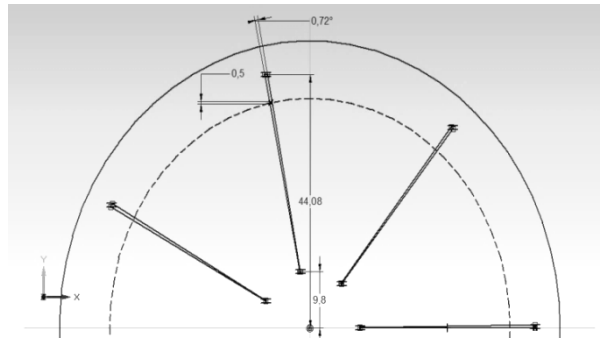


Fig 4. Geometric dimension of chopper

$R_1 = 9.8$ mm, and $R_2 = 44.08$ mm. $\alpha = 0.72$,

$\gamma = 2r = 0.5$ mm.

ω is the constant rotational speed of the chopper wheel. In order to achieve the required modulating frequency of 2700 Hz, a mechanical chopper with 7 slits of the above mentioned dimensions has to rotate at 23142 RPM.

Photoacoustic Chamber Design

In a photoacoustic gas sensor, chamber plays an important role; it is the section of the sensor where the presence of gas is detected. Detection of gas strictly depends on the geometry of the chamber. For the proposed gas sensor, the chamber resonates when the gas expands and contracts at the frequency of Opto-mechanical chopper. Resonance of the chamber shows the presence of the target gas. Therefore at most care has to be taken in designing the chamber.

A modulated laser beam is used to generate cylindrical acoustic waves of low magnitude which can be enhanced by using a resonant cell. Different types of acoustic chamber have been clearly described with their advantages and disadvantages in Miklo's et'al [26].

For the target gas, Helmholtz resonator has many advantages. Helmholtz resonator has a cavity followed by a long neck with smaller diameter. The resonant frequency of the chamber is given by

$$f = \frac{c}{2\pi} \sqrt{\frac{A}{Vl}} \quad (1)$$

Where

$$\begin{aligned} f &= \text{resonance frequency} \\ C &= \text{velocity of sound in air} \\ A &= \text{Area of neck} = \pi d^2/4 \\ D &= \text{diameter of the neck} \end{aligned} \quad (2)$$

$$\begin{aligned} l &= \text{length of neck} \\ V &= \text{effective volume of the two cavity} = \frac{\pi D^2}{4} L \\ D &= \text{Diameter of cavity} \\ L &= \text{length of cavity} \end{aligned} \quad (3)$$

Single cavity acoustic chamber fails to isolate atmospheric noise with the generated photo acoustic signal, to eliminate this drawback, a double cavity Helmholtz resonator is used.

where the volume of the cavity is given by

$$V_{eff} = \frac{1}{\frac{1}{V_1} + \frac{1}{V_2}} \quad (4)$$

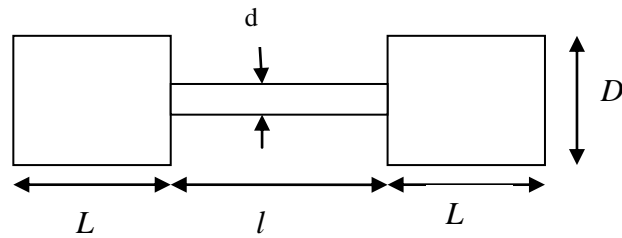


Fig 4: PA chamber

To match the amplitude modulated laser light from the opto-electrical chopper, the acoustic chamber was designed with a neck diameter of 1.75 mm, neck length of 10mm, cavity height of 3.75mm and cavity length of 10mm and it is shown in fig 5. For the geometric dimensions specified above, the resonance frequency was found to be 2880Hz.

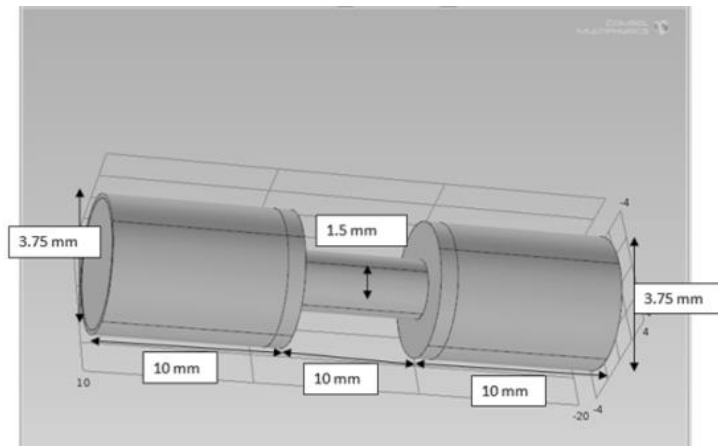


Fig 5. Acoustic chamber with geometric dimensions

SIMULATION RESULTS

The chamber has been designed and simulated using COMSOL Multiphysics. The analysis was carried out by applying pressure inside the acoustic chamber.

From the simulated frequency response of the chamber shown in figure 6 it is seen that the resonance is at 2850Hz which is in close proximity of the calculated resonance value for Formaldehyde gas which is 2880Hz.

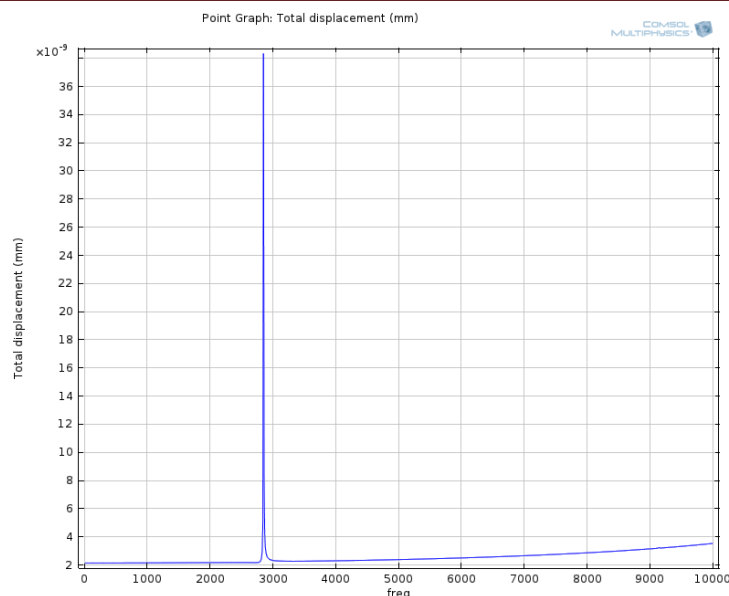


Figure 6: Frequency response of the acoustic chamber under resonance.

From the above results it can be shown that by optimally designing the photo acoustic chamber based on the modulating frequency of the excitation source for a gas, the presence of the gas can be detected.

CONCLUSION

The paper deals with the design and simulation of a photo acoustic Formaldehyde gas sensor. The authors have simulated the sensor using COMSOL Mutiphysics. The calculated value of the resonance frequency for Formaldehyde gas is 2880 Hz and the value as per the simulation result obtained is 2850 Hz. The results indicate that if one can calculate the modulating frequency of the excitation source for a gas, the chamber can be designed for detecting any gas. The designed chamber will be further fabricated, and the results will be correlated with the calculated and simulation results.

REFERENCES

1. Korpan Y.I., Gonchar M.V., Sibirny A.A., Martelet C., El'skaya A.V., Gibson T.D., Soldatkin A.P. Development of highly selective and stable potentiometric sensors for formaldehyde determination. *Biosens. Bioelectron.* 2000;15:77–83.
2. Katakya R., Bryce M.R., Goldenberg L., Hayes S., Nowak A. A biosensor for monitoring formaldehyde using a new lipophilic tetrathiafulvalene-

- tetracyanoquinodimethane salt and a polyurethane membrane. *Talanta*. 2002;56:451–458.
3. Kim W.J., Terada N., Nomura T., Takahashi R., Lee S.D., Park J.H., Konno A. Effect on formaldehyde on the expression of adhesion molecule in nasal microvascular endothelial cells: The role of formaldehyde in the pathogenesis of sick building syndrome. *Clin. Exp. Allergy*. 2002;32:287–295.
 4. Kawamura K., Kerman K., Fujihara M., Nagatani N., Hashiba T., Tamiya E. Development of a novel hand-held formaldehyde gas sensor for the rapid detection of sick building syndrome. *Sens. Actuators B Chem.* 2005;105:495–501.
 5. J.K. McLaughlin, *Int. Arch. Occup. Environ. Health* 66, 295 (1994)
 6. Bell A.G. On the production and reproduction of sound by light: the photophone. *Am. J. Sci.* 1880;20:305–324.
 7. Viegerov M.L. Eine Methode der gasanalyse, beruhend auf der optisch-akustischen tyndall-röntgenerscheinung. *Dokl. Akad. Nauk SSSR*. 1938;19:687–688
 8. Kreuzer L.B., Kenyon N.P., Patel C.K.N. Air pollution: sensitive detection of ten pollutant gases by carbon monoxide and carbon dioxide lasers. *Science*. 1972;177:347–349. [PubMed]
 9. Kreuzer L.B. Ultralow gas concentration infrared absorption spectroscopy. *J. Appl. Phys.* 1971;42:2934–2943.
 10. Dewey, Jr., C. F. (1974). “Opto-Acoustic Spectroscopy,” *Opt. Eng.* (Bellingham) 13, 483–488
 11. Dewey, Jr., C. F., Kamm, R. D., and Hackett, C. E. (1973). “Acoustic Amplifier for Detection of Atmospheric Pollutants,” *Appl. Phys. Lett.* 23, 633–635
 12. Yang, R. Q. (1995). "Infrared Laser based on Intersubband Transitions in Quantum Wells". *Superlattices and Microstructures*. 17 (1): 77–83. Bibcode:1995 SuMi...17...77Y. doi:10.1006/spmi.1995.1017
 13. L.R. Brown, R.H. Hunt, A.S. Pine, *J. Mol. Spectrosc.* 75, 406 (1979)
 14. T. Gilpin, E. Apel, A. Fried, B. Wert, J. Calvert, Z. Genfa, P. Dasgupta, J. Harder, B. Heikes, B. Hopkins, H. Westberg, T. Kleindienst, Y. N. Lee, X. Zhou, and W. Lonneman, *J. Geophys. Res.* 102, 21161 (1990).
 15. Fried, B. Henry, B. P. Wert, S. Sewell, and J. R. Drummond, *Appl. Phys. B* 67, 317 (1998).
 16. Fried, S. Sewell, B. Henry, B. P. Wert, and T. Gilpin, *J. Geophys. Res.* 102, 6253 (1997).
 17. F. Gao, X. Feng, and Y. Zheng, "Photoacoustic phasoscopy super-contrast imaging," *Applied Physics Letters* 104(2014).

18. V. F. Duma. Prototypes and Modulation Functions of Classical and Novel Configurations of Optical Chopper Wheels, January 2013. Latin American Journal of Solids and Structures 10(1):5-18
19. V. F. Duma. Theoretical approach on optical choppers for top-hat light beam distributions. Journal of Optics A: Pure and Applied Optics, 10:064008,2008.
20. V. F. Duma, M. Nicolov, and M. Kiss. Optical choppers: modulators and attenuators. Proc. SPIE, 7469:74690V, 2010.
21. V. F. Duma. Radiometric versus geometric, linear and non-linear vignetting coefficient. Applied Optics, 48(32):6355-6364, 2009.
22. V. F. Duma. Optical choppers with circular-shaped windows: Modulation functions, Communications in Nonlinear Science and Numerical Simulation, 16(5):2218-2224, 2011.
23. F. K. Tittel, D. Richter, and A. Fried, Solid-State Mid-Infrared Laser Sources, I. T. Sorokina and K. L. Vodopyanov, Eds., Topics Appl. Phys. 89, 445 (2003).
24. David G. Lancaster, Alan Fried, Bryan Wert, Bruce Henry, and Frank K. Tittel “Difference-frequency-based tunable absorption spectrometer for detection of atmospheric formaldehyde” APPLIED OPTICS y Vol. 39, No. 24 y 20 August 2000
25. H. Bruhns, A. Marianovich, M. Wolff, “Photoacoustic spectroscopy using a MEMS microphone with inter-IC sound digital output” Int J Themophys (2014) pp 2292-2301
26. András Miklós, Peter Hess,Zoltán Bozóki “Application of acoustic resonators in photoacoustic trace gas analysis and metrology” REVIEW OF SCIENTIFIC INSTRUMENTS, Volume 2 Nov 4

* * * * *

- ❖ **Rachith S.N**, University of Hasselt, Hasselt, Belgium, **Email:** Rachikrishna@gmail.com
- ❖ **Veda S.N.**, Nitte Meenakshi Institute of Technology, Yelahanka, Bengaluru, Karnataka, India.

Synthesis and Characterisation of Sodium Oxide Nanoparticles



- **Dr. Mallikarjuna I.**
- **Triveni M.K.**
- **Dr. Shivalingaswamy T.**

Abstract

Metal Nanoparticles are important class of materials that are widely used in electronic, optoelectronic and chemical sensing devices. The synthesis, characterization and applications of nanoparticles are among the most important section of the wide range of Nano technology. In recent years, nanoparticles have greatly attracted researchers in the field as the transition from micro particles to nanoparticles was seen to lead to immense changes in the physical and chemical properties of a material. We report the synthesis and characterization of Nano sized Disodium oxide particles. The nanoparticles were produced in high temperature and water as a reacting medium by solution combustion method. Fourier Transformed Infrared Spectroscopy(FTIR), Scanning Electron Microscopy (SEM), X-ray Powder Diffractometry(XRD), and Energy Dispersive X-ray Spectroscopy (EDX) were used to characterize the nanoparticles composition, their shape, size, crystallinity, purity etc.

Key words: Disodium oxide, nanoparticles, Characterization and optical activity.

Introduction:

A Nanocrystal is a quantum dot [1] consisting of atoms either in a single or poly-crystalline arrangement, with at least one dimension smaller than 100nm. Nanocrystals are differentiated from larger crystals by their size[2]. Many nanocrystals exhibit different size dependent properties that are not exhibited by their bulk states[3]. Certain class of nanoparticles can be used for memory

components[4]. Nanocrystals made with zeolite are used to filter crude oil into diesel fuel[5]. Nanocrystal solar cells are solar cells based on a nanocrystal coated substrate. Nanocrystals based on silicon are used in solar cells to convert sunlight into electricity[6]. Sodium oxide has been used as a coating precursor on organic polymer films during the plasma modification to analyse antimicrobial properties. Sodium oxide is a strong alkaline oxide, commonly used as an active flux in ceramic glazes. Since, the synthesis and characterisation of these sodium oxide nanocrystals is important due to its variety applications. The present study reports the synthesis of sodium oxide nanocrystals by solution combustion method and so prepared nanoparticles are characterised by various techniques to find its suitability for different needs.

Materials and Methods:

Sodium oxide nanocrystals were successfully synthesized by microwave oven assisted solution combustion method[8]. Reduction of to Na_2O is done with the help of temperature provided by microwave oven. We prepared solution by mixing 10g of $NaNO_3$ with 40 mL of distilled water which subjected to heating on microwave oven for 20 minutes. This results in dry, crystalline and agglomerated nanocrystalline sodium oxide. The reaction can be summarized as follows:

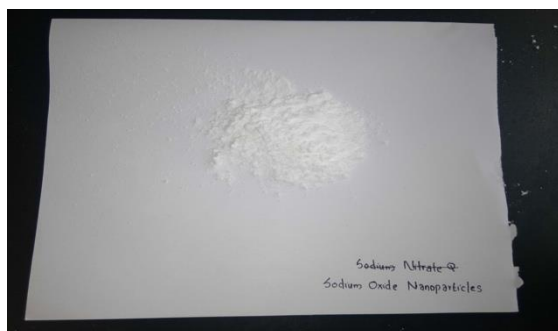
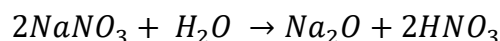


Figure 1: Synthesized Sodium oxide nanoparticles



Figure 2: Calcination of Sodium oxide nanoparticles

XRD measurements

XRD measurements were carried out at room temperature using RIGAKU smart lab X-ray diffractometer at Institute of Excellence (IOE), University of Mysore with monochromatic beam of $Cu\ k_{\alpha}$ radiation (1.5406\AA). An accelerating

tube voltage of 40 kV and a tube current of 15 mA with a scanning speed 0.01 to 1000/m and scanning range 3 to 145° (2θ). Scintillation counter or D/tex ultra-detector with accuracy $\pm 0.02^\circ$ were used. The XRD patterns were recorded in the 2θ range of 10-80°. The values of 2θ , d- spacing, relative intensity and FWHM were obtained from the XRD pattern. This has been done for Na_2O and the XRD graph are as shown in Figure 3.

Determination of crystal sizes were done using Scherer's method and WH plot[9] for Na_2O nanocrystal. The average crystal size by Scherrer's method is found to be 44.0597nm and by W-H Plot the size of the nano crystals were found to be 46.53nm.

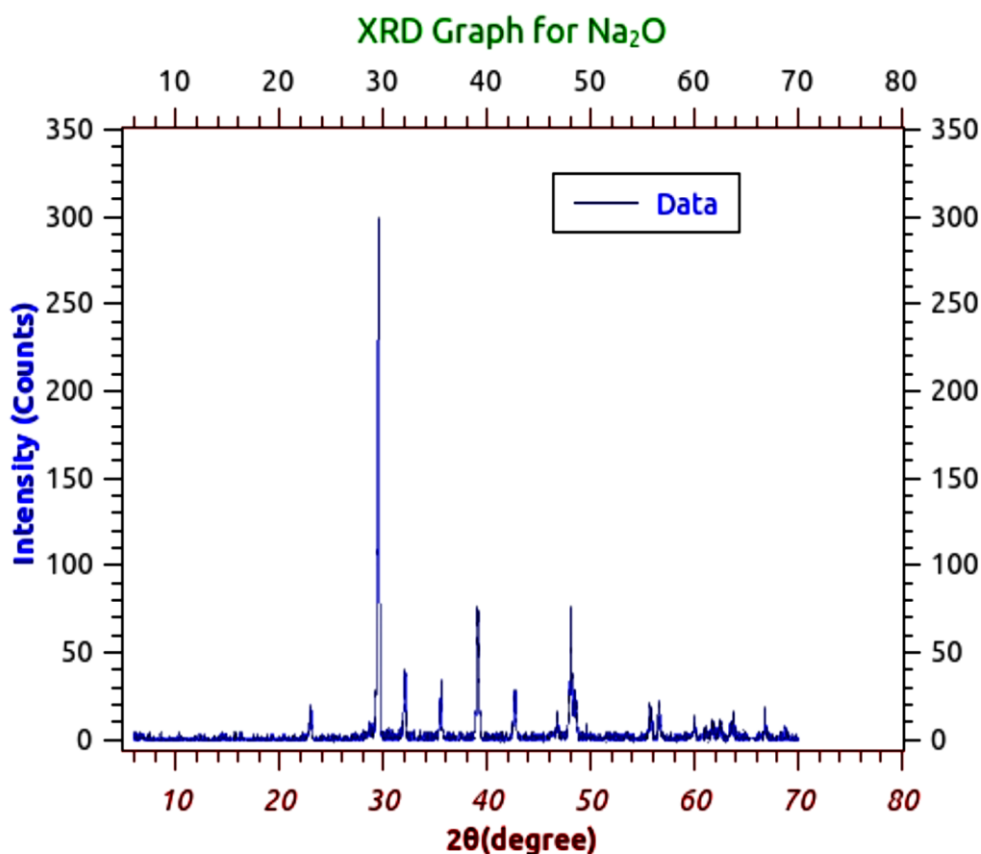


Figure 3: XRD Plot of Sodium oxide nanoparticles

Recent Trends in Physics with Emphasis on Discovery of God Particle

Table 1: XRD data analysis for crystal size determination Na₂O

| 2θ | θ | $\sin\theta$ | β | $\beta \cos\theta$ | $d = \frac{K\lambda}{\beta \cos\theta}$ by Sm (nm) |
|-----------|----------|--------------|-----------|--------------------|--|
| 23.0286 | 11.5143 | 0.1996 | 0.0037906 | 0.0037143 | 36.9221 |
| 29.5119 | 14.7559 | 0.2547 | 0.0037854 | 0.0036605 | 37.4648 |
| 32.0882 | 16.0441 | 0.2763 | 0.0033004 | 0.0031718 | 43.2372 |
| 35.4679 | 17.7339 | 0.3045 | 0.0034452 | 0.0032814 | 41.7931 |
| 39.0686 | 19.5373 | 0.3343 | 0.0041692 | 0.0039292 | 34.9027 |
| 42.6227 | 21.3113 | 0.3634 | 0.0041151 | 0.0038337 | 35.7722 |
| 46.7828 | 23.3614 | 0.3965 | 0.0035374 | 0.0032474 | 42.2334 |
| 48.0110 | 24.0050 | 0.4068 | 0.0029533 | 0.0026978 | 50.8340 |
| 55.7397 | 27.8898 | 0.4674 | 0.0030074 | 0.0026585 | 51.5854 |
| 56.5962 | 28.2981 | 0.4740 | 0.0036162 | 0.0031840 | 43.0716 |
| 59.9806 | 29.9903 | 0.4998 | 0.0037784 | 0.0032527 | 42.1618 |
| 61.7273 | 30.8636 | 0.5129 | 0.0036998 | 0.0031759 | 43.1842 |
| 63.7063 | 31.8531 | 0.5277 | 0.0032877 | 0.0027926 | 49.1115 |
| | | | | | $d_{avg} = 44.0597nm$ |

Table 2: WH data table for Na₂O

| 2θ | θ | $\sin\theta$ | β | $\beta \cos\theta$ | $4\sin\theta$ | W-H Plot $d = \frac{K\lambda}{c}$ (nm) |
|-----------|----------|--------------|-----------|--------------------|---------------|--|
| 23.0286 | 11.5143 | 0.1996 | 0.0037906 | 0.0037143 | 0.7984 | 46.530nm |
| 29.5119 | 14.7559 | 0.2547 | 0.0037854 | 0.0036605 | 1.0188 | |
| 32.0882 | 16.0441 | 0.2763 | 0.0033004 | 0.0031718 | 1.1052 | |
| 35.4679 | 17.7339 | 0.3045 | 0.0034452 | 0.0032814 | 1.2180 | |
| 39.0686 | 19.5373 | 0.3343 | 0.0041692 | 0.0039292 | 1.3372 | |
| 42.6227 | 21.3113 | 0.3634 | 0.0041151 | 0.0038337 | 1.4536 | |
| 46.7828 | 23.3614 | 0.3965 | 0.0035374 | 0.0032474 | 1.5863 | |
| 48.0110 | 24.0050 | 0.4068 | 0.0029533 | 0.0026978 | 1.6272 | |
| 55.7397 | 27.8898 | 0.4674 | 0.0030074 | 0.0026585 | 1.8696 | |
| 56.5962 | 28.2981 | 0.4740 | 0.0036162 | 0.0031840 | 1.8960 | |
| 59.9806 | 29.9903 | 0.4998 | 0.0037784 | 0.0032527 | 1.9992 | |
| 61.7273 | 30.8636 | 0.5129 | 0.0036998 | 0.0031759 | 2.0516 | |
| 63.7063 | 31.8531 | 0.5277 | 0.0032877 | 0.0027926 | 2.1108 | |

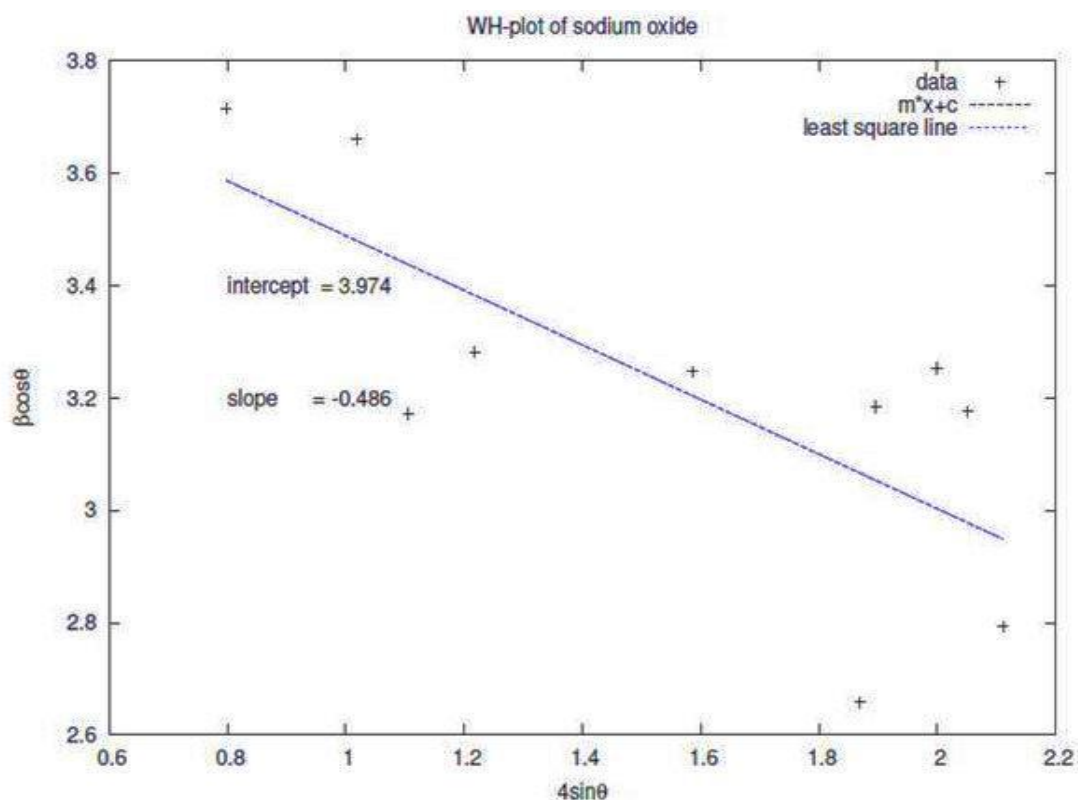


Figure 4:WH-plot for Sodium oxide nanoparticles

Fourier Transform Infrared (FTIR) Spectrometer Studies

The infrared spectra are recorded on Fourier Transform Spectrometer in the mid-infrared region (MIR) with in the range (450-4000/cm)[10]. Due to the complex interaction of atoms with in the molecule, IR absorption of the functional groups may vary over a wide range. However, it has been found that many functional groups give characteristic IR absorption at specific narrow frequency range. Multiple functional groups may absorb at one particular frequency range but a functional group often gives rise to several characteristic absorption. Stretching and bending vibrations are verified by comparing with standard tables.

FTIR Measurements carried out at room temperature using FTIR-4100 type A model of serial number 94102, TGS detector with standard light source of resolution 16/cm and scanning speed-Auto(2mm/sec) with filter-auto(3000Hz) at Institute of Excellence (IOE), university of Mysore.

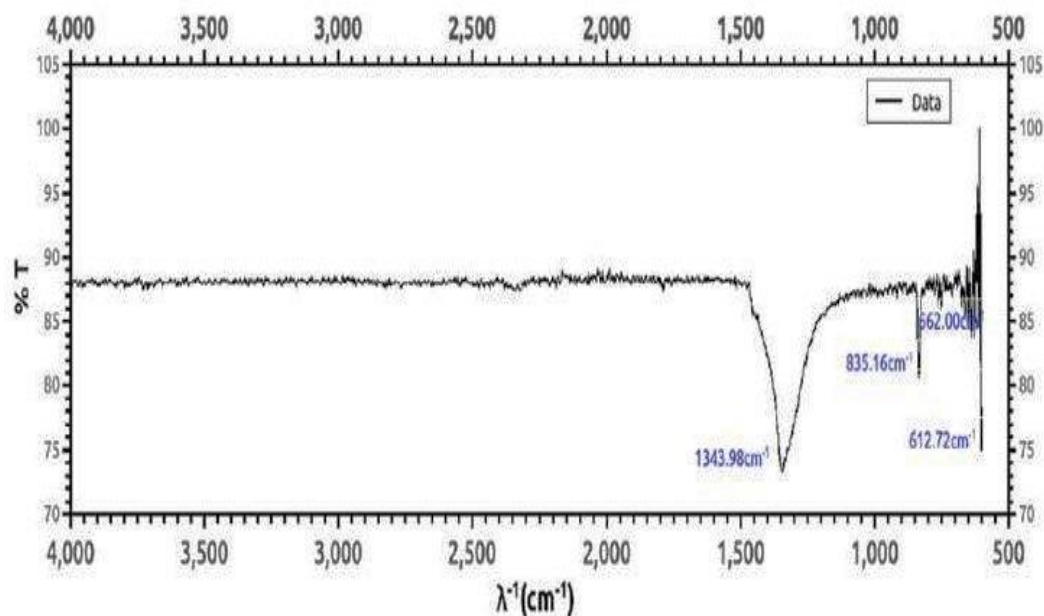


Figure 5: FTIR Spectrum of Sodium oxide nanoparticles

UV-Visible Spectrometry

UV-Visible spectrometry was carried out at room temperature using UV-visible spectrometer labtronics MODEL LT-291 with single beam of range from 200nm to 900nm for Na₂O samples of different concentrations by dispersing them in fixed amount of water medium [11]. This characterization is done at the facility available at P.G department of Physics, Government College(Autonomous), Mandya. For different concentration value of given sample there exist different energy band gap. From the absorbance peak we have estimated the energy band gap of Na₂O samples and are shown in table-3

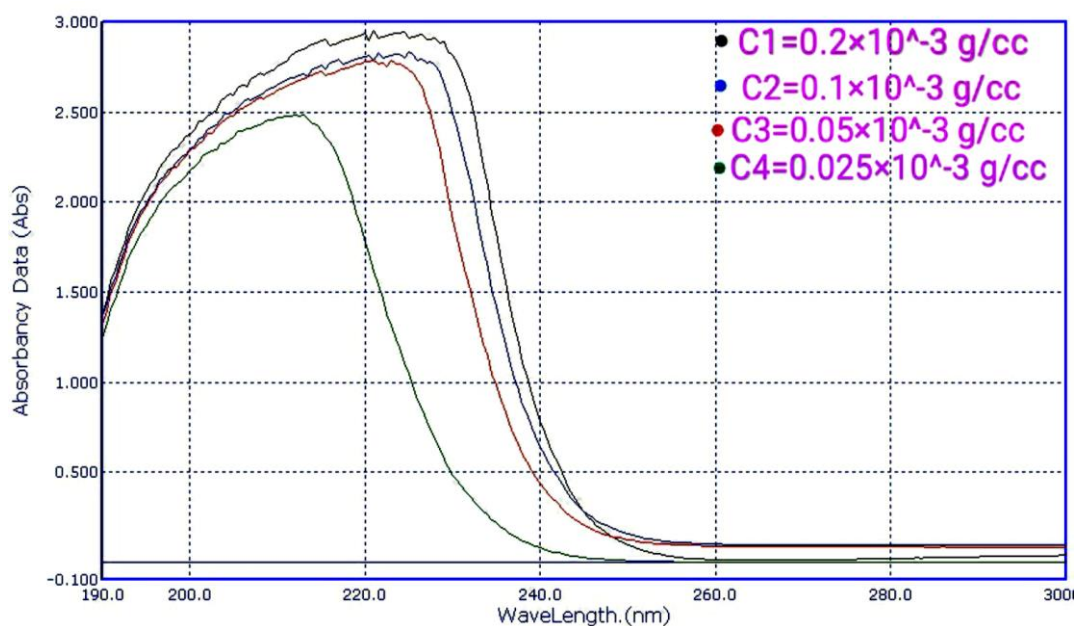


Figure 6: Determination of Energy band gap for different concentration of sodium oxide

Table 3: Determination of Energy band gap for different concentration of Na_2O Nanocrystal

| concentration | $\lambda(\text{cutoff wavelength})$ | Energy Gap ($\times 10^{19}$) (joules) | Energy Gap (eV) |
|----------------|-------------------------------------|--|-----------------|
| C ₁ | 226.5 | 2.9291 | 5.478 |
| C ₂ | 225.0 | 2.8330 | 5.5147 |
| C ₃ | 221.0 | 2.7900 | 5.6145 |
| C ₄ | 213.0 | 2.4858 | 5.825 |

Energy Dispersive X-Ray Spectroscopy

EDS or EDX study was made using energy dispersive spectrometer, Hitachi model S-3400N with magnification range 5X to 300,000X, facility availed from Polymer Science department, Sri Jayachamarajendra College of Engineering (JCE), Mysore. Super conical 50 degree lens and 2-stage electromagnetic condenser lens with both coarse and fine control for the prepared Na_2O by calcination process[12]. From the elemental analysis, we find that the calcinations removes impurity and we get pure Na_2O nanocrystals.

Figure 7: ED spectrum of Na_2O nanocrystal

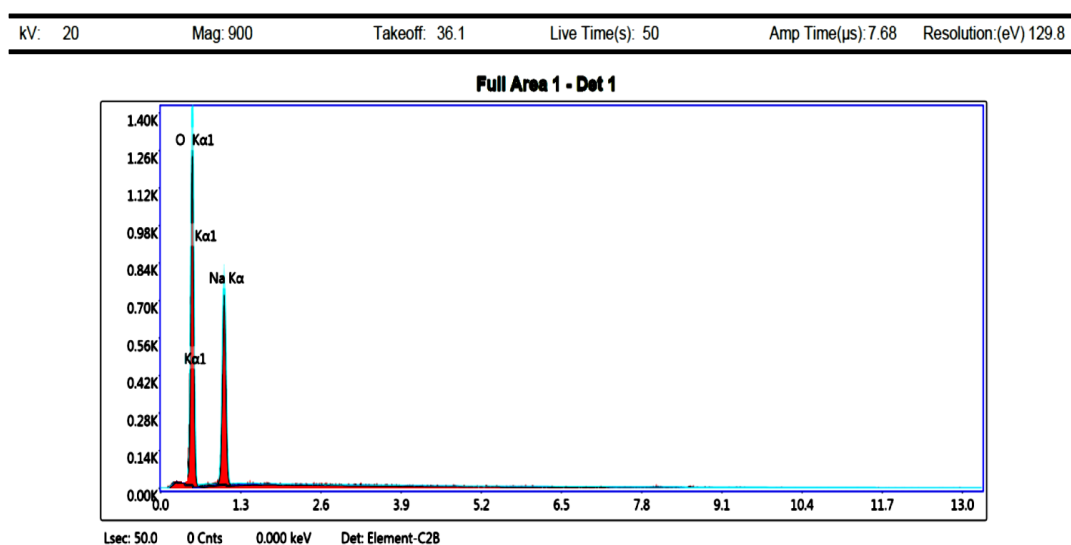


Figure 7:EDX spectrum of Na_2O nanocrystal

Table 4: Elemental analysis of Na_2O Nanocrystal

| Element | Weight% | Atomic% | Net.Int | Error% | K ratio |
|---------|---------|---------|---------|--------|---------|
| O K | 63.46 | 63.38 | 181.64 | 10.10 | 0.0919 |
| Na k | 36.54 | 36.62 | 119.47 | 8.79 | 0.0572 |

Electron Microscopy

The SEM analysis was done using SEM Hitachi model S-3400N with magnification range 5X to 300,000X, facility availed from Polymer Science department, Sri Jayachamarajendra College of Engineering (JCE), Mysore. The morphology of the Na_2O was found to be as shown in the figure below. SEM images of Na_2O as showed agglomerated pattern with an average size of 40 nm. But, this agglomeration has been removed by dispersing these nanocrystals in water and shaking the mixture in ultrasonic desiccators followed by calcination process. After this process, we get Nano crystals which are well distinguished without any agglomeration. This may be due to fact that, some of the volatile impurities present in the sample provide a weak bonds leading to agglomeration of the sample. However, the rigorous shaking of this in ultrasonic desiccators will help in breaking

these weak bonds. Further, heating the substance at high temperature removes volatile impurities, thus we get fine nanocrystals as the output product[13].

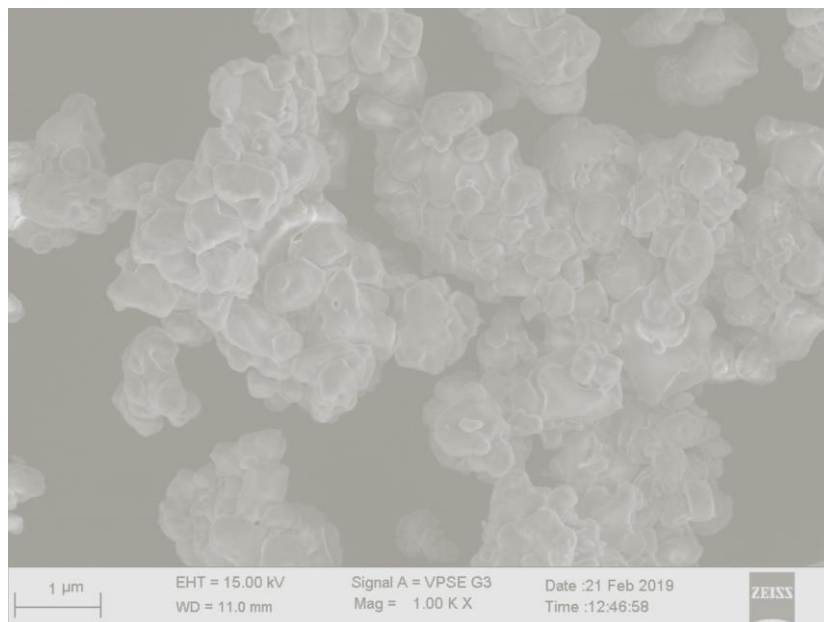


Figure 8:SEM image of Sodium oxide nanocrystals

Conclusion and Outlook

We have successfully synthesized Sodium oxide nanoparticles using solution combustion method with the aid of microwave oven. The so prepared nanoparticles are characterized by different tools such as XRD, EDS, SEM, UV-visible, FTIR etc., Various physical properties such as size, orientation, bond stretching, purity, energy band gap etc., are determined. From XRD crystal size is determined by two methods. Firstly by Debye-Scherrer equation size is found to be 44.0597 nm. Then by W-H plot the average size of the crystal were found to be 46.530 nm. Hence from XRD we identify that synthesized Na_2O nanoparticles were crystalline in nature and average crystal size is 46.530 nm. FTIR spectrum for Na_2O is obtained by plotting wavenumber v/s percentage of transmittance. We obtained peaks at 1343.98 cm^{-1} , 835.16 cm^{-1} , 662.72 cm^{-1} , 612.0 cm^{-1} which confirms various bending and stretching modes of Na_2O . UV-Visible spectrometry was carried out at room temperature with different concentration of samples. For different concentrations we determined different energy gap from absorbance peak. The obtained energy gap were in the region 5.478 to 5.825 eV which indicates that the synthesised Na_2O is an

insulator. EDX study was made using Energy Dispersive Spectrometers. From elemental analysis we find that the calcination process removes impurities and we get pure Na_2O nanocrystals. Finally SEM analysis was done and morphology of Na_2O was found to be in agglomerated pattern with flower like structure. The increased surface area of Na_2O SEM images shows its availability towards surface reaction which has wide variety of applications in industrial and commercial field. From the information obtained by our studies we infer that the so prepared nanocrystals may be a potential candidate to use in supercapacitor applications. More studies have to be performed in order to shower an insight in deducing further details.

Acknowledgments

Authors would like to thank Divyajyothi K. Jyothi S.K, Ranjitha B.C. and Sahana M. for their help in carrying out the work. Authors are also thankful to the Government College (Autonomous), Mandya for providing the necessary infrastructure facilities to carry out this project work. And special thanks to Mr. Ananth Kumar, Lecturer, University of Mysore, Dr. Roopa S, Associate professor Dept. of polymer science and Technology JSS Science and Technology University, Sri Jayachamarajendra college of Engineering, Mysore for their help in characterising the sample.

References:

1. B. D. Fahlman (2007). Material Chemistry. **1**. Springer: Mount Pleasant, Michigan. pp. 282–283
2. J. L. Burt (2005). "Beyond Archimedean solids: Star polyhedral gold nanocrystals". *J. Cryst. Growth*. **285** (4): 681–691.
3. L. Pavesi (2000). "Optical gain in silicon nanocrystals". *Nature*. **408** (6811): 440-444. Bibcode:2000Natur.408..440P. doi:10.1038/35044012.
4. S. Tiwari (1996). "A silicon nanocrystal based memory". *Appl. Phys. Lett.* **68** (10): 1377–1379.
5. P. Dutta and S. Gupta (eds.) (2006). Understanding of Nano Science and Technology(1 ed.). Global Vision Publishing House. p. 72. ISBN 81-8220-188-8.
6. "Publications, Presentations, and News Database: Cadmium Telluride". *National Renewable Energy Laboratory*.
7. <https://www.americanelements.com/sodium-oxide-nanoparticles-nanopowder-1313-59-3#section-properties>

8. Giri, A. K., Nanocrystalline materials prepared through crystallization by ball milling First published: 29 October 2004, <https://doi.org/10.1002/adma.19970090216>, Adv. Mater.,1997, 9, 163-166.
9. Pamela Whitfield And Lyndon Mitchell., X-Ray Diffraction Analysis of Nanoparticles: Recent Developments, Potential Problems And Some Solutions, International Journal of Nanoscience, 2004 757-763(03) 06.
10. Peddinti Nagababu, Vanga Umamaheswara Rao, Pharmacological Assessment, Green synthesis and Characterization of Silver Nanoparticles of Sonneratia apetala Buch.Ham. Leaves, Journal of Applied Pharmaceutical Science Vol. 7 (08), pp. 175-182, August, 2017
11. Robina Begum, Zahoor H. Farooqi et.al, Applications of UV/Vis Spectroscopy in Characterization and Catalytic Activity of Noble Metal Nanoparticles Fabricated in Responsive Polymer Microgels: A Review., Critical Review in Analytical Chemistry., 2018 503-516 (48).
12. Andrew A. Herzing, Masashi Watanabe, Jennifer K. Edwards, Marco Conte, Zi-Rong Tang, Graham J. Hutchings and Christopher J. Kiely., dispersive X-ray spectroscopy of bimetallic nanoparticles in an aberration corrected scanning transmission electron microscope., Faraday discussions., 2008(38).
13. András E.Vladár and Vasile-DanHodoroaba., Characterization of nanoparticles by scanning electron microscopy., Characterization of Nanoparticles., 2020, Pages 7-27.

* * * * *

- ❖ **Dr. Mallikarjuna I.**, P G Department of Chemistry Maharani Science College for Women (Autonomous), Mysore-570 005, Karnataka, India **Ph:** 9482370335 **E-mail :** mallikarjunahiremath4@gmail.com
- ❖ **Triveni M.K.**, Department of Chemistry, Maharaja Institute of Technology, Thandavapura, Mysore-571 438, Karnataka, India
- ❖ **Dr. Shivalingaswamy T.**, P G Department of Physics, Government College (Autonomous), Mandya-571 401, Karnataka, India, E-mail: tssphy@gmail.com

Microwave Oven Aided Synthesis of Potassium Oxide Nanoparticles



- **Eliezer Vishwas**
- **S.N.Namitha**
- **Dr. T. Shivalingaswamy**

Abstract

Metal Nanoparticles are a class of the building blocks of the next generation of electronic, optoelectronic and chemical sensing devices. The synthesis, characterization and applications of nanoparticles are among the most important section of the wide range of Nano technology. In recent years, nanoparticles have been the center of attention for researchers in the field as the transition from micro particles to nanoparticles was seen to lead to immense changes in the physical and chemical properties of a material. We report the synthesis and characterization of nano sized potassium oxide particles. The nanoparticles were produced in high temperature and water as a reacting medium by solution combustion method. Fourier Transformed Infrared Spectroscopy (FTIR), Scanning Electron Microscopy (SEM), X-ray Powder Diffractometry (XRD), and Energy Dispersive X-ray spectroscopy (EDX) were used to characterize the nanoparticles composition, their shape, size, crystallinity, purity etc.

Keywords : Nanoparticles, XRD, FTIR, SEM, EDX

Introduction

Nanotechnology is the creation of useful or functional materials, devices, and systems through control of matter on the nanometer length scale and exploitation of novel phenomena and properties which arise because of the nanometer length scale. Nanotechnology includes the synthesis, characterization, exploration, and utilization of nanostructured materials. The nanostructured materials are very interesting materials both for scientific reasons and practical applications.

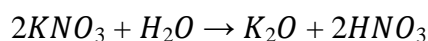
The fundamentals of nanotechnology lie in the fact that properties of substances dramatically change when their size is reduced to the nanometer range. When a bulk material is divided into small size particles with one or more dimension (length, width, or thickness) in the nanometer range or even smaller, the individual particles exhibit unexpected properties, different from those of the bulk materials. Bulk materials possess continuous physical properties. The same applied to macro sized materials also. But when particles assume nanoscale dimension, the principles of classical mechanics are no longer capable of describing their behaviour (momentum, energy, etc). At these dimensions principles of quantum mechanics apply. The same material at the nanoscale can therefore have properties (eg. optical, mechanical, electrical, etc) which are very different from the properties the material has at the macro scale (bulk)[1].

An innovative technique for the synthesis of nanocrystalline oxide powders with high crystalline quality is "Solution Combustion Method" which was invented by S.Park et al.[1] This technique offers added advantages over other methods as the simplicity of experimental setup, the surprisingly short time between the preparation of the reactants and the availability of the final product, and savings in external energy consumption. The idea was arisen from the reaction between the oxidant and fuel of liquid rocket propellants. The explosion energy of the reaction is utilized to synthesize nano crystalline oxide powders [2].

Experimental Procedure

Potassium oxide nanocrystals were synthesized by microwave oven assisted solution combustion method. The solution was prepared by mixing 10g of KNO_3 with 40ml of distilled water which was subjected to heating on microwave oven for 20minutes. This results in dry, crystalline and agglomerated nanocrystalline oxide powder, which is Dipotassium.

Reduction to K_2O is done with the help of temperature provided by microwave oven. The reaction can be summarized as follows.



Results and Discussions

XRD :

XRD measurements were carried out at room temperature using RIGAKU smart lab X-ray diffractometer at Institute of Excellence (IOE), university of Mysore with monochromatic beam of Cu K_{α} radiation (1.5406 Å). An accelerating tube voltage of 40KV and a tube current of 15 mA with a scanning speed 0.01 to 100⁰/m and scanning range 3 to 145⁰ (2θ).

Scintillation counter or D/tex ultra-detector with accuracy +0.02⁰ were used. The XRD patterns were recorded in the 2θ range of 10-80⁰ versus intensity. The values of 2θ , d spacing, relative intensity and FWHM were obtained from the XRD pattern. This has been done for K_2O and the XRD graph are as shown below.

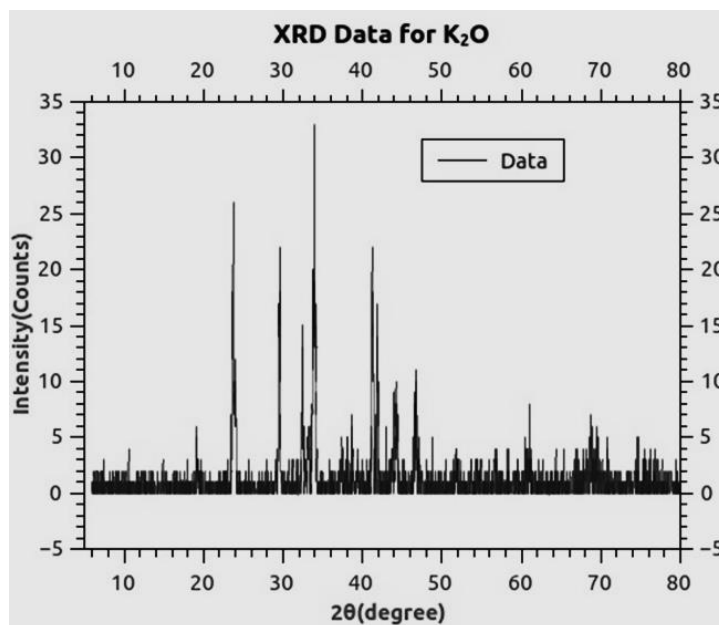


Figure 1: XRD plot of K_2O

Determination of crystal sizes are made using Scherrer's method and W-H plot for K_2O nanocrystal. The average crystal size by Scherrer's method is found to be 47.6007nm and by W-H plot the size of the nano crystals were found to be 49.4506 nm.

Table 1 : XRD data analysis for crystal size determination K_2O

| 2θ | θ | $\text{Sin } \theta$ | β | $\beta \cos \theta$ | $d = \frac{K\lambda}{\beta \cos \theta}$ by Sm (nm) |
|-----------|----------|----------------------|-----------|---------------------|---|
| 19.1181 | 9.5590 | 0.1660 | 0.0030213 | 0.0029793 | 46.0040 |
| 23.6266 | 11.813 | 0.2047 | 0.0030123 | 0.0029485 | 46.4846 |
| 29.4395 | 13.7197 | 0.2540 | 0.0030123 | 0.0029221 | 46.9046 |
| 32.5669 | 16.2834 | 0.2803 | 0.0030123 | 0.0029001 | 47.2604 |
| 34.0000 | 17.0000 | 0.2923 | 0.0030123 | 0.0028892 | 47.4387 |
| 38.8504 | 19.4252 | 0.3325 | 0.0030123 | 0.0028493 | 48.1030 |
| 41.1996 | 20.5996 | 0.3518 | 0.0030485 | 0.0028535 | 48.0332 |
| 41.8579 | 20.9289 | 0.3572 | 0.0030263 | 0.0028266 | 48.4893 |
| 43.9213 | 21.9606 | 0.3739 | 0.0030491 | 0.0028279 | 48.4670 |
| 47.0079 | 23.5039 | 0.3988 | 0.0030851 | 0.0028290 | 48.4482 |
| 61.1181 | 30.5590 | 0.5084 | 0.0033177 | 0.0028568 | 48.9767 |
| | | | | | $d_{\text{avg}} = 47.6007$ nm |

Table 2: WH plot table for K_2O

| 2θ | θ | $\text{Sin } \theta$ | β | $\beta \cos \theta$ | $4 \sin \theta$ | W-H Plot $d = \frac{k\lambda}{c}$ (nm) |
|-----------|----------|----------------------|-----------|---------------------|-----------------|--|
| 19.1181 | 9.5590 | 0.1660 | 0.0030213 | 0.0029793 | 0.6643 | 49.4506nm |
| 23.6266 | 11.8133 | 0.2047 | 0.0030123 | 0.0029485 | 0.8188 | |
| 29.4395 | 13.7197 | 0.2540 | 0.0030123 | 0.0029221 | 1.0160 | |
| 32.5669 | 16.2834 | 0.2803 | 0.0030123 | 0.0029001 | 1.1212 | |
| 34.0000 | 17.0000 | 0.2923 | 0.0030123 | 0.0028892 | 1.1692 | |
| 38.8504 | 19.4252 | 0.3325 | 0.0030123 | 0.0028493 | 1.3300 | |
| 41.1996 | 20.5996 | 0.3518 | 0.0030485 | 0.0028535 | 1.4072 | |
| 41.8579 | 20.9289 | 0.3572 | 0.0030263 | 0.0028266 | 1.4288 | |
| 43.9213 | 21.9606 | 0.3739 | 0.0030491 | 0.0028279 | 1.4956 | |
| 47.0079 | 23.5039 | 0.3988 | 0.0030851 | 0.0028290 | 1.5952 | |
| 61.1181 | 30.5590 | 0.5084 | 0.0033177 | 0.0028568 | 2.0336 | |

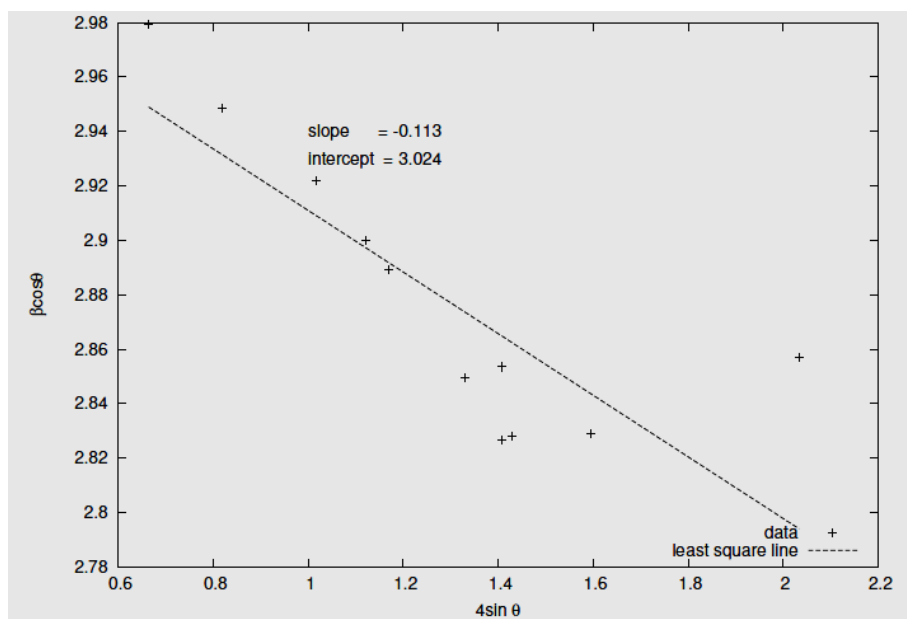


Figure 2: W-H plot of Dipotassium oxide for crystal size determination

Fourier Transform Infrared (FTIR) Spectrometer

The infrared spectra are recorded on Fourier Transform Spectrometer in the mid-infrared region (MIR) with in the range (450-4000/cm). Due to the complex interaction of atoms with in the molecule, IR absorption of the functional groups may vary over a wide range. However, it has been found that many functional groups give characteristic IR absorption at specific narrow frequency range.

Multiple functional groups may absorb at one particular frequency range but a functional group often gives rise to several characteristic absorption. Stretching and bending vibrations are verified by comparing with standard tables. FTIR Measurements carried out at room temperature using FTIR-4100 type A model of serial number 94102, TGS detector with standard light source of resolution 16/cm and scanning speed-Auto (2mm/sec) with filter- auto(3000Hz) at, Institute of Excellence (IOE), university of Mysore.

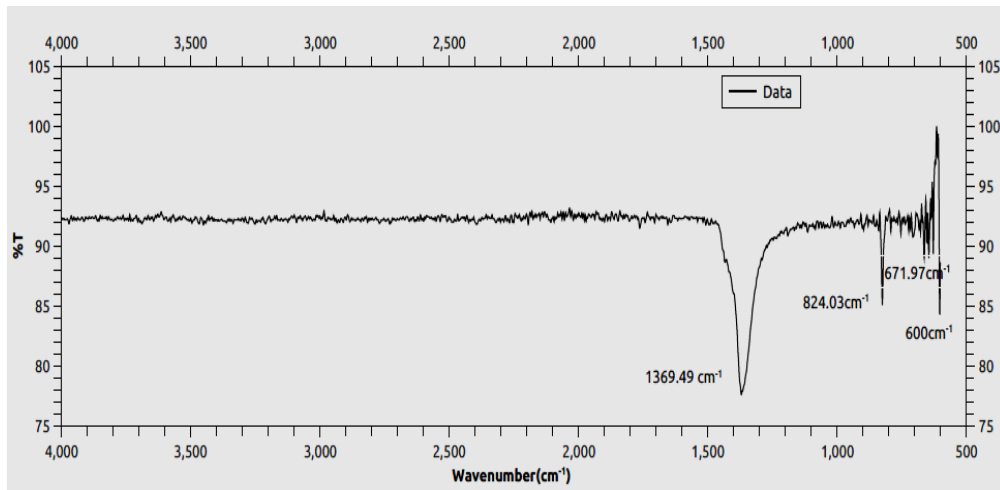


Figure 3 : FTIR Spectrum for K_2O

UV-Visible Spectrometry

UV-Visible spectrometry was carried out at room temperature using UV-visible spectrometer labtronics MODEL LT-291 with single beam of range from 200nm to 900nm for K_2O samples of different concentrations by dispersing them in fixed amount of water medium. This characterization is done at the facility available at P.G department of Physics, Government College (Autonomous), Mandya. For different concentration value of given sample there exist different energy band gap. From the absorbance peak we have estimated the energy band gap of K_2O samples and are shown in table-3

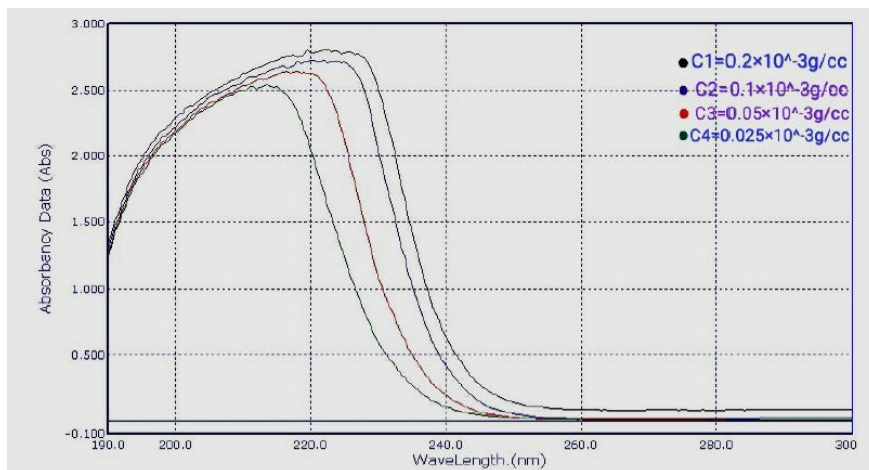


Figure 4: UV-visible spectrum for K_2O

Table 3: Determination of Energy band gap for different concentration of K_2O Nanocrystal

| Concentration | λ (cut off wavelength) | Energy Gap($\times 10^{-19}$) (joules) | eV |
|---------------|--------------------------------|---|-------|
| C_1 | 222.5 | 2.8080 | 5.577 |
| C_2 | 220.0 | 2.7280 | 5.627 |
| C_3 | 218.0 | 2.6433 | 5.692 |
| C_4 | 213.5 | 2.5403 | 5.812 |

Energy Dispersive X-Ray Spectroscopy

EDS or EDX study was made using energy dispersive spectrometer, Hitachi model S-3400N with magnification range 5X to 300,000X, facility availed from Polymer Science department, Sri Jayachamarajendra College of Engineering (JCE), Mysore. Super conical 50 degree lens and 2-stage electromagnetic condenser lens with both coarse and fine control for the prepared K_2O sample by calcination process. From the elemental analysis, we find that the calcinations removes impurity and we get pure K_2O nanocrystals.

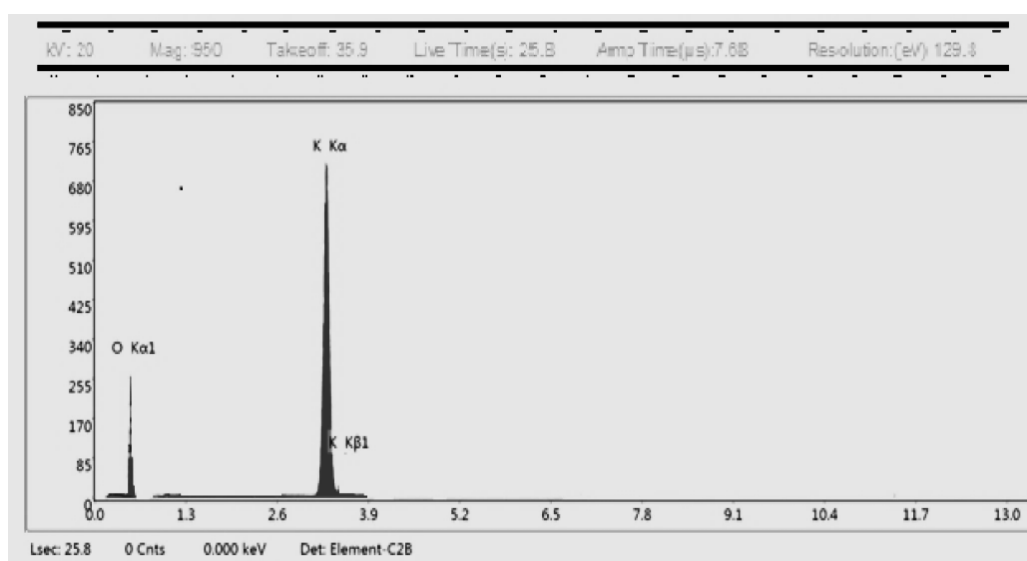


Figure 5: EDX spectrum of K_2O nanocrystal

Table 4: Elemental analysis of K_2O Nanocrystal

| Element | Weight% | Atomic% | Net.Int | Error% | K ratio |
|---------|---------|---------|---------|--------|---------|
| O K | 44.10 | 55.22 | 75.46 | 12.36 | 0.0578 |
| K K | 55.9 | 44.59 | 343.40 | 2.53 | 0.3495 |

Electron Microscopy

The SEM analysis was done using SEM Hitachi model S-3400N with magnification range 5X to 300,000X, facility availed from Polymer Science department, Sri Jayachamarajendra College of Engineering (JCE), Mysore.

The morphology of the K_2O was found to be as shown in the figure below. SEM images of K_2O as showed agglomerated pattern with an average size of 40 nanometer. But, this agglomeration has been removed by dispersing these nanocrystals in water and shaking the mixture in ultrasonic desiccators followed by calcination process. After this process, we get nanocrystals which are well distinguished without any agglomeration. This may be due to fact that, some of the volatile impurities present in the sample provide a weak bonds leading to agglomeration of the sample. However, the rigorous shaking of this in ultrasonic desiccators will help in breaking these week bonds. Further, heating the substance at high temperature removes volatile impurities, thus we get fine nanocrystals as the output product.

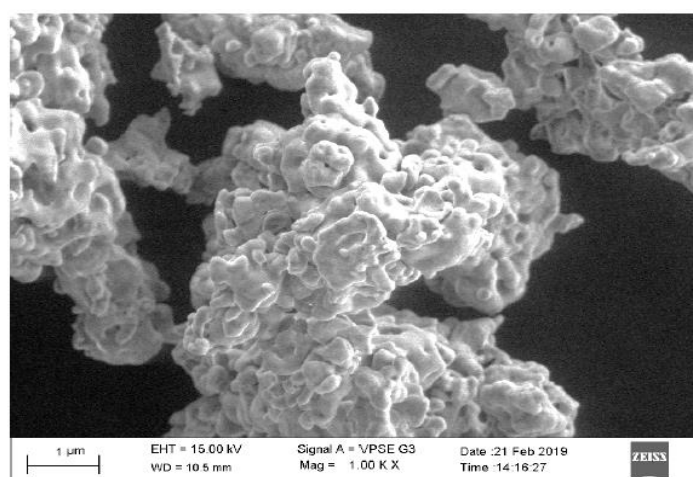


Figure 6: SEM image of K_2O nanocrystal

Conclusions

Synthesized successfully Potassium oxide nanoparticles by using solution combustion method with the aid of microwave oven. The so prepared oxide nanoparticles are characterized by different characterization tools such as XRD, EDS, SEM, UV-visible and FTIR. Various physical properties such as size, orientation, bond stretching, purity, energy band gap etc are determined. From XRD crystal size is determined by two methods. Firstly, by Debye Scherrer equation size is found to be 47.6007nm. Then, by W-H plot the average size of the crystal were found to be 48.570 nm. Hence from XRD we identified that synthesized K_2O nanoparticles were crystalline in nature and average crystal size is 48.570nm. FTIR spectrum for K_2O is obtained by plotting wavenumber v/s percentage of transmittance. We obtained peaks at 1369.49 cm^{-1} , 824.03 cm^{-1} , 671.97 cm^{-1} , 600 cm^{-1} which confirms the various bending and stretching modes of K_2O . UV-Visible spectrometry was carried out at room temperature with different concentration of samples. For different concentrations we determined different energy gap from absorbance peak. The obtained energy gaps were in the region 5.57 to 5.812 eV which indicates that the synthesized K_2O is an insulator. EDX study was made using Energy Dispersive Spectrometers. From elemental analysis we find that the calcination process re- moves impurities and we get pure K_2O nanocrystals. Finally, SEM analysis was done and morphology of K_2O was found to be in agglomerated pattern with flower like structure. The increased surface area of K_2O SEM images shows its availability towards surface reaction which has wide variety of applications in industrial and commercial field. More studies must be performed to shower an insight in deducing further details and discern for a better interpretation of the results obtained. Further it would be better if some morphology, magnetic and thermal characterization are done to widen its role in applied science.

Acknowledgement

The authors thank the efforts of Mr. Karthik A R, Mr. Mahesh B C, Mr. Neeraj E S and Ms. Spoorthi N for their co-operation in carrying out this research work .

References

1. Drexler, Erick (1986). *Engines of creation The coming Era of Nanotechnology*. Doubleday. ISBN 978-0-385-19973-5.
2. Changlong Chen, Xiuling Jiao, Dairong Chen, Yuting Zhao: *Materials Research Bulletin* 36 (2001) 2119-2126.
3. Mukasyan, Alexander S., Paul Epstein, and Peter Dinka. "Solution combustion synthesis of nanomaterials." *Proceedings of the combustion institute* 31.2 (2007): 1789-1795.
4. GAO Dao-jiang, XIAO Ding-quan, ZHANG Wen, ZHU Jian-guo and SHEN Lin: *Functional Materials (Gong Neng Cai Liao, in Chinese)* 33(2002) 251-252.
5. D. M. Tahan, A. Safari and L. C. Klein: *J. Am. Ceram. Soc.* 79 (1996) 1593-1598.
6. F. Jin, G. W. Auner, R. Naik, N. W. Schubring, J. V. Mantese, A. B. Cataian and A. L. Micheli: *Appl. Phys. Lett.* 73 (1998) 2838-2840.
7. O. G. Vendik, E. K. Hollmann, A. B. Kozyrev and A. M. Prudan: *J. Supercond.* 12 (1999) 325-326.
8. D. E. Kotecki, J. Baniecki, H. Shen, R. Laibowitz, K. Saenger, J. Lian, T. Shaw, S. Athavale, C. Carbral, P. Duncombe, M. Gutsche, G. Kunkel, Y. Park, Y. Wang and R. Wise: *IBM J. Res. Develop.* 43(1999) 367-340.
9. Masahiro Yoshimura: *Key Engineering Materials* 132-139 (1997) 2196-2199.
10. James O. Eckert Jr., Catherine C. Huang-Houston, Bonnie L. Gersen, Malgorzata M. Lencka, and Richard E. Riman: *J. Am. Ceram. Soc.* 11(1996) 2929-2935.
11. M. E. Pilleux, C. R. Grahann, V. M. Fuenzalida: *Appl. Surf. Sci.* 65/66 (1993) 283-285.
12. E. Ciftci, M. N. Rahaman and M. Shumsky: *J. Mater. Sci.* 36 (2001) 4875-4877.
13. P. C. Joshi and M. W. Cole: *Appl. Phys. Lett.* 77 (2000) 289-291.
14. C. D. Wagner, W. M. Riggs, L. E. Davis and G. E. Muilenberg: *A Reference Book of Standard Data for Use in X-Ray Photoelectron Spectroscopy*, (Published by Perkin-Elmer Corporation and Physical Electronics Division, 6509 Flying Cloud Drive Eden Prairie, Minnesota 553447, USA, (1979) pp. 42-42.

15. M.diaconu,A. Tache,S.A-M.v.Eremia.F.Gatea,S.litescu,G.L Radu,"strucural characterization of chitosam coated silicon nanoparticle-a FT-IR approach" in U.P.B scientific bulletin,VOL,72,2010,115-122
16. Skoog, Douglas A.;Holler,F.James;Crouch,Stanley R.(2007).Principal of instrumenal Anyalsis(6th ed).pp.169-173.
17. Reimer.L.(1993)scanning electron Microscopy,springer-Verlag,Berlin
18. Goldstein,J.I,et al (2003)scanning electron microscopy and X-ray micronalysis,3rd ed,plenum press,new york
19. Wang. J., Wan, D. W., Xue, J. M. and Ng, W. B., Novel Mechanochemical Fabrication of Electroceramics. Singapore Patent 9801566-2, 1998.
20. Ding.J., Ssuzuki.T. and Mc Cormic.P. G., Ultrafine particles prepared by mechanical or thermal processing. J. Am. Ceram. Soc.1996-79, 2956-2958.
21. Giri. A. K., Nanocrystalline materials prepared through crystallization due to instability in amorphous materials after grinding. Adv. Mater.,1997, 9, 163-166.
22. Boldyrev, V. V., Mechanochemistry and mechanical activation. Mater.sci Forum,1996, 227, 511-520.
23. Gaffet. E., Michael. D., Mazerolles. L. and Berthet. P., Effect of high-energy ball-milling on ceramic oxides. Mater.Sci. Forum, 1997 235-238(1), 103-108.

* * * * *

- ❖ **Eliezer Vishwas and S.N.Namitha**, Asst. Professor, Department of Physics, St. Philomena's College (Autonomous), Mysuru, Karnataka, India, **Ph:** 7411820074, **E-mail:** namithasn@stphilos.ac.in
- ❖ **Dr. T. Shivalingaswamy**, Department of Physics, Government College (Autonomous), Mandya, **E-mail:** tssphy@gmail.com

Hierarchical CeO₂:Sm³⁺ architectures synthesized via solution Combustion route for microwave and electronic device applications

- M. V. Hemantha Reddy
- T. Sreenivasulu Reddy
- Dr. K. M. Girish

Abstract

Sm³⁺ doped ceria nanoparticles were prepared by solution combustion route using ODH as a fuel. To correlate structural and surface morphology, Prepared Powders were characterized by Powder X-ray diffraction (PXRD), Scanningelectronmicroscopy (SEM) and Fourier Transmission Infrared Spectroscopy (FTIR) techniques. The synthesized nanopowder was calcined at low temperature (600°C) which resulted in crystallite sizes of 12 – 20 nm. PXRD studies confirms the fluorite structure with JCPDS card No. 034-0394. Furthermore conductivity studies were performed by varying frequency (20 Hz to 7 MHz) at room temperature. The conductivity is found to increase with increasing dopant concentration and highest conductivity was found at room temperature for 6 mol % of the prepared samples. The above results suggest that the prepared powder is a potential candidate for microwave and Electronic device applications.

Keywords: Solution combustion, CeO₂ nanoparticles and Ac conductivity properties

1. Introduction

Now a days, rare earth metal oxides have been widely investigated due to their good thermal, physical, and electrical performances [1]. Cerium oxide has attracted intensive attention of specialists because of its extensive variety of applications in different fields like biomedical sciences, material sciences, etc [2-6]. Compared to pure ceria, doped ceria fluorites are better ionic electrolyte material for operation in intermediate temperature solid oxide fuel cells than traditional yttria-

stabilized zirconia [7]. Although, undoped ceria is not a good ionic conductor, with doping of trivalent positive ion into the ceria lattice, the ionic conductivity increases remarkably [8-12]. This is because in ceria lattice defects like dopant and oxygen vacancies are formed due to the addition of the trivalent cation. In doped ceria, oxygen ion conductivity takes place on basis of hopping mechanism [13] and mainly depends on the type of dopant, dopant concentration ion, oxygen vacancies and defect structure. Therefore, to enhance the ionic conductivity for oxygen ions, the availability of oxygen vacancies should be more inside the electrolytes. The major problem of the solid electrolytes is the increase of electronic conductivity at low oxygen partial pressure and high operating temperature because of reduction of Ce^{4+} to Ce^{3+} [14] and segregation /splitting-up of impurities at grain boundaries [15-16] which lead to poor long-term stability. The likelihood of spread of the impurities over a large interfacial area for smaller grain and the effect of impurities can be reduced. Therefore, grain boundary may provide a faster ionic diffusion pathway for defects resulting in enhanced ionic conductivity and nanoscale doped ceria can be used at lower temperatures to avoid the reduction of Ce^{4+} to Ce^{3+} . The oxygen vacancies and doped cations forming defect associates are not necessarily free but may be bound due to Columbic interaction [17]. The dielectric properties of rare earth doped ceria materials depend on these defect pairs. The correlation between dielectric behaviour and ionic conductivity for perovskite dielectric systems such as multiferroics, ferroelectrics and antiferroelectric have been well studied [18-20]. In the present work, structural, morphology and Ac conductivity are investigated for samarium doped ceria (SDC) (0-10 mol %) nano powders at room temperature. Fortunately, low temperature densification of nanoceria materials has been achieved by employing wet chemical synthesis methods [21-23]. Among the various wet chemical methods, solution combustion synthesis (SCS) technique is considered to be a promising route due to relatively low agglomeration, high homogeneity, low cost, fast reaction time (within 5 minutes) and simple experimental setup [24-26] In the present study, SCS technique has been employed to synthesise the samples.

2. Experimental details

2.1 Synthesis

$\text{CeO}_2:\text{Sm}^{3+}$ (0-10 mol %) nanopowders were prepared by solution combustion route using laboratory prepared oxalyldihydrazide (ODH) as fuel. Stoichiometric amount of cerium nitrate ($\text{Ce}(\text{NO}_3)_3 \cdot 6\text{H}_2\text{O}$) and ODH ($\text{C}_2\text{H}_6\text{N}_4\text{O}_2$)

were mixed with a suitable quantity of double distilled water in pyrex dish and solution was mixed well using magnetic stirrer for about 5 min. Homogenous mixture was placed in muffle furnace maintained at $400 \pm 10^\circ\text{C}$. Further, obtained powder was calcined at 600°C for 2 h to get better crystallinity.

2.2 Results and discussion

The phase structure of the obtained nano powders was characterized by PXRD using X-ray diffractometer. Fig. 1 depicts the PXRD patterns of pure and Sm^{3+} (2-10 mol %) doped CeO_2 nano powders. diffraction peaks at (1 1 1), (2 0 0), (2 2 0), (3 1 1), (2 2 2), (4 0 0) and (3 1 1) were in well agreement with JCPDS card No. 034-0394 with cubic fluorite structure. Scherrer's formula was used to calculate average crystallite size (D) of the prepared powder and was found to be in the range 10-20 nm [27]

$$D = \frac{K\lambda}{\beta \cos\theta} \text{---(1)}$$

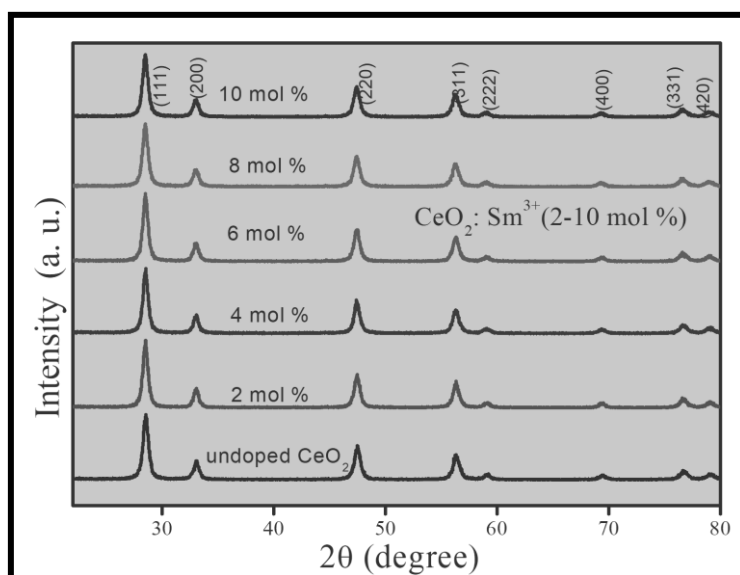


Fig. 1. PXRD patterns of un-doped and Sm^{3+} (2-10 mol %) CeO_2 nanopowders

Scanning electron microscopy (SEM) technique was used to investigate the surface morphology of the synthesized nanoparticles and the obtained SEM images of 6 mol % Sm^{3+} doped ceria nanoparticles were illustrated in Fig 2. which indicates large voids, cracks, agglomerates with an irregular morphology and porous nature of

the powder and the similar morphology was observed for all the samples indicates the negligible influence of Sm^{3+} ions on morphology. This kind of morphology is mainly due to escape of large amount of gases in combustion process [28,29].

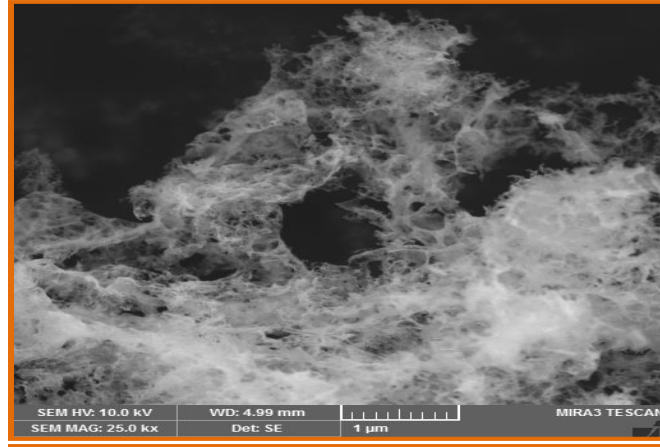


Fig.2. SEM picture of Sm^{3+} doped CeO_2

FTIR spectra of pure and Sm^{3+} (2-10 mol %) doped CeO_2 nanophosphor is depicted in the Fig.3 The band located at 3440 cm^{-1} and 1621 cm^{-1} corresponds to O-H stretching and O-H bending vibration and the peak at 2920 cm^{-1} can be attributed C-H vibrations where as the bands in the range $1008\text{-}1341\text{ cm}^{-1}$ indicates the C-H bending vibrations [30]. The sharp absorption peak located at 853 is due to carbonate ion bending vibration.

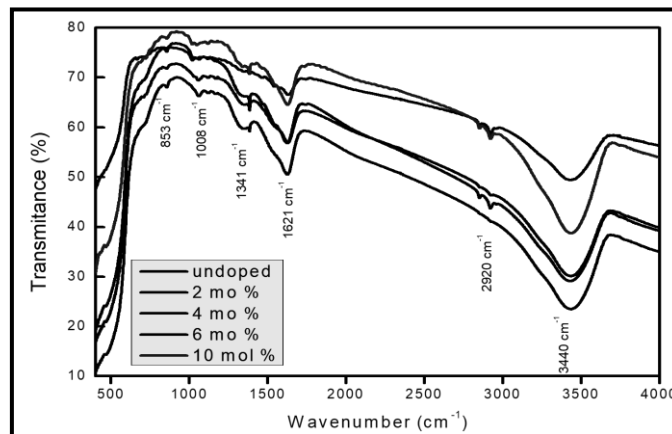


Fig.3. FT-IR spectra of $\text{CeO}_2:\text{Sm}^{3+}$ nanophosphor.

The AC conductivity was calculated by using the following relation for pure and Sm^{3+} (2-10%) doped CeO_2 nanoparticles and studied as a function of frequency at room temperature.

$$\sigma = G \times \frac{d}{A}$$

where G is conductivity, d is thickness of the pellet and A is the area of pellet. The variation of conductivity with the applied frequency as a function of dopant concentration was plotted and depicted in the Fig.4. Conductivity is found to increase with increasing frequency and a very low and nearly constant conductivity was observed at lower frequency and maximum at higher frequency which is the common nature of ceramic materials.

Conductivity increases with addition of Sm^{3+} concentration up to 6 mol % and then decreases even with the increase of dopant concentration. The fall in conductivity at higher dopant concentrations is due to defects are induced in the host which leads the formation of grain boundary defect barriers, barriers produce obstruction in flowing charge carriers which in turn reduces the conductivity [31,32].

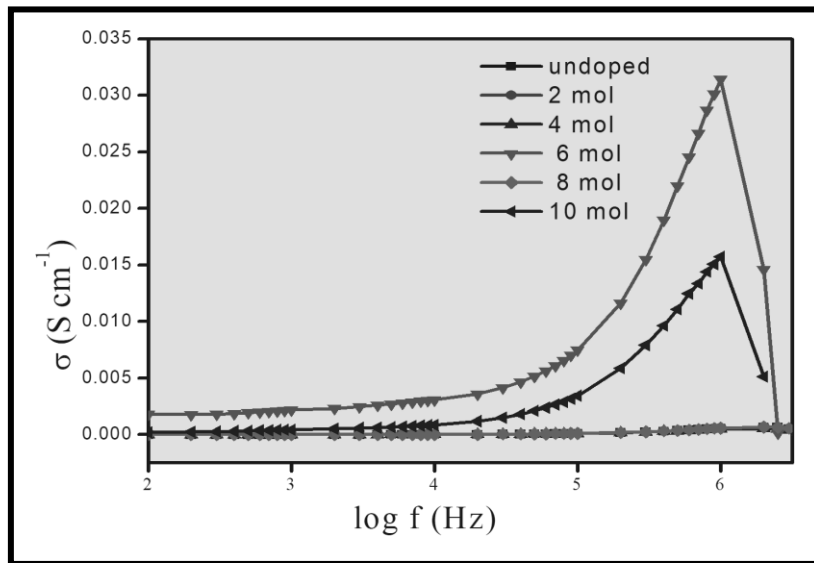


Fig.3. Conductivity spectra of $\text{CeO}_2:\text{Sm}^{3+}$ nanophosphor.

Conclusion:

Sm³⁺ doped CeO₂ nanoparticles were prepared by facile combustion route, PXRD studies indicate the formation of cubic fluorite structure without any impurity and agglomerated, porous nature of the samples confirmed by electron microscopy studies. Conductivity of CeO₂:Sm³⁺ nanoparticles is found to be increase with dopant concentration indicates hopping conduction mechanism in the conduction process. At higher Sm³⁺ concentrations and at high frequencies the conductivity of synthesized samples is found to increases, which shows the capability of the material for using in high frequency applications like ceramic capacitor and high band microwave devices. All the above results suggest that the 6 mol % CeO₂:Sm³⁺ nanoparticles are most suitable for dc and ac electronic devices.

Acknowledgement

The authors acknowledge the continuous support of the Management and Principal of Dr.Ambedkar Institute of Technology. Financial support by TEQIP-II for procuring the Precision Impedance Analyzer is gratefullyacknowledged.

References

1. D. Xue, K. Betzler, H. Hesse, Dielectric constants of binary rareearth compounds. *J. Phys.Condens. Matter* 12, 3113–3118 (2000)
2. A.A. Ansari, J. Labis, M. Alam, S.M. Ramay, N. Ahmad, A. Mahmood, J. *Electroceram.* 36, 150–157 (2016)
3. J. Chen, S. Pati, S. Seal, J.F. McGinnis,. *Nat. Nanotechnol.* 1, 142–150 (2006)
4. J. Colon, L. Herrera, J. Smith, S. Patil, C. Komanski, P. Kupelian, S. Seal, D.W. Jenkins, C.H. Baker, *Nanomed. Nanotechnol. Biol. Med.* 5, 225–231 (2009)
5. A.A. Ansari, P.R. Solanki, B.D. Malhotra,. *J. Biotechnol.* 142, 179–184 (2009)
6. A.A. Ansari, P.R. Solanki, B.D. Malhotra, *Appl. Phys. Lett.* 92, 263901 (2008)
7. B.C.H. Steele, A. Heinzl, *Nature* 414, 345-352. (2001)
8. H. Arai, T. Kunisaki, Y. Shimizu and T. Seiyama, 20, 241-248 (1986).

9. K. C. Anjaneya, G. P. Nayaka, J. Manjanna, G. Govindaraj and K. N. Ganesha. *J. Alloys and Compd.*, 578, 53-59 (2013).
10. N. Jaiswal, D. Kumar, S. Upadhyay and O. Prakash, *J. Power Sources*, 222, 230- 236 (2013)
11. S. J. Hong, K. Mehta and A. V. Virkar, *J. Electrochem. Soc.*, 145, 638-64 (1998)
12. M. Dudek, *J. European Ceram. Soc.*, 28, 965-971(2008)
13. Raghvendra, R. K. Singh and P. Singh, *J. Mater. Sci.*, 49, 5571–5578 (2014).
14. A. K. Baral and V. Sankaranarayanan, *Nonoscale Res. Lett.* 5, 637-643 (2010)
15. M. Mogensen, N. M. Sammes and G. Tompsett, *Solid State Ionics*, 129, 63-94 (2000)
16. R. Gerhardt and A. S. Nowick, *J. Am. Ceram. Soc.*, 69, 641-646 (1986).
17. M. O. Zacate, L. Minervini, D. J. Bradfield, R. W. Grimes and K. E. Sickafus, *Solid State Ionics*, 128, 243-254 (2000).
18. Behera A., Mohanty N. K., Behera B., Nayak P *Adv. Mat. Lett.* 4, 141-145 (2013).
19. C.Suman, C. K.; Prasad, K.; Choudhary, R. N. P., *J. Mat. Sci.*, 41, 369-375 (2006)
20. Parida, B. N.; Das, P.R.; Padhee, R.; Choudhary, R. N. P. *Adv. Mat. Lett.*, 3(3), 231-238 (2012)
21. J.G.Li, T. Ikegami, J.H.Lee, T.Mori, *Acta Mater.* 49, 419-426 (2001)
22. Jennifer L. M. Rupp, Tanja Drobek, Antonella Rossi, Ludwig J. Gauckler. *Chem. Mater.*, 19 (5), 1134–1142 (2007).
23. C.Kleinlogel, I.J.Gauckler, *Adv.Mater.* 13(14) 1078- 1081(2001)
24. S. Ekambaram, K.C. Patil, *J. Mater. Chem.*, 5 [6] 905–908 (1995).
25. H. Nagabhushana B.M Nagabhushana M. Madesh Kumar, Chikkahanumantharayappa, K.V.R Murthy, C.Shivakumara. R.P.S. Chakradhar, *spectrochimica Acta Part A* 78, 64-69 (2011).
26. H.C Madhusudhana S.N. Shobhadevi B.M. Nagabhushana B.V Cheluvvaraju, M.V.Murgendrappa R. Harikrishna H.Nagabhushana, N.R. Radeep, *J.Asian Ceramic soci* 4, 309-3018 (2016).
27. G.K. Williamson, W.H. Hall, *Acta. Metal.* 1953; 1: 22-31.
28. R. Naik, S.C. Prashantha, H. Nagabhushana, H. P. Nagaswarupa, K. S. Anantharaju, S.C. Sharma, B.M. Nagabhushana, H.B. Premkumar, K.M. Girish, *J. Alloys Compd.* 2014;317: 69–75.

29. K.M. Girish, S.C. Prashantha, RamachandraNaik, H. Nagabhushana, H.P. Nagaswarupa, H.B. Premakumar, S.C. Sharma, K.S. Anantha Raju, *Matr Res Expr*, 2016;3: 075015.
30. S. Shrestha, C.M.Y. Yeung, C. Nunnerley, S.C. Tsang, *Sens. Actuators A* 136, 191–198 (2007).
31. Pazhania, H.P. Kumarb, A. Varghesec, A. Moses EzhilRajd, S. Solomone and J.K.Thomasa, *J. Alloys Compd.*, 509, 6819–6823 (2011).
32. D.P. Thompson, A.M. Dickins and J.S. Thorp, *J. Mater. Sci.*, 27, 2267–2271 (1992).

* * * * *

- ❖ **M. V. Hemantha Reddy, T. Sreenivasulu Reddy**, Department of Physics, Dr. Ambedkar Institute of Technology, Bangalore, Karnataka, 560056 and Visvesvaraya Technological University, Belagavi, Karnataka, 590018, India
- ❖ **K. M. Girish**, Department of Physics, Dayanandasagar Academy of Technology and Management, Bangalore, Karnataka, 560082, India, **Ph:** 9880074068, **E-mail:** girishkmphy@gmail.com

Zinc oxide nanoparticles; Green synthesis using Moringa oleifera leaves, characterization and study on its Anticorrosive property

- K. C. Suresh
- Dr. G. N. Venkatareddy
- Dr. A. Balamurugan

Abstract

The green synthesis of zinc oxide (ZnO) nanoparticles has been carried by simple ecofriendly low-cost process using Moringa oleifera leaf extract. The synthesized ZnO nano particles structural and morphological properties are studied by using UV-Visible spectroscopy and particle size analysis by Fourier Transform Infrared Spectroscopy, Field Emission Scanning Electron Microscope and XRD analysis. The synthesized ZnO nanoparticles as the size range of 19.5 to 42.8nm. The anti-corrosive behavior of ZnO nanoparticles is investigated for KCl electrolyte solution and results shows that corrosion decreases.

Key Words: Green Synthesis, ZnO Nanoparticles and Anti corrosive activity.

Introduction:

The synthesis methods of metal oxide nanoparticles have been an interesting area in nanoscience and technology. The nanomaterial which comprises distinctive physicochemical properties has the potential to develop new systems, structures, devices, and Nano platforms with impending bids in extensive variety of disciplines [1, 2]. Nanomaterials are particles that are in nanoscale size, and they are very small particles with improved thermal conductivity, catalytic reactivity, nonlinear optical performance, and chemical stability due to their large surface area-to-volume ratio [3]. The conventional techniques (physical and chemical methods) use less time to synthesize bulk amount of nanoparticles, they require toxic chemicals like protective agents to maintain stability, which leads to toxicity in the environment. Keeping this

in mind, green technology by using plants is rising as an eco-friendly, nontoxic, and safe option, therefore plant extract-mediated biosynthesis of nanoparticles is environmentally and economically advantageous. Basically, biosynthesis of nanomaterials [4] produced through regulation, control, clean up, and remediation process, will directly help to uplift their environment friendliness. Some basic idea of “biosynthesis” can thus be explained by several components like minimization of waste, reduction of pollution and wanted or harmful by-products through the build-up of reliable, sustainable, and eco-friendly synthesis procedures. Natural resources like organic liquids are used as ideal solvents to achieve this goal. biosynthesis of metallic nanoparticles has been adopted to accommodate various biological materials like plant extracts [5], fungi, bacteria algae etc. The plant extracts are can be widely used to produce metal oxide nanoparticles.

Moringa oleifera tree species indigenous to India. It is highly sought after for its tender pods, seeds, flowers, and leaves, all of which are safe for human consumption [6]. Moringa oleifera is a promising resource for food and non-food applications, due to their content of monounsaturated fatty acids with a high monounsaturated/saturated fatty acids (MUFA/SFA) ratio, sterols and tocopherols, as well as proteins rich in sulfated amino acids [9]. The Moringa oleifera leaves, are recognized for their natural healing properties and are popularly consumed in a variety of ways [7 8]. Research has revealed that extracts prepared from the Moringa oleifera leaves possess high natural antioxidant properties and antibacterial properties.

Some published comparisons on nanoparticle yield, quality and bioactivity for extracts prepared with dry and from fresh Moringa leaves represent a promising candidate for green synthesis of bioactive ZnONPs that can be produced by biosynthesis. In the present study we report the biosynthesis of ZnO NPs from Moringa oleifera leaves extract using sunlight as the primary source of energy to produce metallic nanoparticle formation from leaves and seeds [10,11 & 12] in an environmentally friendly manner.

Materials and method of Preparation of extract

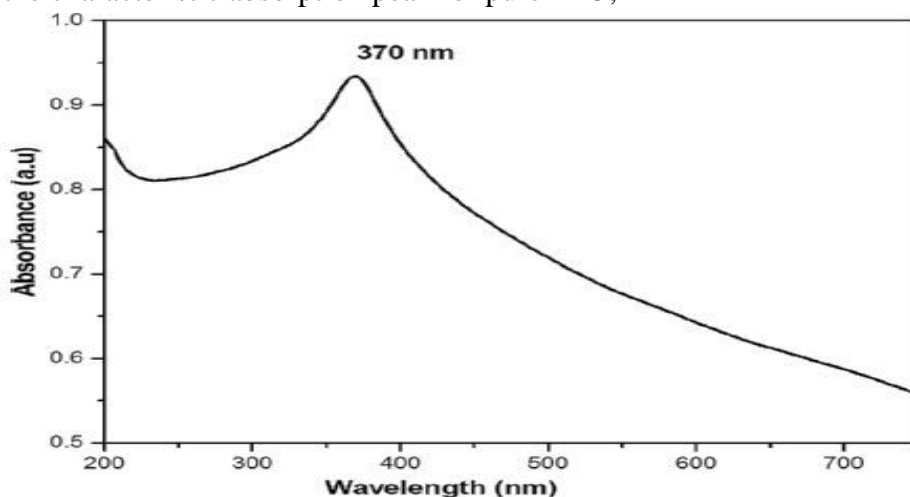
Moringa oleifera leaves are obtained from the healthy and cleaned Moringa oleifera tree. These leaves are washed thoroughly in running tap water and sterilized using double distilled water. Then, the plant leaves are kept for drying at room

temperature followed by crushing it using a mortar and pestle. 2 gram of the fine powder was mixed with 200 ml de-ionized water and boiled for 30 minutes at 50°C using a magnetic stirrer in hot plate. The solution is filtered using Whatman No1 filter paper and the obtained clear solution which was used as an extract. 100 ml *moringa oleifera* leaf extract is mixed with 0.1 M Zinc acetate precursor and stirred for 24 hours at constant rpm, which is called as Base solution. Base solution of ZnO nanoparticles is subjected to sonication effect for 60 minutes with 40Hz frequency. This sonicated solution was kept in hot air oven for overnight and calcinated at 500° C for 3 hours in muffle furnace to obtain ZnO nanoparticles

Characterization

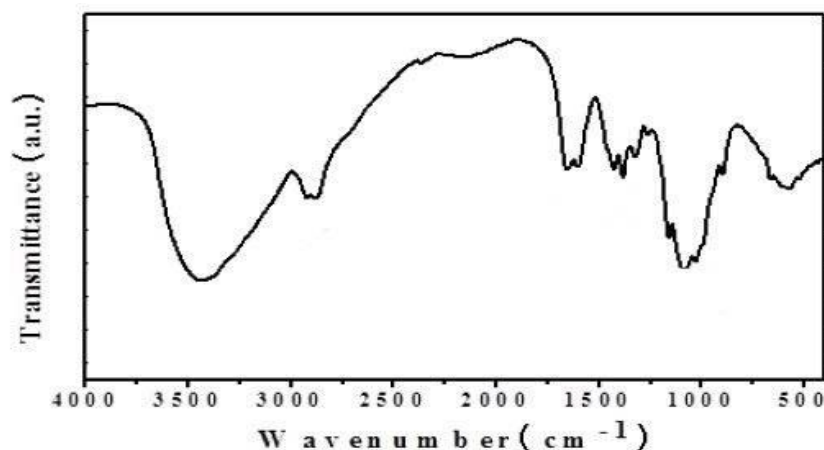
UV–vis spectroscopy

The size of the nanoparticles plays an important role in changing the entire properties of materials. Thus, size evolution of nanoparticles becomes very essential to explore the properties of the materials. A primary indication of zinc oxide nanoparticle formation is represented by a reaction solution colour change to yellow. UV-visible absorption spectroscopy is widely being used technique to examine the optical properties of nano sized particles. Ultraviolet spectra were collected in the range of 200–800 nm at room temperature. The absorption spectrum of ZnO nano powder is shown below. It exhibits a strong absorption band at about 370 nm, which is the characteristic absorption peak for pure ZnO,



IR Spectroscopy

In FTIR spectrum of the plant extract ZnO nanoparticles, the presence of peak at 510cm^{-1} corresponding to the Zn-O bond stretching vibrations the bands shown at 1090cm^{-1} and $3,450\text{cm}^{-1}$ are characteristic to the stretching vibrations of symmetric C-O and O-H groups. The vibrational bands at $1,650\text{cm}^{-1}$, 2920cm^{-1} signifies the stretching of C=O and C-H functional groups.

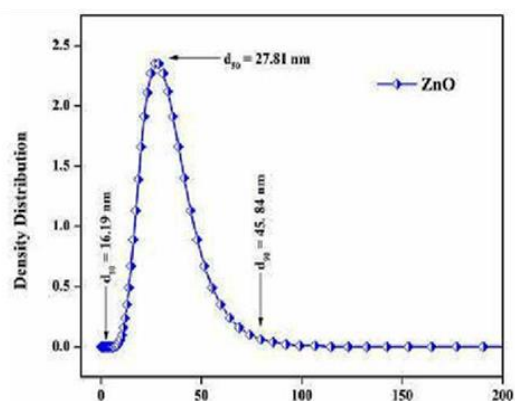
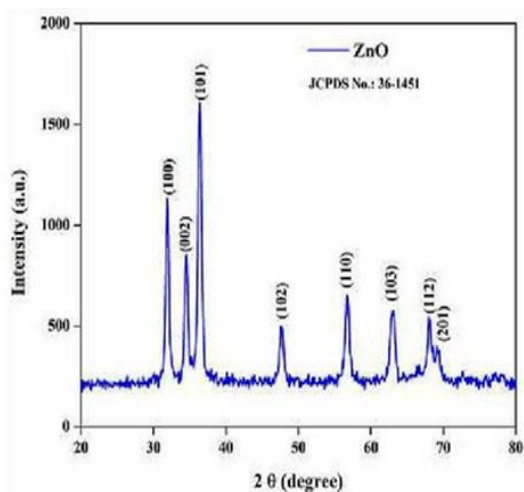


XRD, PSA and SEM analysis

The green synthesized ZnO nanoparticles crystallinity nature, size and average Particle size distribution were evaluated by XRD, PSA and FESEM studies. The following figure represents the XRD pattern of ZnO nanoparticles. Diffraction pattern of ZnO nanoparticles confirms the formation of Hexagonal crystalline structure, which is perfectly matched with JCPDS No. 36 – 1451. The XRD peaks of ZnO nanoparticles were indexed with (100), (102), (101) and (110) appeared at $2\theta = 31.7^\circ$, 34.4° , 36.25° and 56.603° . The crystalline size of the ZnO nanoparticles was calculated using Debye Scherrer's formula. The calculated crystalline size of ZnO nanoparticle is approximately 12.28 nm.

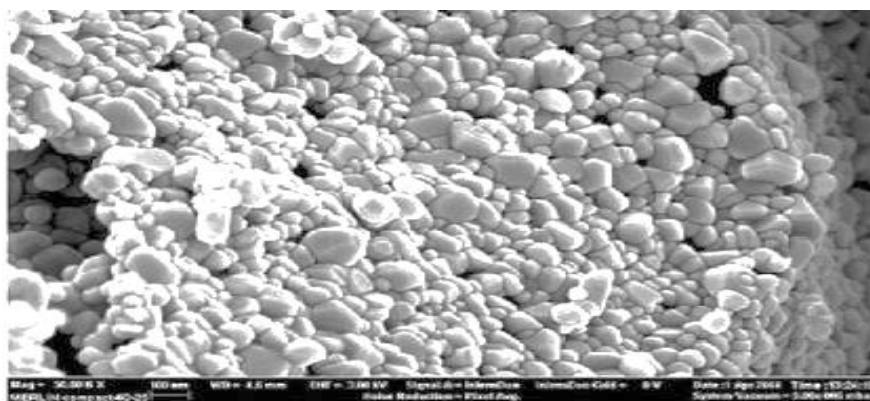
Particle size analysis (PSA) of ZnO nanoparticles shows that the average particle size ranges from 16.19 nm to 45.84 nm respectively for d_{10} and d_{90} ranges. Average particle size d_{50} of the ZnO nanoparticles is 27.81nm which agrees with the average crystalline size of ZnO nanoparticles

The FESEM image of ZnO nanoparticles is as shown in the following figure. The ZnO nanoparticles are spherical shaped with size ranging from 14 to 30 nm



Particle size in nm *PSA*

XRD Pattern



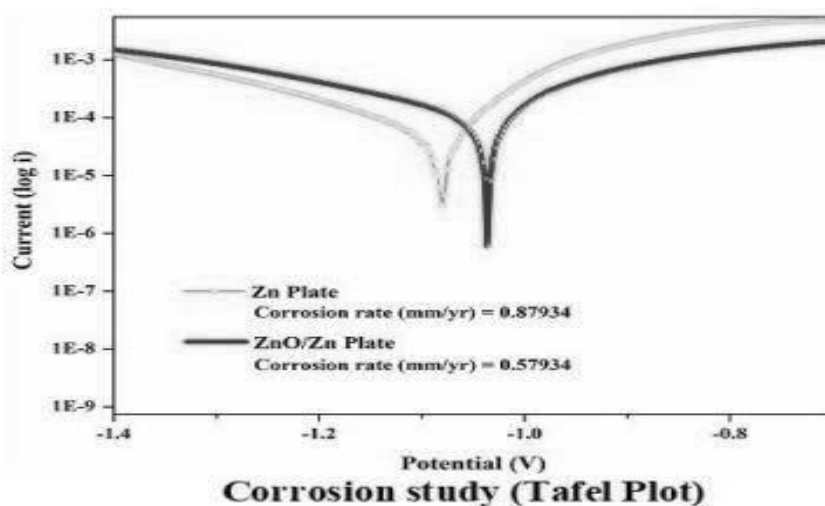
FESEM Pattern

Anti-corrosive activity.

Corrosion is a gradual destruction of materials by chemical or electrochemical reaction with their environment. Effective corrosion protection & control of metals is very important in present days and it should be considered at the design stage. The methods selected must be appropriate for the materials used for the configurations.

In our study zinc metal plate was used to study the anticorrosive behavior. The Zn metal plate subsequently polished with 1 mm silicon carbide grit papers and cleaned with acetone. The prepared ZnO nanoparticles were mixed with PVDF and N-Methyl-2-pyrrolidone (NMP) 80:15:5 weight ratios in order to prepare slurry. The

slurry was further coated on metal surface of the Zn plate using the doctor blade technique. The coated plate was dried in an oven at 353 K for 1 h and then used for electrochemical corrosion study



The comparative corrosion studies are individually carried out for Zn plate and ZnO nanoparticles coated Zn plates (ZnO/Zn) samples in 3.5 % NaCl electrolyte. Initially, the potential is applied at -1.3 V and the corrosion initiated at Zn anode and its potential tends to move for -0.3 V with constant interval of ~5 mV. It is observed that corrosion potential of ZnO/Zn is shifted towards positive side (anodic region) compared to pure Zn plate. The corrosion current (i_{corr}) was calculated from Tafel plot for Zn and ZnO/Zn are 7.197 (A/Cm^2) and 5.343 (A/Cm^2) respectively as shown above figure. It was also obvious that the ZnO/Zn has lower corrosion current compared to pure Zn plate, which suggests enhanced corrosion resistance

The above results assured low corrosion rate and high electrochemical corrosion resistance achieved by a thin layer coating of green synthesized ZnO nanoparticles over the anode surface where Zn acts.

Conclusion

Nanoparticles, compared to bulk materials, exhibit improved characteristics due to their size, distribution and morphology and are widely used in numerous scientific fields. Among metallic nanoparticles, zinc nanoparticles are very important

especially due to their physiochemical and anticorrosive properties, which helps in manufacturing the devices.

Green synthesized ZnO nanoparticles were successfully synthesized using *Moringa oleifera* leaf extract. The crystalline size of the ZnO nanoparticles is smaller and is 12.2 nm. which was confirmed by XRD analysis using the Scherer equation. The observations of their morphology using FESEM revealed that the nanoparticles were spherical in shape. The anti-corrosive activity demonstrate that green synthesized ZnO nanoparticles are promising material for anti-corrosive property

References

1. Zinc oxide nanoparticles: biological synthesis and biomedical applications, H. Mirzaei and M. Darroudi, *Ceramics International*, vol. 43, no. 1, pp. 907–914, 2017.
2. Nanoparticles applied to plant science: a review,” S. C. C. Arruda, A. L. D. Silva, R. M. Galazzi, R. A. Azevedo, and M. A. Z. Arruda, *Talanta*, vol. 131, pp. 693–705, 2015.
3. A review on green synthesis of zinc oxide nanoparticles—an eco-friendly approach,”H. Agarwal, S. V. Kumar, and S. Rajeshkumar, *Resource-Efficient Technologies*, vol. 3, pp. 406–413, 2017.
4. Biosynthesis of nanoparticles and silver nanoparticles, Cheah Liang Keat,,Azila Aziz, Ahmad M Eid & Nagib A. Elmarzugi *Bioresources and Bioprocessing* volume 2, Article number: 47 (2015)
5. Synthesis of metallic nanoparticles using plant extracts Amit KumarMittal,YusufChisti,Uttam ChandBanerjee *Biotechnology Advances*Volume 31, Issue 2, March–April 2013, Pages 346-3
6. *Moringa oleifera* Seeds and Oil: Characteristics and Uses for Human Health AlessandroLeone, AlbertoSpada,AlbertoBattezzati, AlbertoSchiraldi, Junior,Aristil, and Si mona Bertoli. *Int J Mol Sci.* 2016 Dec; 17(12): 2141.
7. Biosynthesis and characterization of ZnO nanoparticles using the aqueous leaf extract of *Imperata cylindrica* L, I S Saputra and Y Yulizar, *International Symposium on Current Progress in Functional Materials, Materials Science and Engineering* ,2017
8. Biosynthesis of zinc oxide nanoparticles using leaf extract of *Calotropis gigantea*: characterization and its evaluation on tree seedling growth in nursery stage, Sadhan Kumar Chaudhuri, Lalit Malodia, *Appl Nanosci* (2017) 7:501–512

9. Green biosynthesis of zinc oxide nanoparticles via aqueous extract of cotton seed, Afsaneh Sadatzadeh , Faramarz Rostami Charati, Reza Akbari , Hossein Hosseini Moghaddam. J. Mater. Environ. Sci., 2018, Volume 9, Issue 10, Page 2849-2853

* * * * *

- ❖ **K. C. Suresh**, Government College for Women, Maddur-571428, Mandya District, India, **Ph:** 9844360464, **E-mail:** kunigalsuresh@gmail.com
- ❖ **Dr. G. N. Venkatareddy**, H.P.P.C. Government First Grade College, Challakere-577522
- ❖ **Dr. A. Balamurugan**, Research and Development Center, Bharathiar University, Coimbatore-641046, India) Department of Physics, Government Arts and Science College, Avinashi-641654, Tamilnadu, India)

Synthesis and characterization of TiO₂ and TiO₂ doped PVA films

○ Dr. M. Vishwas

Abstract

Titanium dioxide (TiO₂) thin films and nanoparticles were synthesized by the sol-gel method using titanium tetraisopropoxide (TTIP) as the precursor material. Poly (vinyl alcohol) (PVA) films were prepared by solution casting method. TiO₂ nanoparticles were doped in PVA films. The optical properties of TiO₂ films were studied using UV/VIS spectrophotometer. The optical transmittance is more than 85% in the visible region. The refractive index decreased with wavelength. FTIR spectra is used to analyze the stretching and bending vibrational modes in PVA and TiO₂ doped PVA films.

Key words: TiO₂, PVA, Optical properties, FTIR.

1. Introduction:

TiO₂ thin films can be prepared by various methods, in which the sol-gel method finds many advantages including cost effective, easy process, large area deposition at room temperature (RT) etc [1]. TiO₂ films can be used for various applications including photocatalysis, antireflection coatings, and anti-bacterial agent [2,3,4]. TiO₂ films exhibit large band gap semiconducting nature with a band gap of 3.3 eV.

2. Experimental procedure:

TiO₂ thin films and nanoparticles were synthesized by the sol-gel method using TTIP as precursor material, absolute ethanol as solvent and concentrated HCl as a catalyst. The flow chart for the preparation of TiO₂ thin films and nanoparticles is shown in Fig.1. The PVA films were synthesized using PVA of 1g (M.W.

=1,15,000) granular powder dissolved in 5 g of de-ionized water. The detailed procedure is published in previous paper [5]. TiO₂ nanoparticles (5, 10 and 15 mg) were doped in PVA films and studied the FTIR spectra of the samples.

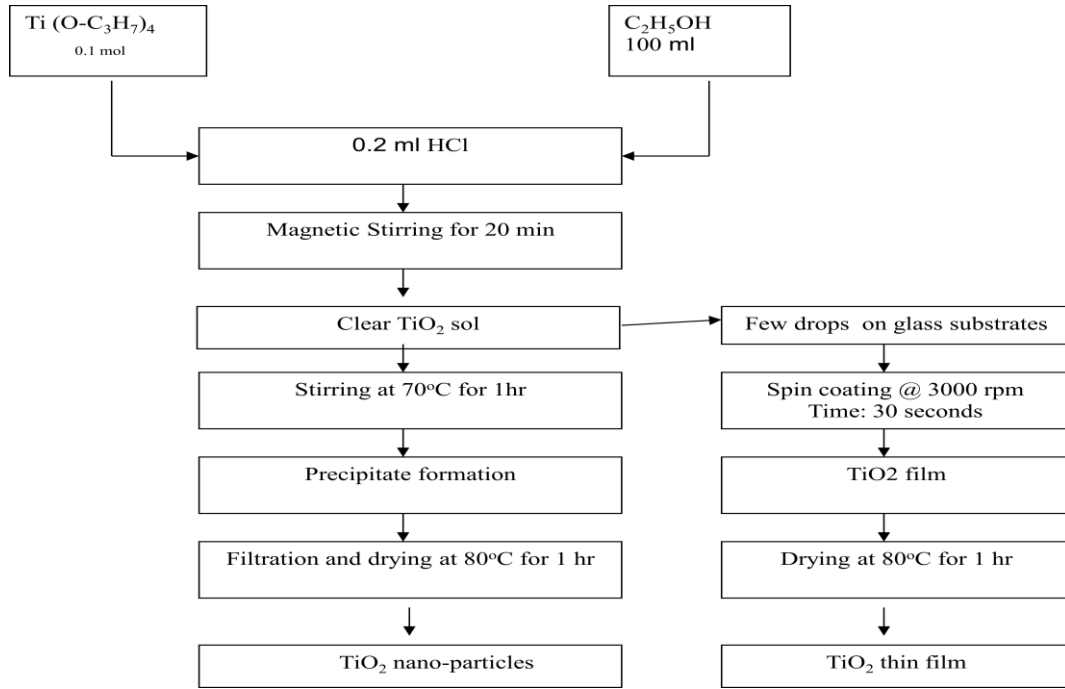


Fig. 1. Flow chart for the preparation of TiO₂ film and nanoparticles

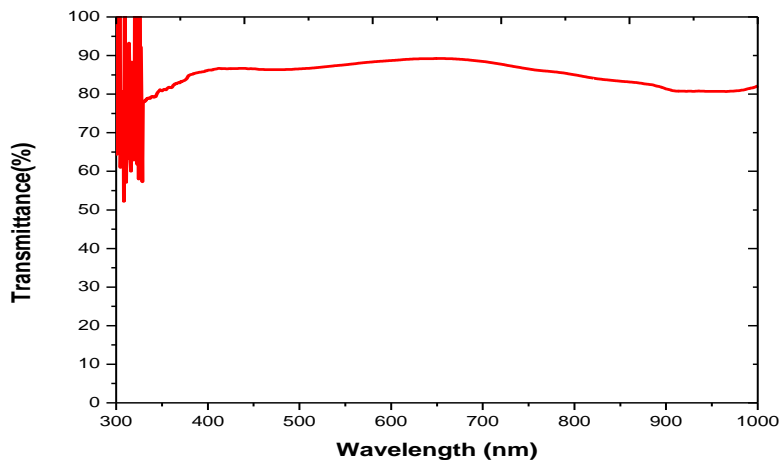


Fig.2. Optical transmittance spectra of TiO₂ film on glass substrates.

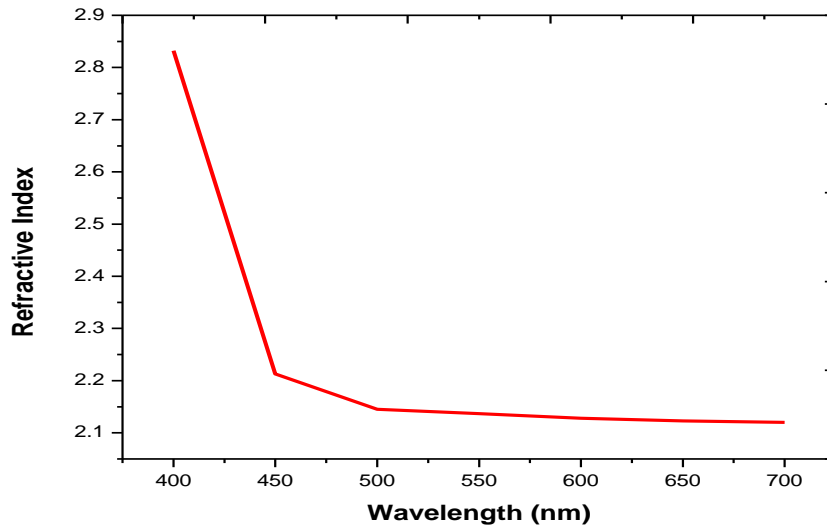


Fig.3. Variation of refractive index of TiO₂ film with wavelength.

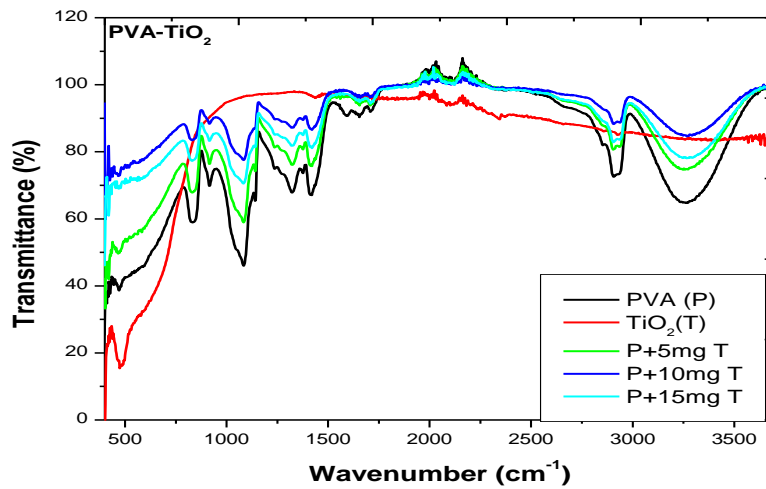


Fig.4. FTIR spectra of TiO₂ doped PVA films.

3. Results and discussions

Fig.2 shows the optical transmittance spectra of TiO₂ film as prepared at room temperature in ambient air. It is clear from the figure that, the optical

transmittance is greater than 85% in the visible region exhibiting very good transparency of the film. The film thickness and refractive index of the film are measured by the envelope technique [6]. The film thickness is 145 nm and refractive index of the film is ~ 2.132 at 550nm (visible region). The refractive index of the film decreased with increasing the wavelength and become almost constant after 550 nm as shown in Fig.3.

The FTIR spectra of pure TiO_2 film and TiO_2 doped PVA films recorded in the range of 3600 cm^{-1} – 400 cm^{-1} are shown Fig.4. A broad band is observed between 3150 cm^{-1} and 3450 cm^{-1} , representing the presence of free hydroxyl groups and bonded O-H stretching vibrations of PVA. The peaks at 2925 cm^{-1} and 1085 cm^{-1} indicates the presence of C-H stretching and C-O stretching vibrations corresponding to inplane and outplane bending vibrations of PVA– TiO_2 nano composite film. The peak at 2950 cm^{-1} is due to the stretching vibration of CH_2 and CH_3 . The several peaks in the region 450 – 1500 cm^{-1} may be due to TiO_2 crystallites embedded in the matrix of PVA. PVA– TiO_2 film showed peaks at 1407 cm^{-1} , 1322 cm^{-1} , indicating the symmetric bending mode (CH_2), wagging vibration of CH_2 and CH respectively [7].

4. Conclusions

TiO_2 thin films and nanoparticles were successfully prepared by the sol-gel method. TiO_2 -PVA films were prepared by solution casting method. The optical properties such as optical transmittance and refractive index were studied from transmittance spectra. The stretching and bending vibrations of TiO_2 and PVA films were analysed from infrared spectrum.

Acknowledgements

Author is thankful to the DST-FIST programme, Central Instrumentation Centre, Government Science College Autonomous, Bangalore for the utilization of facilities.

References

1. Zeeshan Ali, Bharat Raj, M. Vishwas, M. Anisa Athhar, International Journal of Current Microbiolog- and Applied Sciences, 5(4) (2016) 705-712.

2. M. Vishwas, Sudhir Kumar Sharma, K. Narasimha Rao, S. Mohan, K.V. Arjuna Gowda, R.P.S.Chakradhar, Modern Physics Letters B, 24 (2010) 807-816.
3. M. Vishwas, K. Narasimha Rao, D. Neelapriya, Ashok M. Raichur, R.P.S. Chakradhar, K.Venkateswarulu, Proceedia Materials Science, 5 (2014) 847 – 854.
4. M. Vishwas, K. Narasimha Rao, R.P.S. Chakradhar, Ashok M. Raichur, Journal of Material Science: Materials in Electronics, 25 (2014) 4495–4500.
5. M. Vishwas, K. Narasimha Rao, D. Neelapriya, Ashok M. Raichur, R.P.S. Chakradhar, K.Venkateswarulu, Proceedia Materials Science, 5 (2014) 847 – 854.
6. R. Swanepoel, J. Phys. E: Sci. Instrum. 16 (1983) 1214
7. S. Sugumaran, C.S. Bellan, Optik 125 (2014) 5128-5133.

* * * * *

❖ **Dr. M. Vishwas**, Department of PG Studies and Research in Physics, (Nrupatunga University) Government Science College (Autonomous), Bangalore-560001, India. **Ph:** 9513339931 / 080-22212924 **E-mail:** vishwasm46@yahoo.com

Hydrothermal Synthesis of Single Phase Monoclinic ZrO₂ Nano Crystals: Structural and Optical Studies

- Dr. M. Rajendra Prasad
- Anthony Seleen

Abstract

Single phase monoclinic ZrO₂ nano crystals prepared by hydrothermal process. The products were processed from Zirconyl Nitrate Hydrate as the precursor. X-ray diffraction, Scanning Electron Microscopy, Fourier Transform Infrared Spectroscopy, Photo Luminescence and UV are studied exhaustively. The XRD patterns reveals as prepared ZrO₂ have perfect monoclinic phase. The crystalline size is found to be approximately 9.5 nm. The average particle size displayed by the SEM is 35 nm. The observed vibrational bands at 418, 489, 733 cm⁻¹ confirms the monoclinic structure of as prepared ZrO₂. The PL emission spectrum excited at 246 nm consist of intense band centered at 452 nm along with four weak emission bands 482 nm, 575 nm, 608 nm, 650 nm. Band gap of ZrO₂ measured to be 4.7 eV.

Keywords: Monoclinic ZrO₂, Nano crystal, Hydrothermal, Band gap.

1. Introduction

Zirconia nano crystals have attracted very much interest recently due to their specific optical, electrical and potential properties, including transparent optical devices and electrochemical capacitor electrodes, oxygen sensors, fuel cells, catalyst [1], advanced ceramics, electronic nano devices and bio active coatings on bone implants [2]. ZrO₂ has three polymorphic phases: monoclinic, tetragonal and cubic, among these ZrO₂ phases the monoclinic structure which is thermodynamically stable below 1170°C, where control of crystalline phase and the crystalline size of its critical importance. For the synthesis of ZrO₂ nano crystals such as sono chemical method, combustion method, sol-gel and surfactant templating method, however these processes required complicated procedures, such as sequential addition of the

reagents and pretreatment of the precursors, because of the difficulty in controlling the crystal structure and size of the products. Using hydrothermal method we can synthesis metal oxide and their corresponding nano crystals. This method enables to prepare surface modified metal oxide with nano crystalline structure. Nano sized ZrO_2 nano crystals were successfully prepared using hydrothermal method. In this case ZrO_2 was prepared with or without organic molecules as a surface modifier; the advantage of this approach is the simplicity of the process. Only Zirconyl nitrate was used as a precursor, and no other reagents were added in this procedure. The crystallization of ZrO_2 under hydrothermal conditions and the phase composition strongly depend on the solubility of the precursor in water. Greater solubility of the precursor in water results in a greater volume fraction of the monoclinic phase.

2. Experimental

The Zirconyl nitrate was used as a precursor in a hydrothermal method. The solution was prepared using the precursor (2.32 g) and distilled water (50 ml precursor concentration of 0.2 M) stirred using magnetic stirrer for one hour. The prepared solution was placed in a Teflon inner bottle set inside a stainless steel vessel with an inner volume of 100 ml. The hydrothermal reaction was performed using an electric furnace at 200°C for 24 h. After the reaction the vessel was cooled to room temperature inside the furnace. The precipitate was centrifugated, washed with water and absolute ethanol for five times, and then dried in hot air oven at 60°C for 10 h.

X-ray diffraction analysis (XRD) was used to study the crystal phase of the samples. The XRD measurements were performed with the Cu $K\alpha$ radiation ($\lambda = 1.5406 \text{ \AA}$) at 10°/min scanning speed in the 2θ range from 10° to 80°. Scanning Electron Microscope (SEM) micrograph is recorded using JEOL instrument. Fourier transform infra-red (FT-IR) spectra were recorded in MB 102 Spectrometer. Photoluminescence emission (PL) and excitation spectra were obtained from F4500 fluorimeter.

3. Results and Discussion

3.1 X-Ray Diffraction analysis

Fig.1 shows the XRD pattern of pure ZrO_2 nano crystal within the range of 10 to 80°. X-ray diffractogram of the material was confirmed the polycrystalline

structure of the ZrO_2 . It clearly indicates the presence of monoclinic ZrO_2 (JCPDS No. 830944). The strongest peak observed at 27.9069 (-111), 31.2945 (111) and 50 (220). The average particle grain size of ZrO_2 was determined using Debye-Scherrer's formula and was estimated that 7 nm.

$$D = 0.9 \lambda / \beta \cos\theta$$

Where λ is wave length of X-ray Cu $K\alpha$ radiation in \AA (1.542\AA) and β is the full width half maximum in radian.

Dislocation Density is found to be $20 \times 10^{15} \text{ m}^{-2}$ calculated using the formula, $\delta = 1/D^2$

Microstrain is found to be 5.3×10^{-3} calculated using the formula, $\mu = \beta \cos\theta/4$

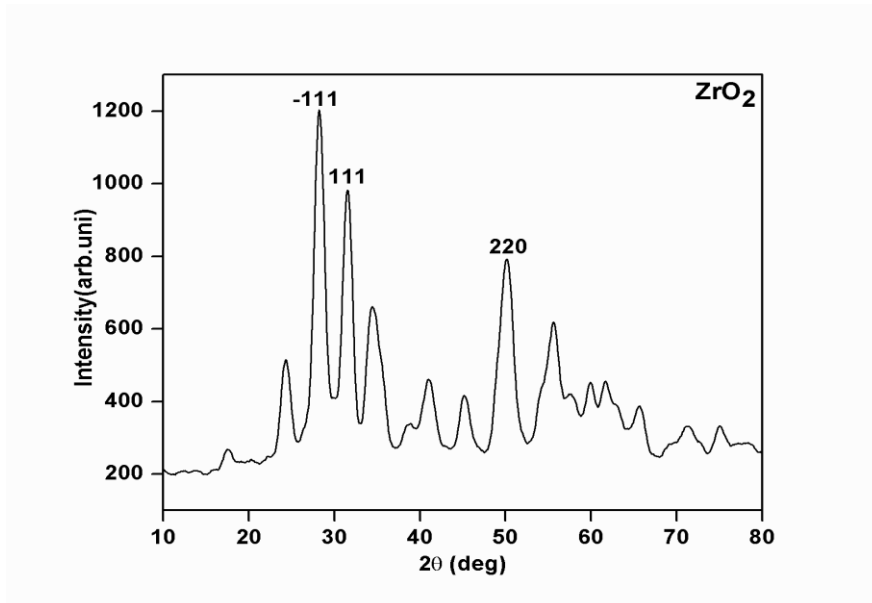


Fig.1 XRD pattern of ZrO_2 Nano Crystal

3.2 Scanning Electron Microscope analysis

The SEM micrograph of the ZrO_2 Fig.2 shows porous, agglomerated and uniform spherical shaped particles. The voids observed can be ascertained due to the evolution of gases formed at the process of smoldering combustion. The average particle size of the ZrO_2 particles is observed to be 35 nm.

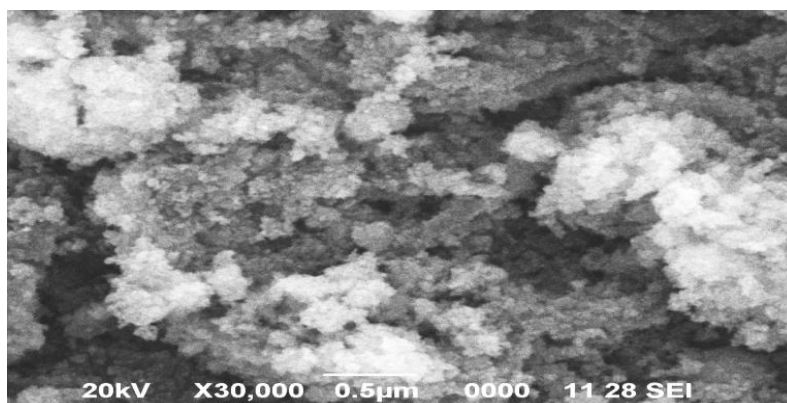


Fig.2 SEM Image of ZrO₂

3.3 Fourier transform infrared (FT-IR) analysis

FT-IR spectroscopy was used to study the surface interaction of adsorbed water in dynamic equilibrium with the gas phase on the ZrO₂ surface. Fig.3 shows the FT-IR spectra ZrO₂. The FT-IR spectra of ZrO₂ nano crystals were recorded in the range of 700 to 3500 cm⁻¹. well known that H₂O and CO₂ molecules are easily chemisorbed onto the ZrO₂ surface when exposed to the atmosphere. The dominant absorption band centered at 735 cm⁻¹ is due to the deformation mode of Zr-O-Zr bond. The peaks centered at 1000 cm⁻¹ and 1141 cm⁻¹ can be associated to stretching vibrations of Zr-O⁻ terminal groups [3]. Weak band centered at 1530 cm⁻¹ assigned to symmetric bending of H₂O and the band at 2308 cm⁻¹ is due to stretching vibrations of C-O in adsorbed CO₂ from atmosphere. The wide band centered at 3390 cm⁻¹ is ascribed to the stretching of O-H group of water. The observed vibrational bands at 418, 489, 733 cm⁻¹ confirms the monoclinic structure of as prepared ZrO₂ [4,5]

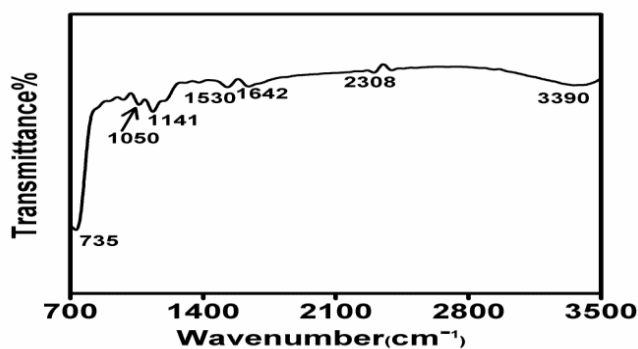


Fig.3 FTIR Spectra of ZrO₂

3.4 UV and PL analysis

Fig.4 shows the absorption spectra of the as prepared nanocrystalline ZrO_2 powder. The sharp of the absorption edge suggests a single phase. The band gap energy is calculated from the absorption spectra is 4.7 eV [6.7].

Fig.5 shows the photoluminescence emission spectra obtained from the sample under excitation wave length 262 nm. The fluorescence emission at 450 nm [8] and very weak two fluorescence emissions at 484, 576 nm could be observed respectively.

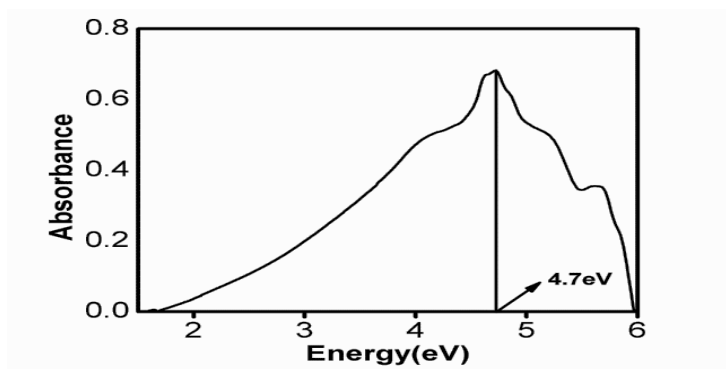


Fig.4 UV Spectra of ZrO_2

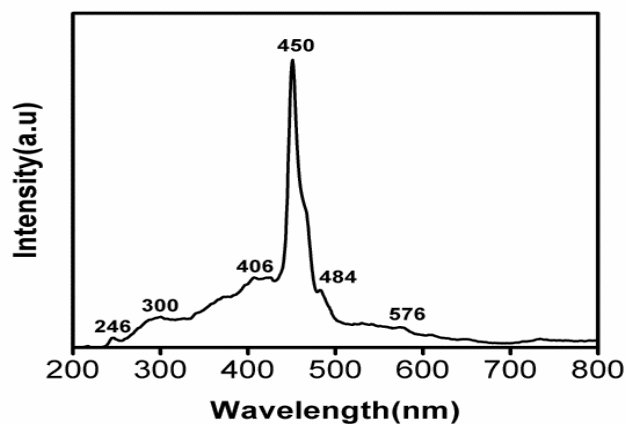


Fig.5 PL Spectra of ZrO_2

Conclusion

ZrO_2 nano-crystals have been successfully synthesized by simple hydrothermal method. XRD pattern indicate that the pure monoclinic phase and crystallite size is found to be 7 nm. The SEM image shows to be the average particle size is equal to

35 nm. From FT-IR the wide band centered at 3390 cm^{-1} is ascribed to the stretching of O-H group of water. The band gap is found to be 4.7 eV and two weak fluorescence bands are observed in PL.

References

1. G. Wang, F. Meng, C. Ding, P.K. Chu, X. Liu, Microstructure, bioactivity and osteoblast behavior of monoclinic zirconia coating with nanostructured surface, *Acta Biomaterialia* 6 (2010) 990–1000
2. D. He, Y. Ding, H. Luo, C. Li, Effects of zirconia phase on the synthesis of higher alcohols over zirconia and modified zirconia, *J. Molecular Catalysis A: Chemical* 208 (2004) 267–271
3. J.A. Badenes, J.b. Vicent, M.A. Tena, G. Monros, *J. Mater. Sci.* 37(2002) 1413–1420
4. Z.W. Quan, L.S. Wang, J. Lin, *Mater. Res. Bull.* 40 (2005) 810
5. S. Sapra, S. Mayilo, T.A. Klar, A.L. Rogach, J. Feldmann, *Adv. Mater.* 19 (2007) 569–572
6. H. Hayashi, A. Ueda, A. Suino, K. Hiro, Y. Hakuta, Hydrothermal synthesis of yttria stabilized ZrO₂ nanoparticles in subcritical and supercritical water using a flow reaction system, *J. Solid State Chemistry* 182 (2009) 2985–2990.
7. N. Zhao, D. Pan, W. Nie, X. Ji, Two-phase synthesis of phase-controlled colloidal Zirconia nanocrystals and their characterization, *J. American Chemical Society* 128 (2006) 10118–10124.
8. S.F. Wang, F. Gu, M.K. Lü, Z.S. Yang, G.J. Zhou, H.P. Zhang, Y.Y. Zhou, S.M. Wang, *Opt. Mater.* 28 (2006) 1222–1226.

* * * * *

- ❖ **Dr. M. Rajendra Prasad**, Department of Physics, Yuvaraja's College, University of Mysore, Mysore, Karnataka, India 570005. **E-mail:** rpsiddartha@gmail.com
- ❖ **Anthony Seleen**, Department of Physics, Government First Grade College, University of Mysore, Chamarajanagar, Karnataka, India-571313. Ph: 8217021982, E-mail: celina.ksa@gmail.com

Nanomanufacturing and Industrial Application of Nanotechnologies



❖ Bakula Keerthi Chandra

Introduction

In industry, nanotechnologies are being applied, based on the generic methods of processing Nanomaterials, output rates and applications in certain main industries. We illustrate how Nano science and nanotechnology can have a longer-term effect on industry and highlight some of the factors that will influence nanotechnology commercialization. The health, environmental and safety impacts of nanotechnology will be addressed in this paper. We have concentrated disproportionately on the development and usage of nanoparticles and nanotubes because they pose concerns, but it should be noted that nanoparticles and nanotubes constitute only a small fraction of the estimated global nanotechnology market.

Characterization

A significant part of the manufacturing process is the characterization of materials: the determination of their form, scale, distribution, mechanical and chemical properties. It serves two broad purposes: quality management and the research and development of new technologies, materials and products as part of research and development. During our industry workshop, evidence revealed that many sectors of industry did not consider nanotechnology to be new (for example, Nano scale structures have been important to the catalyst industry for over 100 years). The manufacturers, however, thought that a 'breakthrough' in nanotechnology had occurred in the instruments used at the Nano scale stage to observe and quantify properties and processes. Sophisticated instruments, such as STEM, AFM and TEM, allow for Nano scale surface and interfacial characterization of materials, enabling the observation and analysis of individual atoms. This leads to a better understanding of the relationship between the properties of shape and

substance and allows for the regulation of Nano scale processes and design materials with unique properties. However, the commercialization of such advanced functional materials requires that they can be produced in adequate amounts, in a consistent, reliable manner. Output will be restricted to academia and R&D departments within the sector until that is achieved.

Fabrication Techniques

There are a wide range of methods capable of manufacturing nanostructures of varying degrees of quality, speed and cost. Such processing methods come into two categories: 'bottom-up' and 'top-down'. The limits of each approach in terms of feature size and quality that can be accomplished have begun to converge in recent years.

Bottom-Up Manufacturing

Bottom-up development includes the creation, atom-by-atom or molecule-by-molecule, of structures. It is possible to classify the broad range of approaches to achieving this objective into three categories: chemical synthesis, self-assembly, and positional assembly. As discussed below, the only technique in which single atoms or molecules can be intentionally positioned one by one is positional assembly (with its many practical disadvantages as a production tool). More generally, through chemical synthesis, large numbers of atoms, molecules or particles are used or formed and then organized into a desired top-down manufacturing structure by naturally occurring processes.

Top-down manufacturing involves beginning with a larger piece of material and extracting material from it by etching, milling, or machining a nanostructure (as, for example, in circuits on microchips). This can be achieved using techniques such as precision engineering, lithography, which has been developed and perfected over the past 30 years by the semiconductor industry. Top-down techniques provide durability and complexity of the device, but they are typically higher in energy consumption and create more waste than bottom-up techniques. For example, computer chip manufacturing is not yet feasible via bottom-up methods; however, techniques using bottom-up (or hybrid top-down/bottom-up) methods are being explored through top-down and bottom-up convergence techniques. The relationship is demonstrated between top-down and bottom-up development. The 'top down'

segment is an updated version of Norio Taniguchi's diagram, which showed the progression in the accuracy of the description of objects from the early 20th century to 1974, extrapolated to the end of the century. The segment 'bottom up' shows how bottom-up processes have developed through developments in chemical processing to manage ever-larger structures. The dimensions that can be managed by either approach are now of a similar order, resulting in exciting new hybrid production methods.

Visions for the Future Precision Engineering

There are clear engineering tolerance reduction drivers, including miniaturization, enhanced wear and durability features, automated assembly and greater interchangeability, reduced waste, and rework requirements. Driven by the electronics and computer industries, research and the industrial application of energy beam processing methods will increase as the trend towards miniaturization continues. In a production sense, techniques such as electron beam lithography (EBL), directed ion beam (FIB), reactive ion etching (RIE) and femtosecond pulsed laser ablation are becoming more precise and cheaper to apply. The following are some examples of potential applications of high-precision engineering.

ICT: The machines used for the manufacture of chips depend primarily on the use of ultra-high-precision techniques for their development and nanometrology techniques for their operation. The manufacture of semiconductor wafers of larger diameter with improved flatness and reduced damage to the sub-surface could lead to improved product yields and reduced costs.

Optics: Together with electrolytic in-process dressing (ELID), revolutionary ductile-mode grinding processes can contribute to the elimination of polishing in high-quality optical system manufacturing. This is likely to be of particular importance for the manufacture of optics for extra-large astronomical telescopes, such as the planned 50m and 100m (Euro50 and OWL) systems, which will consist of a large number of individually measured segments (Shore et al 2003).

Transport: Precision-machined components can be more durable, requiring less new parts and less energy consumption due to decreased wear. For instance, by finishing to 10 nm average roughness followed by laser surface treatment, the ability to manufacture surfaces with managed textures is expected to lead to improved

power transmission trains with slip losses reduced by up to 50 percent. It is anticipated that precision manufacturing can lead to weight decreases in airframe wings and increase the performance of internal combustion chambers. Medical: it is hoped that the use of ultra-precision machining techniques to achieve improved surface finishes on prosthetic implants could lead to lower wear and better reliability. Advances in precision engineering are hoped to make it possible to reduce environmental impacts by, for example, reducing the use of lubricants. However, the whole life cycle needs to be considered for every product before it can be decided if there is a net environmental gain.

The Chemicals Industry

Within the chemical industry, the long-term objective is to use Nano scale 'building blocks' to assemble structured nanostructures, which can in turn be developed into products that are commercially useful. From an understanding of Nano scale materials chemistry and physics, and top-down/bottom-up modeling and calculation, industry can focus on processes that use Nano scale manufacturing in a way that maintains the desired effect and functions as components of the Nano scale are combined into materials and products of the macro scale. This will entail the creation of technologies based on self-assembling materials or, more likely, on guided-assembly methods which, together with modeling and measuring tools, allow for some sort of massively parallel production. The vision is the development of nanomaterial's which are reproducible, precise and designable.

The timescale for commercial exploitation of these types of highly ordered structures or quantum materials for use in the biotechnology and IT sectors is approximately 2020 and beyond. These products would be highly profitable, with production rates of 10-10,000 tons per year, more than \$1,000,000 per ton. It is anticipated that the price will remain relatively high because, while the nanomaterial will have the effect of adding value to consumer goods, it will only make up a small fraction of the final product sold.

By exploiting structure-property relationships, the desired functionality is created. For the characterization and subsequent control of property and functional performance and, therefore, the development of desirable materials, measurement, modeling and simulation are important. The production of Nano scale measurement tools would transition from laboratory-based characterization to in-line and on-line

6-sigma precision monitoring and control methods (99.9997 percent accurate) in terms of reproducible structure, texture and surface properties. The use of advanced structure-property-process predictor codes-based computer simulation will become the main manufacturing-by-design technology, where the material characteristics are essentially 'dialed up' by morphology, texture, structure and reactivity based on the interaction of materials across molecular and Nano-length scales. For economic, secure, and reproducible activity, the structure or shape of the material then determines the processing options. Intelligent material systems would be based on a mixture of calculation, modeling and manufacturing technologies. It is also hoped that the processing of materials with less waste would be feasible.

Synthesis and control of micro- and Nano-scale structures can give rise to unprecedented control of the properties of meso and macro-scale in functional materials for use in applications of direct industry relevance. It has been projected (Chemical Industry 2003) that a material revolution involving synthesis and smart manufacturing will meet many of the needs of trade and society over the course of the century.

The information and communication technology industry

While lithographic processes are still the subject of the future of device manufacturing, there are other methods that are increasingly being applied to both on-roadmap developments and alternative approaches to device materials. For several years, soft lithography techniques have been available when a versatile master is used to stamp out designs on a variety of surfaces. Up to now, the precision standards imposed by the silicon-based industry have banned the use of soft lithography because the elastic nature of the stamp can cause slight, but still undesirable, physical distortions across a wafer surface. Nevertheless, they provide a real alternative to traditional methods for small-area system manufacture and for applications where spatial tolerances are less restrictive, although the manufacture of the master still involves optical or electron beam methods. For plastic electronics, soft lithography can be used, as can alternative inkjet-based methods which use essentially the same technology as desk-top printers. While in terms of critical dimensions, plastic electronics are not truly in the Nano-range, a relatively simple manufacturing technique that can deal with wet chemistry would allow cheap electronic and photonic devices. Such innovations, coupled with advances in targeted self-assembly, will put the semiconductor, materials, and chemical

industries closer together, as the end of the roadmap approaches, to create novel alternative methods for chip production.

Resource Management and Environmental Issues

Several nanotechnology-based applications and processes have been claimed to offer environmental benefits by, for example, less production resources or increased energy efficiency in operation. By verifying that there are indeed net benefits over the life of the material or product, it is important to substantiate such statements. In terms of life cycle assessment (LCA) (sometimes referred to as 'cradle-to-grave' analysis), the possible advantages of nanotechnologies should be evaluated. LCA is the systematic study of resource uses (such as electricity, water, raw materials) and pollution from the 'cradle' of primary resources to the 'grave' of recycling or disposal through the entire supply chain. For example, in photovoltaic (PV) energy converters, one of the areas of application envisaged for nanomaterial is to improve performance. An LCA will explore the degree to which any additional energy used in the manufacture of the device and in the recovery or disposal of its material content at the end of its life would offset the additional energy yield over the service life of a PV device.

An example can be drawn from the potential use of nanotechnology in the transport sector to demonstrate the significance and the related difficulty of such analyses. Aircraft weight reduction is a predictable application, such as with the use of CNT composites and thinner (i.e. lighter) paints and coatings. Accessible LCA aircraft studies indicate that resource usage and environmental effects of aircraft in flight are actually many orders of magnitude greater than those of aircraft construction (Energy Technology Support Group 1992). Therefore, the first theory was that technical advances in 'light weighting' are often helpful. For Nano engineered materials where end-of-life disposal could have an adverse environmental effect, this claim will need to be checked. Also, to avoid drawing simplistically optimistic conclusions, the basis on which aircraft weight reduction is measured needs to be carefully established. In practice, decreases in aircraft weight are likely to be manipulated by raising payload, i.e. carrying more passengers, which would bring environmental advantages due to fewer flights if the demand were set. If this is used to minimize ticket prices, however, it could induce additional passenger movements, albeit using fuel per kilometer of passenger traveled. The true trade-off to be weighed is between the advantages of additional passenger

movements rather than the aircraft's environmental efficiency and the effects of Nano-engineered material production. The superficially simple environmental evaluation, therefore, ends up involving social and ethical problems.

Obstacles to Progress

There are several variables that will influence whether nanotechnologies in industrial processes will be used routinely. Some of these are social or economic, others are technological. In order to be accepted by industry, any new method or technology must be capable of exceeding (in terms of economic value) what is already in operation and must be of value (or perceived value) to the customer. The technology used in current industrial processes is, as we have learned in evidence from Don Eigler and others, already typically very advanced, and so nanotechnologies can only be used where the benefits are high. To moderate their rate of introduction, this economic reality should work well.

The technical barriers should not be underestimated: More fundamental obstacles emerge from a lack of understanding of Nano scale properties and the techniques to classify and engineer them to shape useful materials and generic technical steps for the development of a material with a designed functionality, as well as the difficulty in scaling a process from the laboratory to an industrial activity.

Responsible Development of Nanotechnologies

Nano science and nanotechnology have tremendous potential here. It is recognized that nanotechnologies and their applications can pose new challenges in the fields of protection, regulation or ethics, which, if they are to fulfill this potential, will require social debate. Many of the possible legal, social, health, financial, protection and regulatory impacts will be resolved by the adoption of our recommendations and will help ensure that nanotechnologies grow in a healthy and socially desirable manner. As part of the Government's obligation to the accountable development of nanotechnologies, between two and five years' time, we suggest that the Office of Science and Technology commission an independent committee to review what action has been taken on our recommendations and to examine how science and engineering have evolved in the meantime, and what ethical, social, health, financial, safety and regulatory consequences these developments might

have. This committee should include members of the related stakeholder groups, and should communicate with them. Its results should be open to the public. Academies would also track the application of these guidelines and will be able to take part in this study, of course.

Conclusion

In its broadest sense, nanotechnologies (semiconductors) have been used by companies for decades and, in some cases, considerably longer (chemicals). Nevertheless, advances in the instruments used to classify materials over the past 20 years have contributed to a greater understanding of the behavior and properties of matter on very small scales. Increased knowledge of the relationship between the structure and properties of nanomaterial has allowed higher performance and increased functionality of materials and devices to be developed. We have identified Nano science as the study of atomic, molecular, and macromolecular scale phenomena and material manipulation, where properties of matter vary significantly from those of a larger scale; and nanotechnology as the design, characterization, manufacture, and application of structures, devices, and systems via nanometer scale control of shape and size. We also referred to 'nanotechnologies' in the plural in the article, because the word 'nanotechnology' covers such a wide variety of instruments, techniques and possible applications.

References

1. Donaldson K, Stone V, Seaton A & MacNee W (2001). Ambient particle inhalation and the cardiovascular system: potential mechanisms. *Environmental Health Perspectives* 109 (suppl. 4), 523–527
2. Arnall A H (2003). *Future Technologies, Today's Choices: Nanotechnology, Artificial Intelligence and Robotics – A Technical, Political and Institutional Map of Emerging Technologies*. Greenpeace Environmental Trust: London
3. Borm P J A & Kreyling W (2004). Toxicological hazards of inhaled nanoparticles – potential implications for drug delivery. *Journal of Nanoscience and Nanotechnology*

4. DTI (2002). New dimensions for manufacturing: A UK strategy for Nanotechnology. Department of Trade and Industry: London, UK
5. HSE (2004). Information Note – Nanotechnology, Horizons scanning information note No. HSIN1
6. POST (2001). Open Channels: Public Dialogue in Science and Technology. Report 153. Parliamentary Office of Science and Technology: London
7. Borm P J A & Kreyling W (2004). Toxicological hazards of inhaled nanoparticles – potential implications for drug delivery. Journal of Nanoscience and Nanotechnology 4, 1–11

* * * * *

- ❖ **Bakula Keerthi Chandra**, OrionStr 6, 508, Unterschleißheim, Germany, **E-mail:** bakulachandra@gmail.com

A study of Nano structures-CQDs



- **Dr. Rohini V.S**
- **Nandini Y.V, Nayana J.**
- **Rachana J, Rajanish T.N**

Abstract :

CQDs are of at most importance in our daily life. They can be used for nano fibres in optical quantum communication, medical imaging, virus studies like corona virus, nano medicines etc. In this case study CQDs are prepared using natural resources.

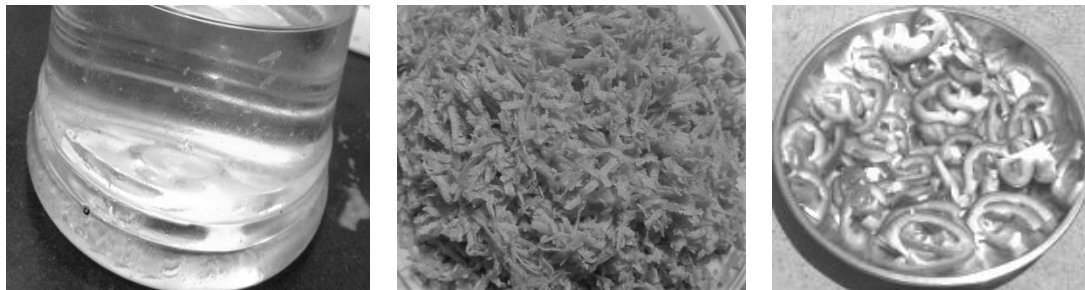
Keywords: CQD-carbon quantum dots, HCQD-hydraulic CQD

1. Introduction:

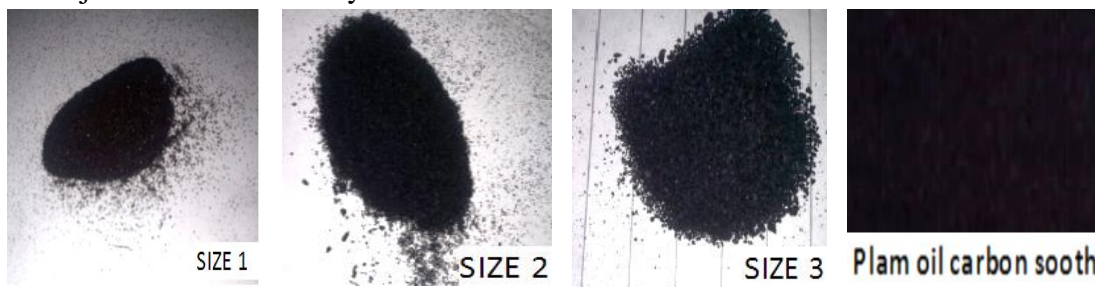
CQDs are of at most importance in our daily life. They can be used for many applications like nano optical quantum communication, virus studies like corona virus etc, nano medicines, bio imaging, quantum magnetism, stellar spectral analysis etc. **CQDs** are the transition stages of an element in nano scale between high density and low density state .They help to distinguish the states by forming contour at the point of localisation which can be identified by their twinkling nature. The carbon CQDs show enhanced green emission at 562nm. In this case study, CQDs are prepared from natural resources like vegetables and fruits like carrot, beetroot, watermelon, palm oil etc In the analysis HCQDs of the order **4500,1030,600 μm** are identified by 1st order magnification and **3.125, 7.152, 4.1667 nm** by 2nd order magnification. CQDs of the order **1400 μm and 0.9722 nm** were identified by 1st and 2nd order magnification method

2. Methodology:

2A. Green synthesis of CQDs



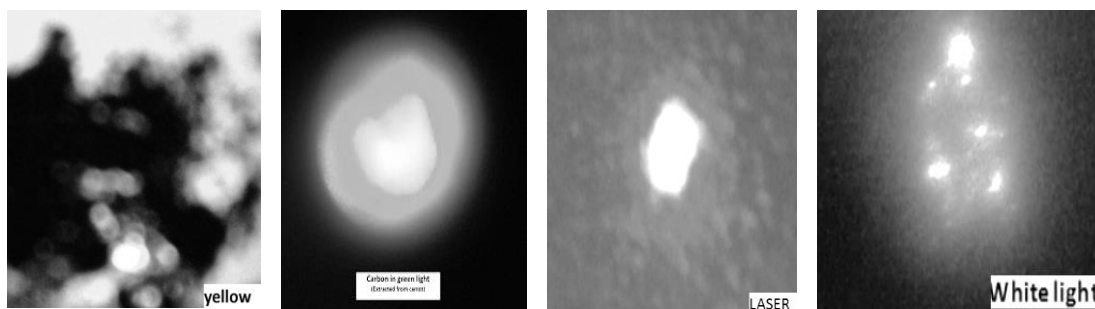
Raw materials like vegetables and fruits are chosen and subjected to physical processing like cutting, grinding, crushing etc followed by heat treatment (direct & indirect) - low degree to high degree which leads to carbonization. Carbon so obtained is in different allotropic forms like crystals, soot etc. Carbon so obtained is subjected to further analysis



Carbon powder (from carrot) of different sizes

1. Analysis of carbon sample:

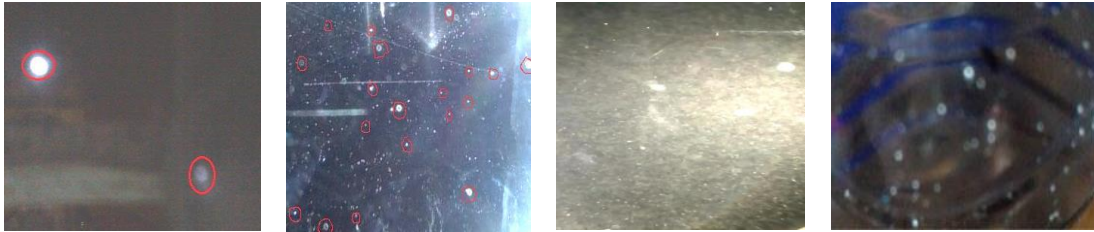
3A. analysis by light scattering



Enhanced green emission ,yellow green emission, laser induced red emission of the carbon sample is observed.

3B. Hydraulic analysis:

3Ba. Identification of HCQDs :When carbon samples so prepared is mixed with distilled water it is found that they form hydraulic carbon quantum dots(HCQD)

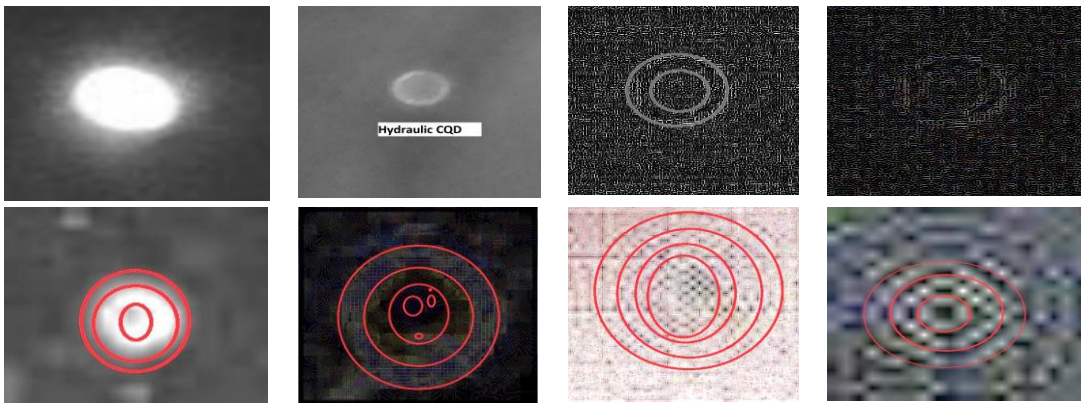


HCQDs in laser light

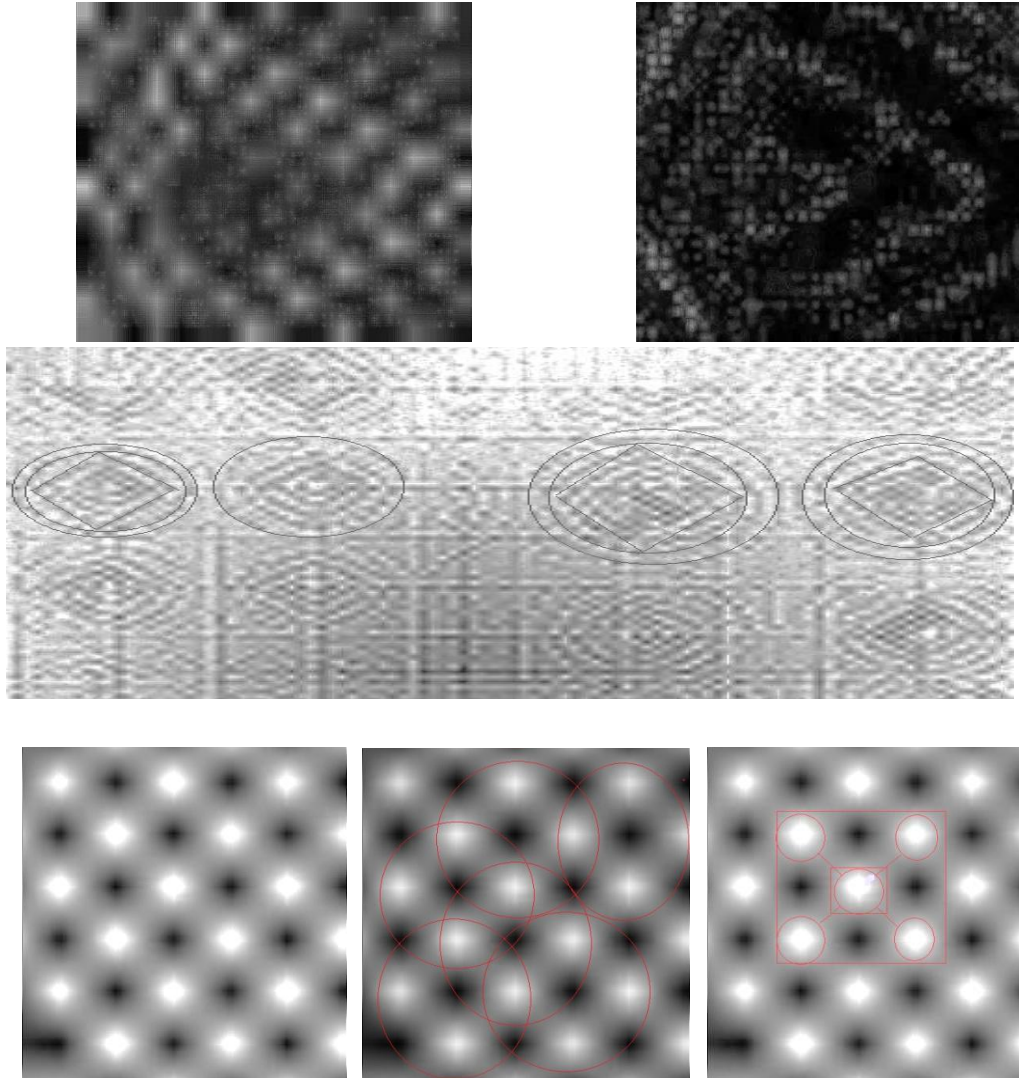


HCQDs in white light

3Bb. Structure of HCQDs:



3Bc: Single HCQD surface in higher resolution shows ring structures. Outer shells are spherical in nature, inner shells triclinic, inner most are rhombic in nature.

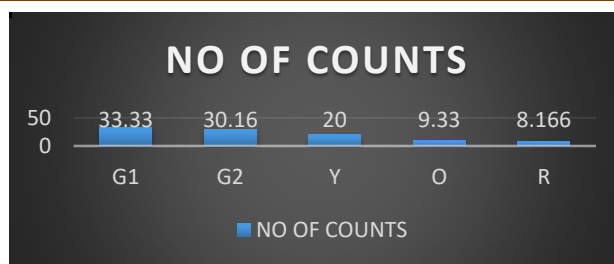


Inner most rings show simple cubic lattice arrangement with covalent sharing and coordination number as 4.

This refers that synthesised nanoparticles in “Diamond”allotropic form of carbon.

3Bd.Photo luminescence statistical analysis

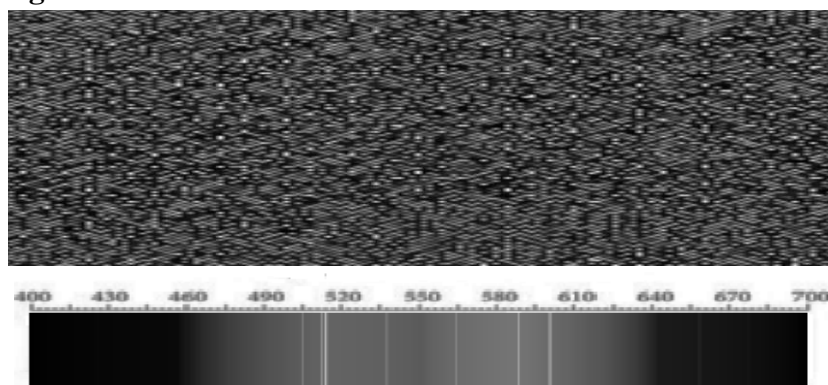
First magnification:



$$I_{G1} > I_{G2} > I_Y > I_O > I_R$$

The statistical analysis of multiwavelength images of CQDs shows maximum emission /absorption in green wavelength 565 nm

Second magnification:



Carbon spectrum(nm)

Maximum green emission by statistical survey is confirmed by very high resolution image of innermost part the core of CQDs

4. RESULT:

Thus CQDs and HCQDs are successfully prepared and their physical, structural, spectroscopic and statistical properties are studied.

5. CONCLUSION:

1. CQDs basically show triclinic structure, covalent bonding and coordination number 4.
2. Beer lambert's study shows maximum absorption wavelengths at 480 nm, 520nm which refers to violet and green wavelengths
3. These wavelengths matches with Raman lines, Fraunhofer lines of carbon

4. With available experimental facilities by HCQD method we were able to identify the HCQDs in **4500,1030,600 μm** ranges by first magnification method and **3.125, 7.152, 4.1667 nm** by second magnification method.
5. CQDs identified are of size **1400 μm** by first magnification method,**0.9722 nm** by second magnification method
6. The statistical analysis by first magnification method gives the spectral intensity distribution correlation of CQDs as $I_{G1} > I_{G2} > I_O > I_Y > I_R$,for green1(538nm),green2(562nm) , orange(601nm), yellow(589nm),red(658nm).
7. Percentage distribution as 51%,18%,14%,9%,8% for G1,G2,O,Y,R respectively
8. Second magnification shows CQDs,**0.0972nm** look **green** ie.absorption/emission in green **562nm**

References:

1. Carbon quantum dots from natural resource: A review Rashmita Das , Rajib Bandyopadhyay , Panchanan Pramanik <https://doi.org/10.1016/j.mtchem.2018.03.003> /2468-5194/© 2018 Elsevier Ltd. All rights reserved
2. Green synthesis of fluorescent carbon dots from carrot juice for in vitro cellular imaging Yang Liu¹ , Yanan Liu¹ , Mira Park², Soo-Jin Park³ , Yifan Zhang³ , Md Rashedunnabi Akanda⁴, Byung-Yong Park⁴ and Hak Yong Kim *Carbon Letters Vol. 21, 61-67 (2017)*/DOI: <http://dx.doi.org/10.5714/CL.2017.21.061>
3. Carbon quantum dots from natural resource: A review Rashmita Das , Rajib Bandyopadhyay , Panchanan Pramanik, *Materials Today Chemistry*© 2018 Elsevier Ltd. All rights reserved.
4. Aqueous Carbon Quantum Dot-Embedded PC60-PC61BM Nanospheres for Ecological Fluorescent Printing: Contrasting Fluorescence Resonance Energy-Transfer Signals between Watermelon-like and Random Morphologies-Yu Jin Kim,Peijun Guo Richard D. Schaller/October 9, 2019/<https://doi.org/10.1021/acs.jpcl.9b02426/> Copyright © 2019 American Chemical Society

* * * * *

❖ **Dr. Rohini V.S., Nandini Y.V., Nayana J., Rachana J., Rajanish T.N,** Nrupatunga University (Govt. Science College), N. T. road, Bangalore-560001, Karnataka, India, **Ph:** 9731349295, E-mail: neelarohini@gmail.com

A study of Nano structures-CQDs



- **Dr. Rohini V.S**
- **Nandini Y.V, Nayana J.**
- **Rachana J, Rajanish T.N**

Abstract :

CQDs are of at most importance in our daily life. They can be used for nano fibres in optical quantum communication, medical imaging, virus studies like corona virus, nano medicines etc. In this case study CQDs are prepared using natural resources.

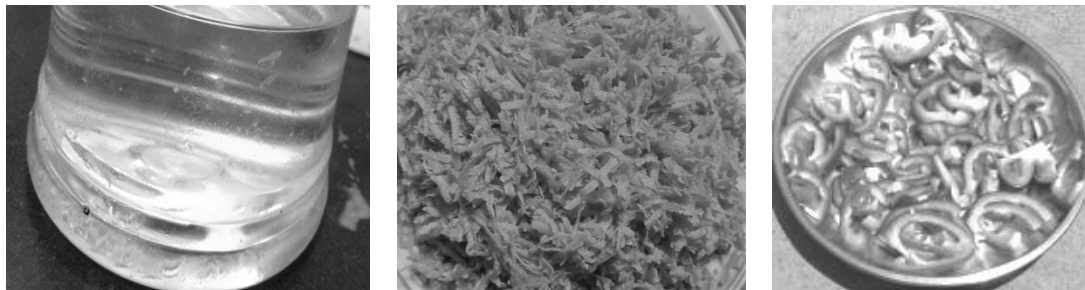
Keywords: CQD-carbon quantum dots, HCQD-hydraulic CQD

1. Introduction:

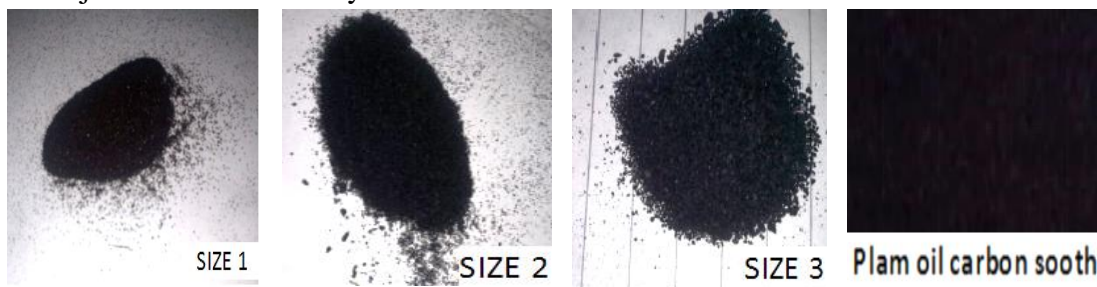
CQDs are of at most importance in our daily life. They can be used for many applications like nano optical quantum communication, virus studies like corona virus etc, nano medicines, bio imaging, quantum magnetism, stellar spectral analysis etc. **CQDs** are the transition stages of an element in nano scale between high density and low density state .They help to distinguish the states by forming contour at the point of localisation which can be identified by their twinkling nature. The carbon CQDs show enhanced green emission at 562nm. In this case study, CQDs are prepared from natural resources like vegetables and fruits like carrot, beetroot, watermelon, palm oil etc In the analysis HCQDs of the order **4500,1030,600 μm** are identified by 1st order magnification and **3.125, 7.152, 4.1667 nm** by 2nd order magnification. CQDs of the order **1400 μm and 0.9722 nm** were identified by 1st and 2nd order magnification method

2. Methodology:

2A. Green synthesis of CQDs



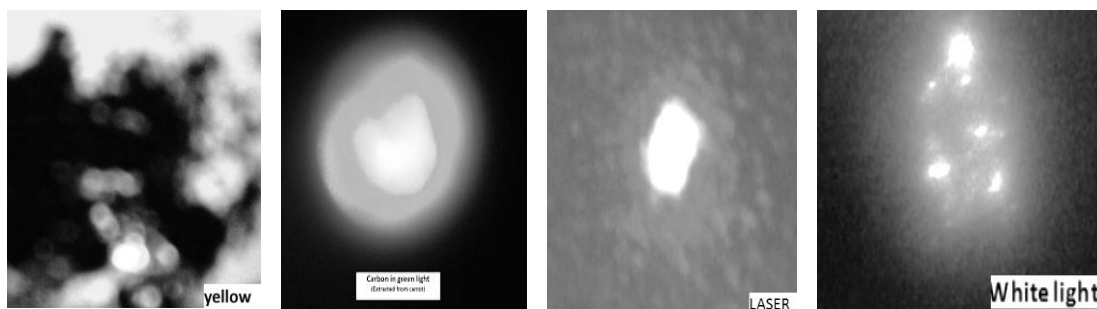
Raw materials like vegetables and fruits are chosen and subjected to physical processing like cutting, grinding, crushing etc followed by heat treatment (direct & indirect) - low degree to high degree which leads to carbonization. Carbon so obtained is in different allotropic forms like crystals, soot etc. Carbon so obtained is subjected to further analysis



Carbon powder (from carrot) of different sizes

1. Analysis of carbon sample:

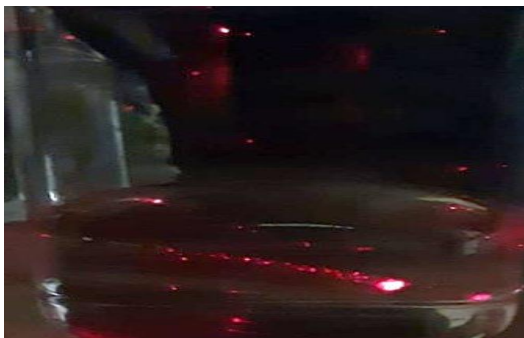
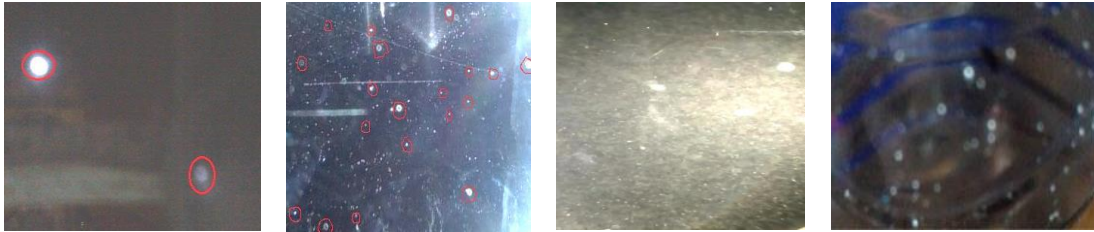
3A. analysis by light scattering



Enhanced green emission ,yellow green emission, laser induced red emission of the carbon sample is observed.

3B. Hydraulic analysis:

3Ba. Identification of HCQDs :When carbon samples so prepared is mixed with distilled water it is found that they form hydraulic carbon quantum dots(HCQD)

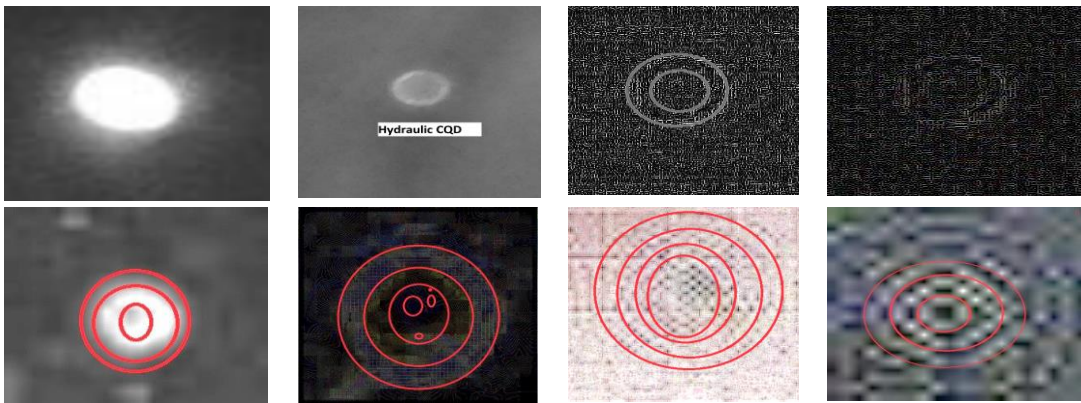


HCQDs in laser light

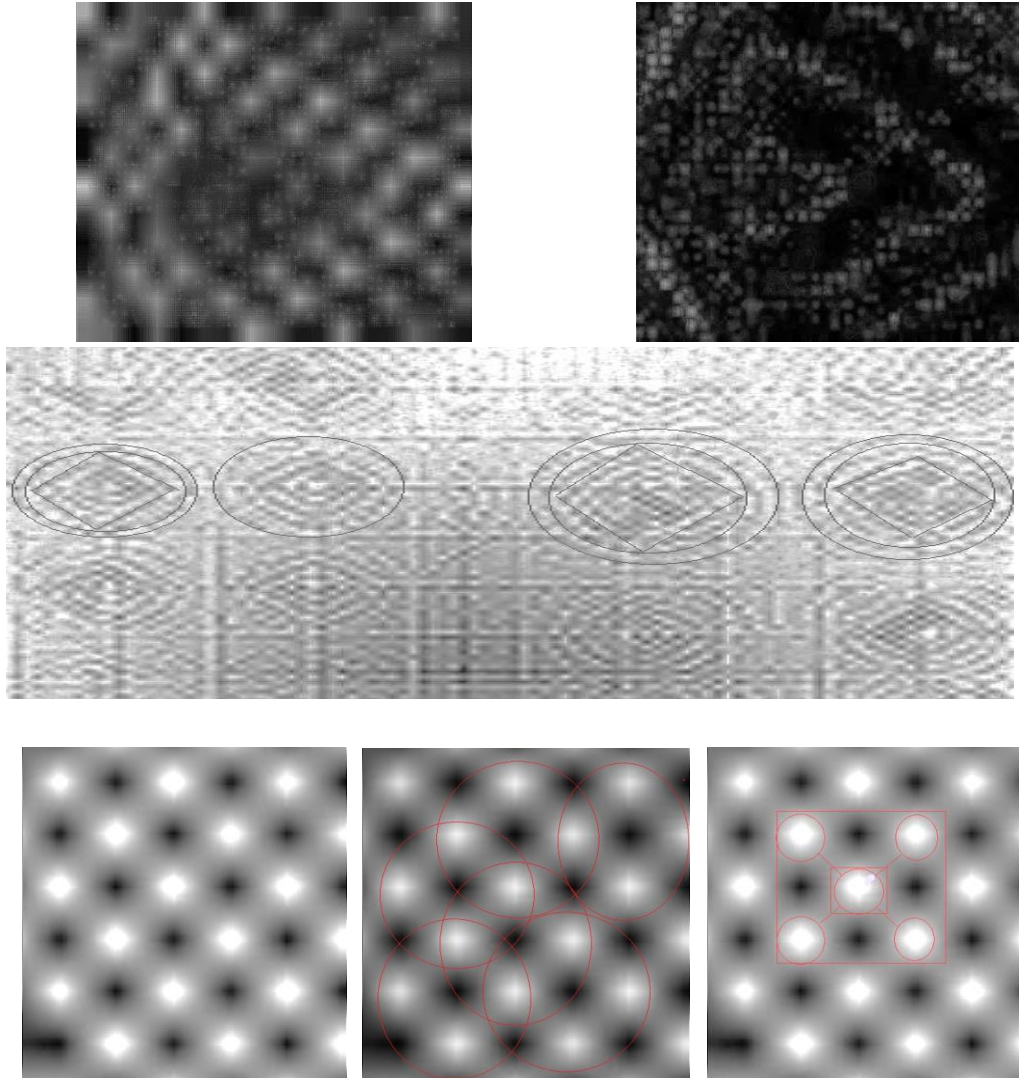


HCQDs in white light

3Bb. Structure of HCQDs:



3Bc: Single HCQD surface in higher resolution shows ring structures. Outer shells are spherical in nature, inner shells triclinic, inner most are rhombic in nature.

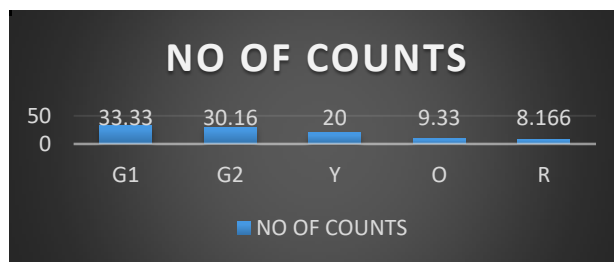


Inner most rings show simple cubic lattice arrangement with covalent sharing and coordination number as 4.

This refers that synthesised nanoparticles in “Diamond”allotropic form of carbon.

3Bd.Photo luminescence statistical analysis

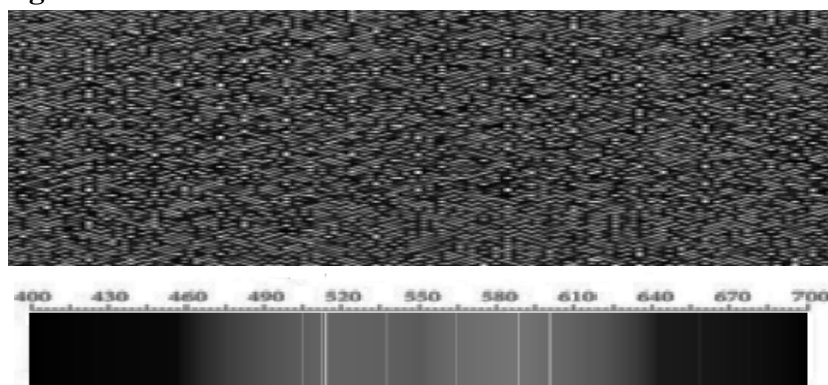
First magnification:



$$I_{G1} > I_{G2} > I_Y > I_O > I_R$$

The statistical analysis of multiwavelength images of CQDs shows maximum emission /absorption in green wavelength 565 nm

Second magnification:



Carbon spectrum(nm)

Maximum green emission by statistical survey is confirmed by very high resolution image of innermost part the core of CQDs

4. RESULT:

Thus CQDs and HCQDs are successfully prepared and their physical, structural, spectroscopic and statistical properties are studied.

5. CONCLUSION:

1. CQDs basically show triclinic structure, covalent bonding and coordination number 4.
2. Beer lambert's study shows maximum absorption wavelengths at 480 nm, 520nm which refers to violet and green wavelengths
3. These wavelengths matches with Raman lines, Fraunhofer lines of carbon

4. With available experimental facilities by HCQD method we were able to identify the HCQDs in **4500,1030,600 μm** ranges by first magnification method and **3.125, 7.152, 4.1667 nm** by second magnification method.
5. CQDs identified are of size **1400 μm** by first magnification method,**0.9722 nm** by second magnification method
6. The statistical analysis by first magnification method gives the spectral intensity distribution correlation of CQDs as $I_{G1} > I_{G2} > I_O > I_Y > I_R$,for green1(538nm),green2(562nm) , orange(601nm), yellow(589nm),red(658nm).
7. Percentage distribution as 51%,18%,14%,9%,8% for G1,G2,O,Y,R respectively
8. Second magnification shows CQDs,**0.0972nm** look **green** ie.absorption/emission in green **562nm**

References:

1. Carbon quantum dots from natural resource: A review Rashmita Das , Rajib Bandyopadhyay , Panchanan Pramanik <https://doi.org/10.1016/j.mtchem.2018.03.003> /2468-5194/© 2018 Elsevier Ltd. All rights reserved
2. Green synthesis of fluorescent carbon dots from carrot juice for in vitro cellular imaging Yang Liu¹ , Yanan Liu¹ , Mira Park², Soo-Jin Park³ , Yifan Zhang³ , Md Rashedunnabi Akanda⁴, Byung-Yong Park⁴ and Hak Yong Kim *Carbon Letters Vol. 21, 61-67 (2017)*/DOI: <http://dx.doi.org/10.5714/CL.2017.21.061>
3. Carbon quantum dots from natural resource: A review Rashmita Das , Rajib Bandyopadhyay , Panchanan Pramanik, *Materials Today Chemistry*© 2018 Elsevier Ltd. All rights reserved.
4. Aqueous Carbon Quantum Dot-Embedded PC60-PC61BM Nanospheres for Ecological Fluorescent Printing: Contrasting Fluorescence Resonance Energy-Transfer Signals between Watermelon-like and Random Morphologies-Yu Jin Kim,Peijun Guo Richard D. Schaller/October 9, 2019/<https://doi.org/10.1021/acs.jpcl.9b02426/> Copyright © 2019 American Chemical Society

* * * * *

❖ **Dr. Rohini V.S., Nandini Y.V., Nayana J., Rachana J., Rajanish T.N,** Nrupatunga University (Govt. Science College), N. T. road, Bangalore-560001, Karnataka, India, **Ph:** 9731349295, E-mail: neelarohini@gmail.com

A Review on Synthesis of Carbon Nanotubes and Its Applications



- M. Thavarani
- N. Abinaya

Abstract

Nanotechnology is one of the comprehensive research components and is a new and advanced technology that has been developed. The market for nanoparticles is 10^{-9} or 10\AA and the scope of the particle is 1000\AA . Nano particles have 106 atoms or fewer, their stuff differs from that of the equal joined atoms that are collected to make up most of the constituents. Carbon nanotubes are carbon rock with a nanostructure that can have a quotient length-to-diameter of over 1,000,000. The three key methods of processing carbon nanotubes are discussed. CNT technologies were evaluated for bio-medical applications, energy storage, catalyst support, and conductive plastics. Present development is calculated in relation to CNT arrangements, mixtures and their implementations with respect to the available types.

1. Introduction:

The forefront of contemporary research is Nano science and nanotechnology. It is the study of ultra-small-scale structures and materials. They come from a variety of disciplines, including chemistry, physics, biology, medicine, computer science, materials science, and engineering. The creation of such alliances and teams of theorists should be encouraged by a new investment in theory, modelling and simulation in Nano science. It deals with a range of materials developed by various chemical and physical methods at a nanometre scale. The properties of carbon nanotubes and their clinical applications, such as medical diagnostics and the delivery of drugs, are discussed in this study. The antibacterial and antifungal function of carbon nanotubes is also being studied here. From the mentioned search

word, "carbon nanotubes", the total number of papers containing the CNT definition is 52,224, with a patent/paper ratio of 0.11 for patents being 5,746.' Up to 2012.

2. CARBON NANOTUBES

Three groups of single-walled carbon nanotubes (SWNT), double-walled carbon nanotubes (DWNT), and multi-walled carbon nanotubes can be grouped into CNTs (MWNT).

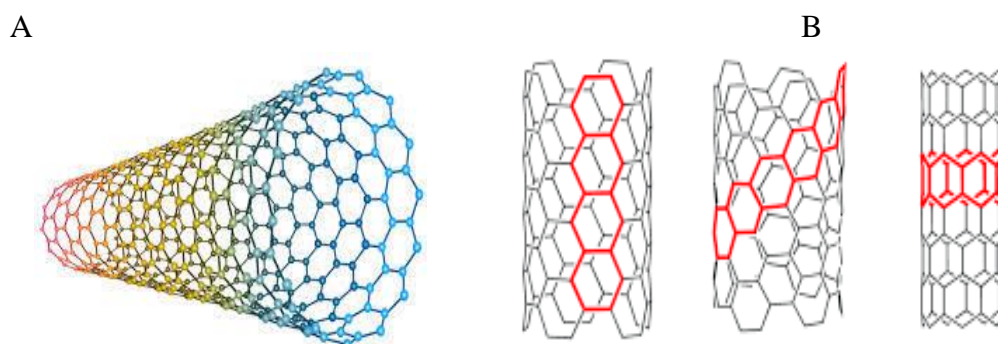


Fig 1(A) Single walled carbon nanotube and (B) Armchair, Chiral and Zigzag forms of single walled carbon nanotube.

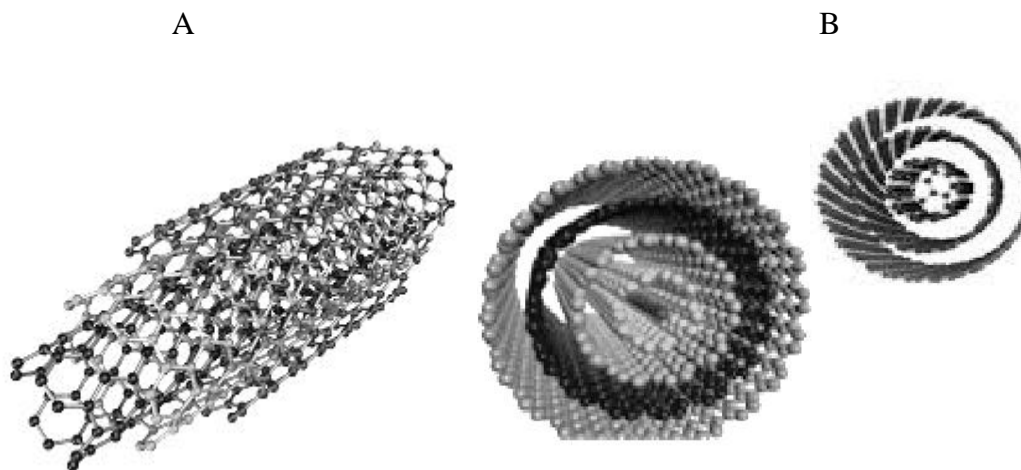


Fig 2: (A) Multi-walled carbon nanotubes and (B) Russian doll model and Parchment model forms of multi-walled carbon nanotubes

Single-walled carbon nanotubes

One of the carbon allotropes is single walled carbon nanotubes. And it is the fullerene and graphene intermediate structure. Three different forms of SWNT can be formed: Armchair, Chiral, and Zigzag.

Multi-walled carbon nanotubes

Elongated cylindrical Nano objects made of sp^3 carbon are multi-walled carbon nanotubes. Two types of MWNT were formed: the Russian doll model and the Parchment model

3. CNT Properties:

Carbon nanotubes have different characteristics, such as high elasticity, high thermal conductivity, low density and chemical inertia, etc. Carbon nanotubes have played an important role in the area of nanotechnology, electronics and other areas of materials science because of these fascinating properties. Carbon nanotubes are used favourably in the delivery of drugs, sensitivity, the handling of water etc. Their surface functionalization can lead to highly soluble materials that can be further extracted from active molecules, making them compatible with the biological system. Surface functionalization allows different molecules or antigens to be adsorbed or attached, which can then be targeted to the appropriate cell population for immune recognition or a therapeutic effect. CNT's are really strong heat conductors. Their thermal conductivity is twice as high as diamond conductivity. The heat conductivity varies with direction as well. The conductivity along the axis of the tube is very strong. At low density, CNT's have a very high strength to weight ratio. Based on their diameter and chirality, the electrical properties of carbon nanotubes. CNT bears much greater currents than metals because of its very low resistivity. With the increased magnetic field applied across the CNT, the resistance decreases at low temperatures. This effect is called resistance to magneto.

4. Morphology and Structure:

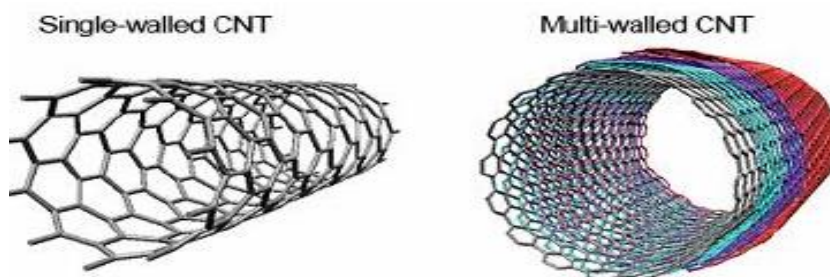


Fig 3: Single-walled carbon nanotube and multi-walled carbon nanotube structure

CNT is one of the normally measured carbons with a nanometre diameter. Carbon Nanotubes are carbon allotropes in which SP² is a hybridized state of the carbon atom. Its diameter ranges between 2 nm and 55 nm, and its length is about several microns. The single wall carbon nanotube is characterized by a vector called the Chiral vector, which depends on the chiral indices (n₁, n₂) and chiral angle. SWCNT may be Zig Zag (almost = 0), Arm Chair (almost = 30) and Chiral (0 < almost < 30). Using this structure, CNT can exhibit metallic or semiconducting properties. A SWCNT is one of the carbon allotropes. It has a diameter of about 1 nanometre with a tube length that could be several million times longer. A single graphite-atom-thick layer called graphene can be hypothesized by unfolding up the SWNT. Multi-walled nanotubes (MWNTs) consist of several layers of graphene rolled or a single sheet of graphene rolled across, known as the parchment model. It has an interlayer distance of around 3.4

5. Synthesis with CNT:

Three key techniques are commonly used to manufacture carbon nanotubes (CNT): ARC discharge, laser ablation, chemical vapour deposition (CVD), and catalyst chemical vapour deposition (CCVD). Laser ablation generates a small amount of clean nanotubes at the moment, whereas arc discharge techniques typically create large amounts of impure material.

5.1 CVD (Method of chemical vapour deposition):

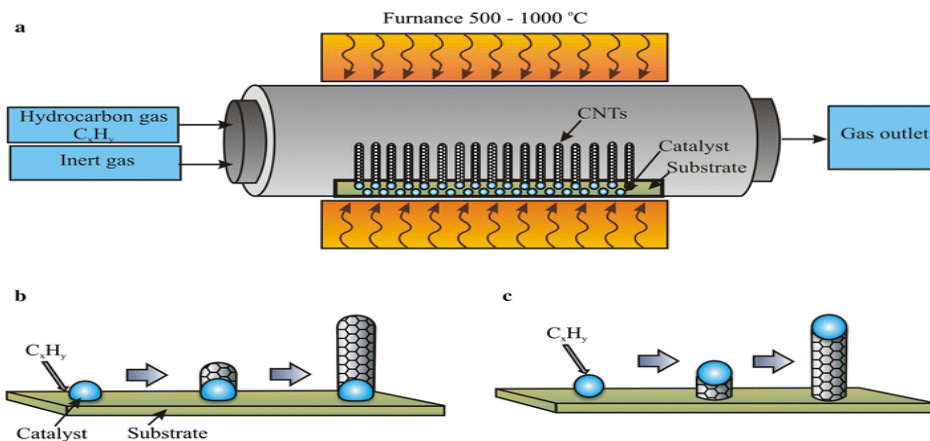


Fig 4: Method for chemical vapour deposition

The most widely used thin-film admittance process used to synthesize CNTs is CVD. The CVD approach for the production of CNTs has the reward of a cheaper and more practical high-yield nanotube process for laboratory requests . It may also be manufactured in other ways, including reducing stable oxide or oxide solutions. The diameters of the nanotubes to be grown are aligned with the size of the particles of the metal. This can be regulated by patterned, annealing, or plasma etching of a metal sheet. The layer is heated to approximately 700 °C. By regulating their orientation, weight, wall number and diameter, this method has the advantage of generating CNTs with the desired structure. Generally, the low-cost method for the processing of CNTs is known to be CVD.

5.2 CCVD (Deposition of Catalytic Chemical Vapours):

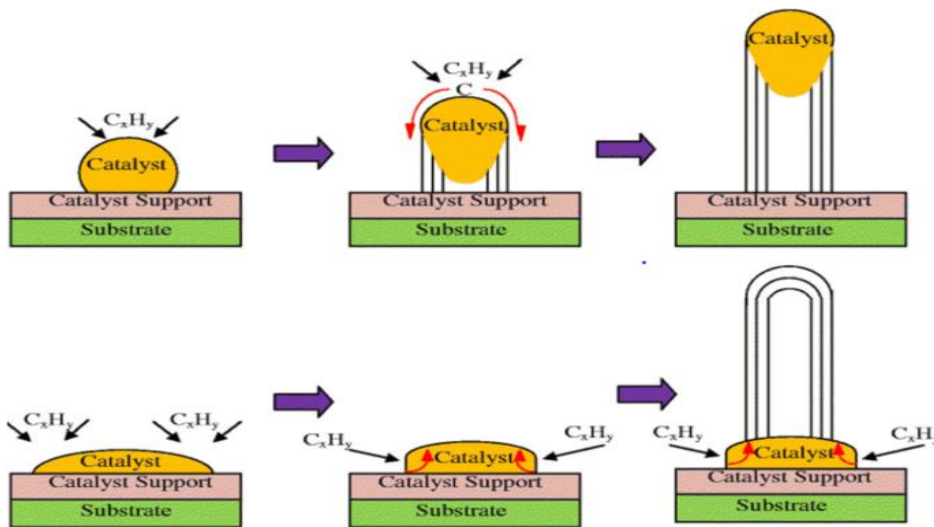


Fig 5: The mechanism of tip-growth is due to poor interactions between catalysts and substrates.

It is considered the most appropriate method for the large-scale and low-cost production of MWNTs. Although its theory is clear, the precisely regulated growth of carbon nanotubes remains very complex because the growth mechanism is affected by several different parameters. An early study by Kumar et al. (2002) [6] defines carbon nanotubes from camphor by the CCVD process. In a research, Hussein and Tallish (2010) reported MWNT growth on an iron-sprayed catalyst using the CCVD method under atmospheric pressure [6].

5.3 Ablation of Laser

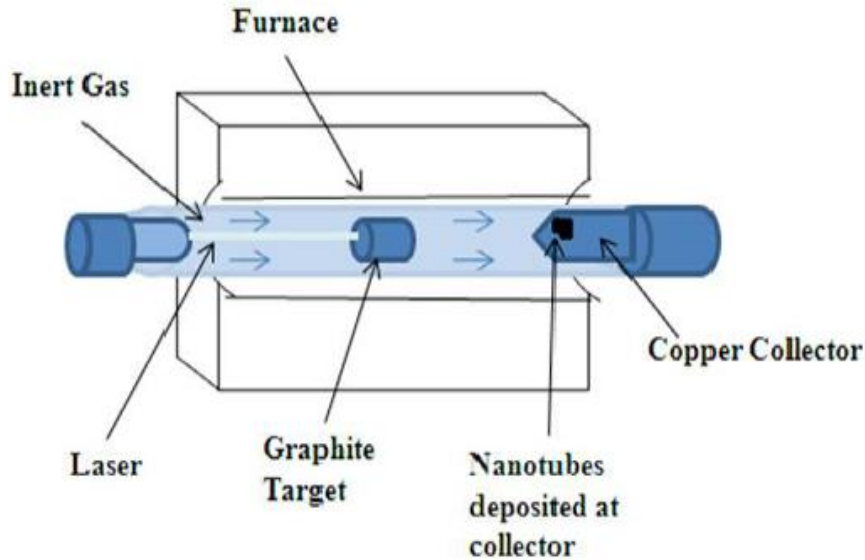


Fig 6: Setup with laser ablation for CNT synthesis

The method of extracting material from a solid (or rarely liquid) surface by irradiating it with a laser beam is laser ablation or photo ablation. The material is heated at low laser flux by the absorbed laser energy and evaporates or sublimates. The substance is usually transformed to plasma at high laser flux. Laser ablation usually refers to removing material with a pulsed laser, but if the laser intensity is high enough, it is possible to ablate material with a continuous wave laser beam. Deep ultra-violet light exciter lasers are predominantly used in photo ablation; the laser wavelength used in photo ablation is approximately 200 nm.

6. Applications from CNT:

The carbon nanotube has found a wide variety of applications as a new miracle material. CNTs are a promising way to extend their use in the biological industry, opening the way for biomaterials to be widely incorporated. CNTs can identify cancer-related molecules easily and sensitively, allowing scientists to detect molecular changes even though they only occur in a small percentage of cells. [7] Antitumor immunotherapy based on .CNT has also been investigated. This approach uses tumour cell vaccines (TCV) made of inactivated cancer cells or tumour antigen presenting dendritic cells to stimulate the patient's immune response

to the tumour itself [7]. By disrupting CA 2+ homeostasis, both single-walled carbon nanotubes (SWCNTs) and multi-walled carbon nanotubes (MWCNTs) were found to induce platelet activation[8,9], an effect that was hypothesized to be induced by the interaction of CNT with plasma and dense tubular system membranes possibly associated with the fibrous shape[8]. CNT has been studied for the growth of a number of tissues or organs, such as bone regeneration, neuron regeneration, in vitro and in vivo delivery of genes. The sienna transmitted via CNT has significantly inhibited tumour growth. CNTs are used to build lightweight materials that are stronger than steel. It can be used as a sensor to detect gases in automotive, aircraft and rocket components .[8]

7. Perspectives for the future:

The analysis highlights the best approach for CNT's synthesis. It is used in various medical fields, such as treatment of cancer, activation of platelets, and regeneration of tissue. Upcoming studies should focus mainly on generating high solubility non-toxic CNTs and extending their efficiency in the biomedical field. In the future, for weight sensitive applications such as Kevlar, CNT's will compete with carbon fibre.

Conclusion:

Due to its durable structure and metallic/ semiconducting properties, the application of CNT in different fields makes it one of the promising materials in nanotechnology. Due to strong synergies between theoreticians and experimentalists, nanotechnology has evolved rapidly as a discipline. CVD is one of the most promising techniques for producing large quantities of CNTs according to various modified synthesis methods. The characteristics of CNTs and their possible use in a wide range of applications and emerging materials that play a significant role in applications on the nano scale. Emerging applications such as sensors, field effect devices, energy storage devices, biological applications, and industrial applications based on their specific properties such as high mechanical power, high surface area, etc., thermal and electrical conductivity. CNT works to deliver bio molecules such as antibiotics, DNA, RNA, proteins, etc. Antimicrobial activity can also be exhibited. Some CNT's can be used as biosensors.

References

1. http://scholar.google.co.in/scholar_url?url=http://www.academia.edu/download/63038289/Introduction_to_Nanotechnology_Poole_Owens20200421-112720-13xi6qd.pdf&hl=en&sa=X&ei=CK_yX9qdG46CywSvq6boBA&scisig=AAGBfm2r-t5V3XkXF-hvzhzULPqALgVhGg&nossl=1&oi=scholar
2. <https://www.cheaptubes.com/privacy-cookie-policy/>
3. <https://www.sciencedirect.com/science/article/pii/S1026309812002477> \l
"br000005
4. <https://images.app.goo.gl/PNbU68z4kw7cynHi6>
5. M. Kumar, X. Zhao, Y. Ando, S. Iijima, M. Sharon, K. Hirahara Carbon nanotubes from camphor by catalytic CVD Molecular Crystals and Liquid Crystals, 387 (1) (2002), pp. 117-121
6. A.A. Hosseini, F. Taleshi Large diameter MWNTs growth on iron-sprayed catalyst by CCVD method under atmospheric pressure, Indian Journal of Physics, 84 (7) (2010), pp. 789-794
7. https://www.researchgate.net/profile/Hanene_Ali-Boucetta2/publication/221716567_Targeting_Carbon_Nanotubes_Against_Cancer/links/0c960517e7b81a6ce0000000/Targeting-Carbon-Nanotubes-Against-Cancer.pdf
8. De Paoli Laced S. H.; Semberova J.; Holada K.; Simakova O.; Hudson S. D.; Simak J. ACS Nano 2011, 5(7), 5808–5813. doi:10.1021/nn2015369

* * * * *

- ❖ **M. Thavarani, N. Abinaya**, Department of physics, Sri adi Chunchanagiri women's college, Cumbum- 625516, Tamilnadu State, **Ph:** 09789609825, **E-mail:** thavarani2009@gmail.com

High Energy Electron Beam Irradiation Effects on Ultra High Molecular Weight Polyethylene (UHMWPE)



- Dr. Ashok G. V
- Dr. Shiva Prasad N. G
- Dr. Niranjana Prabhu.T
- Dr. Harish .V

Abstract

High energy electron beam irradiation of polymers has been used widely as an advanced tool in polymer processing either for enhancement of polymerization or to understand polymer degradation routes. In this paper, irradiation effects of high energy electron beam of energy 1.5MeV and 10MeV at dose rates of 0, 15, 30, 50 and 100MRad on structural parameters of Ultrahigh Molecular Weight Poly Ethylene (UHMWPE) have been presented. Upon irradiation, no visible colour changes were observed but UHMWPE was observed to become more brittle and cracks were developed at higher radiation dose. The peak modifications observed in FTIR spectra gives the evidence of the chemical changes occurring in UHMWPE due electron irradiation. X-ray diffractographs indicate structural degradation in terms decreased crystallinity. Changes in absorbance of UV-Visible radiation in the polymer due electron irradiation. AFM images indicate smoothening of surface roughness at low doses of irradiation. But at higher doses, due to increased brittleness & degradation, surface roughness increases. This paper presents only brief and approximate details obtained from a non rigorous treatment of the data obtained from various experiments.

Keywords:

Irradiation effects, Electron beam, Ultrahigh Molecular Weight Poly Ethylene, UHMWPE

Introduction:

High energy radiation induced effects in polymers is an important subject of research for many reasons. In a negative sense, Polymers are inevitably exposed to radiation during their service in many forms at nuclear installations, aerospace applications and even during sterilization of medical plastics where any degradation is critical. In a more positive sense, polymer degradation by radiation forms the basis of most of the modern lithographic techniques used in electronic devices.

Polymers, as giant organic molecules with their sophisticated structure represent one of the most organized type of materials, leading up to the functions of life. No wonder if these macromolecules are sensitive against excessive energy transfer. The extremely long molecular chains can be broken easily receiving a quantum of energy above a certain level, causing degradation in structure and properties. The minimum energy required to open the covalent bond of the main carbon chain is in the range of 5 – 10 eV. Consequently the energy of beta and gamma photons of 1 to 10 MeV surpasses by many orders of magnitude this minimum value, representing a high risk of degradation to all kind of polymers, naturals and synthetics alike. In spite of the big difference in energetic level, the degradation caused by ionizing radiation, or UV light, and other lower energies of radiation – is not differing in basic principles [1]. The immediate consequence of high energy irradiation is the formation of a range of energetic species including trapped electrons, ions and free radicals. Decay of these excited species usually results in fragmentation to give free radicals. Indeed, high energy irradiation is an excellent means of initiating oxidation due to involvement of free radicals and their reactivity with oxygen. Since oxidation can lead to both cross linking and chain scission depending on the type of polymer and radiation dose, the effects are quite complex. High rate of irradiation can result in oxygen being depleted in the polymer faster than it can be replaced by diffusion. This leads to dose rate dependent behavior.

Several researchers have carried out detailed research work on radiation induced effects in several classes of polymers by exposing them to both low and high energy radiations such as gamma rays, electron, proton, neutron and ion beams. D C Waterman and Malcolm Dole (1970) have shown that alkyl free radicals which persist at room temperature after an electron beam irradiation (Energy 1MeV, a maximum dose of 108MRad) at liquid nitrogen temperature quantitatively convert to allyl free radicals by reaction with trans-vinylene or vinyl double bonds, The decay

of the alkyl radicals was accurately first order and markedly catalyzed by molecular hydrogen[2]. L Costa and et al., (2008) have presented the results of electron irradiation (energy 10MeV, doses ranging from 0.5 to 10MRad) effects in UHMWPE irradiated in vacuum, air or pure oxygen. They have proposed an alternative oxidation mechanism, including the simultaneous formation of hydroperoxides and ketones [3]. A.M. Abdul-Kader and et al., (2009) have shown the change in the surface free energy of ultra-high molecular weight polyethylene (UHMWPE) samples, which was produced by electron beam (and also gamma) irradiation of energy 600KeV and doses ranging from 2.5MRad to 50MRad[4] . A Turos and et al., have reported the effect of electron, ion beams and gamma-rays on UHMWPE irradiated with 600 keV and 1.5 MeV electron beam with doses ranging from 50 to 500 kGy and bombarded with 1–10 MeV He- and 9 MeV Cl-ions to fluences ranging from 10^{12} to 5×10^{16} ions/cm²[5]. R D Mathad and et al., (2010) have carried out post-irradiation studies to elucidate the effects of electron beam irradiation (Energy 1.3MeV, a maximum dose of 36MRad) on the structural, optical, dielectric and thermal properties of ultra-high-molecular weight polyethylene (UHMWPE) films[6]. Krystyna Czaja and Marek Sudol (2011) have shown the separated and combined electron-beam irradiation (doses of 2.6 & 5.2MRad) and plastic deformation effects on the structures of ultra-high molecular weight polyethylene (UHMWPE) [7,8].

Hence in this research work, an attempt has been made to throw some light on high energy electron beam irradiation effects in commercially important polymers as well as novel materials used in radiation research such as Ultrahigh Molecular Weight Poly Ethylene (UHMWPE). Additional objective of this work is to find routes for degradation this polymer after their use. Hence understanding the radiation induced effects in various materials is always a topic of special interest in research community.

Materials and Methods:

Ultra-high-molecular weight polyethylene (UHMWPE) is a high performance thermoplastic polymer having outstanding abrasion resistance in combination with excellent impact and chemical resistance. It has been an important material in electrical industries, shipbuilding, textile industries and even in biomedical usage. Samples for investigation were prepared as thin films (analytical grade) of about 0.2mm thickness using hot press method in a compression mould

machine. Films were then cut into strips of dimension $1 \times 5 \text{cm}^2$ and fastened onto glass slides for support.

Electron beam Irradiation: The samples thus prepared have been irradiated with high energy electron beams from ILU-6 (LINAC) facility at BRIT, Vashi campus (1.5 MeV beam) and Electron beam center facility at Khargar campus (10MeV) of BARC, Mumbai for doses of 0, 15, 30, 50 and 100Mrads at a dose rate of 1.5MRad per minute.

Post irradiation investigations: In order to understand the radiation induced changes in the polymers, irradiated samples are subjected to analysis using Atomic Force Microscope, Fourier Transform Infrared Spectrophotometer, X-Ray Diffractometer and Ultraviolet-Visible Spectrophotometer.

Atomic Force Microscope: NT-MDT, Model SPM Solver P47 was used to understand the topography of the polymer film surfaces. The surfaces of dimension $16 \times 16 \mu\text{m}^2$, $8 \times 8 \mu\text{m}^2$ and $3.5 \times 3.5 \mu\text{m}^2$ were scanned at least at three different locations and the average & r.m.s values of surface roughness were evaluated using an inbuilt program.

Fourier Transform Infrared Spectrophotometer: IRAffinity-1, a supplied by Shimadzu Corporation, Japan was used from wave number 400 to 4500cm^{-1} at a resolution of 4cm^{-1} . The data were recorded and processed in IR-Solution software.

Powder X-ray Diffractometer: From the grazing angle 10° to 60° at a resolution of 0.02° and at a scan speed of 5°min^{-1} . The data were processed and the values such as crystallite size (using scherrer's equation from FWHM values of the peaks) and absolute crystallinity (using manjunath's equation-by considering the resolution of diffraction peaks and Rabek's equation-by considering the ratio of area under crystalline peak to total area under the curve) were determined.

UV-Vis Spectrophotometer: Jasco, V-650 Spectrophotometer was used from wavelength 200 to 900nm at a resolution of 1nm and at a scan speed of 400nm/min. The data were collected using spectra manager version 2 and analyzed using an inbuilt spectrum analyzer.

Results and Discussion:

This part of the paper presents high energy electron irradiation induced effects on the polymers considered UHMWPE and dependence of effects on the

irradiation dose. The following discussion presents only approximate details obtained from a non-rigorous treatment of the data obtained from various experiments. The general changes those observed with a naked eye before and after irradiation in the polymers the have been recorded in the table 1.

| Table 1. | | |
|-----------------|------------------------------|--|
| Polymer | Radiation dose (MRad) | Observed features |
| UHMWPE | 0 | Whitish, Transparent, soft & flexible. |
| | 15 | No colour change, a bit opaque & brittle |
| | 30 | No colour change, a bit opaque & brittle |
| | 50 | No colour change, quite opaque & brittle |
| | 100 | No colour change, more opaque & brittle |

High energy radiation can induce structural & chemical changes in polymers and infrared absorption (FT-IR) spectroscopy is one of the techniques useful for the study of such changes occurred in polymers. FT-IR spectra of the unirradiated and the irradiated UHMWPE samples has been shown in figures 1. The peak modifications observed at wave number 908, 966, 1303 & 1716 cm^{-1} as shown in fig 1, give the evidence of the changes occurring in UHMWPE due electron irradiation.

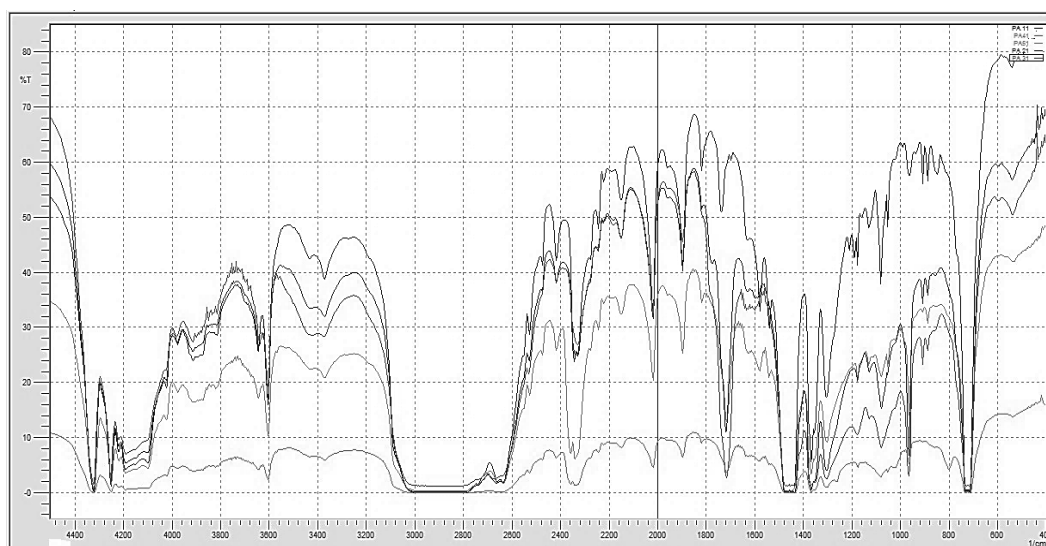


Fig 1. FTIR spectra of UHMWPE.

X-ray diffractographs of the unirradiated and the irradiated UHMWPE polymer has been shown from figure 2. It is evident from the x-ray diffractographs that all the polymers undergo modifications structurally. The evaluated values (approximate values only without any rigorous data treatment) of the crystallite size using scherrer's equation and crystallinity index using manjunath's method as well as an integral method have been listed in the following table 2.

UV-Visible spectra of the un-irradiated and the irradiated UHMWPE polymer samples has been shown from figure 3. One can notice the changes shown in absorbance of UV-Visible radiation in these polymer due electron irradiation.

The surface topography of the un-irradiated and irradiated UHMWPE polymer samples evaluated using an Atomic Force Microscope has been shown in figures 4-6.

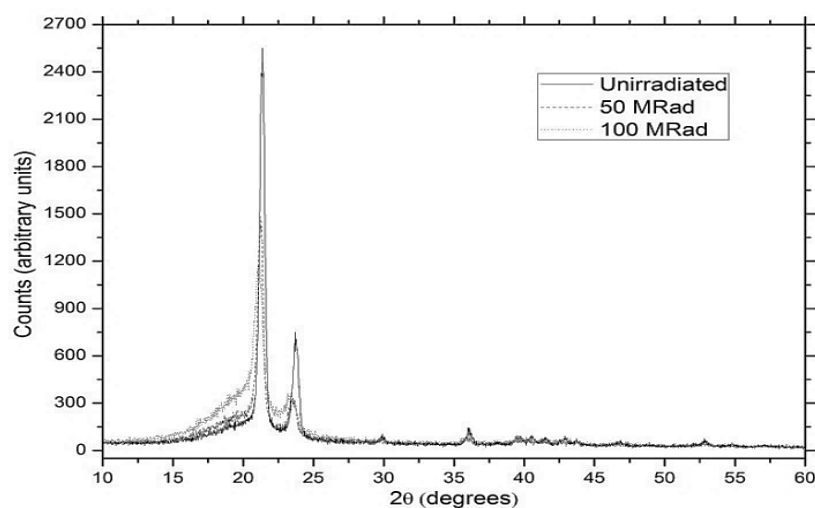


Fig 2. X-ray diffraction traces of UHMWPE.

| Table 2. | | | | |
|-----------------|-------------------------|---|----------------------------|------------------------|
| Polymer | Irradiation Dose | Crystallite size (\AA^0) | Crystallinity index | |
| | | | Manjunath's method | Integral method |
| UHMWPE | 0 MRad | 218.8 | 0.94 | 0.47 |
| | 50 MRad | 151.2 | 0.89 | 0.37 |
| | 100 MRad | 46.3 | 0.76 | 0.33 |

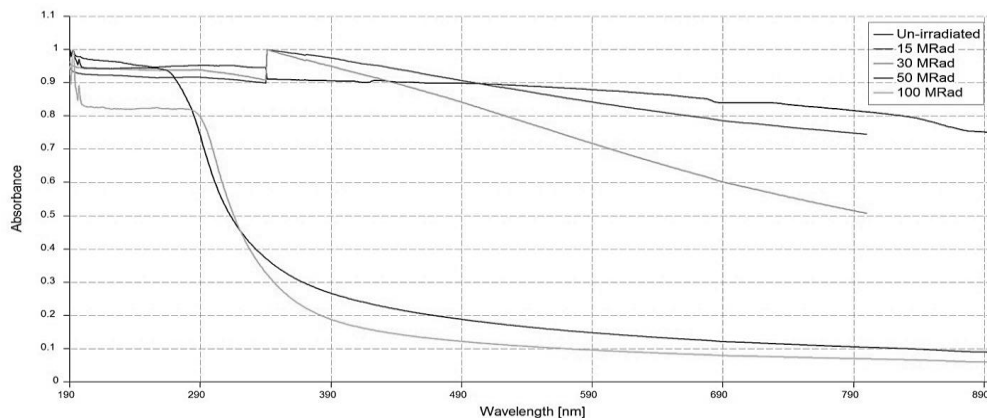


Fig 3. UV-Vis Spectra of UHMWPE.

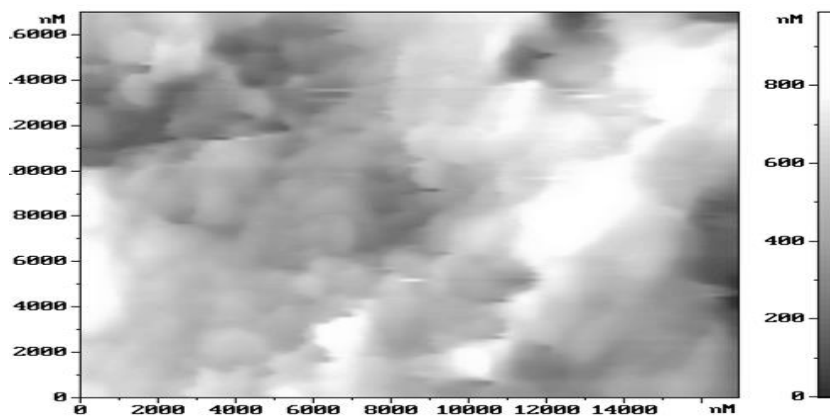


Fig 4. AFM pictures showing the surface structure of the un-irradiated UHMWPE.

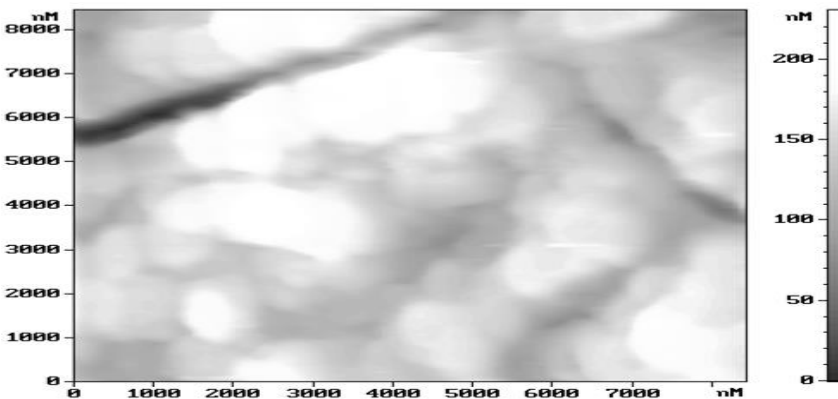


Fig 5. AFM pictures showing the surface structure of the 50 MRad irradiated UHMWPE.

UHMWPE being a very high molecular weight polymer forms an uneven surface containing large grains in the form of lumps containing the fold surfaces of lamellar crystal layers which are shown in figure 4-6. Upon irradiation, long molecular chains are broken and the surface roughness decreases. In addition, cracks are also formed, might be due to segregation of the molecules. With an increased irradiation dose, more numbers as well as deeper cracks are observed. The regions in between the cracks become more uneven forming bigger humps and deep craters due to increased segregation of the molecules.

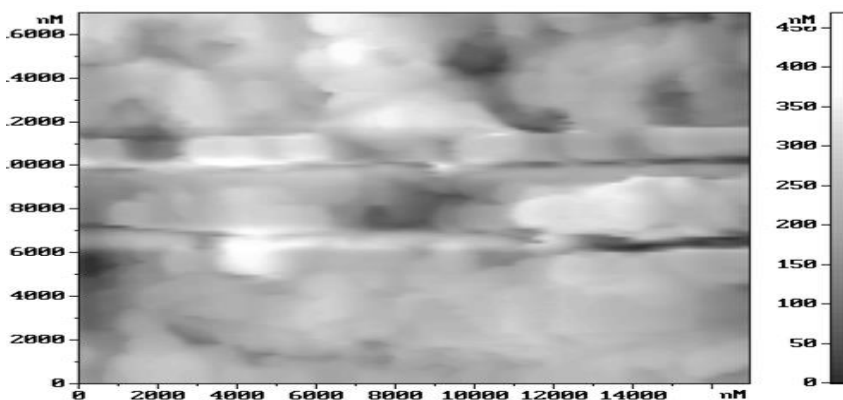


Fig 5. AFM pictures showing the surface structure of the 100 MRad irradiated UHMWPE.

The calculated values of surface roughness are tabulated in the table 3.

| Table 3 | | |
|-------------------------|-------------------------------|------------|
| Irradiation Dose | Surface Roughness (nm) | |
| | Avg. | Rms |
| 0 MRad | 25.4 | 31.6 |
| 50 MRad | 20.6 | 25.6 |
| 100 MRad | 39 | 47 |

Conclusions:

High energy electron irradiation of polymers has been used widely as an advanced tool in polymer processing. It has been used for polymerization process as well as for curing & sterilizing of polymer products. More importantly, it also has been used as a very strong tool in assisting the degradation process of the discarded

non-degradable polymers materials which pose a danger to the environment. In view of this, high energy electron beam irradiation effects have been studied at different irradiation doses of 50 MRad and 100 MRad. The dose levels chosen appear to provide the required information regarding both improving the polymerization (cross linking) as well as degradation of polymer chains (chain scission).

Post irradiation analysis of UHMWPE indicates that it undergoes oxidation and also cross linking. These results are evident from its brittleness as well as being more opaque. A large change has been observed in their physical structure which leads to decrease in their crystallinity. Its surface also undergoes maximum damage and deep cracks are formed due increased brittleness. Only approximate & general discussions have been presented in this paper.

Acknowledgements: The corresponding author, Dr. Harish V, acknowledges the support provided by Science Academies (Indian Academy of Science, Bangalore) through Summer Research Fellowship for Teachers and Bhabha Atomic Research Centre, Trombay, Mumbai for extending the facilities at Radiation and Photochemistry Division and Dr. Tulsi Mukherjee, (Former) Director – Chemistry Group, BARC, Mumbai for guiding this work.

References:

1. T. Czvikovszky, Advances In Radiation Chemistry Of Polymers: Degradation Effects In Polymers, IAEA-TECDOC-1420, 2004, 91.
2. D C Waterman and Malcolm Dole; the Radiation Chemistry of Polyethylene X: Kinetics of the Conversion of Alkyl to Allyl Free Radicals; Journal of Physical Chemistry; Vol 74(9), 1970, 1913-1922.
3. L Costa, I Carpentieri and P Bracco; Post electron-beam irradiation oxidation of orthopaedic UHMWPE; Polymer Degradation and Stability, Vol 93, 2008, 1695–1703.
4. A M Abdul-Kader, A Turos, R M Radwan and A M Kelany; Surface free energy of ultra-high molecular weight polyethylene modified by electron and gamma irradiation; Applied Surface Science, Vol 255, 2009, 7786–7790.
5. A Turos, A M Abdul Kader, R Ratajczak and A Stonert; Modification of UHMWPE by ion, electron and g-ray irradiation; Vacuum, Vol 83, 2009, 554–556.
6. R. D. Mathad, H. G. Harish Kumar, Basavaraj Sannakki, Ganesh Sanjeev, K. S.S. Sarma & Sanju Francis; Electron-beam-induced changes in ultra-high-


molecular weight polyethylene, *Radiation Effects and Defects in Solids: Incorporating Plasma Science and Plasma Technology*, Vol 165(4), 2010, 277-289.

7. Krystyna Czaja and Marek Sudol; Studies on electron-beam irradiation and plastic deformation of medical-grade ultra-high molecular weight polyethylene; *Radiation Physics and Chemistry*, Vol 80, 2011, 514–521.
8. H A Khonakdar, S H Jafari, U Wagenknecht and D. Jehnichen; Effect of electron-irradiation on cross-link density and crystalline structure of low- and high-density polyethylene; *Radiation Physics and Chemistry*, Vol 75, 2006, 78–86.

* * * * *

- **Dr. Ashok G V**, Government College (Autonomous), Mandya, Karnataka, India, **Ph:** 9740110170
- **Dr. Shiva Prasad N. G**, Government First Grade College, Srirangapatna, Karnataka, India, **Ph:** 8792927030
- **Dr. Niranjana Prabhu .T**, MS Ramaiah University of Applied Sciences, Bangalore, India.
- **Dr. Harish .V**, Government First Grade College, Bapujinagar, Shivamogga, Karnataka, India, **Ph:** 9448730669, **E-mail:** harishvenkatreddy@gmail.com,

Photon attenuation studies on human teeth and its substitutes

- 
- Dr. Harish .V, Dr. Shiva Prasad N. G
 - Narasimhamurthy K. N, Navitha .G
 - Dr. Ashok G. V, Shashikumar T. S

Abstract:

The mass attenuation coefficients are computed for total photon interaction in an extended energy range (1keV–100GeV) by using WinXCom program for Original teeth, Artificial teeth of PMMA (Polyethyl methacrylate) and Titanium alloy composites used in dental prosthesis and the partial photon interactions have been studied. The mass attenuation coefficient (μ/ρ) values are found to be higher in the photo-electric absorption region which occurs at photon energies $< 100\text{KeV}$. From the μ/ρ values obtained, effective atomic number (Z_{eff}) and electron densities (Ne) have been computed. The effective atomic numbers show strong energy dependence, especially in the lower energy range where photo electric absorption is dominant. The study helps to understand the radiation effects on these when they are exposed to medical X-rays and gamma rays. The results are systematically analysed and discussed.

Keywords: Human teeth, PMMA, Mass attenuation coefficient, Effective atomic number, Electron density

1. Introduction:

The mass attenuation co-efficient (μ/ρ) is a measure of probability of interaction that occurs between incident photons and matter per unit area. The knowledge of mass attenuation coefficient of x-rays and gamma photons in biological, chemical and other important materials is of significant practical interest in nuclear diagnostics (computerized tomography), nuclear medicine, radiation protection,

radiation dosimetry, gamma ray fluorescence studies, radiation physics, shielding and security screening.

For photon interactions, a single number cannot represent the atomic number uniquely across the entire energy region, as in the case of pure elements. This number for composite materials is known as effective atomic number and it also vary with incident photon energy. The energy absorption in a given medium can be calculated if these necessary constants, Z_{eff} and electron density N_e of the medium are known. As effective atomic number and electron densities are useful in many technological applications, several investigators have made extensive studies of effective atomic number in variety of composite materials like alloys, polymer compounds, dosimetric compounds, semiconductors and biological organs and tissues.

The radiation is used in a wide range of medical fields, in diagnosis and treatment. The photons falling on the teeth are attenuated and it is important to evaluate the amount of energy delivered by the ionizing radiation, in these materials. A dental radiograph gives dentist a picture of hard tissues (teeth and bones) and the soft tissues that surround teeth and jawbones. Implementation of X-ray dental examination is associated with the patient's exposure to ionizing radiation. The amount of exposure depends on the type of medical procedure, the technical condition of the X-ray unit and selected exposure conditions.

The amount of radiation used to obtain dental radiographs is very small. For example, bitewing radiographs—two to four images of the back teeth—expose a patient to about 0.005 mili sieverts (mSv) of radiation (a milli sievert is a unit of radiation dose). By comparison, because radiation is part of our environment, the annual dose due to natural sources of radiation is 2.4 mSv[1]. In view of this, precise knowledge of effective atomic numbers is very important in understanding the effect of radiation on some composite materials like teeth and their substitutes. The results are systematically analysed and discussed.

2. Materials and Methods:

Cross sections and mass attenuation coefficients for elements, number of compounds and mixtures are readily available in tables, like Hubbell and Seltzer (1995) [2] which are then developed as software called XCOM by Berger and Hubbell [3]. XCOM is web-based software that calculates mass attenuation

coefficients or photon interaction cross-sections for any element, compound or mixture at energies from 1 keV to 100 GeV. This software is later transformed under the name WinXCom by Gerward et al. (2001) [4] and Gerward et al. (2004) [5] into Windows platform with added capabilities. WinXCom is a convenient alternative to manual calculations to generate total cross sections, attenuation coefficients as well as partial cross sections for various interaction processes, such as incoherent and coherent scattering, photoelectric absorption and pair production, for elements, compounds and mixtures as needed. Mass attenuation coefficients are computed for Original teeth, PMMA and Titanium alloy composites using their chemical compositions for a wide energy range using WinXCom. From the μ/ρ values Z_{eff} and Ne were calculated as given below.

2.1 Effective atomic number for a composite

Consider a chemical compound, the photon interaction cross section per molecule can be written as

$$\sigma_m = \sum_i n_i \sigma_i$$

Where, n_i is the number of atoms of the i^{th} Constituent element and σ_i is the total photon interaction cross section [6]

The effective (average) cross section per atom is given by

$$\sigma_a = \frac{1}{n} \sum_i n_i \sigma_i$$

The effective (average) cross section per electron is given by

$$\sigma_e = \frac{1}{n} \sum_i n_i \frac{\sigma_i}{Z_i}$$

The effective atomic number can be written as the ratio between the atomic and electronic cross section.

$$Z_{eff} = \frac{\sigma_a}{\sigma_e}$$

The basic relation for calculating the effective atomic number of a chemical compound.

$$Z_{eff} = \frac{\sum_i \sigma_i n_i}{\sum_j n_j \frac{\sigma_j}{Z_j}}$$

The atomic cross section of the constituent element is related to the corresponding *mass attenuation coefficient* through the relation

$$\sigma_i = \frac{A_i}{N_A} \left(\frac{\mu}{\rho} \right)_i$$

Where, A_i is the atomic mass & N_A is the Avogadro number

$$Z_{eff} = \frac{\sum_i n_i A_i \left(\frac{\mu}{\rho} \right)_i}{\sum_j n_j \frac{A_j}{Z_j} \left(\frac{\mu}{\rho} \right)_j}$$

2.2 Electron density

The effective atomic number (Z_{eff}), is related to the electron density (N_e), given by

$$N_e = N_A \frac{Z_{eff}}{\langle A \rangle}$$

Where, $\langle A \rangle = \frac{\sum n_i A_i}{n}$ is the average atomic mass of the compound.

3. Results and discussion

3.1 Original human teeth

Mass attenuation coefficient (μ/ρ) is a measure of probability of interaction that occurs between incident photons and matter of unit mass per unit area. Knowledge of mass attenuation coefficients of X-rays and gamma ray photons in

teeth helps to understand the photon interaction and energy deposition in them. In view of this, mass attenuations coefficients are computed for the original human teeth using WinXcoM program and the results are analyzed and presented.

3.1.1 Variation of Mass attenuation co-efficient of human teeth with photon energy

The weight percentage of different elements present in the teeth are C=52.7%, O=30.4%, Ca= 8.9%, Cl=1%, P=0.6%, Mg = 0.3%, Na=0.6%. Variation in mass attenuation coefficients (sum) for original human teeth, for the gamma ray energy range 1 keV to 100 GeV is obtained from WinXcom and shown in Figure 1. It can be seen that, total sum of μ/ρ due to different photon interactions is low at energies <2 keV, then reaches maximum and decrease rapidly with energy. Also, μ/ρ values decrease sharply up to photon energy of 10 keV, further decrease very slowly. The total sum of μ/ρ attains a maximum value of 5500 Cm^2/g then decreases, reaches an invariable value above 100 keV.

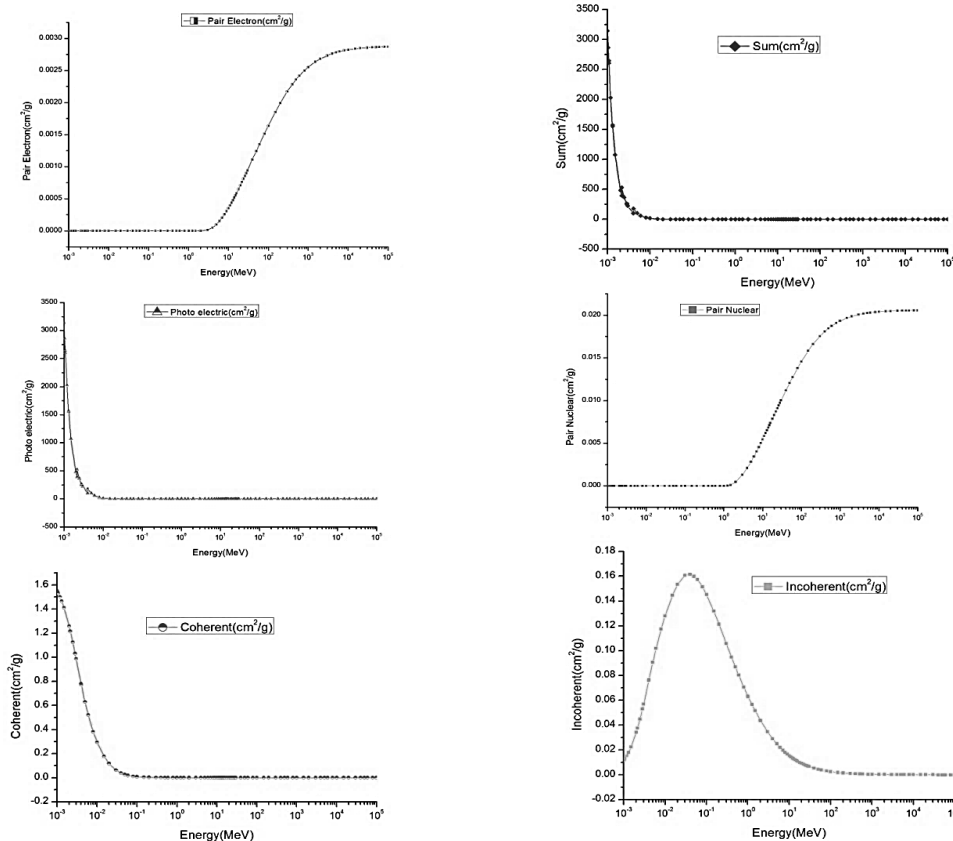


Fig. 1: Variations of Mass attenuation coefficients with different photon interactions in original human teeth

Photon interaction is based on photo-electric absorption, Compton scattering and pair production. Therefore, we studied separately the mass attenuation coefficients for coherent, incoherent, photo-electric absorption and pair (nuclear/electron). The μ/ρ values are higher in the photo-electric absorption region which occurs at photon energies < 100 KeV. The values of μ/ρ (photo) become negligible ($< 10^{-3}$ Cm^2/g) as photon energy reaches 100 keV. The reason for such variation may be due to dependency of the photo-electric cross-section on photon energy as $\tau \propto Z^4/E^3$. Hence, the μ/ρ (photo) values decrease rapidly at low energy. This shows the dominance of photo-electric absorption in the low photon energy region. It can also be seen that μ/ρ coherent is also significant at lower energies, but decreases slowly compared to μ/ρ (photo) and attains almost a constant value for energies > 100 keV. Whereas, μ/ρ Compton increases from 1 keV to 100 keV, thereafter decreases, and becomes insignificant around 200 MeV. From Figure 1, it can be observed that the mass attenuation coefficient values for the pair production process in the nuclear field and electron field, start at the threshold energies of 1.022 MeV and 2.044 MeV and thereafter increase with an increase in the incident photon energy. μ/ρ pair production is found to saturate after a photon energy > 10 MeV.

3.1.2 Effective atomic number and electron density

Variation in Z_{eff} for total photon interaction with incident photon energy for original teeth is shown in Figure 2.

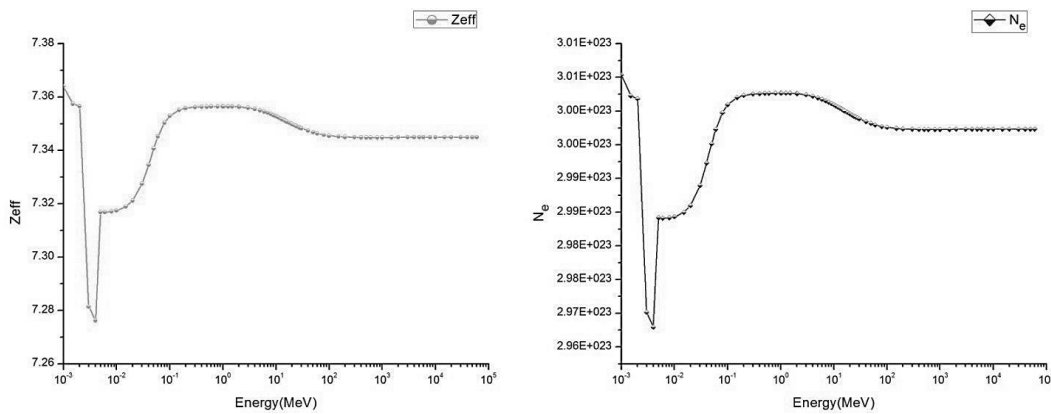


Fig. 2: Variations of Z_{eff} and electron density in original human teeth

The variation in electron density with incident photon energy follows the same trend, as observed for the effective atomic number. The variations can be clearly explained by the Z dependence of total atomic cross-sections, thus effective atomic numbers as Z^4 or Z^5 for photo electric absorption, Z^1 for Compton scattering and Z^2 for pair production. This clearly explains the maximum values of Z_{eff} in the low energy region.

3.2 Artificial teeth PMMA (polymethyl methacrylate)

PMMA (polymethyl methacrylate) is used to fabricate temporary dental restorations for a wide range of cases, including more complex indications such as implants or large span bridges. Acrylate polymers are used widely in medical particularly in dental field. PMMA has lofty surface resistivity, resistance towards moisture and weathering, water clear colour, very towering strength, better flexibility, superior dimensional stability [7]. Because of its excellent physical and chemical properties PMMA material is used in various applications. The chemical formula of PMMA is $(C_5O_2H_8)_n$ and the weight percentage of different elements present in the teeth are H= 8%, C=59.9% and O=32%.

3.2.1 Mass attenuation coefficients

The variation of mass attenuation coefficient with photon energy is presented in Fig. 3. In the energy range (1keV– 100 GeV), the variation of Z_{eff} with energy for PMMA is also found to be mainly dominated by different partial photon interaction processes namely photoelectric absorption, Compton scattering and pair production as discussed earlier in the section. The variation in Z_{eff} is found to be large below 100 keV where photoelectric process dominates over other interactions.

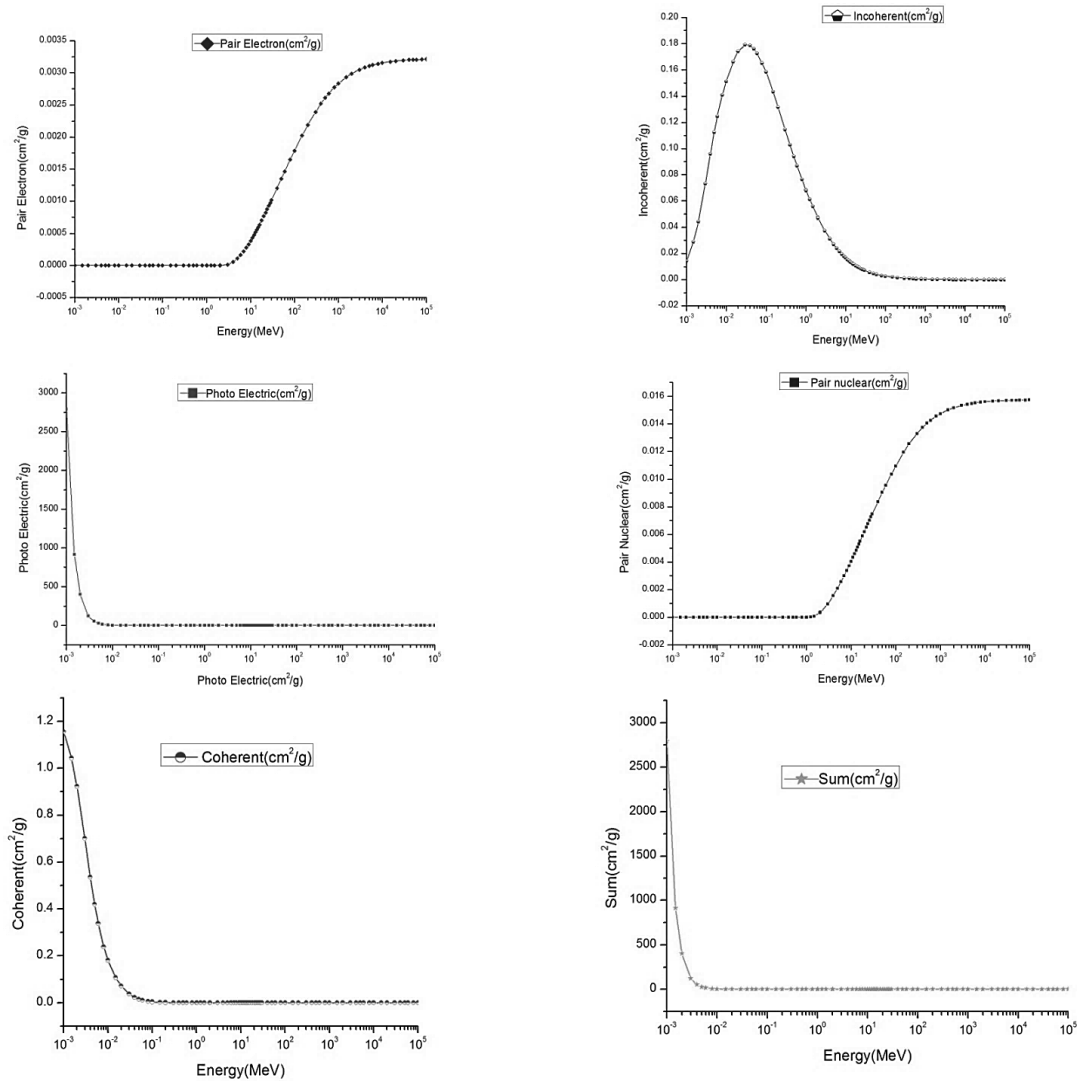


Fig. 3: Variations of Mass attenuation coefficients with different photon interactions in PMMA

3.2.2 Effective atomic number

The variations in effective atomic number with photon energy for PMMA is presented in Fig. 4. The variation in Z_{eff} with incident photon energy follows the same trend, as observed for the original human teeth. These results are in good agreement with the results observed by many researchers [7-9].

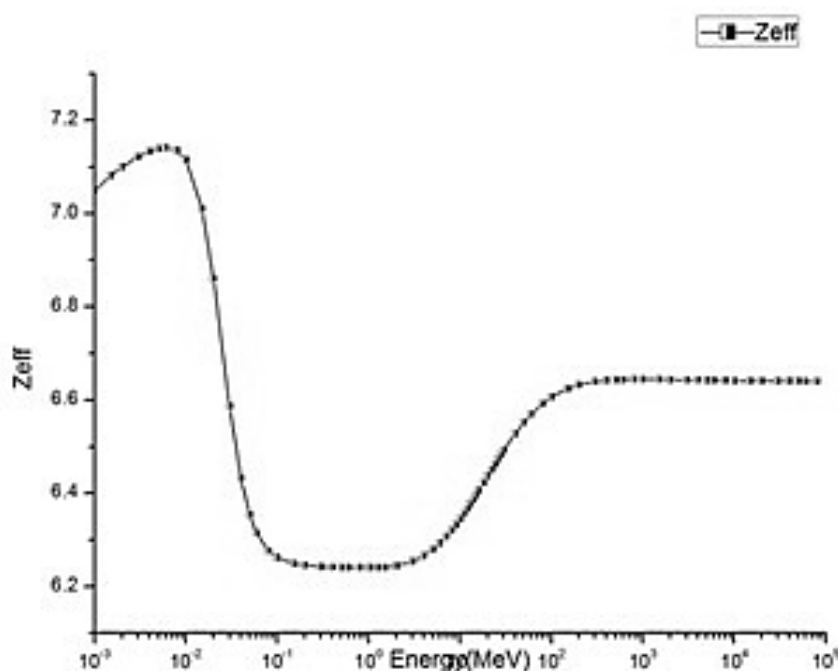


Fig. 4: Variations of Zeff for PMMA

3.3 Titanium alloy in dental prosthesis

A dental prosthesis is an intraoral (inside the mouth) prosthesis used to restore (reconstruct) intraoral defects such as missing teeth, missing parts of teeth, and missing soft or hard structures of the jaw and palate. Titanium is a metallic element known by several attractive characteristics, such as biocompatibility, excellent corrosion resistance and high mechanical resistance. It is widely used in dental prosthesis, with high success rates, providing a favourable biological response when in contact with live tissues. Though many properties of these are extensively studied by Niinomi M (2008) [8] and Steinemann S (1998) [9], the effect of ionizing radiation on these has not been studied either experimentally or theoretically so far. In view of this, mass attenuation coefficients have been evaluated for different photon energies and effective atomic number and electron densities are studied

3.3.1 Mass attenuation coefficients

The weight percentage of different elements present in the titanium alloy used in dental prosthesis are Cr=17.4%, Ni=12.8%, Mo=2.3%, Mn=0.2%, Si=0.8%, C=0.08%, Fe=66.4%, Zn=0.6%. The variation of mass attenuation coefficients with

photon energies is presented in Fig. 5. Again, photoelectric absorption is found to be the dominant contributor for photon attenuation in the x-ray energy range. The dominance of different photon interaction processes at various energy ranges analogous the PMMA. But the difference can be observed in the magnitudes of mass attenuation co-efficient in all the partial photon interaction processes.

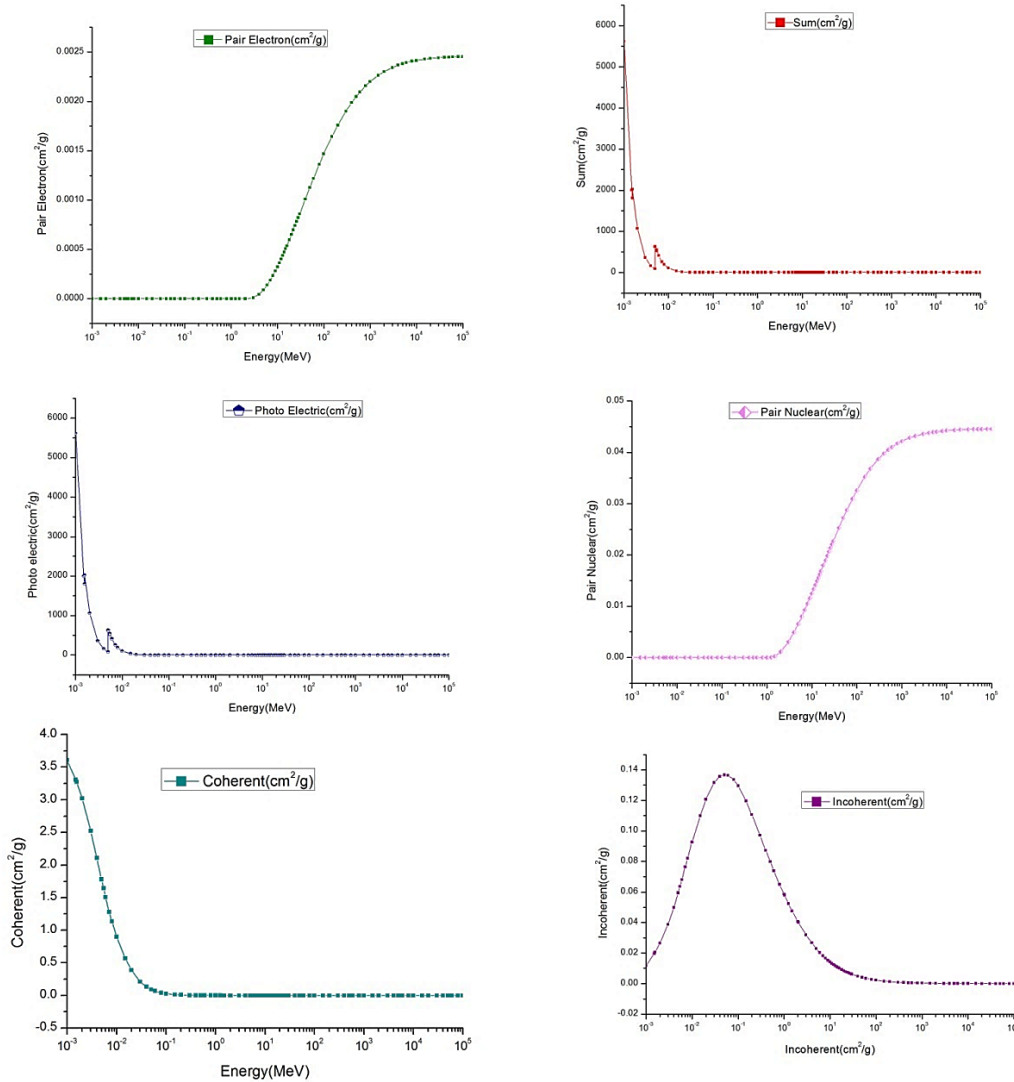


Fig. 5: Variations of Mass attenuation coefficients with different photon interactions

3.3.2 Effective atomic number and electron density

The Z_{eff} and N_e for titanium alloy for photon energies of 1 keV–1 GeV have been computed and the results are shown in Fig. 6 as a function of photon energy. It

is clear from this figure that the effective atomic number is low up to 10 keV and it then increases up to 50 keV, again decreases.

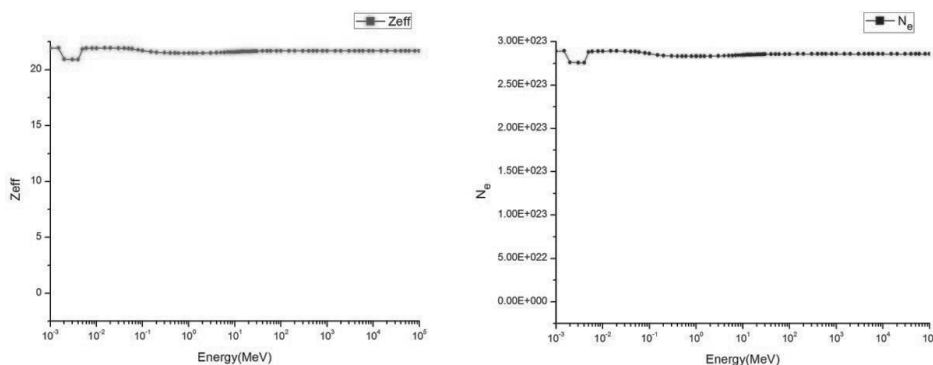


Fig.6: Variations of Z_{eff} and electron density for titanium alloy

4. Conclusions:

When medical x-rays and gamma rays (Natural and medical) fall on the original and artificial teeth, they are attenuated. The mass attenuation coefficients computed for total photon interaction in an extended energy range (1keV–100GeV) by using WinXCom program for Original teeth, PMMA and Titanium alloys dental prosthesis show significant variations with photon energy especially in the energy <1 MeV. The pair electron and pair nuclear process start at the threshold energies of 1.022 MeV and 2.044 MeV and thereafter increase with an increase in the incident photon energy and saturates above 100 MeV. The effective atomic numbers show strong energy dependence, especially in the lower energy range where photo electric absorption is dominant. The study helps to understand the radiation effects on these when they are exposed to medical X-rays and gamma rays.

References:

1. S N Shilfa, B Y E B Jumpeno , Nurokhim , Kusdiana. Ambient dose measurement from high natural background radiation (HNBR) in Botteng Utara Village, Mamuju – Indonesia. Journal of Physics: Conf. Series 1436 (2020) 012027, doi:10.1088/1742-6596/1436/1/012027
2. J.H. Hubbell, S.M. Seltzer, Tables of X-ray Mass Attenuation Coefficients and Mass Energy-Absorption Coefficients 1 keV to 20 MeV for Elements $Z = 1$ to 92 and 48 Additional Substances of Dosimetric Interest, NISTIR 5632, National Institute of Standards and Technology, Gaithersburg, MD 20899, USA, 1995.

3. M.J. Berger, J.H. Hubbell, XCOM: Photon Cross Sections Database, Web Version 1.2, available at <http://physics.nist.gov/xcom> (1999). Originally published as NBSIR 87-3597 XCOM: Photon Cross Sections on a Personal Computer, Washington, DC, 1987.
4. L. Gerward, N. Guilbert, K.B. Jensen, H. Levring, Radiat. Phys. X-ray absorption in matter. Reengineering XCOM, *Radiation Physics and Chemistry*. Chem. 60 (2001) 23-24.
5. L. Gerward, N. Guilbert, K.B. Jensen, H. Levring. WinXCom - A program for calculating X-ray attenuation coefficients. Radiat. Phys. Chem. 71 (2004) 653-654.
6. S.R. Manohara, S.M. Hanagodimath, K.S. Thind, L. Gerward. On the effective atomic number and electron density: A comprehensive set of formulas for all types of materials and energies above 1 keV. Nuclear Instruments and Methods in Physics Research B 266 (2008) 3906–3912
7. Khan AA, Mirza EH, Mohamed BA, et al. Physical, mechanical, chemical and thermal properties of nanoscale graphene oxide-poly methylmethacrylate composites. *Journal of Composite Materials*. 2018;52(20):2803-2813. doi:10.1177/0021998318754642
8. Niinomi M. Mechanical biocompatibilities of titanium alloys for biomedical applications. *J Mech Behav Biomed Mater Vol 1*, (2008) 30–42. doi:10.1016/j.jmbbm.2007.07.001
9. Steinemann S . Titanium—the material of choice. *Periodontol Vol. 17* (2000) 7–21. doi:10.1111/j.1600-0757.1998.tb00119.

* * * * *

- ❖ **Dr. Harish .V**, Government First Grade College, Bapujinagar, Shivamogga, Karnataka, India
- ❖ **Dr. Shiva Prasad N. G**, Government First Grade College, Srirangapatna, Karnataka, India, Ph: 8792927030
- ❖ **Narasimhamurthy K. N**, Government First Grade College, Tumkur, Karnataka, India.
- ❖ **Shashikumar T. S**, PES Institute of Technology, Mandya, Karnataka, India
- ❖ **Navitha .G**, Research scholar, VTU-RRC, Belgavi-590 018
- ❖ **Dr. Ashok G. V**, Government College (Autonomous), Mandya, Karnataka, India, **Ph:** 9740110170, **E-mail:** ashok.godekere@gmail.com

Measurement of indoor radon, thoron and their progeny concentration and Estmation of annual inhalation dose rates in Chikmagalur city, Karnataka, India

- Dr. Srinivasa .E, Guruswamy .K
- Dr. Sannappa .J, Soundar .R
- Dr. Rangaswamy D. R, Suresh .S

Abstract:

In this study indoor radon and thoron concentrations have been measured in twenty different dwellings of Chikamagalur city by using solid state nuclear track detector (SSNTDs) based twin cup dosimeters. The indoor radon and thoron concentrations were found to vary from 25 ± 2.4 to 112 ± 4.5 Bq.m⁻³ and 15 ± 0.9 to 67 ± 3.4 Bq.m⁻³ with an average value of 48.4 ± 2.9 Bq.m⁻³ and 32.5 ± 2.2 Bq.m⁻³, respectively. The progeny concentration of radon and thoron ranged from 2.7 to 12.1 mWL with an average value of 5.2 mWL and from 1.09 to 4.57 mWL with an average value of 2.36 mWL, respectively. The average radon concentrations are found to be less than the lower reference level of 200 Bq.m⁻³ of the International Commission on Radiological Protection. The average value of annual effective dose equivalent to the inhabitants of the study area was found to be 1.48 mSv.y⁻¹ and is below the action level as recommended by the ICRP.

Key words: Radon, thoron. Inhalation dose, annual effective dose, dosimeter

Introduction

The behavior of radioactive gases has received considerable attention over the past few decades due to the radiological risks to humans in indoor atmosphere. The radiation dose, resulting from the indoor radon and its decay products, constitutes a major part of the total natural background radiation received by

population all over the world. The major contribution of dose from natural radiation in normal background regions arises due to inhalation of alpha-emitting radon, thoron and their progenies, which are ubiquitous in both indoor and outdoor environs⁽¹⁾. Worldwide average annual effective dose from the ionizing radiation sources is estimated to be 2.4 mSv of which about 1.275 mSv is due to radon exposure alone⁽¹⁾. Radon is a naturally occurring odorless, colorless, tasteless, imperceptible to senses and chemically inert gas which is produced continuously from the natural decay of ^{238}U , ^{235}U and ^{232}Th in soils, rocks, and water all over the earth. ^{222}Rn has a half-life of 3.82 days and a mean life of 5.51 days and decays to its solid progeny ^{218}Po by alpha emission of energy of 5.49 MeV. Thoron (^{220}Rn), the most important radioactive isotope of ^{222}Rn , it has half-life of 55.6 s and a mean life of 80.2 s, and decays to its solid progeny ^{216}Po by alpha emissions of energy of 6.29 MeV. The main source of the indoor radon and thoron are originate from the wall, floor and ceilings which are constructed of building material, soil and rocks underneath the building structures, water and energy sources⁽²⁾. Radon itself is not hazardous as it is cleared quickly as it is absorbed but its daughter elements can be hazardous. As radon gas is inhaled densely ionizing alpha particles emitted by the short-lived decay products of radon (^{212}Po and ^{214}Po) can interact with biological tissue in the lungs leading to DNA damage and results into lung cancer. Breathing in an environment having high concentration of radon may lead to lung cancer. The US-EPA reports that radon is the second major cause of lung cancer, behind cigarette smoking⁽³⁾. In the present study, the long term average radon, thoron and their progeny concentration have been measured and life time fatality risk and annual effective dose due to radon and thoron and their progeny are discussed.

Study Area

Chikmagalur city is a district head quarter situated in the south western region of the Karnataka state located at 13° 18' north latitude and 75° 49' east longitudes. The Western Ghats start just from the outskirts of the city. Most of the area in Chikmagalur is covered by schist followed by gneissic rocks in southern part of the city. Weathered, fractured and jointed schist and gneiss are potential aquifers in the area. The predominant geological formations are charnockite, gneisses and unclassified crystallines, slates, phyllites and schists. The major soil type in the district comprises of red loamy and red sandy soil (mainly hilly area), mixed red and black soil.

Materials and Methods

The indoor radon and thoron concentrations were measured by using solid state nuclear track detectors (SSNTDs). The dosimeter used in the present study is a cylindrical plastic cup divided into two components having a provision for holding the SSNTD films in a specific concentration. SSNTD₁ is a cup with a suitable membrane like a thin latex rubber sheet that determines ²²²Rn concentration alone because ²²⁰Rn gas is trapped to < 1 % and SSNTD₂ inside the cup with a Whatman filter paper determines the sum of ²²²Rn and ²²⁰Rn concentrations in air. The system used for these measurements is called a double chamber dosimeter. The bare mode exposure film can be fixed conveniently on the surface of the chamber. The size of the films used in the three different modes of exposure is 2.5cm×2.5 cm. The dosimeters with the films as described above were exposed for a period of ~ 90 days. At the end of the stipulated period of exposure, the dosimeters are retrieved and etched with 10% NaOH solution at 60°C for 90 minutes. After etching, the films were washed in distilled water properly, and then they were dried up in the laboratory conditions. Then the track density of alphas in the film was determined using a spark counter. The dosimeter cups were designed, fabricated and supplied by Bhabha Atomic Research Center, Mumbai, India.

The radon and thoron concentrations are calculated by using the following relations (1) and (2)

$$C_R (\text{Bqm}^{-3}) = \frac{T_m}{d \times S_m} \dots\dots (1) \quad C_T (\text{Bqm}^{-3}) = \frac{T_f - d C_R S_{rf}}{d \times S_m} \dots\dots\dots (2)$$

Where, T_m = Track density in membrane compartment,

T_f = Track density in filter compartment

d = Exposure time (90days)

Sensitivity factor for membrane compartment is (S_m) = 0.019±0.003 Tcm⁻²d¹/Bqm⁻³

Sensitivity factor for radon in filter compartments is (S_{rf}) = 0.020±0.004 Tcm⁻²d¹/Bqm⁻³

Sensitivity factor for thoron in filter compartment is (S_{tf}) = 0.016±0.005 Tcm⁻²d¹/Bqm⁻³

The ²²²Rn /²²⁰Rn progeny working level concentrations or potential alpha energy concentration (PAEC) were calculated by the following relations (3) and (4).

$$^{222}\text{Rn (mWL)} = \frac{C_R F_R}{3.7} \dots (3)$$

$$^{220}\text{Rn (mWL)} = \frac{C_T F_T}{0.275} \dots (4)$$

Where F_R and F_T are the equilibrium factors for ^{222}Rn and ^{220}Rn progeny, respectively. The inhalation dose due to radon and thoron was calculated by using conversion coefficient 9 and 40 nSv and equilibrium factor 0.4 and 0.02 for radon and thoron, respectively. The dose coefficient for radon and thoron dissolved in blood are calculated using conversion coefficient 0.17 nSv for radon and 0.11 nSv for thoron.

Finally an estimation of the annual inhalation dose in mSv y^{-1} may be provided using the formula (5)

$$D = \{(0.17 + 9F_R) C_R + (0.11 + 40F_T) C_T\} \times 7000 \times 10^{-6} \dots (5)$$

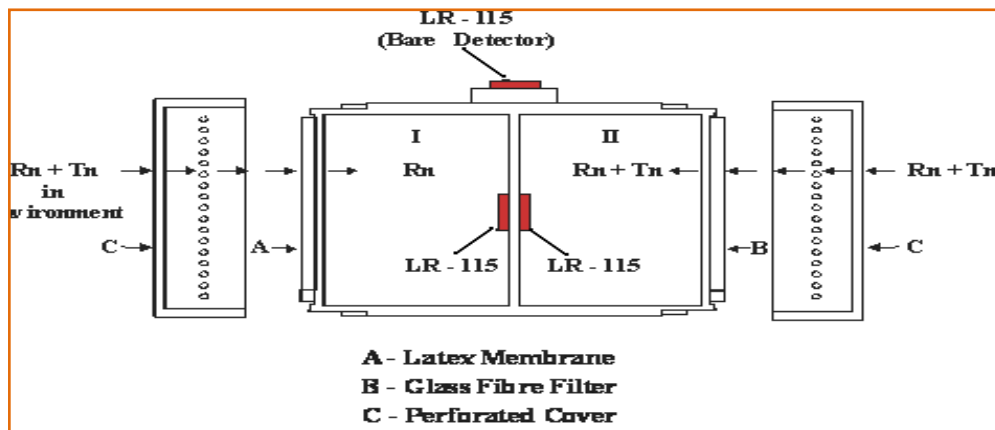


Fig: 1. View of Twin cup dosimeter



Fig: 2. Twin cup dosimeter in open mode

Results and Discussion

The results for average indoor radon, thoron and their progeny concentration obtained from observed track densities in the various dwellings of Chikmagalur City are given in the Table-1. The indoor ^{222}Rn , ^{220}Rn and their progeny concentrations were measured during winter season (i.e. three months, December–February). The results show that there were distinctive variations of radon, thoron and their progeny values in different dwellings. The concentration of radon, thoron and their progeny in dwellings depends mainly on the activity of uranium and thorium present in soil, rocks, building materials, and the types of building, methods of construction of buildings and ventilation rate. The indoor radon and thoron levels in this area are found to vary from 25 ± 2.4 to 112 ± 4.5 Bq.m^{-3} and 15 ± 0.9 to 67 ± 3.4 Bq.m^{-3} with an average value of 48.4 ± 2.9 Bq.m^{-3} and 32.5 ± 2.2 Bq.m^{-3} , respectively. The corresponding standard deviations are 21.6 and 12.9. Similarly, the progeny concentration of radon and thoron ranged from 2.7 to 12.1 mWL with an average value of 5.2 mWL (SD = 2.2) and from 1.09 to 4.57 mWL with an average value of 2.36 mWL (SD = 2.36) respectively. It has been observed that the radon, thoron and their progeny concentration vary considerably with the different construction types. The higher radon, thoron and their progeny levels were observed at Stepping stone school, Rathnagiri bore, Ramana hally, Adharsha nagara, and Housing board. This is due to the fact that the, these places are covered by rocky hills and the houses were built entirely by granite rocks, these rocks contain higher activity of primordial radionuclides. Another important reason for higher radon, thoron levels is, during the winter season the doors, windows and ventilators were kept closed to conserve heat that helped in building up of radon and thoron concentrations. Other important factors that affect radon, thoron and their progeny levels are local geology and uranium and radium content in soil, rock and building materials, radioactive contents of household articles, human habits, unscientific construction pattern of the houses, increased exhalations from ground and building materials, porosity and permeability of the underlying soil/rocks, pressure gradient between interface, soil moisture and water saturation grade of the medium, and faulted and folded bed rocks⁽⁵⁾. It is observed from present results that the radon concentration is higher as compared to thoron. It may be due to the difference in half-life of radon and thoron, which affects the exhalation rate from the wall and the concentration distribution inside the dwellings. Lower concentrations of radon, thoron and their progeny were observed in Basavana halli, Dhantaramakki, Donikana, Kalyana nagara and Near

I.D.S.G. Government College. The geology of these places is characterized by grey granite rocks. The grey granite has less activity concentrations of radium and thorium when compared with pink granites. The houses in these areas are newly constructed with concrete and they have good ventilation. The flooring materials used in the dwellings of these areas are made of marbles and vitrified tiles, which have low concentrations of radium and thorium, and moreover they avoid the emanation of radon and thoron from the ground to indoor atmosphere. The average indoor radon value in different dwellings of the Chikmagalur city is found to be $48.4 \pm 2.9 \text{ Bq.m}^{-3}$, which is much lower than the action level of $200\text{--}300 \text{ Bq.m}^{-3}$ recommended by International Commission on Radiological Protection ⁽⁴⁾. From this study, we have observed that the average radon concentration is higher than the worldwide average value reported for the dwellings of 40 Bq.m^{-3} recommended by UNSCEAR-2000⁽¹⁾. The present result reveals that, the average radon concentration is lower than the action level of 100 Bq.m^{-3} recommended by World Health Organization ⁽⁶⁾.

The annual inhalation dose received by inhabitants due to inhalation of radon, thoron and their progeny in indoor air ranged from 0.76 to 3.38 mSv.y^{-1} with an average value of 1.48 mSv.y^{-1} and the standard deviation of 0.93 , respectively. It has been found that radon and thoron daughters contribute a significant part of the effective dose from natural sources. These estimated values are higher than the world average of annual effective dose (AED) of 1.28 mSv.y^{-1} ⁽¹⁾. Nevertheless, the obtained highest mean values of the present study areas are below the upper reference level of 10 mSv ⁽⁴⁾. Hence, the inhabitants in the Chikmagalur city are free from health risks due to inhalation of radon and thoron, and their progenies. The variations in values among dwellings is due to the difference in the concentrations of radioactive elements, viz. uranium and thorium in the soil, bedrock and building materials and their exhalations ⁽⁷⁻⁸⁾.

Conclusion

Preliminary results from the study showed that, the average indoor radon, thoron and their progeny values in different dwellings of the Chikmagalur city is found to be much lower than the action level of $200\text{--}300 \text{ Bq.m}^{-3}$ recommended by ICRP and WHO. The average radon and thoron concentration in the study area are slightly higher than the worldwide average value reported for the dwellings of 40 Bq.m^{-3} and 10 Bq.m^{-3} respectively, as recommended by UNSCEAR-2000 report.

The average annual effective dose due to inhalation of indoor radon, thoron and their progeny was found to be 1.48 mSv.y^{-1} , which is slightly higher than the global average value of 1.28 mSv.y^{-1} as given by UNSCEAR 2000 report but this value within the action level of $3\text{--}10 \text{ mSv.y}^{-1}$ recommended by ICRP.

Table: The average indoor ^{222}Rn and ^{220}Rn concentrations, ^{222}Rn and ^{220}Rn progeny levels (P_R and P_T) and inhalation dose rates (E) in Chikmagalur city

| SL No | Locations | Concentration | | Progeny concentration | | E (mSv y^{-1}) |
|-------|---------------------------|---|---|-----------------------|-------------|--------------------------|
| | | ^{222}Rn (Bq m^{-3}) | ^{220}Rn (Bq m^{-3}) | P_R (mWL) | P_T (mWL) | |
| 1 | Jayanagara | 48.8±2.8 | 32.5±1.8 | 5.27 | 2.36 | 1.49 |
| 2 | APMC market | 42.5±2.2 | 35±2.6 | 4.59 | 2.55 | 1.34 |
| 3 | Near Bus stand | 35±1.8 | 26±1.2 | 3.78 | 1.89 | 1.09 |
| 4 | Hiremagalur | 58±3 | 42±2.4 | 6.27 | 3.05 | 1.80 |
| 5 | Rathnagiri Bore | 69±3.5 | 38±2 | 7.45 | 2.76 | 2.06 |
| 6 | Near I.D.S.G Govt college | 30±1.6 | 25±1.2 | 3.24 | 1.82 | 0.95 |
| 7 | Housing Board | 60±2.8 | 32±1.8 | 6.48 | 2.33 | 1.79 |
| 8 | Dodda Kurubarahalli | 55±3.2 | 41±2.6 | 5.94 | 2.98 | 1.71 |
| 9 | Kote | 50±2.3 | 38±1.7 | 5.41 | 2.76 | 1.56 |
| 10 | Uppalli | 45±3 | 36±2.4 | 4.86 | 2.62 | 1.42 |
| 11 | Donikana | 28±2.2 | 17±1.4 | 3.02 | 1.24 | 0.85 |
| 12 | Dhanttaramakki | 26±1.8 | 15±1.2 | 2.81 | 1.09 | 0.78 |
| 13 | Jyothi nagara | 34±2.7 | 27±1.8 | 3.67 | 1.96 | 1.07 |
| 14 | Kalyana nagara | 30±2.4 | 24.8±1.5 | 3.24 | 1.8 | 0.95 |
| 15 | Vijayapura | 36±1.7 | 15±0.9 | 3.89 | 1.09 | 1.05 |
| 16 | Gowrikaluve | 40±2.1 | 33±1.6 | 4.32 | 2.4 | 1.27 |
| 17 | Adharsha Nagara | 62±4.7 | 30±2.9 | 6.71 | 2.18 | 1.83 |
| 18 | Near Stepping Stone schol | 112±4.5 | 56±3.5 | 12.11 | 4.07 | 3.31 |
| 19 | Ramanahally | 82±5.9 | 67±3.4 | 8.86 | 4.87 | 2.59 |
| 20 | Basavanahally | 25±2.4 | 20±1.5 | 2.71 | 1.45 | 0.79 |

Recent Trends in Physics with Emphasis on Discovery of God Particle

| | | | | | | |
|--|----------------|-------------------|-------------------|--------------|-------------|-------------|
| | Average | 48.41±2.89 | 32.51±2.21 | 5.23 | 2.36 | 1.48 |
| | Maximum | 112±4.5 | 67±3.4 | 12.11 | 4.87 | 3.38 |
| | Minimum | 25±2.4 | 15±0.9 | 2.71 | 1.09 | 0.76 |
| | SD | 21.59 | 12.95 | 2.33 | 2.36 | 0.93 |

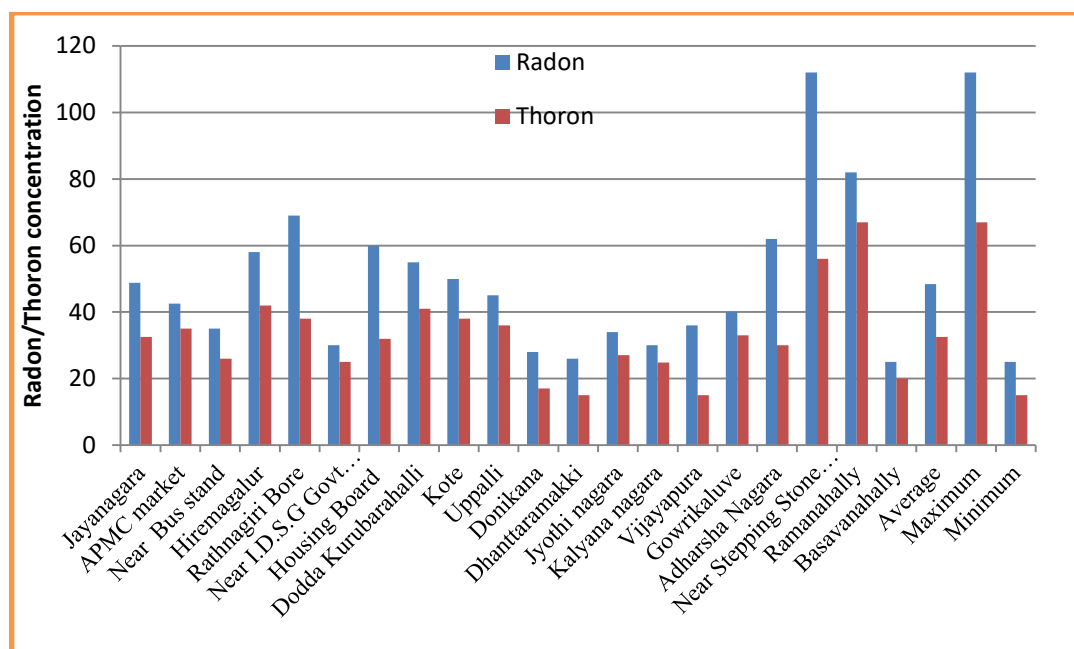


Fig 3: Variation of indoor radon and thoron with locations

References

1. UNSCEAR. *Sources, effects and risks of ionizing radiation*. Report to the General Assembly, United Nations, New York, (2000).
2. Sannappa, J., Chandrashekhara, M.S., Sathish, L.A., Paramesh, L., & Venkataramaiah, P. *Study of background radiation dose in Mysore city, Karnataka State, India*. Radiat. Meas. 37, 55–65 (2003).
3. EPA. *Assessment of risks from radon in homes, air and radiation*. EPA402-R-03-003 (2003).
4. ICRP. *Protection against ²²²Rn at home and at work*. ICRP Publication 65. Ann. ICRP 23 (2). Pergamon Press, Oxford (1993).

5. Schery, S.D., & Gaeddert, D.H. *Factors affecting exhalation of radon from a gravelly sandy loam*. J. Geophy. Res. 89, 7299–7309 (1984).
6. World Health Organization, Sets radon action level of 2.7 less lung cancer risk than EPA 4.0. Global Press. Release Distribution (2009b).
7. Ningappa, C., Sannappa, J., Chandrashekara, M. S. and Paramesh, L. *Concentrations of radon and its daughter products in and around Bangalore city*. Radiat. Prot. Dosim. 130(4), 459–465 (2008).
8. Rangaswamy, D.R., Srilatha, M.C., Srinivasa, E., Ningappa, C., Sannappa, J., *Radiation dose due to Radon, Thoron and their Progeny Concentration in Indoor Atmosphere around Granite Regions of Tumkur District, Karnataka, India*. Proceedings of national conference on recent trends and developments in radiation dosimetry. ISBN 978-81-929777-0-6, 32-37. (2014).

* * * * *

- ❖ **Dr. Srinivasa .E**, Assistant Professor, Department of Physics, IDSG Government College, Chikmagalur-Karnataka, India, 577102, **Mob:** +91 9448842087, **E-mail:** srinivasyadhu@gmail.com
- ❖ **Guruswamy .K**, Assistant Professor, Department of Physics, IDSG Government College, Chikmagalur-Karnataka, India, 577102, **E-mail:** guru.swamy702@gmail.com
- ❖ **Soundar .R**, Assistant Professor, Department of Studies in Physics, Government First Grade College, KGF, Kolar District-Karnataka, India, **E-mail:** Soundarbabu28@gmail.com
- ❖ **Suresh .S**, Assistant Professor, Department of Physics, M.P.E Society's S.D.M Degree College, Honavar, Karnataka, India, **E-mail:** sureshnv@gmail.com
- ❖ **Dr. Rangswamy D. R**, Assistant Professor, Department of Physics, PES University, Bangalore, Karnataka, India, **E-mail:** rangu.dr@gmail.com
- ❖ **Dr. Sannappa .J**, Professor and Chairman, Department of Studies and Research in Physics, Kuvempu University, Shankaraghatta, Shimoga-Karnataka, India, 577451, **E-mail:** sannappaj2012@gmail.com

Concentration of radon in drinking water samples around Nuggihalli-Holenarsipur schist belts, Karnataka State, India



- Dr. R. S. Niranjana
- Dr. C. Ningappa
- V. Nandakumar
- C. N. Harshavardhana

Abstract

Concentration of radon in drinking water samples have been measured using emanometry technique in 36 locations around Nuggihalli-Holenarsipur schist belts, Karnataka State, India. The concentration of radon in drinking water samples in the study area varied from $3.61 \pm 0.23 \text{ Bq l}^{-1}$ to $142.38 \pm 9.76 \text{ Bq l}^{-1}$ with an average value of $54.40 \pm 4.14 \text{ Bq l}^{-1}$. The estimated annual effective dose due to radon inhalation and ingestion varies from 9.87 to $388.67 \mu\text{Sv y}^{-1}$ with an average value of $148.51 \mu\text{Sv y}^{-1}$. The annual effective dose in 21 locations is found to be higher than the safe limit of 0.1 mSv.y^{-1} as prescribed by WHO.

1. Introduction

Radon occurs naturally in ground water as transitional step in the decay of ^{238}U to ^{206}Pb [1-3]. Uranium present in minerals and rocks decays into radium (^{226}Ra) through number of steps, which decays to radon (^{222}Rn) [4]. Radon moves from its source in rocks and soil through voids and fractures and can dissolve in ground water [5]. During the migration of ^{222}Rn from rock to soil, it may be easily dissolved in groundwater [6]. The higher concentration of ^{222}Rn in groundwater have been found at the locations, where radium concentration present in the rocks is higher and depends on other factors, like intensity of joining, presence of shear zones, degree of metamorphism, soil porosity and uranium mineralization [7]. Efforts have been made by various researchers to correlate radon concentrations with factors such as geology, soil porosity, shears, thrust, faults, uranium mineralization, etc [8-11]. In a geological environment, concentration of radon generally varies with different types of rocks [12-14].

The presence of high levels of ^{222}Rn in drinking water results a potential health risk to human through inhalation on account of exhalation of radon and its decay products from water into household air and ingestion of ^{222}Rn from direct consumption of drinking water having ^{222}Rn [15-16]. Two of the ^{222}Rn descendents ^{214}Po and ^{218}Po are alpha emitters and they contribute 90% of the total radiation dose receive due to ^{222}Rn exposure.

However, the dose received by exposure of ingested ^{222}Rn with intake of the water is less than the inhaled ^{222}Rn from the same water. Radon exposure will cause cancer of human organs, mainly the stomach and lungs [17]. Therefore, due to growing concern over the airborne and waterborne ^{222}Rn in drinking waters, many studies have been conducted worldwide to measure the concentration levels of ^{222}Rn [18-23]. Concentration of ^{222}Rn estimation is an important aspect of public health, as it describes the extent of population exposure to radiation. Hence, an attempt has been made for the first time in the current study area by estimating radiogenic isotope ^{222}Rn in the selected locations in and around Nuggihalli-Holenarsipur schist belts. This present study was carried out with a view to bring awareness and concern among the people residing in these areas to save themselves from the radiological hazards due to ingestion of ^{222}Rn dissolved drinking water.

2. Study area

The present field study lying between the latitudes of $12^{\circ} 37'$ and $13^{\circ} 23'$ N and longitude $76^{\circ} 00'$, and $76^{\circ} 53'$ E. The Nuggihalli Schist Belt [NSB] extends for approximately 60 km strike length and maximum 2 km width having large and rich pockets of chromite. Titaniferous vanadiferous magnetite in disconnected patches comprises of major litho units of hornblende schist [24].

Holenarasipura schist belt [HSB] is trident in shape. The belt extends maximum length of 65 km from Doddagudda to Yedegondahalli with a wide range of 0.5 km to 3 km and belt covers an area of 250 Sq.km in which Yenneholerangana betta is a small hillock which is named after the God Rangaswamy. The southern terrain is high grade metamorphic terrain, northern part is metamorphosed [24]. The geological map of Nuggihalli-Holenarsipur schist belts along with the sampling points are shown in Fig.1.

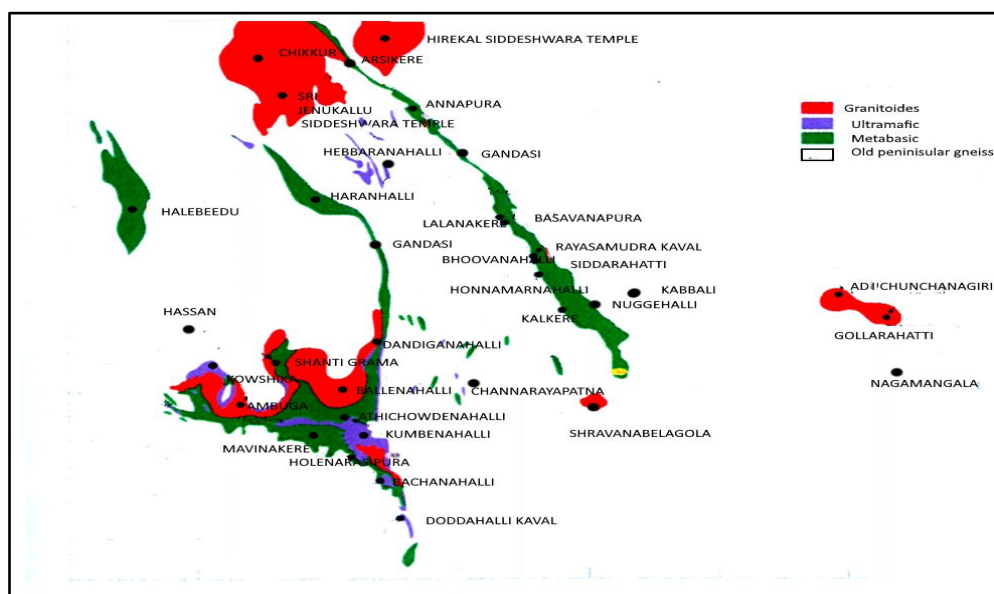


Fig. 1, Geological map of Nuggihalli-Holenarsipur schist belts, Hassan Dist, Karnataka State, India [24].

3. Methodology

The concentration of radon in drinking water has been estimated by radon emanometry technique. Thirty six drinking water samples were collected from bore wells covering different locations of the study area during April and May 2019. Fresh water from bore well was collected after allowing water to run fully for at least ten minutes. Water samples of 100 ml were collected in air tight plastic bottle with minimum disturbance. The plastic bottles were filled completely in a gentle manner without any air space. Care was taken to see that no air bubbles were seeing inside the plastic bottles to avoid aeration during the sampling processes, which might lead to out gassing [25]. The collected water samples were brought to the laboratory with minimal loss of time and were analysed immediately. In the process of analysis 60 ml of the water samples was transferred into the bubbler by the vacuum transfer technique. The dissolved radon in the water was transferred into pre-evacuated and background counted scintillation cell called Lucas cell. The Lucas cell was stored for 180 minutes to allow radon to attain equilibrium with its daughter products and then it was coupled to a photomultiplier and alpha counting assembly and concentration of radon in drinking water samples have been measured using the relation [25].

$$C_{Rnw} (BqL^{-1}) = \frac{6.97 \times 10^{-2} \times D}{V \times E \times e^{-\lambda T} \times e^{-\lambda \theta} \times (1 - e^{-\lambda t})} \quad (1)$$

where, D is difference between background counts and sample counts, V is the volume of water, E is efficiency of the scintillation cell, λ is the decay constant for radon ($2.098 \times 10^{-6} \text{ s}^{-1}$), T is counting delay after sampling (sec), t is counting duration in (sec), θ is build up time in the bubbler (sec) [25].

3.1. Estimation of dose due to radon in water samples

The annual effective doses for inhalation and ingestion from radon in water have been calculated by using the equation [26].

$$(\mu Sv y^{-1}) = C_{RnW} \times R_{aW} \times I \times DCF \quad (2)$$

Where, D_{In} is the effective dose for inhalation, C_{RnW} is the radon concentration in water ($Bq \text{ l}^{-1}$ or $kBq \text{ m}^{-3}$), R_{aW} is the radon in air to the radon in water (10^{-4}), F is the equilibrium factor between radon and its progenies (0.4), I is the average indoor occupancy time per individual (7000 h a^{-1}) and DCF is the dose conversion factor for radon exposure ($9 \text{ nSv (Bq h m}^{-3}\text{)}^{-1}$) [26].

$$D_{Ig} (\mu Sv y^{-1}) = C_{RnW} \times C_w \times EDC \quad (3)$$

Where, D_{Ig} is the effective dose for ingestion, C_{RnW} is the radon concentration in water ($Bq \text{ l}^{-1}$), C_w is the weighed estimate of water consumption (60 L a^{-1}) and EDC is the effective dose coefficient for ingestion (3.5 nSv Bq^{-1}), respectively. Dose to the stomach and lungs have been obtained from the product of tissue weighting factor for lung and stomach with annual effective doses for inhalation and ingestion [26].

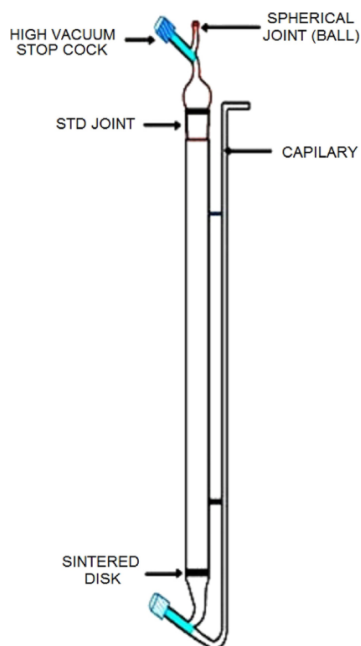


Fig.2. Schematic diagram of Radon bubbler [25]

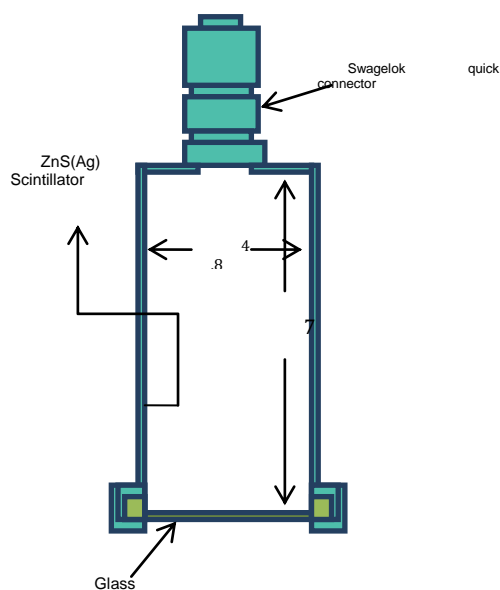


Fig.3. Schematic diagram of Scintillation cell (Lucas cell)[25]

4. Results and discussion

4.1. Analysis of ^{222}Rn concentration in drinking water samples

Concentration of ^{222}Rn in and around Nuggihalli-Holenarsipur schist belts for drinking water was performed first time. Average values of ^{222}Rn concentrations inhalation, ingestion and annual effective doses are estimated. Concentration of ^{222}Rn in drinking water varies from $3.61 \pm 0.23 \text{ Bq l}^{-1}$ to $142.38 \pm 9.76 \text{ Bq l}^{-1}$ with an average value of $54.40 \pm 4.14 \text{ Bq l}^{-1}$. Radon concentration in drinking water samples are found higher at Shravanabelagola, Channarayapatna, Chikkur, Sri Jenukallu Siddeshwara temple, Hirekal Siddeshwara temple, Adichunchanagiri, Gollarahatti and Ballenahalli, rocks in these locations are attributed by Granitoides [24]. Minimum concentration has been found at Doddahalli Kaval, Honnamarnahalli, Bachanahalli, Siddarahatti and Kumbenahalli, rocks in these locations are attributed by metabasic rocks [24]. Radon in water depends on the local geology, radium and uranium dissolved in water and hydro geological conditions and rock of the aquifer and the presence of thrusts, faults and shears

which facilitate upward migration of radon gas [27]. US Environment Protection Agency has proposed that the allowed maximum contamination level (MCL) for radon concentration in water is 11 Bq l^{-1} [28]. It was observed that 64% of the samples had radon concentration below this recommended value. The remaining 36% of the samples from the study area the recorded values were found to be higher than the prescribed value. Similarly, World Health Organization (WHO) has prescribed 100 Bq l^{-1} of radon activity in water as a safe limit for drinking purposes [29]. From this study it is evident that except 17% all remaining water samples analyzed can be considered as safe for household use and drinking according to the limits of WHO.

The estimated inhalation and ingestion dose is varies from $9.11 \mu\text{Sv y}^{-1}$ to $358.79 \mu\text{Sv y}^{-1}$ with an average value of $137.09 \mu\text{Sv.y}^{-1}$ and $0.76 \mu\text{Sv.y}^{-1}$ to $29.90 \mu\text{Sv y}^{-1}$ with an average value of $11.42 \mu\text{Sv y}^{-1}$ respectively. The estimated annual effective dose due to radon inhalation and ingestion varies from 9.87 to $388.69 \mu\text{Sv y}^{-1}$ with an average value of $148.51 \mu\text{Sv y}^{-1}$.

The dose contribution to the lung due to inhalation varies from $1.09 \mu\text{Sv y}^{-1}$ to $43.02 \mu\text{Sv y}^{-1}$ with an average value of $16.44 \mu\text{Sv.y}^{-1}$. The dose contribution to the stomach varies from $0.09 \mu\text{Sv y}^{-1}$ to $3.58 \mu\text{Sv y}^{-1}$ with an average value of $1.37 \mu\text{Sv y}^{-1}$. Annual effective dose of six locations are found to be greater than the safe limit of 100 Bq l^{-1} [29].

Conclusion:

Radon concentration in drinking water samples are found higher at the locations attributed by Granitoides. Minimum concentration has been found at the locations attributed by metabasic rocks. At six locations Annual effective dose are greater than the safe limit of 100 Bq l^{-1} .

Table 5.10 Average radon concentration and their annual effective doses in drinking water samples collected from various locations of Nuggihalli-Holenarsipur schist belts.

Recent Trends in Physics with Emphasis on Discovery of God Particle

| Location | Location | | C_{Rnw} $Bq l^{-1}$ Mean $\pm SD$ | D_{in} $\mu Sv y^{-1}$ | Dose to lungs μSv y^{-1} | Dig μSv y^{-1} | Dose to stomach $\mu Sv y^{-1}$ | Annual effective dose $\mu Sv y^{-1}$ |
|--|------------------|-----------------|--|-----------------------------|---|-----------------------------|---------------------------------------|--|
| | Latitud e | Longitude | | | | | | |
| Nuggihalli schist belt | | | | | | | | |
| Nagamangala | 12°49'41" N | 76°45'25" E | 6.14 ± 0.66 | 15.46 | 1.85 | 1.29 | 0.15 | 16.75 |
| Gollarahatti | 13°19'44" N | 76°18'16" E | 102.47 ± 5.78 | 258.22 | 30.96 | 21.52 | 2.57 | 279.74 |
| Shravanabelagola | 12°51'29" N | 76°29'13" E | 133.91 ± 8.86 | 337.46 | 40.46 | 28.12 | 3.36 | 365.58 |
| Adichunchanagiri | 13°01'30" N | 76°44'37" E | 111.60 ± 6.78 | 28.22 | 33.72 | 23.44 | 2.80 | 304.66 |
| Channarayapatna | 12°54'00" N | 76°23'23" E | 45.27 ± 4.32 | 114.08 | 13.68 | 9.51 | 1.14 | 123.59 |
| kalkere | 12°58'35" N | 76° 25'34" E | 35.09 ± 2.67 | 88.43 | 10.60 | 7.37 | 0.88 | 95.97 |
| Nuggehalli | 12°58'50" N | 76°31'53" E | 52.48 ± 3.89 | 132.26 | 15.86 | 11.02 | 1.32 | 143.28 |
| Kebballi | 12°58'56" N | 76°06'49" E | 54.13 ± 4.32 | 136.40 | 16.35 | 11.37 | 1.36 | 147.77 |
| Honnamarnahalli | 12°58'26" N | 76°36'20" E | 3.64 ± 0.58 | 9.17 | 1.10 | 0.76 | 0.09 | 9.93 |
| Siddarahatti | 12°58'56" N | 76°26'35" E | 3.90 ± 0.23 | 9.83 | 1.18 | 0.82 | 0.10 | 10.65 |
| Bhoovanahalli | 12°26'32" N | 76°05'11" E | 66.65 ± 5.03 | 167.96 | 20.14 | 14.00 | 1.67 | 181.96 |
| Rayasamudra kaval | 13°10'31" N | 76°18'20"E | 69.21 ± 5.73 | 174.40 | 20.91 | 14.53 | 1.74 | 188.93 |
| Lalanakeri | 13°07'48" N | 76°19'02" E | 62.58 ± 4.83 | 157.69 | 18.19 | 13.14 | 1.57 | 170.83 |
| Basavanapura | 13°01'24" N | 76°30'05" E | 54.13 ± 3.86 | 136.42 | 16.36 | 11.37 | 1.36 | 147.79 |
| Gandasi | 13°07' 39" N | 76°24'02" E | 7.01 ± 1.02 | 17.67 | 2.12 | 1.47 | 0.11 | 12.39 |
| Hebbaranahalli | 13°13' 28" N | 76°14'36" E | 5.24 ± 0.32 | 13.21 | 1.58 | 1.10 | 0.13 | 14.31 |
| Annapura | 13°14' 43 " N | 76°14'51" E | 44.98 ± 3.90 | 113.36 | 13.59 | 9.45 | 1.13 | 122.80 |
| Sri Jenukallu Siddeshwara Temple | 13°17' 49 " N | 76°12'55" E | 142.38 ± 9.76 | 358.79 | 43.02 | 29.90 | 3.58 | 388.69 |
| Arsikere | 13°19' 02" N | 76°15'20" E | 71.53 ± 4.67 | 180.25 | 21.61 | 15.02 | 1.80 | 195.27 |
| Chikkur | 13°21' 35" N | 76°10'46" E | 122.45 ± 8.85 | 308.59 | 37.00 | 25.72 | 3.08 | 334.30 |

Recent Trends in Physics with Emphasis on Discovery of God Particle

| | | | | | | | | |
|---|-----------------|----------------|--------------------------|---------------|--------------|--------------|-------------|---------------|
| Hirekal siddeshwara temple | 13°23' 39" N | 76°18'35" E | 117.97 ± 8.79 | 297.29 | 35.64 | 24.77 | 2.96 | 322.06 |
| Holenarsipur schist belt | | | | | | | | |
| Doddahalli Kaval | 12°39' 32" N | 76°18'53" E | 6.97 ± 0.53 | 17.57 | 2.11 | 1.46 | 0.18 | 19.04 |
| Bachanahalli | 13°11' 53" N | 76°18'52" E | 3.61 ± 0.98 | 9.11 | 1.09 | 0.76 | 0.09 | 9.87 |
| Holenarasipura | 12°47' 12" N | 76°14'33" E | 45.06 ± 2.34 | 113.56 | 13.62 | 9.46 | 1.13 | 123.02 |
| Kumbenahalli | 12°51' 30" N | 76°18'59" E | 4.54 ± 0.78 | 11.44 | 1.37 | 0.95 | 0.11 | 12.39 |
| Mavinakere | 12°50' 08" N | 76°10'24" E | 34.93 ± 2.76 | 88.02 | 10.55 | 7.34 | 0.88 | 95.36 |
| Athichowdenahalli | 12°53' 19" N | 76°17'53" E | 44.96 ± 7.12 | 113.30 | 13.58 | 9.44 | 1.13 | 122.74 |
| Ambuga | 12°55' 16" N | 76°09'06" E | 96.29 ± 5.78 | 242.64 | 29.09 | 20.22 | 2.42 | 262.86 |
| Ballenahalli | 12°56' 50" N | 76°17'22" E | 95.40 ± 5.63 | 240.41 | 28.82 | 20.03 | 2.40 | 260.44 |
| Kowshika | 12°57' 22 "N | 76°08'33" E | 36.21 ± 1.82 | 91.26 | 10.94 | 7.61 | 0.91 | 98.87 |
| Shantigram | 12°59' 01" N | 76°13'08" E | 36.16 ± 3.83 | 91.12 | 10.93 | 7.59 | 0.91 | 98.71 |
| Dandiganahalli | 12°58' 22" N | 76°16'25" E | 71.62 ± 7.12 | 180.47 | 21.64 | 15.04 | 1.80 | 195.51 |
| Hassan | 13°00' 45" N | 76°06'14" E | 27.59 ± 2.35 | 69.53 | 8.34 | 5.79 | 0.69 | 75.32 |
| Attavara | 13°05' 46" N | 76°15'16" E | 36.44 ± 7.12 | 91.82 | 11.01 | 7.65 | 0.92 | 99.48 |
| Haranhalli | 13°14' 52" N | 76°13'22" E | 69.21 ± 4.78 | 174.40 | 20.91 | 14.53 | 1.74 | 188.93 |
| Halebeedu | 13°12' 47" N | 75°59'35" E | 36.65 ± 1.26 | 92.37 | 11.07 | 7.70 | 0.92 | 100.06 |
| Minimum | | | 3.61 ± 0.23 | 9.11 | 1.09 | 0.76 | 0.09 | 9.87 |
| Maximum | | | 142.38 ± 9.76 | 358.79 | 43.02 | 29.90 | 3.58 | 388.69 |
| Average | | | 54.40 ± 4.14 | 137.09 | 16.44 | 11.42 | 1.37 | 148.51 |

References

1. Alam, M. N., Chowdhry M. I., Kamal M., Ghose S., Islam M. N., Awaruddin M.: 'Radiological assessment of drinking water of the Chittagong region of Bangladesh', *Radiat. Prot. Dosim.*, 82, 207–214, 1993.
2. Dickson, B.L.: 'Radium in groundwater. In: The environmental behaviour of radium', vol 310. International 27th Atomic Energy Agency Reports Series No.1. 335–372, 1990.
3. Banks, D., Royset, O., Strand, T., Skarphagen, H.: 'Radioelement (U, Th, Rn) concentrations in Norwegian bedrock groundwaters', *Environ. Geol.* 25,165–180, 1995.
4. Ramola, R.C., Choubey, V.M., Saini, N.K., Bartarya, S.K., 'Occurrence of radon in drinking water of Dehradun City, India', *Indoor Built Environment* 8, 67–70, 1999.
5. Wiegand, J., 'A guideline for the evaluation of the soil radon potential based on geogenic and anthropogenic parameters', *Environ. Geol.* 40, 949–963, 2001.
6. Hoehn, E., Von Gunten, H.R., 'Radon in groundwater: a tool to assess infiltration from surface waters to aquifers', *Water Resour. Res.*, 25, 1795–1803, 1989.
7. Choubey, V.M., Ramola, R.C., 'Correlation between geology and radon levels in groundwater, soil and indoor air in Bhilangana Valley, Garhwala Himalaya, India', *Environ. Geol.* 32 (4), 258-262, 1997.
8. Kuntsson, G., Olofsson, B., 'Radon content in groundwater from drilled wells in the Stockholm regions of Sweden', *NGU-bulletin*, 79-85, 2002.
9. Ningappa, C., Sannappa, J., Karunakara, N., 'Study on radionuclides in granite quarries of Bangalore rural district, Karnataka, India', *Radiat. Prot. Dosim.* 131(4), 495-502, 2008.
10. Yalim, H.A., Akkurt, I., Ozdemir, F.B., Unal, R., Sandıkcıoğlu, A., Akkurt, A., 'The measurement of radon and radium concentrations in well water in the Afyonkarahisar area of Turkey', 'Indoor. Built. Environ.' 16, 77–81, 2008.
11. Choubey, V. M., Mukherjee, P. K., Bajwa, B. S., Walia, V., 'Environ Geological and tectonic influence on water– soil–radon relationship in Mandi–Manali area, Himachal Himalaya', *Environ. Geol.* 52, 1163–1171, 2007.

12. Walia, V., Bajwa, B. S., and Virk, H.S., 'Radon monitoring in ground water of some area of Himachal Pradesh and Punjab states, India' *J. Environ. Monit.*, 5, 122–125, 2003.
13. Choubey, V. M., Bartarya, S. K. and Romala, R. C., 'Radon in groundwater of Eastern Doon Valley, outer Himalaya', *Radiat. Meas.* 36, 401–405, 2003.
14. Choubey, V. M., Bartarya, S. K., and Romala, R. C., 'Radon in groundwater of Eastern Doon Valley, outer Himalaya', *Radiat. Meas.* 36, 401–405, 2003.
15. Brutsaert, W. F., Norton, S. W., Hess, C. T., Williams, J. S., 'Geologic and hydrologic controlling Radon-222 in ground water in Maine, *Groundwater*, 19, 407-417, 1981.
16. WHO, International standards of drinking water, 3rd edn. , 1971.
17. Lisa, A.S., 'Radon-222 in the Ground Water of Chester County, Pennsylvania' 'Water Resources Investigations Report, 98, 41-69, 1998.
18. Cho, J.S., Ahn, J.K., Kim, H.C., Lee, D.W., 'Radon concentrations in groundwater in Busan measured with a liquid scintillation counter method', *J. Environ. Radioact.*, 75(1), 105–112, 2004.
19. Singh, J., Singh, H., Singh, S., Bajwa, B.S., 'Estimation of uranium and radon concentration in some drinking water samples', *Radiat. Meas.* 43, 523–526, 2008.
20. Prasad, G., Prasad, Y., Gusain, G. S., and Romala, R. C., 'Measurement of radon and thoron levels in soil, water and indoor atmosphere of Budhakedar in Garhwal Himalaya, India', *Radiat. Meas.* 43, 375–379. 2008.
21. Nikolopoulos, D., and Louizi, A., 'Study of indoor radon and radon in drinking water in Greece and Cyprus: implications to exposure and dose', *Radiat. Meas.* 43, 1305–1314, 2008.
22. Marques, A. L., Dos Santos, W., and Geraldo, L. P., 'Direct measurements of radon activity in water from various natural sources using nuclear track detectors'. *Appl. Radiat. Isot.* 60, 801–804, 2004.
23. Walia, V., Bajwa, B. S., and Virk, H. S., ' Radon monitoring in ground water of some area of Himachal Pradesh and Punjab states, India', *J. Environ. Monit.* 5, 122–125, 2003.
24. Dinesh Pandit, R., Chandrashekar and Namratha, 'A geological field report on Nuggihalli-Holenarsipur schist belts, Geological Society of India, 2012.
25. Raghavayya, M., Iyengar, M. A. R., Markose, P. M., 'Estimation of Radium-226 by emanometry, *Bull Radiat. Prot.*, 3, 11–14, 1980.

26. UNSCEAR., 'Sources, effects and risks of ionizing radiation', United Nations, New York, 1–35, 2000.
27. Choubey, V. M., Mukherjee, P. K., Bajwa, B. S., Walia, V., 'Environ. Geological and tectonic influence on water–soil–radon relationship in Mandi–Manali area, Himachal Himalaya', Environ. Geol. 52, 1163–1171, 2007.
28. United States Environmental Protection Agency (USEPA), 'National primary drinking water regulations' radionuclides, proposed rule. U.S. Government Printing Office, 1991.
29. The World Health Organization (WHO), 'Guidelines for Drinking Water Quality', 1993.

* * * * *

- ❖ **Dr. R. S. Niranjana**, Department of Physics, Govt. First Grade College for Women, Holenarasipura, Karnataka, India, Ph: 9964529059, **E-mail:** niranjanrs1977@gmail.com
- ❖ **V. Nandakumar, C. N. Harshavardhana**, Department of Mathematics, Government First Grade College for women Holenarasipura, Karnataka, India.
- ❖ **Dr. C. Ningappa**, Department of Physics, Vidya Vikas Institute of Engineering and Technology, Mysore-570028, Karnataka, India.

Intermolecular Interactions Studies in Binary Mixtures of Curcumin Particles with Primary Alcohols



- Dr. Manjunatha .M. S
- Dr. Sannappa .J

Abstract:

Ultrasonic velocity, density, and viscosity for Curcumin with Primary alcohols binary mixture viz., 1-propanol is determined at 303K using Ultrasonic Interferometer. The result shows values for thermodynamic parameters such as adiabatic compressibility, intermolecular free length, free volume, acoustic impedance, and the molecular association have been calculated and tabulated. The data are used study to correlate the properties and relevant interaction parameters with the nature of intermolecular interaction between the binary mixture compounds. The results show a nonlinear variation of acoustical parameters which confirms the presence of molecular associative nature.

Key words: Intermolecular interaction, Curcumin, Ultrasonic velocity, Adiabatic compressibility, intermolecular free length.

INTRODUCTION

Curcumin (Diferuloylmethane) is a natural yellow dye derived from the rhizome of *Curcuma Longa* Linn. Curcumin is a poly phenol di-ketone from extracted from turmeric [1]. It is yellow in color and is responsible for most of the therapeutic effects of turmeric used widely as a food coloring [2]. It has been known as an Ayurvedic medicine for centuries on the Indian subcontinents a pharmacological safety drug Because of its antioxidant and anti-inflammatory effect; it has wide application in medical fields. Alcohols are industrially and scientifically important organic compounds and its property is largely depending on hydroxyl groups. Interaction between two or more molecules is called intermolecular interaction. Intermolecular interaction is particularly important in terms of how

molecules interact. Inter molecular forces are responsible intermolecular interaction [3].

To understand the intermolecular interaction, it is necessary to determine the various ultrasonic parameters, which are related to molecular association.

I. MATERIALS AND METHODS

Analytical research grade of Primary Alcohols were purchased from SD Fine Chemicals Ltd, India and purified by the standard methods [4, 5, 6]. Curcumin isolated from local turmeric rhizome.

The turmeric rhizomes are powdered and sieved through a mesh of 0.5mm thickness mesh to obtain uniform size of sample. It is mixed with acetone to get mixture of oil and a resin. It mixed with solvent and kept for overnight to get a yellow precipitate of Curcumin. The precipitate is washed and purified for several times with solvent. Various concentrations of the binary liquid mixtures were prepared in terms of mole fraction varied from 0.1 to 0.7.

An ultrasonic interferometer supplied by M/s. Mittal Enterprises, New Delhi, having the maximum frequency 2 MHz with an overall accuracy of $\pm 2 \text{ ms}^{-1}$ has been used for ultrasonic velocity measurement.

The density of pure liquids and liquid mixtures are determined using a 10 ml specific gravity bottle by relative measurement method with an accuracy of $\pm 0.1\text{mg}$. An Ostwald's viscometer which is 10 ml capacity is used for the viscosity measurement of pure liquids and experimental liquid mixtures.

Ultrasonic velocity is calculated for using relation

$$U = n \lambda \text{ m/s} \quad (1)$$

Adiabatic compressibility

$$\beta = \frac{1}{\rho U^2} \text{ ms}^2 \text{ kg}^{-1} \quad (2)$$

Intermolecular free length

$$L_f = \sqrt{\beta} K_T \text{ Kg m}^{-2} \text{ s}^{-1}$$

Acoustic impedance

$$Z = U\rho \quad (3)$$

Free volume

$$V_f = \left[\frac{MU}{K\eta} \right]^{\frac{3}{2}} \quad (4)$$

Where n , ρ , η , M is the frequency of the ultrasonic wave, density, viscosity and molecular weight of the mixtures. K and K_T are the constant. They are temperature dependent and the values are 361×10^{-6} and 4.28×10^9 respectively.

RESULT AND DISCUSSION

The experimentally determined values of density (ρ), viscosity (η) and ultrasonic velocity (U) of all the pure liquids and the mixture are tabulated in Table - 1 at a temperature 303K. The values of adiabatic compressibility (β), inter molecular free length (L_f), free volume (V_f) and acoustical impedance (Z) at the temperatures of 303k are reported in Table - 2.

From the table 1, the results show value for density and viscosity is increases with the increasing the mole fraction of the binary mixture. But a reverse trend is observed for ultrasonic velocity, that is with all the weight fraction the ultrasonic velocity decreases and reaches a minimum value. Similar result is reported by Pandey et al [7]. The nonlinear variation of ultrasonic velocity with mole concentration of primary alcohol indicates the existence of interaction between the curcumin with primary alcohols.

The data from table 1 shows adiabatic compressibility is increasing with the increasing the mole concentration of the Primary alcohols. The result shows that a slightly steeper values for the binary mixture of curcumin with primary alcohols. The adiabatic compressibility shows a reverse trend as that of ultrasonic velocity. The structural geometry of molecules in the mixture is depends on the adiabatic compressibility, the increasing in the adiabatic compressibility showing the progressive intermolecular interaction between the molecules [8].

The variation of ultrasonic velocity in a mixture depends upon the increase or decrease of intermolecular free length [9]. The results show the variation of intermolecular free length for different value concentration. Since the free length L_f is proportional to the adiabatic compressibility (β) the same trend of variation similar to the variation of adiabatic compressibility has observed. However, the increase in adiabatic compressibility and inter molecular length also be attributed to the internal interaction between the molecules of the binary mixtures [10].

The value for acoustic impedance (Z) from table 1 shows, it is gradually decreasing with increasing the mole concentration of the primary alcohols. This result shows presence of interaction between the curcumin and primary alcohols. Table - 1 shows the value of free volume with variable concentration of primary alcohols. The free volume is decreases with increasing the mole concentration of the alcohols with. This result confirms inter molecular interaction between the curcumin with primary alcohols.

Table 1

VALUE OF ULTRASONIC VELOCITY (U), DENSITY (P) AND VISCOSITY (H)

| Mole Fraction | | For 1-Propanol with Curcumin | | |
|----------------|----------------|------------------------------|--|-----------------------|
| X ₁ | X ₂ | ρ in Kg m ⁻³ | $\eta \times 10^3$ in Ns m ⁻² | U in ms ⁻¹ |
| 0.1 | 0.7 | 756.21 | 0.7835 | 1453 |
| 0.2 | 0.6 | 768.43 | 0.8116 | 1356 |
| 0.3 | 0.5 | 792.11 | 0.8745 | 1289 |
| 0.4 | 0.4 | 860.08 | 0.9612 | 1174 |
| 0.5 | 0.3 | 883.22 | 1.1281 | 1014 |

TABLE 2

VALUES OF ADIABATIC COMPRESSIBILITY (B), NTERMOLECULAR FREE LENGTH (LF), FREE VOLUME (VF) AND SPECIFIC ACOUSTIC IMPEDANCE (Z).

| Mole Fraction | | For 1-Propanol with Curcumin | | | |
|----------------|----------------|---|--------------------------------------|--|--|
| X ₁ | X ₂ | $\beta \times 10^{-10}$ N ⁻¹ m ⁻² | L _f x 10 ⁻¹⁰ m | V _f x 10 ⁻⁷ ms ⁻¹ | Z x 10 ³ N·s/m ³ |
| 0.1 | 0.7 | 6.2636 | 1.579 | 1.859 | 1098.7 |
| 0.2 | 0.6 | 7.0774 | 1.678 | 1.466 | 1041.9 |
| 0.3 | 0.5 | 7.5981 | 1.739 | 1.229 | 1021.0 |
| 0.4 | 0.4 | 8.4357 | 1.832 | 0.096 | 1009.7 |
| 0.5 | 0.3 | 11.011 | 2.093 | 0.072 | 895.58 |

II. CONCLUSION

From measured ultrasonic velocity, density and viscosity, the related acoustical parameter for the binary mixture are calculated. It is noticed that ultrasonic velocity is decreases with increasing mole concentration and adiabatic compressibility is increases with increasing mole concentration. Inter molecular free length is increases and free volume increases with concentration. This result shows existences a molecular association and it can be conclude that there is a intermolecular interaction present in the binary mixture.

REFERENCES


1. G.K. Jayaprakasha, J.M. Rao, J. Agric. Food Chem, 50 (13), 3668-72, 2000.
2. C.A.C. Ara'ujo and L.L.Leon, "Biological Activities of Curcumalonga L", Mem Inst Oswaldo Cruz, Rio de Janeiro 96, 723-728, 2001.
3. P.E. Savage "Organic chemical reactions in supercritical water", Chem.Rev, 99, 603-622,1999.
4. A weissberger "Technique of Organic chemistry", New York, Wiley Interscience, 1970.
5. A I Vogel " Text book of practical organic chemistry", Longman, 1957, London.
6. S. Thirumaran and K. Job Sabu. Ind J Pure & Appl Phys., 47, 87, 2009.
7. S. Thirumaran and J Earnest Jaya Kumar. Ind J Pure & Appl Phys. 47, 265, 2009.
8. H C Pandey, R P Jain and J D Pandey, "Temperature and pressure dependence of free volume and intermolecular free length "Acustica 34, 123,1975.
9. V A Tabhane and B A Patki, Acoustica. 52, 44 1982.
10. Nithya, S. Nithiyantham, S. Mullainathan, and M. Rajasekaran, "Ultrasonic Investigation of Molecular Interactions in Binary Mixtures at 303 K", E-Journal of Chemistry, 6, Pages 138-140,2009.
11. R. S.Thirumaran and P.Thenmozi, "Study of molecular interaction in ternary liquid mixture by ultrasonic veleocity measurements", Asian J. Applied Sci, 3(2), 153-159, 2010.

* * * * *

❖ **Manjunatha M. S**, Department of Physics, Government First Grade College, Chamarajanagar, Karnataka, India, **Ph:** 9242221982, E-mail: manjumsphy@gmail.com

❖ **Dr. Sannappa J**, Professor and Chairman, Department of Studies and research in Physics, Kuvempu University, Shankaraghatta, Shimoga, Karnataka, India, 577451, **Ph:** 9449089870 E-mail: sannappaj2012@gmail.com

Comparative Study of the Elemental Concentration in Soil Sample of Open Site and Solid Waste Sites of Bengaluru Region of Karnataka, India

- 
- Dr. Sudarshan .M, Gowtham .S
 - Sathya Narayana .P, Shilpa .D
 - Jagadeesha B. G

Abstract

Bengaluru is one of the most polluted cities in India. Industrial activities are one of the major anthropogenic activities in the region, which increases the accumulation of heavy metals concentration in soil. In view of this, 36 soil samples were collected in the dumped solid waste sites and un-dumped site of Bangalore. The trace element concentration in soil of different locations were found in the order Si > Al > Fe > K > Na > Ca > Ti > P > Mn > Ba > Sr > Cr > V > Ni > Zn > Cu > Pb > As. The elemental concentration in soil such as Si, Al, Ti, Ni, Cr, V and Pb were exceeded than the permissible limit. The study showed that the elemental concentration in dumped solid waste site was comparable with the un-dumped site of Bangalore.

Key words ED-XRF Spectrometer, Trace elements, Statistical analysis, Pollution load Index.

Highlights

- Bengaluru is one of the most polluted cities in India.
- The trace element concentration in soil of different locations were found in the order Si > Al > Fe > K > Na > Ca > Ti > P > Mn > Ba > Sr > Cr > V > Ni > Zn > Cu > Pb > As. .
- The elemental concentration in soil such as Si, Al, Ti, Ni, Cr, V and Pb were exceeded than the permissible limit

Introduction:

The soil pollution is the major problem in the environment. Trace elements in soils are necessary to understand the spatial variation, behavior, sources and pollution condition. The trace element in soil originates from the anthropogenic and natural process, leads to spatial variations in elemental concentration (Libo Hao et al., 2016). Naturally trace elements are emitted to the atmosphere from biogenic sources, soil-derived dusts, volcanic emissions and sea salt aerosols (Fayme Cai et al., 2016). The accumulation of trace element can be significant in the areas of intense human activities like urban and industrial area (Wajid Rehman et al., 2008). The determination of geochemical background, concentration of point source pollution and thresholds of trace elements are the key processes for the soil environmental quality assessment.

Trace elements in soils are necessary to understand the spatial variation, behavior, sources and pollution condition. Trace element in soil originates from the anthropogenic and natural process, leads to spatial variations in elemental concentration (LiboHaoet al., 2016). Naturally heavy metals are emitted to the atmosphere from biogenic sources, soil-derived dusts, volcanic emissions and sea salt aerosols (Fayme Cai et al., 2016). The accumulation of trace element can be significant in the areas of intense human activities like urban and industrial area(WajidRehmanet al., 2008). The determination of geochemical background, concentration of point source pollution and thresholds of heavy metals are the key processes for the soil environmental quality assessment.

Bengaluru is one of the most polluted cities in India (CPCB, 2019). There are many dumped sites contains tonnes of both organic and inorganic wastes in the city. In those sites, some of the locations were selected which are located outside of the Bangalore where agricultural lands are present, because of those sites surrounding land will affected by the solid wastes and it will affect all the living beings. Over seven years, open dumping of solid waste has created mounds the size of hillocks in the Avalahalli forest area and near Mavallipura of Southern Bengaluru. The solid waste occasionally set on fire. Since by inhaling the gas, people of the region suffering from serious health issues [Nguyen et. al., 2009]. The present study will show light on the serious health issues of the people who are living in the solid waste dumped sites.

Materials and methods:

A total of 36 soil samples were collected in open site and solid waste sites of southern Bangalore. The soil were collected by marking the surface of soil in the shape of a circle about 15 cm radius and digging the soil in and around the mark about 15 cm and collected in an air tight polythene bags. The soil sample is then transferred to the laboratory. Then, the sample were transferred to porcelain tray and dried in an oven at 110 °C at 24hours to remove the moisture content. The samples were crushed and sieved in a 250-micron sieve. To estimate the trace elemental concentrations, the soil samples were made into pellets (1 mm thick and 13 mm diameter) using a tabletop pelletizer of a pressure of about 100 – 110 kg/cm² for 1 min (Ch. Bino Devi et al., 2011). Equal amount of soil (150 mg) were taken for the preparation of pellets. Three pellets were prepared from each sample for the analysis and their average was taken. These pellets form the representative of the sample. The entire soil samples were carried to Energy Dispersive X-ray Fluorescence (ED-XRF) spectrometer for the estimation of elemental concentration. The sampling location were shown in the below Table 1.

The ED-XRF spectrometer is very sensitive instrument for the analysis of trace elements in the environmental matrices. The sample size was chosen as per the protocol for the measurement keeping in view of the Minimum Detection Limit (MDL) and statistics (Sudarshan, et al., 2011). There are several advantages in the measurement of trace elements using thin samples than thick samples by the ED-XRF spectrometer (T1ras oglu et al., 2006). The absorption and enhancement effects were found to be more dominant in thicker samples. For thin samples, however, these effects could be corrected or neglected (T1ras oglu et al., 2006). The ED-XRF spectrometer consists of oil cooled Rh anode X-ray tube, with maximum voltage of about 50 kV and current of about 1 mA. The analysis was carried out using different filter in a vacuum condition between the source and sample, for optimum detection of elements. The EDXRF spectrometer has a Fe filter of about 0.05 mm thickness was used for elements with higher atomic numbers, such as As with voltage of 35 kV and current 500 mA. To determine the elements with lower atomic number ($Z < 19$) such as Na, Si and Al, filter was not used. The voltage was maintained at 8 kV and current at 85 mA. The X-rays were detected using a Si (Li) semiconductor with a resolution of 150 eV at 5.9 keV. The spectra of X-ray fluorescence were quantitatively analyzed using the software ExWIN and

Recent Trends in Physics with Emphasis on Discovery of God Particle

integrated with the system (Raychaudhuri et al., 2008). An overview of the estimation of trace element is shown in Fig. 1.

Table 1: Sampled locations.

| Sl.No | Code | Sampling locations | Lattitude and Longitudes | |
|-------|-------------------------------------|--------------------|--------------------------|---------------------------|
| 1 | R1 | Ramagondanahalli | 12.9558° N & 77.7409° E | |
| 2 | R2 | Mavallipura | 13.1193° N & 77.5247° E | |
| 3 | R3 | Doddabyalakere | 13.2957° N & 77.5364° E | |
| 4 | Solid waste dumped locations | R4 | Manduru | 13.0829° N & 77.7381° E |
| 5 | | R5 | Gunduru | 12.8767° N & 77.8378° E |
| 6 | | R6 | Cheemasandhra | 12.9797° N & 77.7616° E |
| 7 | | R7 | Hosapete | 12.9577° N & 77.2261° E |
| 8 | | R8 | Thirumale | 12.9604° N & 77.2534° E |
| 9 | | R9 | Bychapura | 12.96710° N & 77.7291° E |
| 10 | Undumped locations | R10 | Agara | 12.92310° N & 77.6465° E |
| 11 | | R11 | Doddasadenahalli | 12.972442° N & 77.80643°E |
| 12 | | R12 | kallibheemasandhra | 12.66655° N & 77.49687° E |



Figure 1: An overview of estimation of trace element (a) Tabletop palletizer, (b) Pellets in a mould cups, (c) EDXRF-3600 Spectrometer

Results and discussions:

Soil acts as essential source of trace element as well as source of toxic trace elements for plants, animals and for humans. In view of this, study has been carried out to estimate the baseline data on trace element concentration of soil in and around the region of Bangalore.

Calcium concentration was found to be highest in R10(Undumped site) and below the average crustal value 22100 ppm (Turkian and Wedpohl, 1961). The highest concentration of potassium was observed in R7(Dumped site) and below the average crustal value 26600 ppm (Turkian and Wedpohl, 1961). The higher concentration of manganese was observed in R10(Undumped site) and below the crustal average value 850 ppm (Turkian and Wedpohl, 1961). The higher concentration of zinc was observed in R1(Dumped site) and below the crustal average value 95 ppm (Turkian and Wedpohl, 1961). The concentration of Zn is absorbed by the clay minerals and carbonates (Krishna et al., 2007). The higher concentration of strontium was observed in R7(Dumped site) location due to the presence of limestone(Krishna et al., 2007) and found below the average crustal value 300 ppm (Turkian and Wedpohl, 1961). However, the concentration of Strontium is within the permissible limit.

The highest silicon concentration was observed in R4(Dumped site) higher than the average crustal value 73,000 ppm (Turkian and Wedpohl, 1961). The highest concentration of aluminum was observed in R5(Dumped site) and higher than the average crustal value 80000 ppm (Turkian and Wedpohl, 1961). In R10(Undumped site) location, the Titanium concentration was highest. The average concentration of Titanium was above the average crustal value 4600 ppm (Turkian and Wedpohl, 1961). The highest concentration of Nickel was observed in R3(Dumped site) location due to the anthropogenic activities and industrial activities in the region (Geological survey of India, 2006). The average concentration of Nickel was exceeded the crustal average value 68 ppm (Turkian and Wedpohl, 1961). The obtained iron concentration exceeded the crustal average value 47200 ppm (Turkian and Wedpohl, 1961). The lead concentration exceeded the average crustal value 20 ppm (Turkian and Wedpohl, 1961). This is due to the dumping of chemical and industrial waste (Vandana et al., 2011). The observed Vanadium concentration was above the average crustal value 130 ppm (Turkian and Wedpohl, 1961). The Vanadium concentration increases with increase in organic matter

(Tyler, 2004). The higher concentration was observed in the location R10(Undumped site) due to higher content of organic matter.

Copper is an essential element for human health and plays an important role in metabolic process. However, higher concentration affects liver, immune system, and reproductive ability (ATSDR, 2004b). The highest concentration of copper was observed for the R1(Dumped site) location and it is below the crustal average value 45 ppm (Turkian and Wedpohl, 1961). Copper concentration is more in acidic soil and less in alkaline soil (Ginocchio et al., 2002). The concentration was high due to the anthropogenic activities in the region (Geological Survey of India, 2006). Anthropogenic activity in the environment is the main source of Chromium and is quite abundant in soil (El-Bady, 2014). The high level of chromium concentration was obtained in the R3(Dumped site) and exceeded the crustal average value 90 ppm (Turkian and Wedpohl, 1961).

Among 18 elements, lowest concentration was observed for As (6.32 ppm) and highest concentration was observed for Si (304679.77 ppm). Due to the greater heterogeneity in the environmental condition, trace element concentration showed high standard deviation. The trace element concentration in soils of different locations are found in the order $Si > Al > Fe > K > Na > Ca > Ti > P > Mn > Ba > Sr > Cr > V > Ni > Zn > Cu > Pb > As$. The obtained values varied due to the different environmental condition. In all sampling locations, the concentration of trace elements such as Ca, K, Zn, Cu, Fe and Sr are lower than the average crustal value (Turkian and Wedpohl, 1961). In case of Si, Al, Ti, Ni, Cr, V and Pb concentrations are greater than the average crustal value due to the industrial activities in the region (Geological survey of India, 2006; BhaskarRao et al., 1991). The usage of bio-degradable and non-biodegradable materials may also affect the soil quality and plant growth. The physical, chemical and biological properties of the soil vary with the use of bio and non-biodegradable materials. The pollution of soil is the major problem in the environment. Results obtained in 2587 Apple Leaf Standard Reference Material is presented in Table 1. The elemental concentration in soil with the sampled location is shown in Fig. 3. The statistical parameters of the elemental concentration is presented in the Table2.

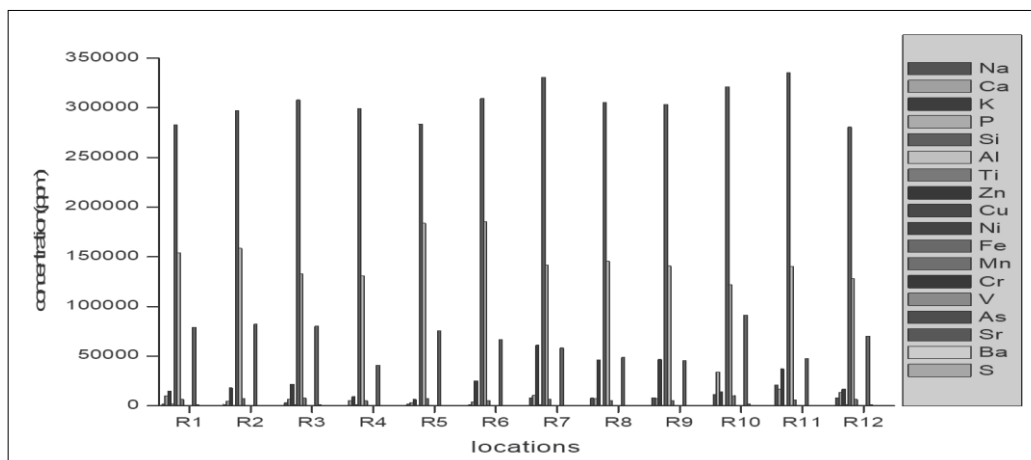


Fig2: Elemental concentration in soil

Table 1: Results obtained in 2587 Apple Leaf Standard Reference Material

| Elements | Certified values | Elemental concentration |
|----------|------------------|-------------------------|
| | (ppm) | (ppm) |
| Mn | 1000 | 820 |
| P | 800 | 823 |
| Cr | 200 | 192 |
| Sr | 50 | 199 |
| V | 150 | 171 |
| Ni | 100 | 105 |
| Zn | 80 | 67 |
| Cu | 70 | 40 |
| Pb | 16 | 38 |
| As | 5 | 6.32 |
| Ca | 2500 | 10248 |
| K | 20000 | 26377 |

Recent Trends in Physics with Emphasis on Discovery of God Particle

Table2: Statistical parameters of the elemental concentration

| | Na | Ca | K | P | Si | Al | Ti | Zn | Cu |
|---------------|---------|---------|---------|--------|----------|----------|---------|-------|------|
| Min | 765.4 | 3014.8 | 6339.4 | 134.4 | 280519.4 | 121944.4 | 4946.8 | 49.1 | 23.7 |
| Max | 21078.7 | 33916.6 | 60856.8 | 1891.6 | 335190.0 | 185455.7 | 10282.8 | 109.4 | 63.3 |
| Average | 6125.9 | 10248.2 | 26377.5 | 823.4 | 304679.8 | 147033.8 | 6586.3 | 67.7 | 40.2 |
| Std.Deviation | 5734.1 | 8103.7 | 16584.4 | 427.2 | 17089.3 | 19510.3 | 1404.9 | 14.8 | 11.8 |
| Skewness | 1.5 | 2.3 | 0.8 | 1.0 | 0.3 | 1.0 | 1.5 | 1.8 | 0.2 |
| Kurtosis | 2.6 | 5.8 | -0.4 | 2.3 | -0.7 | 0.2 | 2.9 | 4.7 | -0.6 |

| | Ni | Fe | Mn | Cr | V | As | Sr | Pb | Ba |
|---------------|-------|---------|--------|-------|-------|-----|-------|------|-------|
| Min | 25.5 | 40794.7 | 545.2 | 0.6 | 94.6 | 6.1 | 39.3 | 8.2 | 364.7 |
| Max | 294.4 | 91219.7 | 1658.4 | 734.3 | 330.4 | 6.6 | 525.4 | 78.3 | 410.2 |
| Average | 105.1 | 65454.7 | 819.9 | 192.6 | 171.8 | 6.3 | 199.4 | 38.8 | 397.6 |
| Std.Deviation | 75.8 | 16173.0 | 321.9 | 202.3 | 61.2 | 0.1 | 163.3 | 16.0 | 12.2 |
| Skewness | 1.3 | -0.1 | 1.7 | 1.6 | 1.3 | 0.4 | 0.7 | 0.8 | -1.7 |
| Kurtosis | 1.8 | -1.5 | 2.6 | 3.2 | 2.6 | 1.8 | -0.8 | 2.8 | 3.5 |

Conclusion:

The main aim of the present study is to compare the trace elemental concentration in dumped solid waste site and un-dumped sites of Bangalore. The trace element concentration in soil of different locations were found in the order Si > Al > Fe > K > Na > Ca > Ti > P > Mn > Ba > Sr > Cr > V > Ni > Zn > Cu > Pb > As. The obtained elemental concentration is varied from region to region. The highest concentration of Silicon was observed in the sampling location R4(Dumped site) location due to the solid waste from industries and community areas is disposed in an unscientific manner. The elemental concentration in soil such as Si, Al, Ti, Ni, Cr, V and Pb were exceeded than the permissible limit. From the present study, the obtained elemental concentration in the dumped solid waste sites is comparable with the un-dumped site of Bangalore.

References :

1. Balaram.V rare earth elements: a review of application, occurrence, exploration, analysis, recycling and environmental impact. *geoscience frontiers*,10(4)2019-1285-1303.
2. Borkert, C.M., Cox.,F.R., Tucker.,M.R.,1998. Zn and Cu toxicity in peanut, soybean, rice and corn in soil mixtures. *Commun. Soil Sci.Plant Anal*,29, 2991-3005.
3. Central Pollution Control Board(CPCB), 2019.
4. Ch bino Devi, Sharath Singh N K ,Raj Mohan Singh N, Sudarshan M.Chakraborty A, and Ram.S.S(2011) trace elements in nungsum, the red edible algae of manipur *international journal of applied biology and pharmaceutical technology*,2(1),0976-4550.
5. Du Laing, G., Van de Moortel, A.M., Moors, W., De Grauwe, P., Meers, E., Tack, F.M.G., Verloo, M.G., 2009. Factors affecting metal concentrations in reed plants (*Phragmites australis*) of intertidal marshes in the Scheldt estuary. *Ecol. Eng.* 35, 310–318.

6. EML.,(1983).procedure manual edited by Herbert L Volchok and gail de planque, 26thedn environmental measurement laboratoty .
7. Fawzy, Manal Ahmed, Badr, Nadia El-Sayed, El-Khatib, Ahmed, Abo-El-Kassem, Amany, 2012. Trace element biomonitoring and phytyoremediation potentialities of aquatic macrophytes in Rivers Nile. Environ. Monit. Assess. 84, 1753-1771.
8. Geological Survey of India, 2006. Geology and mineral resources of the states of India.
9. Kabata-Pendias, A., 2004. Soil–plant transfer of trace elements—an environmental issue. Geoderma 122, 143–149.
10. Keane, B., Collier, M.H., Shann, J.R., Rogstad, S.H., 2001. Metal content of dandelion (*Taraxacum officinale*) leaves in relation to soil contamination and airborne parti-culate matter. Sci. Total Environ. 281, 63–78.
11. LiboHAO ,mitian ,xinyumhao,yuyanzhao,jilonglu , Rongjie bai.2016. Spatial distribution and the source of trace elements in surface soil, changeum china.Insight from stotastic models and geo stastical analysis,geoderma 273,54-63.
12. Nguyen et al,contamination by trace elements at e-waste recycling site in Bengaluru. India chemosphere, 2009,9-5.
13. Shiddamallayya, N., Yasmeen, Azra, Gopakumar, K., 2010. Hundred common forest medicinal plants of Karnataka in primary health care. Indian J. Tradit. Knowl. 9 (1), 90–95.
14. Tiras-oglua, E., Sogut, O., Apaydina, G., Aylıkci, V., Damla, N., 2006. Elemental con- centration analysis in some plant samples by EDXRF at Trabzon. J. Quant. Spectrosc. Radiat. Transf. 102, 396–401.
15. Tianjialiu, et.al. second impact of regional outdoor biomass burning on air pollution in three indian cities :delhi, bengaluru and pune ,atmosphere environment172(2018)83-912.
16. Turekian, K. K.,Wedepohl, K.H., 1961. Distribution of the elements in some major units of the Earth crust. Geol. Soc. Am. Bull. 72, 175-192
17. Wajid rehman, akifzeb,nayyananor ,mohsan nawaz,2008 trace element pollution assesmention various industries of pakistan, environmental geology.55,353-358.
18. Wang, Cheng, Yang, Zhongfang, Yuan, Xuyin, Browne, Patrick, Chen, Lingxiao, Ji, Junfeng, 2013. The influences of soil properties on Cu and Zn

availability in soil and their transfer to wheat (*Triticum aestivum* L.) in the Yangtze River delta region, China. *Geoderma* 193–194, 131–139.

19. World Health Organization, 2005. Quality Control Methods for Medicinal Plant Materials. WHO, Geneva, Switzerland.
20. Yiannisfiamegos, mariabeatridelacalleguntinas, validation strategy for an ED-XRF method to determine trace element in a wide range of organic and inorganic matrices based on fulfillment of performance criteria, *spectrochimica Acta part-b*, 150(2018)59-66.

* * * * *

- ❖ **Dr. Sudarshan M**, UGC-DAE Consortium for Scientific Research, Kolkata Centre, Bidhan Nagar- 700 098, West Bengal, India, Ph: 9831201860, E-mail: sude@alpha.iuc.res.in
- ❖ **Sathya Narayana .P, Gowtham .S, Shilpa .D, Jagadeesha .B .G**, Department of Post Graduate studies and Research in Physics, National College Jayanagar, Bangalore-560070, Karnataka India, E-mail: jagguphysics@gmail.com, Ph: 7338012796, 973181895

Application and Development of MEMS Technology in Industry



○ Raghavendra J L

Abstract

The present paper elaborates a critical evaluation of the applications of micro electromechanical systems (MEMS) in the industrial field. The study has focuses on historical perspective of the sources and improvement of MEMS, as well as the customary and advanced fabrication techniques. The paper emphasizes the process flow of computer-aided design and simulation. The study highlighted the most significant applications of micro systems in the manufacturing and production sectors.

Introduction

Micro-Electro-Mechanical Systems (MEMS) is a mixture of electronic and mechanical elements, sensors, and active components on a silicone sub-layer adjusting the micro-fabrication technology. The MEMS has made it possible to implement an entire system on a single chip, and that is the reason it has obtained an extensive scope of application. The underlying assumption is that the integrated microelectronic circuits are the core element of a system, the MEMS sensors, by way of gathering the information, acknowledges the system to quantify the framework and control the atmosphere. Electronic developments in modern vehicles have grown both in quantity and complexity in recent years. These developments have led to significant vehicle changes, such as higher protection and lower fuel consumption, which in developing countries are critical issues. To a great degree, this is due to the change in the vehicles' electronic systems. All these electronic systems are based on sensor inputs and an increasing proportion of them are manufactured using MEMS technology. The MEMS sensors, because of their significant advantages, compared with the other sensors,

In the automotive industry, they have a range of applications, and now at least 30 sensor nodes of a new vehicle with 100 sensor nodes are MEMS. Over the past decade, hundreds of millions of MEMS sensors in cars have also been used. In this article, a technology scouting approach introduces the most current and key applications of MEMS technology in the automotive industry.

Technology scouting is a powerful instrument that, by detecting emerging technologies and channeling knowledge related to technology into an organization, contributes to technology management.

A Short MEMS History

As a crucial element in process and environmental monitoring, sensors have been around in industrial environments for over a hundred years. In 1889, one of the first accelerometers was developed and was purely mechanical. These sensors have also been developed for a target application with unique operating conditions and are relatively expensive and time-consuming to manage. MEMS (Micro-Electronic-Mechanical-Systems) sensors, smaller and more power-efficient, were originally designed to replace or update some of these industrial sensors. However, the emphasis on industrial markets was side-tracked because, thanks to their scale, efficiency, and low power consumption, MEMS quickly took off in consumer applications such as gaming and smartphones. The probability was Especially important. Produce MEMS in very large amounts using semiconductor technologies. As a consequence, in the last decade, manufacturers have sent tens of billions of sensors into high-volume market applications, with STMicroelectronics shipping more than 15 billion alone. As manufacturing systems become more autonomous and as artificial intelligence and big data processes proliferate,

MEMS MECHANISM AND ITS ADVANTAGES

Mechanical components, actuators, sensors and electronics are incorporated into a micro-manufacturing technology on typical silicon substrates, called micro-electromechanical systems (MEMS) In the dimensions of the micrometre scale, a variety of methodologies along with instruments together form a small structure. The most critical component of every system is the brain, and there are integrated microelectronic circuits here. MEMS are eyes, and control systems are the supporting weapons linked with the microsystems to hear. The overall functioning of systems is

defined in the MEMS system mechanism. In the world, sensors collect information with the assistance of mechanical, optical, thermal, chemical and magnetic phenomena. And the integrated circuits are given this knowledge, and these circuits build a control system to control different parameters responsible for the proper functioning of any micro-electro-mechanical system.

MEMS Device Types and its applications in Industry

A. Accelerometer Speedometer

A mass in a frame is often used by the accelerometer to measure both static acceleration (i.e. gravity) and dynamic accelerations such as vibration, rotation, tilt, shock, etc. Inclometers, shock sensors, concussion sensors, tilt sensors, and motion sensors include devices grouped under accelerometers. Various combinations of axes often come with accelerometers: single-axis devices are often found in automotive crash sensors, and three-dimensional units appear in robotics, vibration-monitoring, and anti-tampering implementation

B. Sensors of Distress

Pressure sensors measure pressure in a MEMS structure by the deflection it causes. There are variants that measure the pressure referred to a vacuum-sealed chamber compared to ambient, or absolute pressure.

C. Magnetometer

Magnetometers A range of physical phenomena are used, such as the Hall Effect, and the mechanical effects caused by magnetic fields are calculated. There are available single- and three-axis models. inertial measurement unit of magnetometer.

By integrating a three-axis accelerometer and a gyroscope into a single unit, the IMU measures both linear and angular acceleration; the IMU may also provide a magnetometer and a pressure sensor to provide information on the three-dimensional orientation and motion of the unit: x-, y-, and z-axis acceleration; pitch, roll, and yaw; altitude; and heading. Unmanned autonomous vehicles (UAVs), robotics and factory automation, avionics, smartphones and tablets, virtual reality, and gaming are among the applications.

Microphones with MEMS

When a sound wave reaches a variable capacitive part consisting of a movable membrane and a fixed backplate, MEMS microphones work by measuring the change in capacitance. They are commonly used in consumer applications such as smartphones and tablets that are space-constrained.

A. MEMS biosensor

In a MEMS system, bio molecular interactions cause an observable motion. For instance, in tuberculosis (TB) detection, when an infected blood sample is placed on it, a MEMS cantilever coated with TB antibodies deflects.

B. MEMS gas sensor

By measuring the resistance shift it causes on the surface of a coated sensor, the MEMS gas sensor detects the presence of a gas. With a standard response time of less than one second, the sensor can detect low concentrations of the target gas. To detect water vapour, a humidity sensor is optimized.

C. RF MEMS switch

To replace unreliable, bulky electromechanical relays in RF switching applications, an RF MEMS switch uses electrostatically actuated cantilever beams in combination with a separate driver IC. There are a range of switch configurations available: ADGM1304 from Analog Unit, for example, comes in an SP4T configuration and can handle DC to 14 GHz signals.

D. MEMS optical actuator,

MEMS optical actuators, such as Texas Instruments' Digital Micro Mirror System (DMD), use MEMS technology to construct a wide range of independently operated mirrors. To switch between "on" and "off" states, each mirror can be tilted under electronic control. The pixel, when on, reflects light through a lens from a projector lamp, making it look white. The light is focused elsewhere in the off state, which makes the pixel appear dim.

E. MEMS oscillators

MEMS oscillators contain a resonator which vibrates from an analog driver chip under electrostatic excitation. With excellent stability, low power consumption and high resistance to electromagnetic interference, MEMS oscillators can produce frequencies from 1Hz to hundreds of MHz (EMI)

APPLICATION OF MEMS IN INDUSTRIAL AUTOMATION

The interdisciplinary nature of MEMS relies on a wide variety of technical areas for engineering, design and manufacture. Material science, control systems, sensors, integrated circuits, mechanical and electrical engineering are among these fields. MEMS, however, includes microcontrollers dedicated to the functioning of the model. The complexity of MEMS is growing with a variety of interdisciplinary fields, but precision will also be improved. In designing these systems, along with integrated circuits, the control system plays an important role. Electronic integrated circuits are manufactured at a very high cost, thereby marginally increasing the cost of these products. Due to advanced semiconductor technology, the MEMS design is very sophisticated; it includes both mechanical moving parts and the electrical design of the device. In electronics, it brings together many technologies such as Complementary Metal Oxide Semiconductor (CMOS), Bi-CMOS (Bipolar Junction Transistor Integration and CMOS Technology), Silicon on Insulator (SOI), Pipelining and single-chip manufacturing. MEMS technology has provided sensitivity, reliability, scalability and cost-effective design. In the area of automation, it gives more possibilities. For greater throughput and production rate with less time, an industry depends on these technologies. Regulation of humidity, pressure control and many other types of measurement meters are available in the markets to improve accuracy and are swift in nature. For industrial robots, MEMS technology can be particularly useful, as it can be applied to tactile sensors, navigation or proximity sensors. In terms of adapting MEMS technology for the development of proximity or location sensors, research has been limited due to the pattern of low commercial viability and MEMS technology. However, allows for the creation or manufacture of lower-cost tactile sensors, which can enable a robot to obtain sensory information in order to make decisions and to perform actions in a more flexible, autonomous way. In applications such as robotics, manufacturing processes, process control, as well as biotechnology and life sciences, the trend of miniaturization has led to opportunities to use multisensory.

The MEMS Future

Industry Challenges: Some of the MEMS industry's main challenges include:

- a) **Access to Foundries:** MEMS companies today have very limited access for prototype and product manufacturing to MEMS manufacturing facilities, or foundries. Moreover, the majority of organizations anticipated to benefit from this technology do not currently have the skills and competencies needed to support the manufacture of MEMS. Telecommunications firms, for example, do not currently operate micromachining facilities for optical switch manufacturing. For the commercialization of MEMS, inexpensive and responsive access to MEMS fabrication facilities is essential.
- b) **Design, Simulation and Modelling:** It is difficult to distinguish device design from the dynamics of production because of the highly integrated and interdisciplinary nature of MEMS. Consequently, to design a MEMS system, a high level of manufacturing and manufacturing expertise is required. In addition, during this production and subsequent prototype period, considerable time and money is expended. An interface should be developed to differentiate design and production in order to improve innovation and creativity and minimize excessive 'time-to-market' costs. As effective system creation often involves modeling and simulation, it is critical that adequate analytical tools are accessible to MEMS designers. MEMS devices still use older design tools and are manufactured on a 'trial and error' basis. Therefore, for accurate prediction of MEMS system behavior, more efficient and advanced simulation and modelling tools are required.
- c) **Packaging and Testing:** Perhaps the biggest challenge facing the MEMS industry is the packaging and testing of devices. As previously mentioned, compared to conventional IC packaging, MEMS packaging poses specific problems in that a MEMS package usually needs to provide security from and access to an operating environment. There is currently no standardized solution for MEMS packaging, with each device needing a specific format. Consequently, packaging is the most costly manufacturing phase and sometimes accounts for 90 percent (or more) of a MEMS device's final cost.
- d) **Standardization:** Standardization has been very difficult because of the comparatively limited number of commercial MEMS devices and the speed at which the latest technology is evolving. To date, only multi-million dollar (or billion dollar) investment facilities are typically found to have high quality

control and basic types of standardization. Progress in industry communication and information sharing, however, was made in 2000 through the creation of a MEMS trade association. In addition, a MEMS industry roadmap funded by the International Organization for Semiconductor Equipment and Materials (SEMI) has also been established for the exchange of pre-competitive knowledge on MEMS processes, technology, applications and markets. To lay the groundwork for a structured standardization structure, the networking of these smaller companies and organizations on a global scale is extremely essential and required.

- e) **Education and Training:** The complexity and interdisciplinary nature of MEMS needs a well-trained and informed market for the field. Graduate education is typically required, and while the number of universities offering MEMS-based degrees is growing, it is a costly and time-consuming process to acquire information. Therefore, an effective and lower cost education approach is required to match the expected demand for these MEMS scientists and engineers. For instance, Industry-led (or driven) academic research centers providing technology-specific programs with commercial incorporation, training, and technology transfer are one approach.

Conclusion

The current and most important applications of MEMS technology in the automotive industry have been presented in this paper. Many of the previous sensors have been shown to be easily replaced by more cost-effective, simpler, and smaller MEMS sensors, and hundreds of millions of MEMS sensors have been used in automobiles. Besides, most projections say that their use in the vehicles will continue to expand to address automotive safety requirements as well as government mandates. In addition, because of the tremendous technological and economic advantages of such sensors, car engineers are constantly discovering new uses for them so that the protection and performance of vehicles can be improved. Today, in terms of automotive safety parameters, manufacturers typically use MEMS sensors. However, MEMS Technology's performance-related applications are safe and secure and can be used in industries to achieve better production rates. The technique often needs less effort and is cost-effective.

References

1. De Los Santos, H.J., Introduction to Microelectromechanical (MEM) Microwave Systems, Artech House Microwave Library, Artech House, Boston, MA, 1999.
2. By ELE Times -September 10, 2018
3. Tanaka, M., "An industrial and applied review of new MEMS devices features", Elsevier Journal of Microelectronic engineering, Vol. 84, pp. 1341-1344, 2007.
4. Automotive MEMS Market Brief", IHS iSuppli Research, 2011.
5. David S. Eddy and Douglas R. Sparks, "Application of MEMS Technology in Automotive sensors and Actuators", proceedings of the IEEE, vol. 86, no. 8, august 1998.
6. Walker, S. J., Nagel, D. J., Report on "Optics & MEMS," Naval Research Laboratories, Materials Science and Technology Division, May 15, 1999.

* * * * *

- ❖ **Raghavendra J L**, Technical lead, functional safety, Matrickz GmbH, OhmStr 1, Unterschleißheim, Germany, **E-mail:** raghavendra.lokesha@gmail.com

MEMS Sensor Technologies for Humanist Applications in Safety and Environmental Sensing



- **C. T. Chandrashekhara**
- **S. Boregowda**
- **M. Gunavathi**

Abstract

Now a day's increased level of social knowledge of safety and environmental sensing has now created an evolving need for MEMS sensor technologies and monitoring devices capable of sensing, classifying and providing input on the health status and physical activities of users, as well as universal, accurate. This analysis paper will concentrate on MEMS sensor technologies developed in addition to the incorporation of smart systems, as part of investigation successes for protection and ecological detecting. Innovative and smart integrated sensing system systems pursued and implemented in research centres, along with practical implementations will be highlighted. Finally, the paper will demonstrate the potential outlook of sensor developments and related prospects for exploitation.

Introduction

Micro-Electro-Mechanical Systems (MEMS) are mechanical and electro-mechanical components produced through micro-manufacturing methods. MEMS technologies have increasingly evolved a wide range of lightweight, high-performance and often inexpensive sensors capable of sensing and thus responding to many physical variables (e.g. pressure, location, motion, strain, radiation and flow), from low-volume/high-cost industrial and to ultra-high-volume/very low-cost consumer electronics products. MEMS-based devices now range from simple arrangements without moving parts to complex electromechanical structures with several moving elements under integrated microelectronics control. It should be noted that MEMS technology has consistently been effective in the sense of

physical. In addition, with the integration of low-power circuits, wireless communication modules and moved along with information and communication technologies, allowing the design of lightweight, high-performance, low-power and low-cost solutions for a wide range of applications. Several applications and scenarios are now leading the business in the next decade.

Efficient ecological devices are frequently connected with new and growing apps. Checking the mechanical uprightness of vehicles, such as mixtures used in flying machine and arrangements, is only one example of the wonderful exploitation and scattering in this field of MEMS sensor technologies. In so-called 'smart cities', another big application would include, for example, active traffic management and interactive transport systems, smart grids for lighting and energy supply, monitoring of high spatial/temporal resolution emissions and weather forecasting, most of which are expected to be activated by wireless sensor networks and clouds. Finally, in contact processes in general, supply of services, food industry, agriculture, media and gaming, other important scenarios where MEMS sensors are commonly used. The aim of this review paper is to present MEMS sensor technologies developed by explaining the implementation of research and innovations in the field of safety and environmental sensing for specific emerging applications.

MEMS sensing devices

The micro-electromechanical systems (MEMS) technology, some detecting tools, containing inertial and ecological devices can be contracted and measured with negligible power depletion. An important step is to distinguish the action of the MEMS structure from the design board to the recognition of the sensor. For this reason, application-specific analog circuitry (ASIC) is often developed, but this technique makes the process of iterative sensor creation tedious and time consuming. Thus, a quick and detailed method of characterization for MEMS devices is important.

Strategies for Measurements

The response of the MEMS structure under the influence of a drive signal or as a function of changes in the sensing environment needs to be studied in order to obtain a full understanding of the actions of a sensor. To cover a wide range of parameters, several measurements are needed, which are listed below.

Analysis of frequency response is important for finding the optimal drive signal to optimize the output of the sensor. This also helps the characterization of the resonance and sidebands of the sensor. By varying drive parameters with a parametric sweeper, backbone measurements can then be carried out; instead, parametric resonances can be used.

The structural properties of the sensor, such as damping and consistency factor, are revealed by these time-resolved measurements.

To characterize the transducer structure of the MEMS system, impedance analysis is used: the impedance depends on the structure as well as the drive signal and environmental conditions. Thus, accurate measurements are important.

This is accomplished by locking the sensor phase with a phase-locked loop (PLL) or by locking other parameters with a proportional-integrative-derivative (PID) controller, such as the amplitude. This kind of locking method often greatly increases the bandwidth of the calculation.

Lock-in Amplifier

In fields such as optics and photonics, nanotechnology and materials science, quantum technologies, scanning probe microscopy and sensing, lock-in amplifiers are an integral part of research laboratories. Thanks to the ability of a lock-in amplifier to retrieve very tiny signals hidden in noise, new research can be discovered and the spectrum of experimental setups can be expanded. A lock-in amplifier's working theory, called demodulation or phase-sensitive detection, relies on mixing the measured signal with a reference frequency accompanied by low-pass filtering. The choice of the modulation frequency of the measured signal enables it to be moved away from dominant sources of noise, which are particularly important near DC.

Phase-Locked Loop

Two 50 MHz phase-locked loops (PLLs) with two separate 50 MHz lock-in amplifiers are combined with this powerful product. The PLLs provide completely configurable support for precise frequency control, while the lock-in amplifiers provide best-in-class signal recovery.

- Atomic Force Microscopy (AFM)
- Scanning Tunneling Microscopy (STM)
- Near-field scanning Optical microscopy (NSOM)
- Microelectromechanical devices (MEMS)
- Resonators and magnetometers
- Frequency combs: description of time reference
- Characterization of semiconductors and testing

Impedance Products

For all modes of impedance calculation, this instrument provides a powerful toolset. All tools are fitted with control software and it is possible to add additional options to satisfy the requirements of the most challenging applications. The MFIA is a wireless impedance analyzer and precision LCR meter that works in the frequency range from 1 mHz to 500 kHz or to 5 MHz. It has a simple precision of 0.05 per cent and spans the spectrum of measurements from 1 m to 1 T. This includes both time- and frequency-domain tools for data acquisition impedance.

The Benefits of Instruments

- With Zurich Instruments lock-in amplifiers, all measurement strategies discussed above can be implemented and checked, thus removing the need for time-consuming ASIC development: take advantage of an all-in-one approach for your applications with MEMS sensors.
- Track and monitor several resonances simultaneously using the multiple demodulators and oscillators in a single instrument.
- To minimize the input noise and improve the signal-to-noise ratio for periodic signals, Zurich Instruments' analog electronics deliver multiple input levels.

Environmental sensors

Environmental sensors are linked artefacts capable of providing different types of information: place, position, movements of the individual and contextual

Recent Trends in Physics with Emphasis on Discovery of God Particle

elements that can be correlated with data collected via sensors embedded or implanted in the individual, including alarm validation, as in the case of falls. They pose unique ethical problems since they are a form of surveillance that, depending on where they are mounted, may affect the private life of the person, including their privacy. In the case of video capture, this argument is especially sensitive.

Robotic devices in which they communicate may also be associated with this form of sensor to allow them to respond to the context or the need of the individual with whom they are intended to interact. For certain sensors, the tracking of individuals and their wellbeing is not the first objective, as there are air quality sensors, light sensors, smoke detectors, etc. However, the data they collect can contribute to the development of potentially personalized health information and eventually to the generation of alarms through cross-referencing with data from other sources.

➤ **Air Pollution Monitoring:**

Environmental sensor networks have grown and many applications of WSNs for earth science research are now available. This entails volcanoes, seas, glaciers, trees, etc. being found. Below are some other major areas mentioned.

➤ **Forest Fire Detection:**

In order to track the concentration of hazardous gases, WSNs have been deployed in many cities. These will take advantage of wireless ad hoc connections, making them more mobile in different areas for checking readings.

➤ **Forest Fire Detection:**

To detect fires, a network of sensor nodes in a forest can be mounted. The nodes can be fitted with sensors to measure temperature, humidity, and gases created by fires in the trees or vegetation. Early detection is crucial; with WSNs, when a fire begins and how/where it spreads, the firefighters know.

➤ **Landslide Detection:**

To detect the subtle motions of soil and changes in different parameters that may occur before or during a landslide, a landslide detection device uses a WSN. With

data, long before it actually occurs; it might be possible to predict the occurrence of a landslide.

Safety and Environmental Sensing

Intelligent systems put together a range of leading technologies and solutions to improve safety at work, in offices, in cars, etc., and to track environmental conditions. MEMS-based sensors play a key role in this article. Often, from a generalized point of view, no design methodologies for smart systems can accommodate and apply high-level functional limitations at various abstraction levels. This approach can be aligned with design paradigms guided by constraints, prevalent in applications for protection and environmental sensing. Thus, it is appropriate to apply ad hoc devices and sensing strategies.

Non-invasive and efficient solutions capable of detecting falls in regulated environments are inertial sensors and accelerometer-based systems, and vehicle safety is concerned with the prospect of introducing automated urban navigation strategies that can minimize or eliminate incidents. A relevant percentage of bad solutions (gaps and outliers) caused by obstructions and multipath were shown by systems based on GPS standalone receivers. Due to GPS outages, a low-cost MEMS system was able to bridge gaps, but for short time periods. MEMS sensors have also been used to track buildings and seismic areas. The results showed that the accuracy of the displacement time histories obtained by double acceleration data integration was 98 percent accurate. We conclude that the displacement measurement system based on inertial sensors for seismic monitoring is best for structures remaining in the elastic range of displacement, but without residual displacement after the earthquake, whereas a vision measurement system is more appropriate for estimating the structure's residual post-earthquake displacement. MEMS implementations can also be found in the literature for environmental monitoring. Electroplated nickel cascaded bent beams were formed over a silicon nitride isolation layer using a high aspect ratio method called Metal MUMPs. Both analytically and numerically, sensor behavior was modeled and experimental characterization was then performed. In response to temperature variation, an integrated inductor was also designed to achieve an LC resonator coupled with a remote readout circuit to feel the resonance frequency change.

For environmental control, gas sensors are also of primary importance. By coupling a MEMS cantilever with a low temperature co-fired ceramic differential photo acoustic cell and spatial interferometer, portable methane sensors have recently been developed. The device included four separate gas chambers, namely a sample cell, a reference cell, and a differential photo acoustic cell consisting of two parts: the top sample beam chamber (SBC) and the bottom reference beam chamber (RBC). Between the SBC and RBC chambers, all filled with the target gas, the MEMS cantilever microphone was found. The sensor displayed a high radiation sensitivity whose optical wavelengths corresponded to the target gas absorption lines.

When monitoring in harsh environments is needed, not only sensors, but also conditioning and memorization systems must be properly built using four metal layer 0.35 μm CMOS technology and proposed for applications in extreme environments.

Future Perspectives

Further incorporation of MEMS sensor technologies within devices and artifacts already used by people on a daily basis (e.g., smartphones) could be considered for future trends and research/industrial perspectives; it would represent a kind of 'everyday technology' for regularly tracking behavior and wellbeing, more and more in a multisensing and multimodal cloud framework. The introduction of MEMS sensor-based technologies will allow a large number of different information to be handled continuously and integrated, representing a smart ecosystem that is intended to cohabit and develop along with the improvement of microprocessor computational efficiency. In this context, as stated by the company STMicroelectronics, one of the key future drivers is the ability to always keep the sensors on, in order to continuously track the operation of the users (also indoors without the need for a GPS) and environmental conditions. Energy consumption, one of the key consequences of the above-mentioned scenario, is an open research problem that, as again reported by STMicroelectronics, has to be tackled with even more integrated sensors and that will implement smart power management and signal processing systems in a single device.

To provide better efficiency, less invasiveness, more predictability and extensibility, sensor technologies must be more accessible to users and be part of a

convenient and non-impact environment, such as smartphones, tablets and clothing. A required improvement to be addressed would also be the reduction of the necessity for conscious human action in the sensing phase (e.g. system calibration) through well-consistent and accurate detection, classification and prediction techniques. Progress towards high-performance computing, cloud computing, big data analysis and so on would provide the main resources in this context to make these scientific and technical breakthroughs possible.

Conclusions

It is expected that the pace of development in MEMS technologies will increase, powered by rising commercial demand to understand and control personal health and well-being and track environmental conditions. New MEMS sensors would also have greater selectivity and sensitivity, with greater stability and the ability to identify events and prevent false alarms. The continuous developments in MEMS technology and the evolution of semiconductor manufacturing techniques will allow the production and manufacture of large-scale, cost-effective and highly reliable and stable MEMS sensors based on the principles of electrochemical, chemo-optical and kinematic sensing. These approaches/trends will represent a paradigm shift in the quest for more technology improvements in this paper: "innovation based on community needs with regard to standardized offerings, local applications with high impact and resources for global technology improvement". This analysis paper, in which a central role was played by MEMS sensor technologies. The development of creative technologies to enhance the quality of life in a pervasive network environment has been moved forward by main application drivers, such as environment monitoring. The introduction of wireless communications sets the stage for the development of wellness, well-being, assistance, recovery and environmental sensing wireless sensor networks.

References

1. McGrath, M.J.; Clíodhna, N. *Sensor Technologies: Healthcare, Wellness and Environmental Applications*; Apress: New York, NY, USA, 2013.
2. Nihtianov, S.; Luque, A. *Smart Sensors and MEMS: Intelligent Devices and Microsystems for Industrial Applications*; Woodhead Publishing: Amsterdam, The Netherlands, 2014.
3. Caldara, M.; Colleoni, C.; Guido, E.; Re, V.; Rosace, G.; Vitali, A. A wearable sweat pH and body temperature sensor platform for health, fitness, and wellness applications. In *Sensors and Microsystems*; Springer: Berlin, Germany, 2014; pp. 431–434.
4. Bogue, R. MEMS sensors: Past, present and future. *Sens. Rev.* 2007, 27, 7–13. 8. Bogue, R. Recent developments in MEMS sensors: A review of applications, markets and technologies. *Sens. Rev.* 2013, 33, 300–304.
5. MNX Company. What Is MEMS Technology? Available online: <https://http://www.mems-exchange.org/MEMS/what-is.html> (accessed on 13 March 2015).

* * * * *

- ❖ **C. T. Chandrashekhara**, Asst. Professor, Dept. of Physics, SAC College, Nagamangala, Karnataka, India, **Ph:** 7760505231
- ❖ **S. Boregowda**, Asst. Professor, Dept. of Physics, SAC College, Nagamangala, Karnataka, India, **Ph:** 9164061264
- ❖ **M. Gunavathi**, Asst. Professor, Dept. of Computer Science, SAC College, Nagamangala, Karnataka, India

Normal Co-Ordinate Analysis of High Temperature Superconductor $\text{PrHo}_{0.1-x}\text{Ba}_2\text{Cu}_3\text{O}_7$.



○ Dr. K. Sonamuthu

Abstract:

The prime application of Nano technology is High temperature superconductor. Since the discovery of high T_c superconductor $\text{YBa}_2\text{Cu}_3\text{O}_{7-6}$, elemental substitution has been used to make clear the mechanism of high T_c superconductivity. Early studies showed that the replacement of Y site in $\text{YBa}_2\text{Cu}_3\text{O}_7$ by the lanthanide elements except Ce, Tb, and Pr did not destroy its superconductivity. Only $\text{PrBa}_2\text{Cu}_3\text{O}_7$ compound which is iso-structural to $\text{YBa}_2\text{Cu}_3\text{O}_7$, is neither metallic nor superconducting.

Systematic studies of the lattice vibrations and the free carriers are important for understanding the physical nature of the high T_c superconductors. These systems have similar orthorhombic crystal structures with the oxygen composition almost 7, however with the increase of the Pr concentration T_c is decreased and finally superconductivity disappears. In this report Raman scattering and infrared (IR) reflection of $\text{Pr}_x\text{Ho}_{1-x}\text{Ba}_2\text{Cu}_3\text{O}_7$ system is studied. The lattice dynamical calculations on high T_c superconductors $\text{Pr}_x\text{Ho}_{1-x}\text{Ba}_2\text{Cu}_3\text{O}_7$ system are also studied using the shell model in order to understand the characteristic shifts of phonon frequencies observed by Raman and IR measurements with the substitution of Pr for Ho.

1. Introduction

HTSC marks the beginning of a new era of material science. Researchers are looking beyond the simple metals. Their alloys, binary and ternary compounds to the almost limitless range of complex molecular solids, many of which will be based on the rich chemistry of the transition metals. These materials can be expected to have interesting and technologically important electronic and magnetic properties as the

familiar materials of modern day technology. The important legacy has been the major investment in new research equipment and the powerful range of theoretical, experimental and material processing techniques developed primarily for HTSC but equally applicable to a much wider range of materials of potential importance to future material scientists.

The introduction of superconductivity above 30 K in CuO-pervoskites by Bednorz Muller[1-3] initiated tremendous efforts in solid state physics and material sciences with the aim to isolate the phases which are responsible for the superconductivity.

One direction(Set) of experiments has the intention to find out what is the contribution of lattice vibrations to the superconductivity. Neutron scattering, as the method to determine the vibration spectrum throughout the whole Brillouin zone, could at the beginning of these activities only measure the phonon density of states, as shown by Ramirez et al.[4] Renker et al.[5,6], Bruesch et al.[7],Burer et al.[8], and Belushkin et al.[9], because large single crystals were not available. Raman and infrared (IR)-spectroscopy, however, can yield at least some of the phonon frequencies, namely the long wavelength optical phonons at the center of the Brillouin zone, from polycrystalline materials. Even tiny single crystals embedded in polycrystalline samples can be investigated in Raman experiments with the use of microscope.

The published results of experimental work on Raman and IR-spectroscopy have been published in many papers. They cover detailed information about the lattice vibrations of the superconducting materials and their dependence on oxygen contents, element substitution and impurity phases, which appeared in various samples and partly yielded controversial results. In addition, the temperature variations of the optical phonon spectrum and the superconducting gap have been investigated.

It is the intention of this review to summarize the literature about the Raman and IR-experiments. The author hopes to have considered every article in these fields which have appeared in the first two years of investigations on the La_2CuO_4 and $\text{YB}_2\text{Cu}_3\text{O}_7$ series. Regarding the enormous number of papers, however, one or the other may have been overlooked, and the author apologies all colleagues whose works have been omitted here unintentionally.

The method of isotopic contrast in inelastic neutron scattering makes it possible to experimentally restore the partial oscillating spectra of single atoms.

The study of normal coordinate analysis and the free carriers is important for the understanding of the physical nature of high temperature superconductors. Raman and far-infrared studies of these superconductors have contributed significantly to the understanding of new class of superconductors. Cardona and coworkers [11-35] studied the infrared and Raman spectra of the super conducting cuprate perovskites MBaCu_2O_2 ($M = \text{Nd, Er, Dy, Tm and Eu}$) and reported the possible origins of phonon softening and the systematic variation of phonon frequencies with the ionic radius.

Where PED is the combination of the i -th symmetry coordinate to the potential energy of the vibration whose frequency is $V_k F_{ij}$ are potential constants, L_{ik} are L matrix elements and $\lambda_k = 4\pi^2 C^2 v_k^2$.

Systematic studies of the lattice vibrations and the free carriers are important for understanding the physical nature of high T_c superconductors. Recently, anomalous behaviour of the phonon band vibrating in the c -axis direction has attracted much interest, and strong coupling theory of phonon and the free carriers has been reported. In this paper infrared reflection spectra of $\text{Pr}_x\text{Ln}_{1-x}\text{Ba}_2\text{Cu}_3\text{O}_{7-y}$ (Lan=Lanthanide) are studied. Optical constants are calculated by the Kramers-Kronig analysis and anomalously large oscillator strength is denied for the “Barium mode” at 154 cm^{-1} at low temperatures. The origin of this anomalously large oscillator strength at low temperature is attributed to the increase of the broad background reflection due to the increase of superconducting gap in the low temperature range. Free carrier concentrations for these systems are estimated by the fitting of the reflection spectra with the calculated one from the model of the oscillators and the Drude term.

The discovery of superconductivity with transition temperatures (T_c) in the 90-K range in $\text{YB}_2\text{Cu}_3\text{O}_{7-6}$, has generated a great deal of interest in the oxide superconductors. The substitution of Y by trivalent rare-earth elements, with the exception of Ce, Pr, Pm, and Tb, yields a superconducting phase with a T_c almost identical to the $\text{YB}_2\text{Cu}_3\text{O}_{7-8}$, compound. Samples of $\text{Rb}_2\text{Cu}_3\text{O}_{7-8}$ with $R=\text{Ce and Tb}$ prepared by the standard solid-state reaction technique yield multiphase materials consisting of BaCeO_3 or BaTbO_3 , CuO , and BaCeO_2 which are not superconducting.

No investigations have been reported for the $\text{PmBa}_2\text{Cu}_3\text{O}_{7.8}$ compound because the Pm nucleus is radioactively unstable. The $\text{Y}_{1-x}\text{Pr}_x\text{Ba}_2\text{Cu}_3\text{O}_{7.8}$ system is particularly interesting since it is iso-structural to the $\text{YBa}_2\text{Cu}_3\text{O}_{7.8}$ superconductor, yet the superconductivity is strongly suppressed as a function of Pr concentration. This quenching of the superconducting state is not understood in detail. Extensive measurements have been carried out as a function of Pr concentration which includes magnetization, heat-capacity, thermo power, Hall Effect, neutron-diffraction, pressure effects, x-ray-absorption, and Raman spectroscopy. The effect of the Pr ion on the superconducting properties may help our understanding of the interplay between magnetism and superconductivity and provide insight as to the origin of the superconductivity in the high- T_c oxides.

One problem in studying the $\text{Y}_{1-x}\text{Pr}_x\text{Ba}_2\text{Cu}_3\text{O}_{7.8}$ system is its tendency to phase separate into $\text{YBa}_2\text{Cu}_3\text{O}_{7.8}$ with $T_c=90$ and $=90$ and $\text{Y}_{1-x}\text{Pr}_x\text{Ba}_2\text{Cu}_3\text{O}_{7.8}$ of varying x value and a reduced T_c . This type of phase separation can be clearly seen in the field-cooled Meissner measurements, while not showing up at all in the powder x-ray diffraction patterns. The resistivity data on these phase separated samples showed broad transitions. It has been overcome this problem through specific annealing conditions of time, temperature, and atmosphere. Various explanations have been given for such suppression of the superconductivity [37-39]. But this suppression by Pr has not been understood yet.

Recently, anomalous behavior of the phonon band vibrating in the c -axis direction has attracted much interest [40-43], and strong coupling theory of phonon and free carriers has been reported [44]. The study of the phonon of the $\text{Pr}_x\text{Ln}_{1-x}\text{Ba}_2\text{Cu}_3\text{O}_{7-y}$ systems (Ln is a lanthanide element) are also important. It has been reported in the earlier literature that the preparation, structure, oxygen, content, resistivity, magnetization, and critical field in the single phase $\text{Y}_{1-x}\text{Pr}_x\text{Ba}_2\text{Cu}_3\text{O}_{7.8}$ system. The electronic coefficient of specific heat, γ , the density of states, $N(O)$, and the Ginzburg-Landau parameters $\xi_{GL}, \lambda_{GL},$ and κ_{GL} are estimated along with the exchange interaction parameter, from the measured temperature dependence of H_{c2} and the Pauli susceptibility. Free carrier concentration for $\text{Pr}_x\text{Ln}_{1-x}\text{Ba}_2\text{Cu}_3\text{O}_{7-y}$ systems has been estimated by the fitting of the reflection spectra calculated using Lorentzian oscillators and a Drude term to the experimentally-obtained reflection spectra [45].

2. Normal Coordinate Analysis of $\text{Pr}_x\text{H}_{01-x}\text{Ba}_2\text{Cu}_3\text{O}_7$

The high Tc superconductor $\text{Pr}_x\text{H}_{01-x}\text{Ba}_2\text{Cu}_3\text{O}_7$ System crystallizes in the simple tetragonal (st) system, which belongs to the space group $P4/mmm(D'_{4h})$. The simple tetragonal (st) unit cell of $\text{Pr}_x\text{H}_{01-x}\text{Ba}_2\text{Cu}_3\text{O}_7$ and the numbering of the atoms are shown in Fig 1. The 14 atoms of the unit cell yield a total of 36 optical vibrational modes. All the above calculations are made at $q = 0$. Once of B_{1u} and E_{3u} modes correspond to acoustic vibrations with frequency $\omega = 0$. These normal modes are distributed as follows.

| | |
|---|------------------------------|
| $B_{1u} + B_{2u} + B_{3u}$ | from the motion of Pr atom |
| $B_{1u} + B_{2u} + B_{3u}$ | from the motion of Ho atom |
| $A_{1g} + B_{2g} + B_{3g} + B_{1u} + B_{2u} + B_{3u}$ | from the motion of 2Ba atom |
| $A_{1g} + B_{2g} + B_{2g} + B_{1u} + B_{2u} + B_{3u}$ | from the motion of 2Cu atom |
| $B_{1u} + B_{2u} + B_{3u}$ | from the motion of 9Cu atom |
| $2A_{1g} + 2B_{2g} + 2B_{2g} + B_{1u} + B_{2u}$ | from the motion of 4(1) atom |
| $A_{1g} + B_{2g} + B_{2g} + B_{2u} + B_{3u}$ | from the motion of O(2) atom |
| $B_{1u} + B_{3u}$ | from the motion of O(3) atom |

Subtracting the translation modes $B_{1u} + B_{2u} + B_{3u}$ the $q = 0$ optical modes involved in an irreducible representation are as follows.

$$\Gamma_{\text{opt}} = 5 B_{2g} + 5 B_{3g} + 5 A_{1g} + 8 B_{1u} + 7 B_{2u} + 8 B_{3u}$$

The species belonging to $A_g + B_{3g}$ and B_{2g} are Raman active modes whereas $B_{1u} + B_{2u} + B_{3u}$ are infrared active modes. The B_{1u} and A_g modes involve displacement along crystallographic c-axis, the B_{2u} and B_{2g} modes along the b-axis and B_{3u} modes along the a-axis. The normal coordinate calculation was performed using the programs GMAT and FPERT given by Fuhrer et al [36]. The general agreement between the evaluated and observed normal frequencies of $\text{Pr}_x\text{H}_{01-x}\text{Ba}_2\text{Cu}_3\text{O}_7$ is good. The calculated force constants using the above programs are given in Table

1.1. It is interesting to note that the evaluated frequencies given in Table 1.2 agree favourably with the experiment values.

3. Results and Discussion.

3.1 Normal co-ordinate analysis of $\text{Pr}_x\text{Ho}_{1-x}\text{Ba}_2\text{Cu}_3\text{O}_7$

The evaluated frequencies using the normal coordinate analysis method listed in table 1.2 agrees favourably with the calculated lattice dynamical frequencies and observed experimental frequencies.

The lowest calculated Raman phonon frequency at 290 cm^{-1} is due to the vibration of Pr atoms it agrees very well with the observed values at 360 cm^{-1} . The calculated Raman phonon frequency at 330 cm^{-1} is due to the vibration of the Ho atoms and it agrees with the observed phonon frequency at 340 cm^{-1} and it is due to the stretched vibration of Ho-O(1) atoms. The calculated Raman phonon frequency at 355 cm^{-1} is due to the vibration of Ba atom and agrees with the observed phonon frequency at 360 cm^{-1} . And it is due to the stretched vibration of Ba-Cu atoms. The calculated Raman phonon frequency at 400 cm^{-1} is due to the vibration Cu atom and it is due to the bending vibration of Ca (1)–Ba-Ca (2) atom. The highest calculated Raman phonon frequency at 502 cm^{-1} in this symmetry is due to the vibration of O(1) atom and it is due to the stretched vibration of Pr-O(1) atom. The observed value at 500 cm^{-1} agrees very well with the calculated Raman phonon frequency.

The calculated Raman phonon frequency at 300 cm^{-1} in B_{2g} symmetry is due to the vibration of Pr atom and it agrees very well with the observed value at 320 cm^{-1} and it is due to the bending vibration of O(1)-Pr-O(2) atoms. The calculated Raman phonon frequency at 480 cm^{-1} is due to the vibration of Pr-O(1) atoms and Cu atom in 180° out of phase to Ho-O(1) atoms and it agrees very well with the experimental value of 420 cm^{-1} . The calculated Raman phonon frequency at 450 cm^{-1} is due to the vibration of Ba atom and it is due to the bending vibration of O(1)-Ba–O(2) and it agrees very well with the experimental value at 480 cm^{-1} . The highest calculated Raman phonon frequency in this symmetry is 530 cm^{-1} and it is due to the vibration of O(1) and it is due to the stretching vibration of Cu-O(1) atom.

The calculated Raman phonon frequency at 290 cm^{-1} in B_{3g} symmetry is due to the vibration of Pr atom and agrees very well with the experimental values at 300 cm^{-1} . And it is due to the stretched vibration of Pr-O(1) atoms. The calculated

Raman phonon frequency at 415cm^{-1} and it is due to the bending vibration of Pr-O(1) atoms. The Raman phonon frequency in this symmetry in(is) 535cm^{-1} and it is due to the vibration of O(1) atom and it is due to the bending vibration of O(1)-Pr-O(1) atoms.

The lowest infrared phonon frequency at 138cm^{-1} and 168cm^{-1} are in the B_{1u} symmetry is due to the vibration of Pr and Ho atoms. Here the observed experimental frequencies agree very well with the calculated frequency at 140 and 160cm^{-1} respectively. The calculated infrared phonon frequency at 290cm^{-1} is due to the vibration of Ba atoms and it is due to the bending vibration of O(1)-Ba-O(2) atoms. And it agrees very well with the experimental frequency at 300cm^{-1} . The calculated infrared phonon frequency at 317cm^{-1} is due to the vibration of Cu atoms. The observed frequency agrees with the calculated frequency at 320cm^{-1} . The frequency at 336cm^{-1} in this symmetry is due to the O(1) atoms and it is due to the bending vibration of O(1)-Cu-O(2) atoms and it agrees very well with the calculated frequency at 340cm^{-1} . The highest calculated infrared phonon frequency at 482cm^{-1} in this symmetry is due to the vibration of O_2 atom and it is due to the stretched vibration of O_2 atoms and it agrees very well with the experimental values at 480cm^{-1} .

The calculated infrared phonon frequency in B_{2u} symmetry at 135cm^{-1} and 300cm^{-1} are due to the vibration of Pr and Cu atoms. These are due to the stretched vibration of PrO(1) and Cu-O(1) atoms and this experimental frequencies agree very well with the calculated frequencies at 160cm^{-1} and 260cm^{-1} respectively. The calculated infrared phonon frequency at 158cm^{-1} and 320cm^{-1} are due to the vibration of Ho and O(1) atoms respectively. These vibrations are due to the bending vibration of O(1)-Ba-O(1) atoms and O(1)-Cu-O(2) atoms respectively and their experimental frequencies at 180cm^{-1} and 280cm^{-1} agrees very well with the calculated frequencies. The calculated infrared phonon frequency in this symmetry at 198cm^{-1} is due to the vibration of Ba atoms and Cu atom is 180° out of phase to Ba-O(1) atoms and this experimental frequency at 200cm^{-1} agrees very well with the calculated frequency. The highest frequency in this symmetry is 580cm^{-1} is due to the vibration of O(3) atom and it is due to the stretched vibration of Cu-O(3) atoms.

The calculated infrared phonon frequency at 180cm^{-1} and 255cm^{-1} in B_{3u} symmetry are due to the Pr and Ho atom. These vibrations are due to the stretched vibrations of Pr-O(1) and Ho-O(1) respectively. Hence the experimental frequency

at 140cm^{-1} and 260cm^{-1} agrees very well with the calculated frequencies. The calculated Raman phonon frequency at 310cm^{-1} is due to the vibration of Ba atom.

The calculated infrared phonon frequency at 330cm^{-1} is due to the vibration Cu atom and it is due to the bending vibration of Cu(1)-Ba-Cu(2) atoms. The experimental frequency at 340cm^{-1} agrees very well with calculated frequency. The calculated infrared phonon frequency at 560cm^{-1} is due to the vibration of O(1) atoms and O(2) atom is 180° out of phase to Ba-O(1) atom. And experimental frequency at 560cm^{-1} in calculated phonon frequency in this symmetry is 581cm^{-1} is due to vibration of O(2) atom and it is due to the stretched vibration of Cu-O(2) atoms. The observed value at 580cm^{-1} agrees very well with the calculated frequency.

4. Conclusion

In this work the normal coordinate analysis techniques have been adopted to give the evidence for electron, phonon interaction in **Pr H_{0.1-x} Ba₂ Cu₃ O₇**. It is observed from the tables that the agreement between the calculated and observed frequencies were in good agreement with the systems that are considered here. This fact supports that the present vibrational assignments made for the infrared and Raman spectra are adequate. Therefore it is concluded that the normal coordinate analysis is the optically active vibrations of the vibrational spectra in cuprate oxides.

Lastly, these calculations yielded not only the zone center phonon modes but also the stable dispersions. Hence, it also supports the strong electron phonon interaction in high temperature super conductor (HTSC). The vibrational frequencies calculated by the method of normal coordinate analysis are compared theoretically and experimentally, and they appears to be in good agreement that are further confirmed by the potential energy distribution calculation.

References

1. J.G.Bednorz and K.A.Muller. Z.Phys.B 64(1986)189
2. M.K.Wu,J.R.Ashbirn,C.J. Torng, P.H Hor,R.LMeng,L.Gao, Z.J.Huang, Y.Q Wangand C.W. Chu., Phys. Rev. Lett. 58(1987)908.

3. Z.Z.Sheng, A.MHermann,A.Elali,C.Almasan,J.Estrada,T.Datta and R.J.Matson, Phys. Rev Lett.60(1988)937.
4. A.P.Ramirez, B.Batlogg, G.Aeppli R,J.Cava, E.Rietman, A.Goldman and G.Shirane, Phys.Rev B35(1987)8833.
5. B.Renker,F.Gompf,E.Gering,N.Nucker,D.Ewert,W.Reichardt and H. Rietchel, Z. Phys. B 67(1987)15.
6. B.Renker, F.Gompf, E.Gering, G.Roth, D.Ewert, and W.Reichardt, Z.Phys.B 71(1988)437.
7. P.Bruesh and W.Buhrer, Z.Phys.B 70(1988) 70.
8. P.Bruesh and W.Buhrer,P.Unternaehre and A.Taylor,Physica C 153-155(1988) 300.
9. A.V.Belushkin, E.A.Goremychkin, Inatkaniec, I.L.Sashin, W.Zajac, A.R.Kadyrbaev and B.P.Michailov, Physica C 156(1988) 259.
10. S.Sugai, M.Sato. S.Hosoya, S.Uchida, H.Takagi, K.Kitazawa and S.Tanaka, Jpn. J.Appl. Phys. Part 2, Suppl.26-3(1987)1003.
11. K.Ohbayashi,N.Ogita,M.Udagawa,Y.Aoki,Y.Maeno and P.Fujita,Jpn. J.Appl.Phys.Part 2,25(1987) L423.
12. Torben Burn,M.Grimsditch, K.E.Gray,R.Bhadra,V.Maroni and C.K.Loong, Phys.Rev B35(1987)8837.
13. S.Sugai, M. Sato, S.Hosoya, Jpn.J.Appl.Phys.Part 2,.26 (1987)L495.
14. S.Blumenroder, E.Zirngiebl, J.D. Thompson, P.Killough, JL Smith and Z.Fisk Phys.Rev B35(1987)8840.
15. M.Copic, D.Mihailovic, M. Zgonit, M. Prester, K. Biljakovic, B. Oreal and N.Brnicovic, Solid State Commun. 64 (1987)297.
16. B.Batlogg, G.Kourouklis, W.Weber,R.J.Cava, A.Jayaraman, A.E. White, K.T.Short, L.W.Rupp and E.A.Rietmann. Phys. Rev. Lett.59(1987)912.
17. G.A.Kourouklis, A.Jayaraman, W.Weber, J.P Remeika, G.P.Espinosa, A.S.Cooper and R.G.Maines Sr., Phys.Rev B36(1987)7218.
18. K.B.Lyons, P.A.Fleury, J.P Remeika, A.S.Cooper and T.J.Negeren, Phys.Rev b 37 (1988)2353.
19. S.Zhang, He-Tian Zhou,Chongde Wei and Qin Lin, Solid State Commun. 66 (1988) 1085.
20. A.I Maksimov, O.V.Misochko, I.T.Tartakovosky, V.V.Timofeev, J.P.Remeika, A.S.Cooper and Z.Fisk Solid State Commun. 66 (1988) 1077.
21. J.D.Jorgensen, H.B.Schuttler, D.G.Hinkds, D.W.Capone II, K.Zhang, M.B.Brodsky and D.J.Scalapino. Phys. Rev. Lett.58(1987)1024.

22. D.C.Johnston, J.P.Stokes, D.P.Goshorn and J.T.Lewandowski, Phys.Rev b36 (1987) 4007 .
23. D.L.Rousseau, B.P.Baumann and S.P.S.Porto, J.Raman Spectr. 10(1981) 253.
24. B.Renker,F.Compfe,E.Gering *et al* , Z.Phys.B 67,15(1987) .
25. B.N.Goshitskit, C.A.Davydov,M.G.Zemlyanov *et a* , Fiz. Met, Metalloved. [Phys. Met.Metallogr.] 67,188(1987).
26. I.Natkanets, A.V.Belushkin,Ya.Mayer *et al* ,Pis'ma Zh. Eksp.Teor. Fiz.48,166 (1988) JETP Lett. 48,181 (1988)].
27. L.Pintschovius, N.Pyka, W.Reichardt *et al* ,Progress in HTSC 21,36(1989).
28. F.Gervais,P.Echegut,J.M.Bassat, and P.Odier,Phys.Rev.B 37,9364 (1988) .
29. Yu .S.Ponosov and G.A.Bolotin, Pis'ma Zh.Eksp. Teor. Fiz.49, 16 [JETP Lett. 49,16 (1988)].
30. M.Shimada,M.Shimizu,J.Tanaka *etal*, Physica C 193, 277(1992).
31. S.Ikeda, M.Misawa, S.Tomiyoshi *et al*, Phys.Lett. A 134, 191(1988).
32. H.A.Mook,J.A.Harvey,and N.W.Hill, Phys.Rev.B 41,764 (1990).
33. P.P.Parshin, M.G.Zemlyanov , I.E.Graboi, and A.P.Kaul', Sverkhpr.Fiz.Khim.Tekh [Supercond. Phys.Chem.Tech.] 2,29 (1989).
34. P.P.Parshin, M.G.Zemlyanov, and P.I.Soldatov, Zh.Eksp. Teor. Fiz.101,750(1992) [JETP 74,400(1992)].
35. C.T.Thomsen, M.Cardona,W.Kress,L.Genzel,M.Bauer,W.King and A.Wittlin, Solid State Commun. 64,727 (1987).
36. H.Fuhrer, V.V.Kartha, K.G.Kidd, P.J.Krueger, and H.H.Mantasch, Computer Programmes for infrared Spectrometry, Vol.V, Normal Coordinate Analysis National Research Council of Canada, Ottawa 1976.
37. Jee Cs, Kebede A, Nichols D. Crow JE, Mihalisin T, yer GH, Perez I, Salomon RE, Schlottmann P, Solid State Commun, 69:1139 (1988)
38. Fink J, Nuckeer N, Romberg H, Alexander M, Maple MB, Neumeieer JJ, Allen JW, Phys.,Rev. B.42:4823, (1991).
39. Neumeier JJ, Bjornholm T, Maple MB, Rhyne JJ, Gotass JA Physssssica C, 1166:1191 (1990)
40. Friedl B, Thomsen C, Schonheeerr E, Cardona M, Solid Statte Commun. 76:1107, (1990)
41. Friedl B, Thomsen C, Cardona M, Phys. Rev. Lett., 65:915, (1990)
42. Ltvinchuk AP, Thomsen C Caaardona M, Solid State Commun, 80:257, (1991)

43. Thomsen C, Friedl B, Cieplak M, Cardona M, Solid State Commun, 78:727 (1991)
44. Zeyher R, Zwicknagl G, Phys; B 78:175 (1990)
45. Onari S, Hidaka S, Ara T, Mori T, Solid State Commun. 71:195(1989)

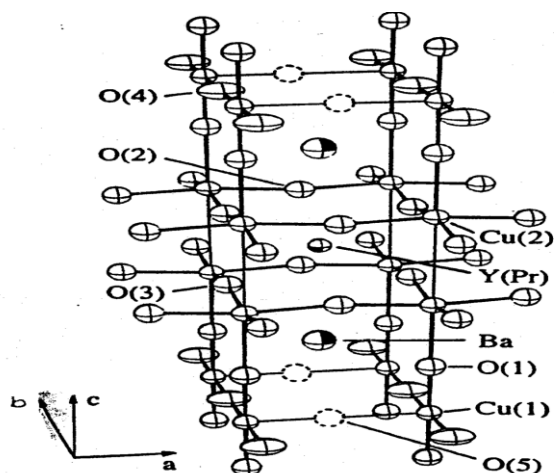


Fig.1 $\text{Pr}_x \text{H}_{01-x} \text{Ba}_2 \text{Cu}_3 \text{O}_7$

Table 1.1

Force Constants for $\text{Pr}_x \text{H}_{01-x} \text{Ba}_2 \text{Cu}_3 \text{O}_7$ (in units of 10^2Nm^{-1}) (Stretching) and $10^{-18} \text{Nm rad}^{-2}$ (bending).

| Force Constants | Bond Type | Distance (A°) | Initial Value Constants |
|-----------------|--------------|-------------------------------|-------------------------|
| f_a | Pr-O(1) | 2.452 | 2.41 |
| f_b | Pr-Cu | 3.265 | 3.258 |
| f_c | Cu-O(1) | 1.976 | 1.982 |
| f_d | Cu-O(2) | 2.43 | 2.43 |
| f_e | Cu-O(3) | 2.45 | 2.45 |
| f_g | Ba-O(1) | 2.956 | 2.98 |
| f_h | Ba-O(2) | 2.811 | 2.810 |
| f_i | Ba-O(3) | 2.594 | 2.596 |
| f_j | Ba-Cu | 3.389 | 3.381 |
| f_k | Ho-O(1) | 2.12 | 2.11 |
| f_l | Ho-O(2) | 3.18 | 2.08 |
| f_n | O(1)-Pr-O(1) | 68.80 | 70.06 |

Recent Trends in Physics with Emphasis on Discovery of God Particle

| | | | |
|------------|-----------------|--------|-------|
| f_q | Cu-Pr-Cu | 73.74 | 73.83 |
| f_r | O(1)-Ba-O(1) | 89.06 | 88.58 |
| f_s | Cu-O(1)-Cu | 165.26 | 161.9 |
| f_t | O(1)-Ba-O(1) | 56.01 | 55.24 |
| f_v | O(2)-Ba-O(2) | 88.37 | 88.29 |
| f_α | Cu-Ba/Ho-O(2) | 70.62 | 70.73 |
| f_β | O(1)-Ba/Ho-O(1) | 58.51 | 57.54 |
| f_r | O(2)-Ba/Ho-O(2) | 88.31 | 88.36 |
| f_s | Cu-Ba/Ho-Cu | 71.64 | 71.39 |

Table 1.2

Calculated Phonon Frequencies of $\text{Pr}_x \text{Ho}_{1-x} \text{Ba}_2 \text{Cu}_3 \text{O}_7$
(Values in the parentheses are experiment frequencies)

| Symmetry Species | Frequency Using Normal Coordinate Analysis | Potential Energy Distribution(%) |
|------------------------|--|--------------------------------------|
| $A_{1g}(\text{Raman})$ | 290 (360) | f_c (58) f_d (24) f_a (11) |
| | 330 (340) | f_c (55) f_l (30) |
| | 355 (360) | f_l (71) f_d (12) f_p (11) |
| | 400 (480) | f_a (51) f_α (20) |
| | 502 (500) | f_a (68) f_u (20) f_c (10) |
| B_{2g} | 300 (320) | f_a (56) f_k (14) f_a (10) |
| | 418 (420) | f_a (52) f_k (20) f_β (6) |
| | 330 (440) | f_c (60) f_c (14) f_β (6) |
| | 450 (480) | f_m (70) f_e (18) f_β (10) |
| | 530 (520) | f_m (70) f_l (21) |
| B_{3g} | 298 (300) | f_l (45) f_n (31) f_c (20) |
| | 415 (420) | f_a (42) f_g (25) f_n (15) |
| | 456 (460) | f_α (68) f_n (21) |
| | 500 (500) | f_n (70) f_a (24) |
| | 535 (540) | f_m (65) f_u (20) f_d (11) |
| B_{1u} | 138 (140) | f_a (81) f_e (16) |
| | 168 (160) | f_p (54) f_n (30) |
| | 290 (300) | f_p (62) f_β (18) f_n (10) |
| | 317 (320) | f_a (40) f_g (30) f_n (10) |

Recent Trends in Physics with Emphasis on Discovery of God Particle

| | | |
|----------|-----------|--|
| | 336 (340) | $f_{\beta}(40)f_p(30)f_m(26)$ |
| | 482 (480) | $f_a(60)f_e(21)f_m(16)$ |
| B_{2u} | 135 (160) | $f_a(71) f_e(20)$ |
| | 158 (180) | $f_{\beta}(46) f_d(18) f_b(10)$ |
| | 198 (200) | $f_{\alpha}(52) f_a(17) f_e(24)$ |
| | 300 (260) | $f_a(55) f_d(18) f_n(10)$ |
| | 320 (280) | $f_c(61) f_e(16) f_u(14)$ |
| | 400 (360) | $f_a(55) f_e(14) f_s(20)$ |
| | 580 (560) | $f_q(64) f_r(16)$ |
| B_{3u} | 180 (140) | $f_{\beta}(66) f_p(25)$ |
| | 255 (260) | $f_n(65) f_{\alpha}(21)$ |
| | 310 (300) | $f_{\delta}(68) f_a(25)$ |
| | 330 (340) | $f_{\delta}(61) f_{\beta}(20) f_m(10)$ |
| | 560 (560) | $f_{\beta}(56) f_k(17) f_g(16)$ |
| | 581 (580) | $f_k(80) f_l(14)$ |

* * * * *

- ❖ **K.Sonamuthu**, J N R Mahavidyalaya, Port Blair, South Andaman, India.744104, **E-mail** : sona_muthu2008@rediffmail.com

Study of Phase transition of mixture of Smectic and Cholesteric Liquid Crystal with temperature



- Dr. P. Srinivas
- Sushma
- Dr. J. Mahadeva

ABSTRACT

The present investigation is to study the texture analysis of mixture of liquid crystalline samples as a function of temperature. The organic compound Diethyl 4-4¹Hexaloxo Azoxy Benzoate exhibits Smectic liquid crystalline phase and the compound cholesteryl nonanoate is cholesteric liquid crystal. Mixture of 70% Diethyl 4-4¹Hexaloxo Azoxy Benzoate and 30% of cholesteryl nonanoate molecules exhibits cholesteric, SmA and SmE sequentially when specimen is cooled from its isotropic phase. This is found to exhibit for all concentrations of given mixture. These phases have been characterised by using microscopic technique. The temperature variations of optical anisotropic measurements have also been discussed.

Key words – Binary mixture, Phase transition, Optical texture, Optical anisotropy.

I. INTRODUCTION

Many of materials showing liquid crystalline behaviour belong to two general classes: Thermotrophics and Lyotropics. Transition into mesophases obtained by purely thermal process is called “Thermotrophics” where as in which mesophases are obtained by the influence of a solvent on solid is called “Lyotropics”. Thermotropic liquid crystals generally exhibits three types of Phases, namely, Nematic, Cholesteric and Smectic phase. Liquid crystalline compounds exhibit optical anisotropy, which has remarkable significance. The compound cholesteryl nonanoate is a thermotropic liquid crystal exhibits Cholesteric liquid crystalline phase with helical structure. Its molecular formula is $\text{CH}_3 (\text{CH}_2)_7 \text{COOC}_{27} \text{H}_{45}$ and melting point is 77°C to 82°C . The organic compound Diethyl 4-

4¹Hexaloxo Azoxy Benzoate is a thermotropic liquid crystal exhibits smectic liquid crystalline Phase. Its molecular formula is C₁₈ H₁₈ N₂ O₅ and melting point is 122⁰C to 123.5⁰C . In the present investigation textural changes of mixture of Diethyl 4-4¹Hexaloxo Azoxy Benzoate and cholesteryl nonanoate as a function of temperature is observed and recorded. The present investigation also covered the temperature variations of refractive indices of liquid crystalline binary mixture.

II. MATERIAL AND METHODS

In the present investigation, the mixtures of different concentrations of liquid crystal compound Diethyl 4-4¹Hexaloxo Azoxy Benzoate and cholesteryl nonanoate were prepared. The mixtures of different concentrations of samples were kept in desiccators for a long time. The samples were subjected to several cycles of heating, stirring and centrifuging to ensure homogeneity. The optical textures of these mixtures at different temperature are observed and recorded with the help of a Gippon-polarising microscope in conjunction with a hot stage. The samples are sandwiched between the slide and coverslip, then sealed well for microscopic observations.

III. OPTICAL TEXTURE STUDIES

Molecular Orientations of Optical textures shown by the sample were observed and recorded using Gippon polarising microscope in conjunction with hot stage. The specimen, in each case, is taken in the form of thin film and sand witched between the slide and covering slip. The specimen of 70% of Diethyl 4-4¹Hexaloxo Azoxy Benzoate and 30% of cholesteryl nonanoate molecules exhibits cholesteric, SmA and SmE Phases sequentially when it is cooled from isotropic phase This has been recorded. While sample is cooled from its isotropic phase, the genesis of nucleation starts in the form of small bubbles growing radially, which are identified as spherulitic textures of cholesteric phase, shown in fig(a). The cholesteric phase exists from 207⁰C to 197⁰C. On further cooling the specimen, the texture slowly transform to composite of Isogyres like structure and SmA phase. This composition of Isogyres like structure and SmA phases exists from 197⁰C to 189⁰C. On further cooling the specimen, the texture slowly transform to SmA phase in which molecules are arranged in layers as shown in fig(c). The SmA phase exists from 189⁰C to 121⁰C. On further cooling the specimen, the unstable SmA phase changes to SmE phase as shown in fig-1(d). The SmE phase exists from 121⁰C to 119⁰C. The specimen enters to the crystalline phase on further cooling.



Fig-1(a)



Fig -1(b)



Fig-1(c)



Fig-1(d)

Figure1. Microphotographs obtained in between the crossed polars.

1(a) Spherulitic texture of Cholesteric phase ,

1(b) Texture of composition of Isogyres and SmA phase(250 X),

1(c) Texture of SmA phase(250 X)

1(d) Texture of SmE phase(250 X)

IV. OPTICAL ANISOTROPY

Temperature variations of refractive indices for sample of 70% Diethyl 4-4¹Hexaloxo Azoxy Benzoate and 30% of cholesteryl nonanoate is presented in Figure (2). From figure it is clear that, value of ordinary refractive index is more

than the extraordinary refractive index for all temperatures. The value of extraordinary refractive index decreases non-linearly upto 190°C and remains same after 190°C . The value of ordinary refractive index decreases non-linearly upto 170°C and increases upto 200°C . The value of ordinary refractive index as well as extraordinary approaches same at cholestric- isotropic transition, both the values remains same from 200°C to 210°C .

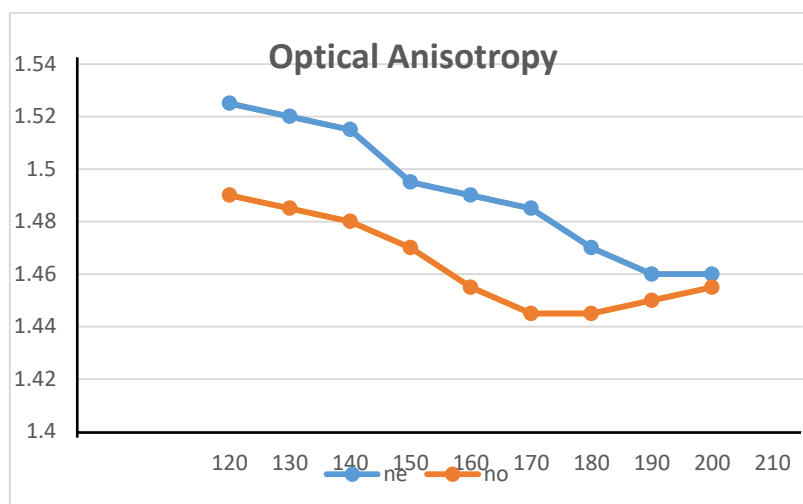


Figure -2

V. CONCLUSION

Microscopic investigation of mixture of liquid crystal compound 70% of Diethyl 4-4¹Hexaloxo Azoxy Benzoate and 30% of cholesteryl nonanoate exhibits cholestric, SmA and SmE phases sequentially when the mixture is cooled from isotropic phase, for all concentration of given mixture. The optical texture studies clearly indicates the above sequential phase changes for binary mixture of Diethyl 4-4¹Hexaloxo Azoxy Benzoate and cholesteryl nonanoate for all concentrations. The temperature variations of refractive indices of liquid crystalline binary mixture shows almost decrease in ordinary as well as extraordinary refractive indices.

REFERENCES

1. N.D.Mermin, "crystalline liquid: the blue phases", Reviews of Modern physics, Vol.61, PP. 385-432, 1989
2. Ujjie, S and Yano, Y.Chem(2000) Commun 79-80.

3. Govindaiah.T.N., Sreepad.H.R., Nagappa and Mahadeva.J.(2014). Mol.Cryst.liq.cryst.593,51-60.
4. Mahadeva, J and Govindaiah.T.N, Optical and Electro optical studies on liquid crystalline material, Mol.cryst.liq.cryst.,631,646(2016).
5. Porov.P.et.al, Optical studies of dye doped cholesteric liquid crystal, Jon of liquid crystals, V-1 (2016)
6. Mahadeva, J.et.al, Optical studies on cholesteric and sematic phases of Ternary mixtures of liquid crystalline materials, proceedings of National level seminar on crystallography, Bharathi college, Bharathinagar, Karnataka(2018).
7. Nagappa, Nataraj, & Krishnamurthy, D(1986).Mol.Cryst.Liq.Cryst.133,31
8. Neugebaur, H.E.J (1954). Canad. J. Phys, 32,1.

* * * * *

- **Dr. P. Srinivas, Sushma**, PET Research Foundation, PES Engineering college campus, Mandya, India, **Ph:** 9448643148, **E-mail:** ssdisha@gmail.com
- **Dr. J. Mahadeva**, Principal, PES College of Science, Arts & Commerce, Mandya, India, **Ph:** 9448872283,

Thermo-Optical Studies on Reentrant Smectic Phase of Liquid Crystalline Materials



○ Dr. T.N. Govindaiah

ABSTRACT

In the present work, our investigation is to study on the optical and electrical properties of multi-component system of cholesteryl nonanoate (CN), laurylpyridinium chloride (LPC) and Orthophosphoric acid (H_3PO_4). Mixtures of these molecules exhibits cholesteric, SmA, SmC, ReSmA, SmE, and SmB phases sequentially when the specimen cooled from its isotropic phase. These phases have been characterized by using microscopic technique. The temperature variation refractive indices and electrical conductivity has been discussed.

Keywords: Optical textures; Temperature dependence; Electrical conductivity.

INTRODUCTION

Liquid crystals are primarily liquids but also share properties of crystalline materials. Usually, liquids are characterized by isotropic macroscopic properties and by the ability to flow while crystals are characterized by long range positional order which leads to anisotropic macroscopic properties. Like liquids, liquid crystals exhibit fluidity. They are made up of organic molecules characterized by anisotropic molecular properties and by short range molecular interactions which couple over many molecular diameters to produce long range orientational order [1, 2]. These characteristics results are in anisotropic macroscopic properties such as birefringence, density, susceptibilities and optical studies etc.

In the present investigation, our aim is to study the multi-components, namely, cholesteryl nonanoate (CN), laurylpyridinium chloride (LPC) and Orthophosphoric acid (H_3PO_4), which exhibits cholesteric and induced smectic phases such as SmA, SmC reentrant SmA, SmE and SmB respectively at different temperatures. These phases were observed using microscopic technique. Optical and

thermal studies have also been carried out to understand the intermolecular interactions of the given multi-component system.

EXPERIMENTAL STUDIES

In the present study, we use the materials, namely, cholesteryl nonanoate (CN), laurylpyridinium chloride (LPC) and Orthophosphoric acid (H_3PO_4). Mixtures of different concentrations of CN in $LPC+H_3PO_4$ were prepared and they were mixed thoroughly. These mixtures of concentrations were kept in desiccators for 6 hours. Samples were subjected to several cycles of heating, stirring, and centrifuging to ensure homogeneity. Phase transition temperatures of these mixtures were measured with the help of a Gippon-Japan polarizing microscope in conjunction with a hot stage. The samples were sandwiched between the slide and cover slip and were sealed for microscopic observations. The refractive indices in the optical region are determined at different temperatures by employing the techniques described by the earlier investigators [3-5]. Electrical-conductivity measurements of the mixture at different temperatures were carried out using digital LCR meter and a proportional temperature control unit.

RESULTS AND DISCUSSIONS

OPTICAL TEXTURE STUDIES

For the purpose of optical texture studies, the sample was sandwiched between the slide and cover glass and then the optical textures were observed using Leitz-polarizing microscope in conjunction with specially constructed hot stage. For our experimental studies, we have considered the ternary system of cholesteryl nonanoate (CN) molecules are at 11% of concentration and 50% concentration of laurylpyridinium chloride (LPC) molecules mixed with 39% concentrations of Orthophosphoric acid (H_3PO_4). The ratio of these mixtures prepared and mixed thoroughly and they were kept in desiccators for a long time. The samples were subjected to several cycles of heating, stirring and centrifuging to ensure homogeneity. The phase transition temperatures of these concentrations were measured with the help of Gippon-Japan polarizing microscope in conjunction with a hot stage. The concentration of given mixtures are slowly cooled from its isotropic melt, the genesis of nucleation starts in the form of small bubbles and slowly grow radially, which form a fingerprint pattern of cholesteric phase with large values of pitch [6, 7]. On further cooling the specimen, the cholesteric phase slowly changes

over to focal conic fan shaped texture, which is the characteristics of SmA phase as shown in Figure 1(a). On further cooling the specimen, SmA phase changes over to schlieren texture of SmC phase, which as shown in Figure 1(b). The SmC phase is unstable and then this phase changes over to bubbles in the form of battonnets, which are the characteristic of SmA phase and this phase has been termed as the reentrant SmA (ReSmA) phase. On further cooling, this phase changes over to the radial stirrations of SmE phase and then this phase changes over to the hexagonally highly ordered smectic-B phase, which remains stable at room temperature [8].

OPTICAL ANISOTROPY

Results of this investigation are further supported by the optical studies. The refractive indices for extraordinary ray (n_e) and ordinary ray (n_o) of the mixture were measured at different temperatures for different concentrations using Abbe Refractometer and precession Goniometer Spectrometer. The temperature variations of refractive indices for 11% of CN in LPC+H₃PO₄ are as shown in Figure 2. The value of n_e is greater than n_o , indicating that the material is uniaxial positive. The values of electrical susceptibility for 11% of CN in LPC+H₃PO₄ have been calculated using Neugebauer relation [9] at different temperatures. The temperature variations of electrical susceptibility for the mixture are as shown in Figure 3. From the figure, it can be observed that wherever there is an isotropic-liquid crystalline phase transition, the value of electrical susceptibility changes appreciably, which indicates that each change corresponds to the occurrence of different liquid crystalline phases. Further, with increase in the concentration of CN, the value of electrical susceptibility decreases with temperature, because the effective optical anisotropy associated with the molecules of CN also decreases.

CONDUCTIVITY MEASUREMENTS

Electrical-conductivity measurements are helpful in the study of phase behavior with temperature. An abrupt increase or decrease of electrical-conductivity with temperature relates to the phase behavior of the lyotropic/thermotropic system [10]. Temperature variations in electrical conductivity are shown in Figure 4. The figure clearly illustrates that there is a change in the value of electrical conductivity from 35 to 98^oC while cooling from isotropic phase for the mixture of 11% of CN in LPC+H₃PO₄. With further decrease in temperature, the electrical conductivity starts decreasing as we move toward room temperature. For the given concentrations of

11% of CN in LPC+H₃PO₄, the sequence of phases changes from Cho→SmA, SmA→SmC, SmC→ReSmA, ReSmA→SmE and SmE→SmB phases. If some value of electrical conductivity goes on increasing with decreasing temperature. Changes in electrical conductivity are observed only after further cooling of specimen. This suggests that the size of aggregates starts growing toward decreasing temperature and the system moves toward more orderliness. Finally, below 40 °C, the size of aggregates becomes large that the specimen starts moving toward crystalline nature [11-13].

CONCLUSIONS

Microscopic investigation of the ternary mixture of CN in LPC+H₃PO₄ shows the existence of reentrant smectic-A phase in addition to the cholesteric, SmA, SmC, SmE, and SmB phases for different concentrations and respectively at different temperature. The phase behavior is discussed with the help of phase diagram. The changes in value of electrical susceptibility and electrical conductivity with the variation of temperature unambiguously correspond to smectic and cholesteric phases. Drastic changes in these parameters are expected to be due to changes in the dimension of disc along with changes in the orientation order of the arrangement.

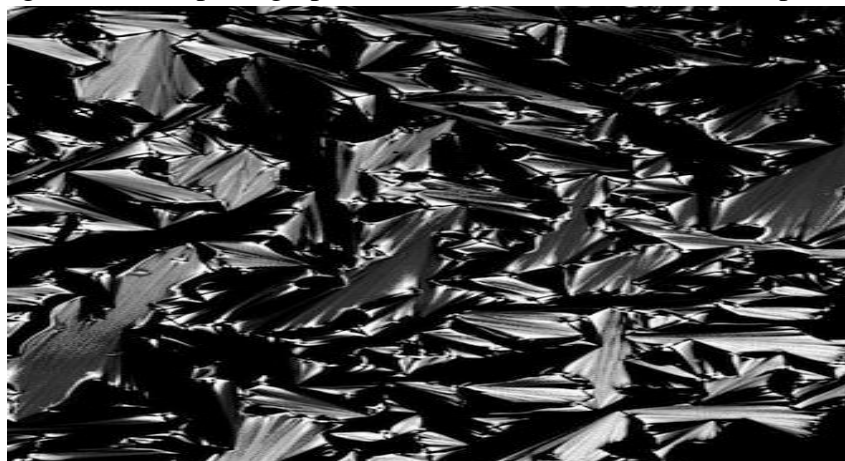
REFERENCES

1. de Gennes, P. G. and Prost, J. The Physics of Liquid Crystals, Clarendon Press: Oxford, U.K. (1975).
2. Bahadur, BEdtn. Liquid Crystals-Applications and Uses. Singapore: 1-3 World Scientific. (1990).
3. Nagappa, Revanasiddaiah, D. and Krishnamurti D. (1983). *Mol. Cryst. Liq. Cryst.*101, 103–127.
4. Govindaiah T. N, Sreepad H. R, Nagappa. (2014). *Mol.Cryst. Liq. Cryst.*592, 82-90.
5. Govindaiah, T. N., Sreepad, H. R., & Nagappa. (2013). *Mol. Cryst. Liq. Cryst.* 574, 9–18.
6. Demus D, & Richter C. 1978. *Textures of Liquid Crystals*, Weinheim: New York, Verlag Chemi.
7. Govindaiah, T.N. (2015). *Mol. Cryst. Liq. Cryst.* 623, 74–79.

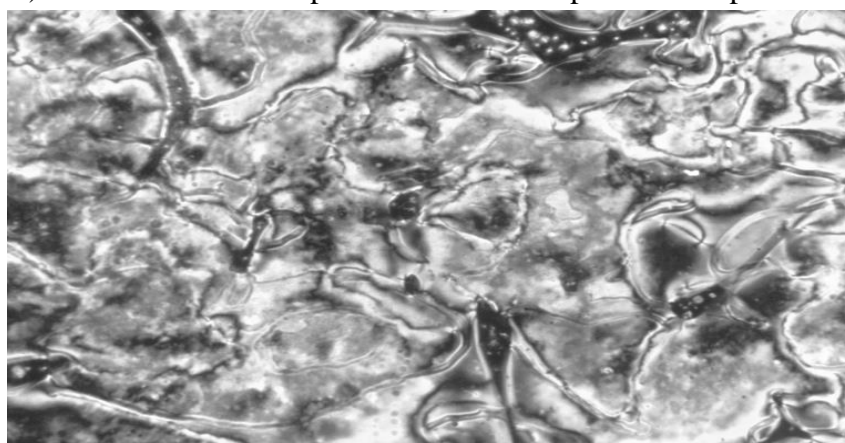
8. Govindaiah, T. N., Sreepad, H. R., Kempegowda, B. K., & Nagappa. (2013). *Mol. Cryst. Liq. Cryst.*, 587, 54–59.
9. Neugebauer, H. E. J. (1954). *Canad. J. Phys.* 32, 1.
10. Marthandappa, M., Nagappa, & Lokhanatha Rai, K. M. (1991). *J. Phys. Chem.* 95, 6369.
11. Franeois, J. (1971). *Kolloid, Z. Z. Polym.* 246, 606.
12. Govindaiah, T. N., Sreepad, H. R., Sathyanarayana, P.M., Mahadeva, J., & Nagappa. (2012). *Mol. Cryst. Liq. Cryst.* 552, 24–32.
13. Djavanbakht, A., Kale, K. M. and Zana, R. (1977). *J. Coll. Int. Sci.*, 59(1), 139–148.

Figure Captions

Figure 1. Microphotographs obtained in between the crossed polars,



a) Focal conic fan shaped texture of SmA phase at temperature (250X).



b) Schlieren texture of SmC phase at temperature (250X).

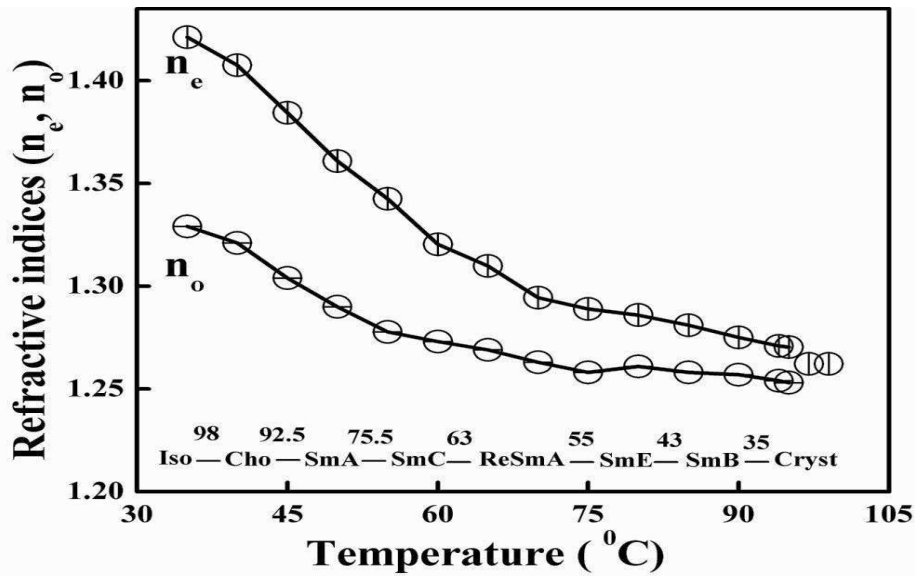


Figure 2. Temperature variations of refractive indices for the mixture of 11% of CN in $\text{LPC}+\text{H}_3\text{PO}_4$.

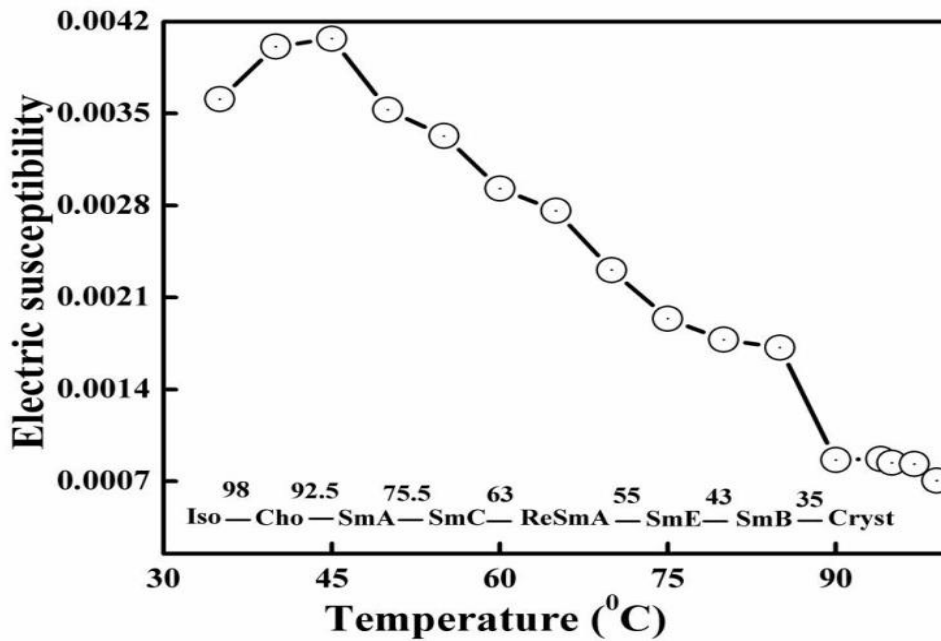


Figure 3. Temperature variation of electrical susceptibility for the mixture of 11% of CN in $\text{LPC}+\text{H}_3\text{PO}_4$.

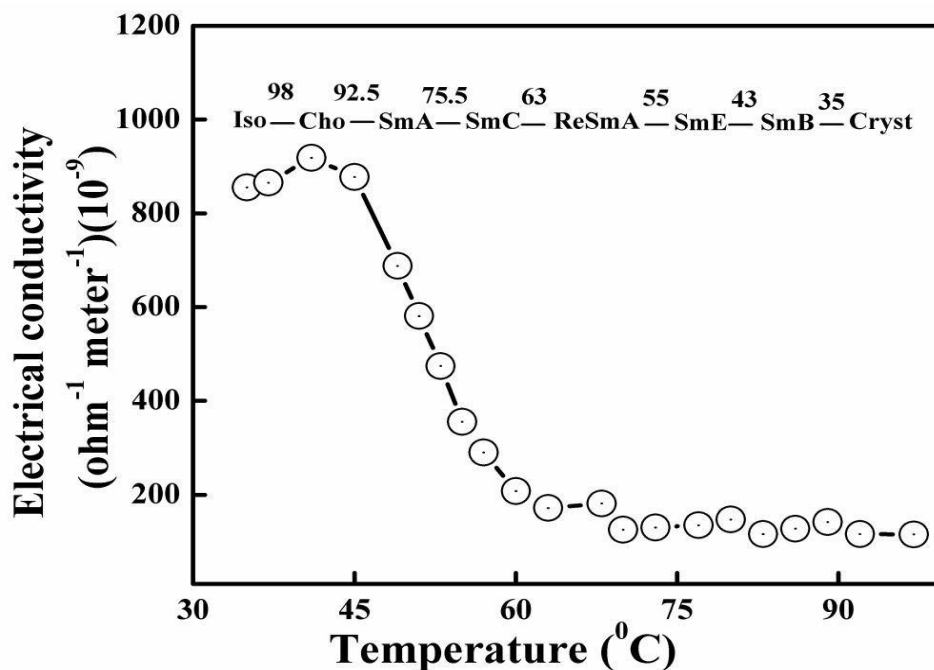


Figure 4. Temperature variation of electrical-conductivity σ ($\times 10^{-9} \Omega^{-1} \text{ m}^{-1}$) for the mixture of 11% of CN in $\text{LPC} + \text{H}_3\text{PO}_4$.

* * * * *

❖ **Dr. T.N. Govindaiah**, Asst. Professor, P.G. Department of Physics, Government College (Autonomous), Mandya-571401, India. **Ph:** 8073901643, **E-mail:** tngovi.phy@gmail.com



'Current Trends in Physics 2021' is a compendium of 30 peer reviewed articles on contemporary interests and investigation in Physics with an emphatic focus on the discovery of God Particle. However, included are also articles on topics like the Quantum computation and information, Quantum cryptography, Quantum teleportation, Nano Science and Nano Technology, MEMs, Paradoxes in Relativity, Nuclear and Particle Physics that have enriched this volume. These were presented at the International Seminar and cover both theoretical and experimental features of the subject including instrumentation and device parameters. Articles in this book are categorised primarily in two sections, one dedicated to theoretical aspect and the other devoted to the experimental facet. This book is being brought out to convey the excitement of Physics to students, Researchers, Professors and Industry experts and prod the concerned to check on the application potential of ideas and refining of experimental set up.

Dr. B.K. Lokesh



9 789388 956413